Automated assessment of measurement performance in optical coordinate metrology

Sofia Catalucci

Faculty of Engineering

University of Nottingham

Thesis submitted to the University of Nottingham for the degree of

Doctor of Philosophy

June 2021

Coraggio lasciare tutto indietro e andare

partire per ricominciare

che non c'è niente di più vero di un miraggio.

E per quanta strada ancora c'è da fare

amerai il finale.

C. Cremonini

Declaration

I hereby declare that except where specific reference is made to the work of others, the contents of this thesis are original and have not been submitted in whole or in part for consideration for any other degree or qualification in this, or any other university. This thesis is my own work and contains nothing which is the outcome of work done in collaboration with others, except as specified in the text and Acknowledgements. This thesis contains fewer than 65,000 words including appendices, bibliography, tables and equations and has fewer than 150 figures. This work has been carried out with the support of the Engineering and Physical Sciences Research Council (EPSRC), the Manufacturing Metrology Team, and the Faculty of Engineering at the University of Nottingham. Support was given by BMW Group, in particular the BMW Research and Development Centre team in Munich, for providing one of the test samples and allowing the use of their facilities. This work has been funded by EPSRC and by the University of Nottingham Vice Chancellor's Scholarship for European Research Excellence.

Sofia Catalucci

June 2021

Acknowledgements

I would like to acknowledge my supervisors Richard Leach and Samanta Piano for their guidance throughout the PhD, and for given me the opportunity to join a great team of researchers. A special thanks goes to Nicola Senin, my mentor and trusted adviser, my friendly "bridge" to Italy, who's always motivated me since the very beginning of this adventure.

I would like to dedicate this thesis to my beautiful family and to all those that have supported me along the way. To mum and dad, who've always stood by my side and supported my dreams and choices. To my gramps, both here and up there, who've showed me their love in all possible imaginable ways. To Martina, my person. To Violetta, my night out amazing companion. To Amrozia, my dearest confidant. To Damiana, source of all my smiles. To Caterina and Federica, my inspirations. To Danny, my wingman. To Luke and Lewis, the best office fun and fellow advisors. To my MMT colleagues, for their help, shared expertise, laughs and fun time together. To the members of my band Luca, Davide, Mattia, Andrea, Sabino, my music mates. To Giorgio, the rhythm of my heart. And most importantly to my favourite drummer (and brother) Raffaele: I will always be your biggest fan. Ain't no me without you all.

Abstract

The measurement of parts of high geometrical complexity, such as those fabricated via additive manufacturing technologies, represents a fundamental challenge for the quality assurance of manufactured components. The pressing need shared nowadays by numerous industrial sectors for obtaining increased product quality while reducing development times and costs, as well as achieving faster speed of production and inspection planning in mass customisation (ideally performed in real-time), are leading towards the design of smart measurement systems that, integrated directly in the production line, can achieve part quality inspection in a fully automated way. The future possibility of developing such "intelligent" instruments implies their capability of autonomously planning a measurement process and assessing measurement performance while the inspection task is in progress, making use of available pre-existing knowledge of parts, instruments and technologies, and employing smart algorithms for the optimisation of measuring procedures. In this context, optical coordinate measurement technologies appear as suitable candidates, due to their potential in featuring high densities in point-based sampling acquired at relatively fast rates, and in accessing complex surfaces despite line-of-sight issues. However, without metrics for quality, the

employment and integration of such smart instruments cannot be fully accomplished.

This thesis addresses the issue of quality in measurement, proposing algorithmic solutions to compute indicators of measurement performance directly from the measured point clouds and in a fully automated way. Starting solely from the knowledge acquired of the measured data and the underlying nominal geometry, these indicators are based on algorithmic point cloud processing pipelines, and make use of computational geometry and spatial statistics to primarily extract information about the quality of the measurement result. A first set of measurement performance indicators investigates the relationships between the measured point cloud and the reference geometry (in the form of triangle meshes) to automatically assess coverage and sampling density in relation to the individual surfaces of the measured part. Additionally, local dispersion of the measured points with respect to the underlying part region is evaluated. A second set of indicators investigates local dispersion of the point cloud, as well as local bias, by using a statistical point cloud models fitted to repeated measurement data. The second set of indicators is useful to assess metrological performance in repeatability or reproducibility conditions. The proposed sets of indicators are illustrated and validated through application to selected test cases of industrial relevance, generated via additive manufacturing technologies.

The solutions developed and discussed in this thesis represent novel measurement performance assessment tools, which can be integrated into smart measurement systems. In the future, such instruments will be capable of self-assessing their own performance in-process (*i.e.,* while measuring), and

will be capable of planning the most suitable corrective actions, in the case that issues are detected in the quality of the measurement result (for instance, insufficient degree of coverage, unacceptable measurement error). Furthermore, such intelligent measuring systems will be suitable for integration with manufacturing machines, leading to the realisation of more flexible and more autonomous production systems.

Table of contents

List of figures

List of tables

List of abbreviations

AM Additive Manufacturing
AI Artificial Intelligence
ML Machine learning
CMS Coordinate Measuring System
VIM International Vocabulary of Metrology
SI International System of Units
GUM Guide to Expression of Uncertainty in Measurement
ISO International Organisation for Standardisation
3D Three-dimensional
CMMs Coordinate Measuring Machines
SfM Structure from Motion
TOF Time-of-flight
IRM Information-rich metrology
NBV Next Best View
STL STereoLithography
2D Two-dimensional
AABB Axis-aligned bounding box
OBB Oriented bounding box
PCA Principal component analysis
BSP Binary space partitioning
k-NN k-nearest neighbours
EMST Euclidean minimum spanning tree

DT Delaunay triangulation
NURBS Non-uniform rational basis splines
FPFH Fast Point Feature Histograms
PFH Point Feature Histograms
SPFH Simplified Point Feature Histogram
TLS Total-least-squares
OLS Ordinary-least-squares
RANSAC Random sample consensus
ICP Iterative closest points
cRMSE Coordinate root mean squared error
dRMSE Distance root mean squared error
GRF Gaussian random field
DSLR Digital single-lens reflex
LPBF Laser Powder Bed Fusion
NIST National Institute of Standards and Technology
MMT Manufacturing Metrology Team
MPE Maximum Permissible Error
MC Monte Carlo
PG Photogrammetry
FP Fringe projection
SL Structured light
SIFT Scale invariant feature transform
NPL National Physical Laboratory
TRL Technology readiness level

Chapter 1

Introduction

1.1 Background

Additive manufacturing (AM) or additive layer manufacturing, defined in ISO/ASTM 52900 [1] as the "process of joining materials to make parts from 3D model data, usually layer upon layer, as opposed to subtractive manufacturing and formative manufacturing methodologies", allows for increased design freedom. Components can be fabricated with hollow features and freeform geometries, where "freeform" indicates that the shape of a part does not conform to any mathematical known primitive form (for example ellipsoids, paraboloids, *etc.*) [2,3]. Additionally, unlike conventional surfaces, such as planes, spheres and cylinders that usually possess rotational and translational symmetry, by definition, freeform shapes are surfaces without

rotational or translational invariance [3]. In traditional manufacturing complex geometries were previously impossible to fabricate [4]; the fabrication of parts was mostly characterised by high production volumes of less complex shapes, generated by conventional means. On the other hand, AM presents nowadays the appealing advantage of allowing for mass-customisation of parts in flexible manufacturing scenario characterised by low volumes of production. Examples of additively manufactured parts presenting high geometrical complexities are given in Figure 1.1.

Figure 1.1 Examples of freeform complex additively manufactured components

Because of this new gained freedom, the increased application of AM in many industries, which includes the automotive, aerospace and biomedical sectors [5], is creating a series of measurement challenges that have not been completely solved yet. Parts are required to withstand demanding inspection and verification processes, and the correct measurement of their form and surface texture is a key aspect for product quality, along with feedback for effective process control [2,5]. One of the issues of measuring an AM part is related to the high diversity of shapes that one may be called to inspect. The

quick turnaround of geometries may work against the time and resources required to properly plan an inspection process, which includes finding the optimal measurement set-ups, fabricating optimised measurement fixtures, planning poses, selecting measurement technologies, *etc.* In addition to the variety of shapes, the design freedom and geometrical complexity of AM components require high sampling density in point-based measurement, and limit current contact and non-contact coordinate measuring systems, which appear to lack flexibility, struggle to measure parts presenting high slope angles or difficult to access regions, and , if optical, are unsuitable for surfaces with high reflectivity [5–10].

In this context, the development of "smart" coordinate metrology systems and applications able to overcome the aforementioned limitations is therefore becoming vital, especially into the frame of advanced manufacturing technologies and Industry 4.0 [11–13]. A system is defined as "smart" when it is able to incorporate functions of automatic operability and consequent corrections in order to quickly target issues and respond to specific situations, making decisions based on the available data in a predictive or adaptive way [14,15]. For instance, intelligent measurement systems are envisioned as capable of merging the advantages of the underlying measurement technologies with increased capability of self-adaptation and flexibility [16]. In particular, flexibility is defined in the roadmap "Manufacturing Metrology 2020" (VDI/VDE-GMA [17,18]) as the "adaptation to changes in measurement tasks", meaning respond flexibly to changes in measurement requirements and be able to inspect different features and new components in a fully-automated way. Flexibility can be achieved for instance through the

elaboration of available information (*i.e.,* information-rich metrology paradigm, specifically aimed at improving measurement quality) and *a priori* knowledge (*i.e.,* knowledge of the manufacturing process, knowledge of measured object, knowledge of the measurement technology principles, *etc.*) [19–21], concepts recurrent in this thesis and later extensively discussed (see Chapter 2). Pre-existing information would help to improve the measurement procedure, guide the inspection and verification of part quality, or monitor the manufacturing process [19–21]. In addition to the use of available knowledge, the smart property of a system resides in its ability to perform autonomous operations with the integration of new functionalities for the optimisation of the measuring process, automation of process quality control, autonomous decision-making and corrections [14,15]. Examples of smart functionalities are for instance integrated features of sensing, control, and actuation, artificial intelligence (AI) technologies and machine learning (ML) integrated algorithms (for example, optimisation algorithms for increasing parts accessibility, surface feature recognition, pose estimation, *etc.*), adaptability to combine multiple sensors and/or measuring technologies (for example, multi-view/multi-sensors systems).

An example of an optical coordinate measuring system (CMS) embedded with AI technology is schematically shown in Figure 1.2. Available *a priori* information (for instance, the CAD model of the part, *etc.*) fed into the measuring pipeline and combined with AI technologies would help determine the optimal views needed to fully acquire a part, whilst keeping the number of views to a minimum in order to save time for further measurement and processing actions. In addition, the smart system would include feedback loops

in the measuring process in order to understand how the measurement is proceeding, while the measurement itself has been executed.

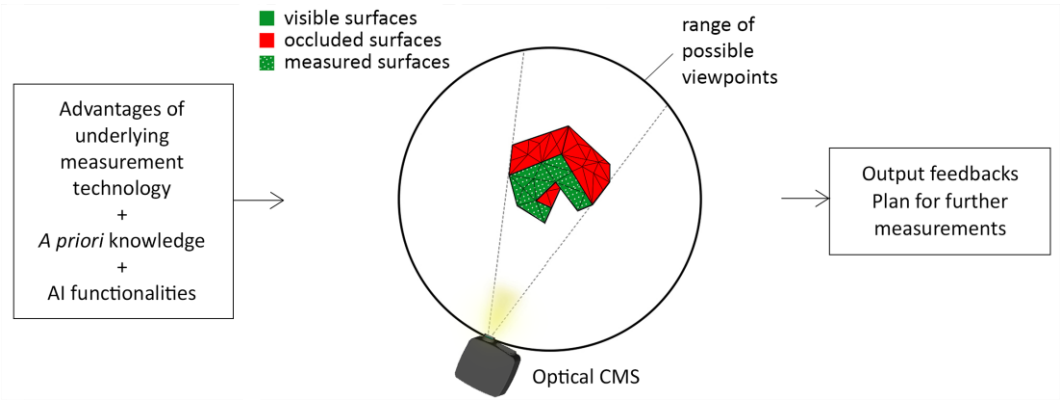

Figure 1.2 Schematic representation of an AI-powered decisional smart system. The advantages of optical technologies are merged with *a priori* information and AI functionalities, in order to maximise measurement accessibility. Surfaces with no associated points (marked in red) are usually outside of the viewing range, or covered by other surfaces. The system returns feedback of the measurement performance and suggestions for additional measurement actions

Intelligent systems and their consequent optimised measurement results will enable industries to increase volumes and speed the production, especially in large scale manufacturing where measuring the complete geometry of a part is essential, as it allows the manufacturer to perform fast and reliable inspections performed in real-time [11,16,22].

1.2 Proposed work

The ultimate vision of fully automated smart measuring systems is accompanied by the assessment of measurement performance accomplished in real-time (*i.e.,* in-process quality assessment while the measurement is being performed). Based on the resultant feedbacks and outputs from the measuring procedure, the smart system will then be able to correct itself and streamline the additional measurements required in order to increase the quality of the results.

The work presented in this thesis focuses on the preliminary development of a set of algorithmic solutions designed to guide optical CMSs towards future full automation of part inspection and intelligent measurement planning. The integrated smart functionalities previously introduced in Section 1.1 are assumed as achievable thanks to the potential of the measuring system to compute the quality of a measurement via the use of performance indicators.

In this work, the proposed set of algorithmic solutions define an intelligent instrument prototype based on the assumptions that

a) quality is assessed after the measurement has been performed (preliminary prototype algorithms are implemented on available high-density point clouds - *i.e.,* post-measurement quality assessment);

b) detection of potential issues in the measurement results is addressed following a semi-automated approach (*i.e.,* the prototype provides indications in form of quality indicators to an operator in order to plan

further measurement activities for correction or improvement of the measurement result).

The designed performance indicators provide insights not only related to measurement uncertainty, but also describe the intrinsic properties of a measurement, outline ways to identify regions of the measured part where the scan has not been successful, and assess the metrological performances of a measurement when compared to its underlying nominal geometry. The indicators are intended to be integrated in future physical systems towards full automation of optical CMSs, enabling the measurement system to automatically identify regions of the measured part where the scan has not been successful, streamlining the additional measurement plans required.

In the context of the research objectives, a series of research questions will be answered throughout the thesis and summarised in the thesis conclusions. The research questions are the following:

1) How can we define the quality of a measurement?
2) Coordinate metrology frequently relies on the concept of measurement uncertainty. Is measurement uncertainty enough to define the quality of a measurement or are there other aspects of the measurement pipeline that are not covered by uncertainty?
3) Is it possible to define a series of quality indicators that cover all the relevant aspects, including – but not limited to – measurement uncertainty?
4) Can the computation of such quality indicators be integrated (and performed in an automated way) into the measurement pipeline?

1.3 Measurement quality definition and novelty of work

Quality in measurement is intended in this thesis as a generic term encompassing multiple aspects. Improving the quality of a measurement or a measurement process includes achieving fast rates in the measurement time, improving indicators of metrological performance (such as accuracy, precision, *etc.*), expanding the range of covered scales (spatial resolution and range), improving the degree of coverage of a measurement (meaning the actual percentage of the external surface of an object successfully covered, *i.e.,* measured), augmenting the part accessibility or, in other words, the capability for a given measurement technology to reach surfaces which may be occluded or hidden from the line-of-sight (for instance, hollow features and high slope angles). Improving measurement quality may also mean that it is possible to obtain results equal to the ones achievable without employment of any particular optimised strategy, but at fractions of the time and costs, deploying new technologies and employing more affordable instruments.

The novelty of this Ph.D. work resides on the development of new approaches for the assessment of quality in measurement in the context of complex additively manufactured products. A set of algorithms for computing unique indicators of measurement performance have been developed, based on the knowledge of measured point clouds and their underlying registered CAD geometry. As quality in measurement does not only refer to measurement uncertainty but addresses elements related to extents and density of surface

coverage, two separate sets of novel performance indicators have been designed as contribution to the field: measurement quality indicators and indicators derived from a statistical point cloud model. For the first time, the developed performance indicators do not simply provide a scalar number representative of the entire part, but they offer a detailed map of measurement performance and behaviour in correspondence to every region of the part.

The first set of indicators, defined in this thesis as measurement quality indicators, is computed from single high-density measurements, and do not require any additional information apart from the knowledge of the nominal reference geometry (in form of triangle mesh) and of the dataset itself. The majority of the indicators of the first set rely on the point cloud being finely registered to the reference mesh and subsets of points associated to specific triangles. The measurement quality indicators address multiple perspectives, not only limited to the computation of conventional metrological criteria (for example the uncertainty associated to features of size), but also performance and behaviour at the point cloud level, for example coverage, accessibility of critical regions of a part surface, sampling and density representativeness, and spatial dispersion of the points with respect to the associated, reference surface. These indicators are the most directly applicable for implementing the "smartness" (and future full automation) of optical CMSs.

The second set of indicators is derived from the development of a statistical point cloud model used to propose a novel approach for the investigation of the precision of measurements (*i.e.,* random error in repeatability/reproducibility conditions). The approach is based on the construction and fitting of a statistical model to high-density point clouds

produced by optical measurement repeats. The derived indicators are directly useable in a smart measurement system only if it implements a measurement technology where taking multiple measurements is viable and does not imply excessive cost. However, even when measurement repeats are not convenient, these indicators can be computed in preliminary experimental campaigns and provide insight on the interaction between the measurement system and the measured part.

Figure 1.3 illustrates the complete measurement pipeline defined in this thesis for the computation of the aforementioned sets of indicators, implemented as preliminary prototypical algorithms that can act as proof-of-concept for the development of future fully-automated smart CMSs.

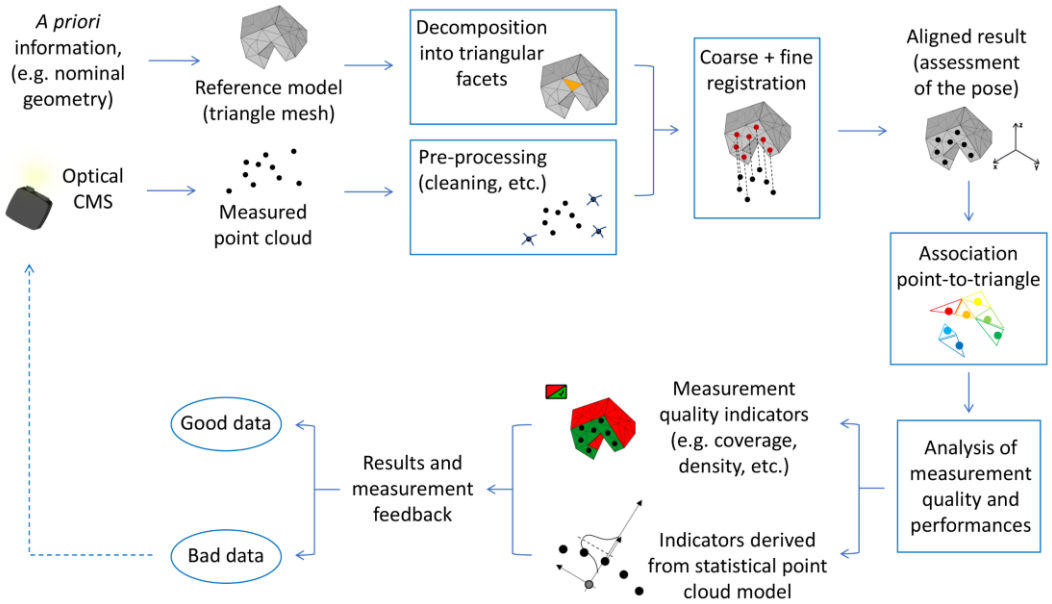

Figure 1.3 Schematic representation of the semi-automated workflow procedure for the assessment of the quality of measurement results via the definition of performance indicators

The algorithmic implementation mainly focuses on results coming from optical measuring technologies, given that non-contact instruments reproduce high-density point cloud surface data compared to tactile CMSs. However, for the evaluation of several indicators contact measurements are utilised as reference given their high accuracy. The pipeline starts from the input of the reference geometry in form of triangle mesh (utilising the *a priori* information available) and the point cloud measured with an optical CMS. While the point cloud is processed and cleaned from the artefacts caused by the measurement, the structure connectivity of the elements composing the triangle mesh (*i.e.,* triangle facets) is analysed and indexed. The two datasets are then finely registered, and subsets of points are associated to regions of the mesh (*i.e.,* point-to-triangle associations). As previously stated, the association of the point cloud with the triangle mesh is required for the definition of the majority of the indicators presented in this thesis. Once the two sets of indicators are computed, the operator is provided with indications and feedbacks of the measurement results, in order to evaluate if additional measurement activities are required. Details, discussion and examples regarding each specific step of the described pipeline will be illustrated and provided to the reader throughout the thesis.

1.4 Thesis outline

Chapter 2 begins by giving an overview of metrology and measurement uncertainty, discusses the basics of current optical coordinate technologies for

the measurement of the external shape of a part, and illustrates some of the advances recently made towards the development of smart systems and intelligent measurement strategies. A state-of-the-art review in point cloud analysis and processing is then presented, covering formal representation, pre-processing, partitioning, fitting, registration and comparison to CAD, and additionally illustrating methods for the incorporation of uncertainty into point cloud data. The chapter ends with a discussion and a summary of the key areas addressed in this project, which reflect the gaps found in research.

Chapter 3 describes the steps required to achieve registration of the measured point cloud to the underlying reference geometry representing the measured part, and the consequent assessment of the pose. Registration is a fundamental step of the measurement pipeline, especially for the computation of the measurement quality indicators and the development of the statistical point cloud model discussed respectively in Chapters 4 and 5. The registration approach based on landmark matching using similarity metrics is applied to selected industrial cases featuring AM components.

Chapter 4 introduces the first set of performance indicators computed on individual point clouds. Here, aspects such as measurement effort, intrinsic properties of measured point cloud, part coverage, and metrological performance of measurements are presented, along with the definitions of the indicators and the method developed to estimate them.

Chapter 5 illustrates the statistical point cloud model, generated and fitted to high-density point clouds produced by optical measurement repeats. Indicators derived from the statistical model are then illustrated, useful to assess metrological performance in repeatability or reproducibility conditions.

Chapter 6 shows the application of the indicators defined in Chapters 4 and 5 on the selected industrial cases described in Chapter 3, measured with different optical instruments, reporting a complete summary and discussion of the results obtained from the indicators defined and methods developed.

Finally, Chapter 7 concludes the thesis by giving a summary of the main findings, and highlighting the contributions of the Ph.D. to the field. The opportunities for future work, which can expand upon what is introduced here to increase its scope and impact, highlight the concept that the proposed indicators represent only a building block for the development of future smart fully-automated measuring systems.

Chapter 2

Background and related work

Three-dimensional point clouds play a central role in coordinate metrology: they are the product of coordinate measurement systems, and the starting point for the data processing methods that produce inspection and verification results. As measurement technologies evolve, increasingly denser point clouds are being produced, capable of capturing geometric information at unprecedented level of detail, which is particularly important for complex freeform and multi-scale surfaces typically found in additively manufactured components.

A general overview of metrology and uncertainty in measurement, basic concepts of the most suitable non-contact coordinate technologies for the measurement of parts produced by additive manufacturing (AM) are discussed hereafter, along with an overview of some of the current solutions towards the development of "smarter" systems, in particular the integration

of *a priori* knowledge and performance indicators into the measuring pipeline. It is worth mentioning that this PhD project did not focus in depth on the study of the physical principles of the measurement technologies, although optical instruments were employed in order to test the performances of the developed set of algorithmic solutions applied to the measurements of selected test cases. In particular, this research project concentrated on the development of a pipeline for point cloud processing, and on the design at an algorithmic level of point cloud analysis strategies for the assessment of quality in measurement. For this reasons, a comprehensive review of the state-of-the-art in point cloud analysis is presented in this chapter, covering formal representation, pre-processing, partitioning, registration, and incorporation of measurement error and measurement uncertainty into point clouds. The contents related to the state-of-the-art review are published in the book *Advances in Optical Form and Coordinate Metrology* [23].

2.1 Metrology overview

2.1.1 Metrology and measurement uncertainty

According to the international vocabulary of metrology (VIM) [24], metrology is "the science of measurement and its application", including all theoretical and practical aspects of measurement, measurement uncertainty and its field of application. Metrology broadly encompasses various fields of research primarily related to the measurement of any of the seven base quantities from

the International System of Units (SI) [25], or any of the units derived from these base quantities (*i.e.,* length, mass, time, electric current, thermodynamic temperature, amount of substance and luminous intensity). Measurement is specifically defined as the "process of experimentally obtaining one or more quantity values that can reasonably be attributed to a quantity", referred to as a measurand [24]. After (or during) the manufacturing process of a part, measurements (dimensional or otherwise, with dimensional defined in Ferrucci et al. [26] as the geometrical measurements more critical in industrial scenarios, for example length, area, volume, flatness and roundness) are routinely made in order to compare measurands to specifications. For example, the designer will generally specify a dimension with a related tolerance; if the measured quantity lies within the defined tolerance, the component will successfully pass the inspection process.

Each measured quantity will always have an uncertainty associated to it [27]. Measurement uncertainty is defined as a "non-negative parameter characterising the dispersion of the quantity values being attributed to a measurand, based on the information used" [24] or, in other words, the doubt that exists about the result of any measurement [28]. General methodological aspects related to how uncertainty contributions may be estimated and combined can be found in the *Guide to the Expression of Uncertainty in Measurement* (GUM) [27–29].

2.1.1.1 Approaches to the estimation of measurement uncertainty

One approach to estimate measurement uncertainty consists of starting from first principles, *i.e.,* starting from the detailed study of all possible error

sources affecting a measurement pipeline, and the development of mathematical models representing each source [27,30]. Error models are then aggregated through further mathematical modelling, with the ultimate goal of producing comprehensive analytical representations of uncertainty which may be applied to any circumstance, by utilising the appropriate model parameters. In particular for three-dimensional (3D) point clouds, the starting from first principles approach has proven to be difficult because of the multitude of possible error sources and the complexities of their interactions, leading into significant challenges for the mathematical modelling (see later Section 2.2.8 for a discussion on uncertainty associated to point clouds). Thus, existing models following this approach have been limited so far for providing models applicable to the measurement of elementary prismatic parts or simple smooth spheres, in most cases exclusively addressing measurement by contact-probing (*i.e.,* tactile coordinate measuring systems (CMSs)) (ISO 10360 series). Research on uncertainty for non-contact measurements is less mature, though recent work has begun highlighting the main issues for several optical technologies [5,9,29,31,32].

To overcome the complexity of uncertainty estimation from first principles, the ISO Technical Committee TC 213, Working Group 10 has proposed alternative methods. One of the main ideas is to focus on the quantification of traceability. Uncertainty estimation is generally performed by making measurements that are traceable to the definition of the SI standards. Traceable measurements allow for the successful estimation of uncertainty and are generally a base requirement for the verification of manufactured goods. Traceability refers to the comparison of a measurement

result with a reference value, through a documented unbroken chain of passages (calibrations) each contributing with a known amount of measurement uncertainty (see definition in [24,28]). Traceability requires an established calibration hierarchy (traceability pyramid shown in Figure 2.1), which relates the workpiece being measured to the international standard (for instance the metre in the case of a linear dimension). In general, the uncertainty of each calibration increases moving down the traceability chain towards the workpiece [28].

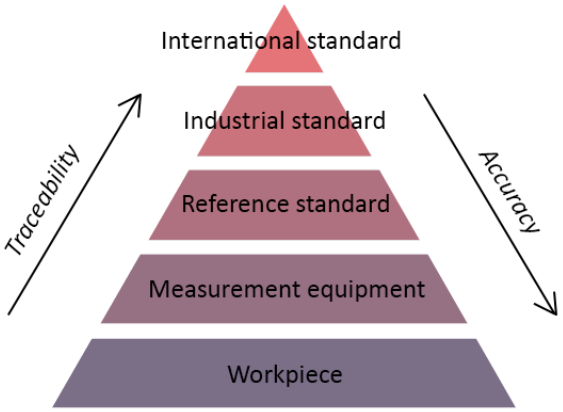

Figure 2.1 Calibration hierarchy or traceability pyramid

Uncertainty quantification can in some cases be simplified by comparing the measurement to a similar one of a reference object. For example, a method has been proposed in ISO 15530 part 3 (2011) [33], known as the substitution method. In the substitution method, the uncertainty evaluation is based on a sequence of measurements on a calibrated object or objects, performed in the same way and under the same conditions as the actual measurements. The differences between the measurement of the object of interest and the

measurement of the reference artefact are used as the starting point to estimate uncertainty. A different approach, described in ISO 15530 part 4 (2008) [34], goes back to the idea of estimating uncertainty without the use of a reference object, but instead attempting to create mathematical models of the measurement process from first principles using simulation. Simulated models are constructed to represent specific aspects of the measurement pipeline (either hardware or software components of the measurement system). Each part of the simulation is developed to address a limited set of parameters and describes a limited range of scenarios (*i.e.,* "task-specific" simulation), therefore, accepting a limited range of values in its input parameters. The aggregation of simulation models leads to the creation of "virtual CMSs" [29,35,36]. Determination of measurement uncertainty using a virtual CMS is carried out by performing repeated simulated measurements with varying inputs (influence quantities) and determining how those inputs affect the measurand. Propagation through the modules comprised within the simulation is usually achieved through Monte Carlo methods [27]. The simulation is repeated a significant number of times until a statistical evaluation of these virtual measurements is made. However, since typically the virtual CMS have been constructed to match specific scenarios, the results are often referred to as "task-specific".

Research on virtual CMS has so far concentrated on tactile ones. Initial work has been carried out to model virtual optical CMSs [31,37,38], but this is still an open research area, in particular given the challenges of developing reliable simulations to capture the interactions between light and the measured surface.

2.1.2 Measurement technologies

In recent years, the design and fabrication of AM parts has been accompanied by the development of new and efficient inspection and verification solutions for the fast and accurate conformance check of the dimensional and functional quality of printed components [39]. Metrology and inspection procedures have become vital and inexpensive means for enhancing the quality of products manufacturing, confirming whether the parts are within the required tolerances, and establishing standardised methods minimising the inspection costs and maximising measurement accuracy [39]. In order for the manufacturing field to keep advancing, the current demand in the metrology world is to develop novel analysis approaches that can overcome the significant measurement challenges presented by AM geometries, specifically a) freeform shapes, b) rough surface texture, c) occlusions and difficult-to-access features, and d) a wide range of materials with different surface and optical properties [1]. In this context, coordinate metrology, the science and application of measuring the physical geometry of a part collecting three-dimensional (3D) coordinate information [40], plays a leading role [41].

Contact probing CMSs, such as tactile coordinate measuring machines (CMMs), have been used for decades in various industrial applications for their capability to measure parts with high accuracy [42]. Contact methods measure the geometry of a part by touching the probe at several discrete points around the object and use the machines motion to find the x, y and z coordinates of each point creating a 3D point cloud. However, the unique geometrical complexity introduced by AM parts creates accessibility

challenges to the contact probe and decrease the measurement flexibility of contact methods [42,43], additionally limited by slow measurement rates and low sampling of points in comparison to non-contact CMSs [43].

The recent growth in both software and hardware solutions have allowed optical, non-contact methods to be increasingly employed in multiple industrial sectors for the measurement of AM parts [5,10], providing fast inspections results often in real-time, clear advantage for high production volume environments typical in AM. The non-contact nature of optical methods leads to fast measurement rates, achieving high densities in point-based sampling with no risk in damaging the surface of the measured part [41,44]. Optical measuring solutions are generally classified into two groups: passive and active methods [45,46]. The main difference is given by their use of light. More specifically, active systems use their own light sources to vary the illumination of the surrounding environment. In other words, active systems can recreate the shape of an object by capturing the modulation of the projected illumination onto the surface of a measured part. On the contrary, passive systems do not require modulated illumination to operate, but do require homogeneous and static ambient light as they are mostly based on processing information extracted from photographs.

Research into optical coordinate metrology solutions for the measurement of form of complex AM parts and design of standardised procedures for components inspection and verification is on-going, especially due to the urgent demand of instruments' performances to withstand current metrological industrial requirements. Triangulation-based techniques are commonly employed in manufacturing industries, in particular structured

light and laser triangulation technologies. Stavroulakis and Leach [10] reviewed the optical measuring systems currently available for post-process form measurement of metal AM parts, identifying the advantages and limitations of several solutions for the measurement of freeform surfaces. In their review, they concluded that the most applicable form measurement principles for metal AM are laser triangulation and fringe projection. Guerra et al. [47] presented a comparison between four optical systems suitable for verification of damaged industrial components: two laser triangulation systems, a fringe projection and a photogrammetry system. The comparison on a calibrated freeform artefact demonstrated the suitability of fringe projection and photogrammetry for the verification of AM parts. Several authors [2,38,48,49] have proposed the use of photogrammetry for the measurement of AM components, demonstrating that 3D point measurement uncertainties of less than 10 µm are achievable, even with low-cost systems. Sims-Waterhouse et al. [50,51] demonstrated that AM parts with different geometries, materials and post-processing textures can be measured to high accuracy by using photogrammetry combined with laser speckle pattern projection.

Photogrammetry, laser triangulation–based solutions and structured light technologies have been therefore identified in the literature as the most suitable and promising solutions for the measurement of form in the AM context [5,10,39]. As such, the basic concepts of the aforementioned non-contact technologies will be presented in the following sections (Sections 2.1.2.1, 2.1.2.2 and 2.1.2.3).

2.1.2.1 Photogrammetry

Photogrammetry is a fast and simple low-cost metrology solution for the measurement of the form of a part via the use of photographs acquired with a simple camera [52]. Based on the principle of triangulation, photogrammetry measures millions of points per image, capturing the information related to corresponding points in two or more images [52]. The term triangulation comes from the fact that a point $\boldsymbol{p}$ on the surface of the object can be reconstructed from the triangle [45] formed by the baseline (*i.e.,* the distance between the two camera origins or optical centre of their lenses) and the two coplanar vector directions defined by the left camera centre to image point $\boldsymbol{p'}$ and the right camera centre to image point $\boldsymbol{p''}$ (Figure 2.2). The object is observed from two or more viewpoints, by either multiple cameras at the same time (stereo) or a single moving camera at different times (structure from motion) [45]. Specifically, stereo-photogrammetry is the most common application of photogrammetry, in which the measurement process is applied using only two images acquired from a fixed viewpoint. On the other hand, structure from motion (SfM) [53] corresponds to the use of a single camera and acquisitions from variable viewpoints, where subsequential images are captured over a period of time.

Correspondences are determined through a variety of methods, including physical targets or the detection of common features in the images collected [54]. As the correspondences are found between photographs, photogrammetry requires homogeneous and static ambient light and may require the use of retroreflectors or laser speckle [50] in order to measure optically smooth parts.

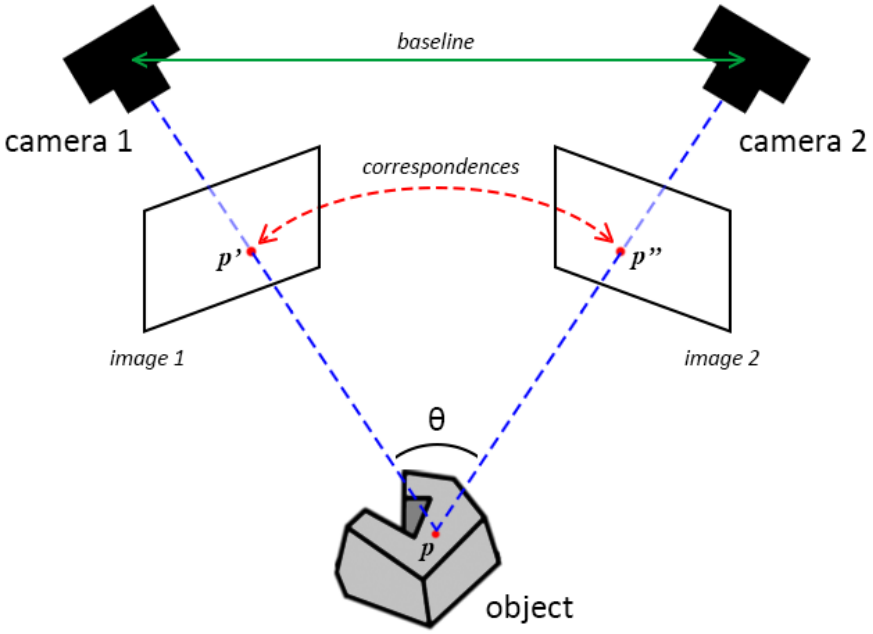

Figure 2.2 Experimental configuration for a photogrammetry (stereo) system with two cameras. Point $\boldsymbol{p}$ on the surface of the object can be reconstructed from the triangle formed by the baseline (calculated as the distance between the two camera sensors), and the two coplanar vectors defined by camera 1 centre to image point $\boldsymbol{p'}$ and camera 2 centre to image point $\boldsymbol{p''}$

Although micro-scale measurements are feasible with photogrammetry [49,55], modern applications are still applied in the majority of the cases to large scales. For instance, photogrammetry is widely employed in archaeology, architecture, automotive, aerospace, medicine, crime scenes and accident reconstructions [56,57]. Most relevant to metrological applications are the uses of photogrammetry in automotive and aerospace engineering, applied as a means of quality control inspections during machining and manufacturing processes [58].

2.1.2.2 Laser triangulation-based solutions

Laser triangulation-based solutions use their own laser light source projecting a laser spot or a line onto the surface of the measured part (point-based and stripe laser solutions [46]), determining the position of a target by measuring the reflected light from the object surface to the receiving sensor [46,59]. As the laser, sensor positions and angle between them are known, the distance to the surface of the part can be calculated with trigonometry [41]. The principles of laser triangulation-based technologies are shown in schematic form in Figure 2.3.

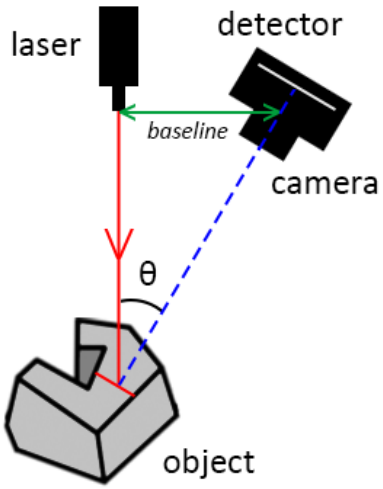

Figure 2.3 Experimental configuration for a laser triangulation-based solution (composed of a camera and a laser source) based on the principle of triangulation to measure the height of each point on the objects surface. The light from the laser strikes the surface of the object and is registered at a specific point on the receiving detector (in the camera). If the distance between the object and the laser changes, the angle θ between the laser and detected reflection will also change. This will cause the laser spot to be registered at a different point on the detector, to calculate the different heights at each specific point

Laser triangulation is widely employed in industry, in particular for part inspection and reverse engineering [60]. However, the measurement speed is relatively slow, due to the single point (or line of points) measuring nature of this technology. Currently, the measurement range of commercial instruments is 40 mm to 650 mm, with accuracies up to 10 µm [61].

A different type of laser-based solution is time-of-flight (TOF), mainly employed for long-distance and large-scale measurements (such as surveying [62] and military range finding applications [63]). Differently from the aforementioned laser-based (point-based and stripe laser) solutions, the TOF method does not require triangulation for 3D reconstruction, and thus the entire system can be very compact, making it applicable for mobile applications. Specifically, its working principles consist of measuring the elapsed time between a projected pulse of light and its detection after reflection from the target, thus using the measured time to calculate the source-target distance [60,64]. TOF techniques currently offer measurement accuracies of the order of 500 µm at a measurement distance of 5 m [65], dependent on the resolution of the electronics used to measure the time elapsed.

2.1.2.3 Structured light projection techniques

Structured light systems are composed by one or a pair of high resolution cameras and a projector, which shines coded structured light patterns onto the surface of the measured object [66,67]. The camera (or pair of cameras) captures the distorted structured images. The projected structured patterns

carry encoded information to resolve the correspondences problem, established by analysing the distortion of captured structured images with known features projected. After the correspondences problem is solved and the system is properly calibrated (*i.e.,* the relationship between a point in the world coordinates and that on the camera or projected image plane coordinates is determined), the $x,\ y,\ z$ coordinates can be reconstructed using a method similar to that used in stereo-photogrammetry (see Section 2.1.2.1).

Numerous codification methods have been developed [66,68] and can be split in two categories: spatial and temporal encoding [46]. Spatial encoding techniques project just a unique single pattern onto the surface of the object, and local neighbourhood information are used to perform the correspondences matching. On the other hand, in temporal encoding techniques patterns are projected one after the other and, for each of them, an image is captured. Correspondence matching is done based on the time sequence of imaged intensity captured by the camera.

A well-known type of structured light technology is fringe projection, an important branch of optical measurement techniques showing large potential for application in the manufacturing industry for both subtractive machining as well as AM [10,69]. The name fringe projection comes from the unique coded light pattern of vertical lines, commonly referred to as “fringes”, which is projected onto the object surface; the resultant information of the projected light are then captured by the camera [70–72]. The experimental configuration for fringe projection is shown in Figure 2.4.

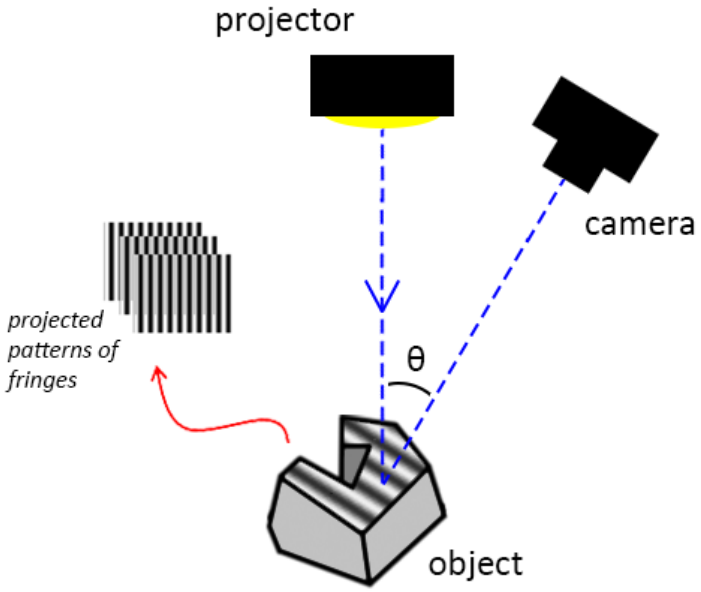

Figure 2.4 Experimental configuration for fringe projection solution. Fringe patterns are projected from the light source (projector) onto the surface of the measured object (θ is the angle of projection); the resultant information of the projected light are then captured by the camera

The different fringe projection patterns can be split into two main categories based on the method used to reconstruct the part: discrete and continuous techniques [73]. Discrete fringe projection uses triangulation on a pixel-by-pixel basis using the coded patterns to find correspondences between images. The most widely used discrete patterns are binary, which vary horizontally with black and white vertical stripes [74]. On the other hand, continuous fringe projection measures the height of the part by extracting the varying phase intensity of the captured fringe patterns at each pixel [68]. A well-known example of continuous fringe projection technique is represented by sinusoidal fringe projection, which produces dense point clouds through extraction of the angular phase of the projected pattern from every pixel in

the image deterministically, by projecting at least three phase-shifted versions of the same sinusoidal pattern [69]. More details about fringe projection technique are comprehensively reviewed elsewhere [69,72].

A popular kind of structured light systems is represented by portable handheld devices, which use a speckle pattern (*i.e.,* spatial encoding category of a single unique static random pattern [69]) projected onto the surface of the measured object [75,76]. As the name suggests, this kind of instruments are held by an operator, who moves the system around the object, whilst the system performs range image alignment and fusion in real-time, providing the user with instantaneous feedback on the measurement outcome. 3D reconstruction is based on triangulation and correspondences are uniquely located for each camera pixel analysing the statistical pattern [69].

Due to their ease of use and portability, handheld devices are nowadays more and more employed in industry, in particular for quality control, reverse engineering, and maintenance [77], as well as in surveying and cultural heritages [78].

2.1.3 Towards smarter measuring solutions

Current optical form measurement technologies have been identified as theoretically able of achieving in ideal laboratory conditions the required performances and tolerances in line with industrial sectors [10]. Nevertheless, their application in real industrial scenarios with high measurement speeds of production, large variety of product designs, wide variety of surface textures, is still characterised by complex and multi-faceted challenges. As an example,

a clear issue is given by the inherent limitation of optical techniques such as structured light and laser triangulation to operate successfully within the line-of-sight, making inaccessible the acquisition from a single measurement position of complex structures, typically generated by additive technologies [10]. Furthermore, smooth AM surfaces with high reflectivity make for instance structured light and laser-based solutions ineffective, while photogrammetry presents itself as a better measurement candidate thanks to the use of retroreflectors or additional projected laser speckles [50]. However, photogrammetric systems still show a user-dependency issue in the image acquisition stage, due to the need of iteratively reviewing and re-processing the measuring plan until a satisfying set of images is taken. In addition, the high amount of generated points per image exponentially augments the computational time while the processing and reconstruction of the acquired data is taking place [79,80]. Expensive and time-consuming manual methods are still employed for planning of measurement procedures or positioning of sensors and instruments around a part, looking for the best strategies to minimise the effects of occlusions, maximise object coverage, and reduce human intervention [81].

Advancements in the fields of electronics, mechanics, mechatronics, optics, and computer science have recently contributed towards the development of systems that can address the aforementioned limitations, merging the advantages of existing measuring technologies with emerging smart functionalities and intelligent measurement strategies [16]. Thus, some of the current advances in the industrial and academic scenarios include the following:

- proprietary software platforms for virtual simulation of the measurement environment combined with optical sensors mounted on industrial robotic-based inspection systems (see for instance commercial instruments such as GOM ATOS ScanBox [82] and Hexagon BLAZE 600A [83]);
- combination of multiple sensors and measuring technologies within the same instrument, taking advantage of the strengths of different metrological solutions (*i.e.,* multi-sensor data fusion [84–86]);
- optical multi-view systems for maximisation of measurement coverage and increased part accessibility [87–91];
- machine learning (ML) integrated algorithms for data acquisition optimisation, pose estimation, feature recognition, *etc.* [92–95];
- incorporation of *a priori* knowledge into the measuring pipeline [19,20];
- incorporation of real-time or post-measurement feedbacks in form of performance indicators for the assessment of the quality of the measurement results [96].

The information-rich metrology (IRM) paradigm and integration of *a priori* knowledge into the measurement pipeline, as well as the definition of performance indicators are recurrent throughout this thesis. Therefore, literature and an introduction overview to the aforementioned concepts will be given in Sections 2.1.3.1 and 2.1.3.2 respectively. References on advances and applications related to multiple sensors data fusion, integration of machine learning algorithms, as well as recent developments in form and coordinate metrology can be found elsewhere [40,84,97].

2.1.3.1 Information-rich metrology paradigm and incorporation of *a priori* knowledge

Information-rich metrology (IRM) is a term that Leach at al. [21] utilised to indicate the enhancement of any measurement process through the use of pre-existing additional (*i.e., a priori*) information, coming from knowledge of the object being measured, knowledge of the measuring instruments employed, and knowledge of the unique physical interactions/principles underlying the measurement technology itself with respect to the object being measured [19–21]. The use of the aforementioned additional sources of information contributes to the enhancement of the performances of a measurement system, and thus increases the final quality of its measurement output. The IRM paradigm is shown in schematic form in Figure 2.5.

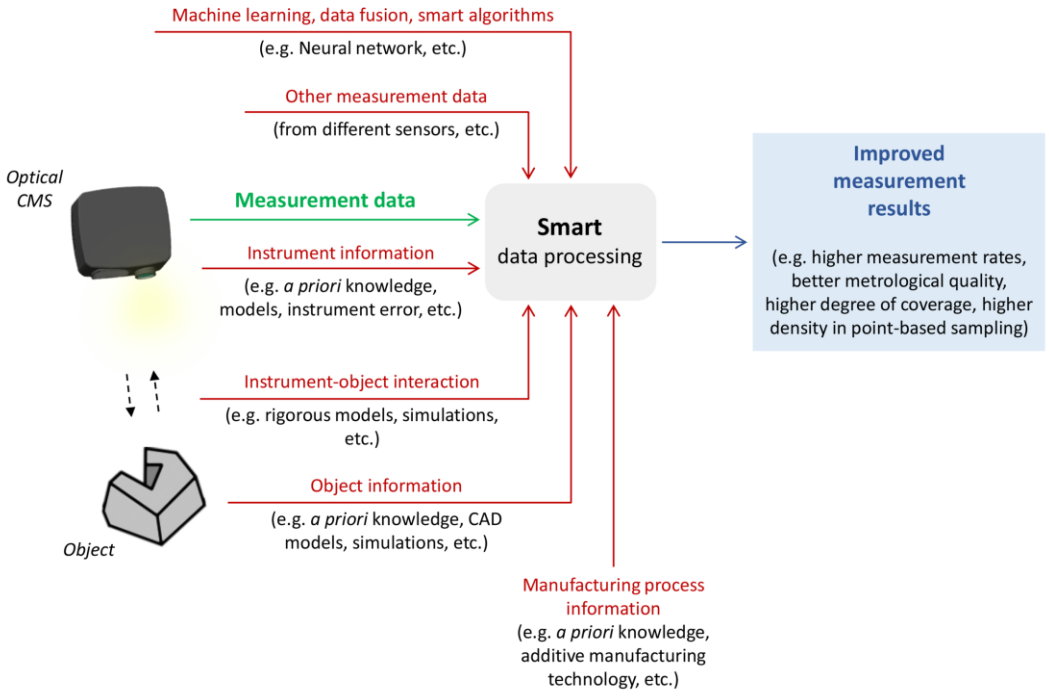

Figure 2.5 The information-rich metrology (IRM) paradigm

Adaptive or intelligent data reduction and sampling techniques for data manipulation [98–100], as well as incorporation of information about a process or product to implement advanced statistical models for quality process control [101] are only a few of the application examples of the IRM paradigm.

Several researchers have offered examples of the integration of *a priori* information into the measurement pipeline/instruments, aiming at showing how primarily improve the quality of the measurement [102–104]. An attempt to incorporate pre-existing knowledge to the measurement and characterisation of surface topography is illustrated for instance in Senin and Leach [19]. The advantages and challenges of introducing heterogeneous sources of information in the surface characterisation pipeline were discussed, in particular providing examples about the incorporation of knowledge of part nominal geometry, the manufacturing process, and the measurement instrument selected. A fundamental role in the IRM paradigm is covered by the development of smart machine learning (ML) algorithmic solutions. Kinnell et al. [105] presented an algorithm for determining the best position for a robot-mounted 3D vision system. In their work, the *a priori* information of the CAD model was used to identify visible key points on the surface of the model per camera viewpoint, and thus determining the best positions. A similar approach can be found in Zhang et al. [106], who proposed a technique to optimise the number of cameras and the positions of these cameras for the measurement of a given object using visible point analysis on CAD data.

In this thesis, the exploitation of available *a priori* information is depicted by the use of CAD data (in form of triangle meshes), which benefit several aspects of the measurement pipeline illustrated in Chapter 1. It will become clearer throughout the thesis the fundamental need of this specific type of pre-existing information; in particular, the nominal forms of selected samples will be used as main reference for point cloud registration (later discussed in Chapter 3) and consequent definition of the measurement quality indicators (see definition in Section 2.1.3.2 and later contributions in Chapter 4 and Chapter 5).

2.1.3.2 Measurement performance indicators

As previously introduced in Section 1.3, an example of smart functionalities with direct implementation into intelligent systems is given by performance "indicators" or "criteria", firstly introduced in literature by Hoppe et al. [96]. More specifically, performance indicators express means of assessing the quality of a measurement, implementing smart features and feedback mechanisms, such as the triggering of a corrective action, or the modification of some measuring parameters, which can be assessed at a point cloud level, thus representing the intelligent "skills" of a measuring instrument. Such indicators underly the capability of combining both data acquisition and data processing, autonomously addressing aspects not only limited to the computation of conventional indicators of metrological performance (for instance the uncertainty associated to features of size, scalar results from a measurement), but also covering performance and behaviour at the point cloud level, encompassing a larger range of viewpoints.

Hoppe et al. [96] suggested in their early work related to the reconstruction of surfaces from unorganised point clouds to qualify the data according to indicators of noise and density. Both indicators appeared to be representative of the digitising point quality, in particular highlighting their influence on the accuracy of the surface reconstructions. Inspired by this work, Lartigue et al. [107] proposed a set of four quality indicators for point clouds obtained with non-contact probes. These indicators were noise, density, completeness, and accuracy of the point cloud data. Similar indicators can be found in Mehdi-Souzani et al. [108], to support measurement planning for freeform surfaces in reverse engineering. In both works, the methods relied on an initial scan of the object set as reference, without the involvement of a CAD model. The point cloud was converted into a voxel space representation to evaluate the density indicator, considering the number of points which belong to each voxel (*i.e.,* volumetric density). To compute the completeness and rate of coverage indicators, the point cloud was converted to a triangle mesh and the distances between neighbouring points in the mesh were evaluated. Other authors [109] presented a comparison between three optical measuring instruments based on noise, trueness, measured area, and surface accessibility indicators. The trueness indicator was based on the measurement of a linear distance set as reference (*i.e.,* the distance between two parallel planes fit to a calibrated step height). The accessibility indicator quantified the ability of a measurement system to access critical areas; those were identified by the measured area indicator, which computed the areas where the data was missing. Quantitative indicators related to point clouds have also been used in the context of pose estimation: Karaszewski et al. [110]

compared the results obtained for thirteen next best view (NBV) planning algorithms based on four criteria: the number of directional measurements, digitisation time, total positioning distance, and surface coverage, the latter specifically computed on the point cloud.

2.2 State-of-the-art in point cloud analysis

2.2.1 Three-dimensional point clouds

In this thesis, the term "point cloud" is used to refer to point cloud of surface data, *i.e.,* a set of points representative of the surface of a part. A point cloud is, therefore, seen as a primitive representation of a 3D object (Figure 2.6), identified as a set of points in a coordinate system [111–113]. In a Cartesian coordinate system, a point cloud is defined by the x, y and z coordinates of each specific point. Due to their simplicity, point clouds have been introduced into a variety of areas related to geometric reconstruction, processing, modelling and rendering. Point clouds are considered as unstructured sets, as the points are stored with no information concerning topological connectivity [114,115]. Point clouds can only provide an approximation of a 3D geometry, because of the intrinsic nature of point-based samplers [114], a problem exacerbated when points are taken on curved surfaces.

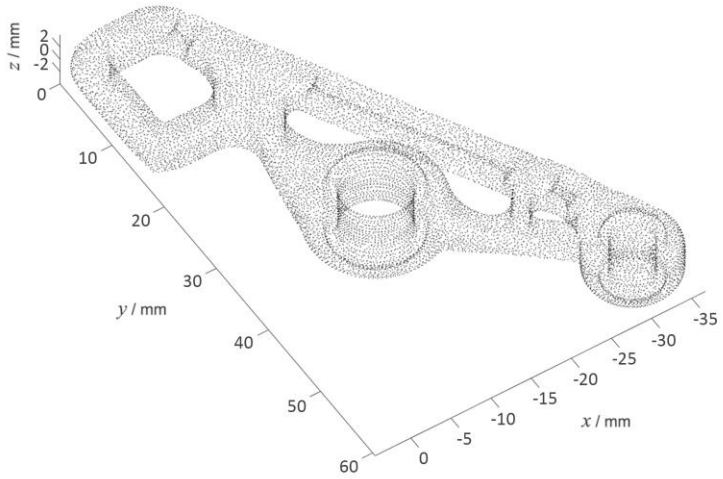

Figure 2.6 Point cloud obtained by optical measurement of an automotive part (roof bracket; part designed by the Centre for Additive Manufacturing, University of Nottingham)

2.2.1.1 Mathematical representation of 3D point clouds and triangle meshes

A point cloud in Cartesian space is generally represented as a $N \times 3$ matrix:

$$\begin{bmatrix} x_1 & y_1 & z_1 \\ x_2 & y_2 & z_2 \\ \vdots & \vdots & \vdots \\ x_N & y_N & z_N \end{bmatrix}, \tag{2.1}$$

where N is the number of points and each point is represented by its three coordinates x, y and z [116]. Within a point cloud, additional point-related attributes may also be stored [117], for example curvature, which is then visually mapped to a RGB colour space – see Figure 2.7). When used to represent surfaces, point clouds may also store the local normal vector of the surface in correspondence to each sampled point (*i.e.,* additional set of three scalar values associated with each row of the matrix defined in equation (2.1)).

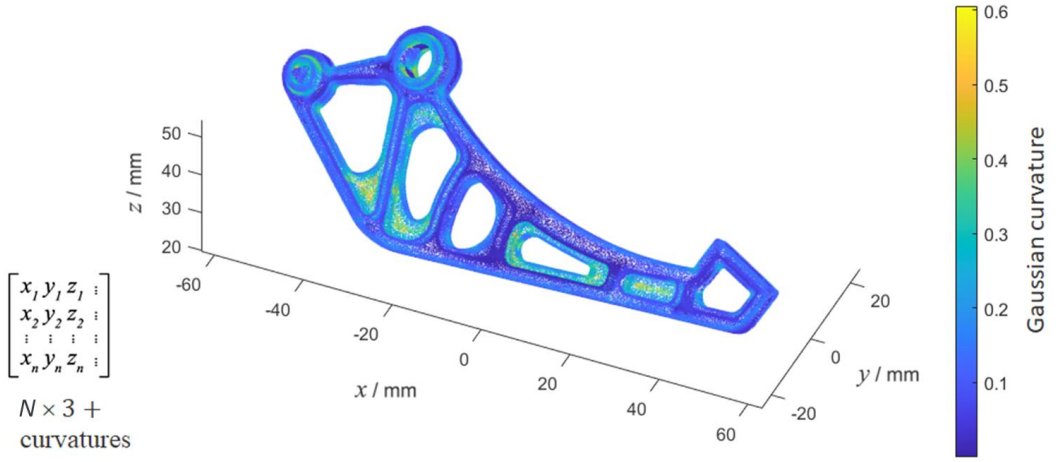

Figure 2.7 Point cloud augmented with Gaussian curvature information. Curvature is visualised by mapping curvature values to a RGB colour map

The mathematical representation of a point cloud can, therefore, be generalised into a collection of multidimensional points [111], where the number of dimensions is the number of spatial coordinates plus any additional attribute which needs to be recorded for each point.

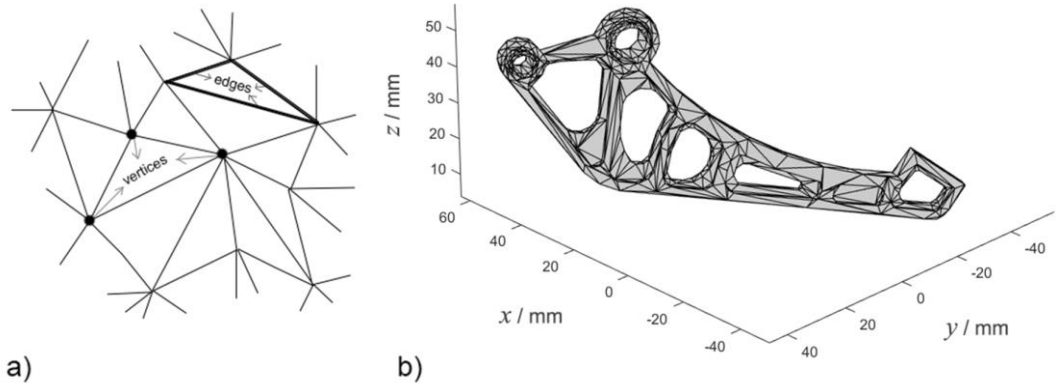

Figure 2.8 Example of triangle mesh representation: a) detail of vertices, edges and triangles defining the mesh; b) automotive part (roof bracket) represented as a triangle mesh (designed by the Centre for Additive Manufacturing, University of Nottingham)

A triangle mesh is a set of topologically connected triangles in a 3D space, typically defined by a set of vertices, and connectivity between vertices (two connected vertices form an edge, three connected vertices – or three connected edges – form a triangle; vertices may be shared by multiple edges and triangles) [116]. Example of triangle mesh representations are shown in Figure 2.8.

2.2.1.2 Common 3D point cloud and mesh file formats

A point cloud can be stored into a file using several formats [118]. All formats must accommodate the x, y and z scalar values associated with each point, as well as any additional information that may be stored for the points. File formats for point clouds are further classified based on how structured the information is encoded in the file, *i.e.,* text or binary formats. In text files, numerical values are first converted into sequences of characters, then characters are encoded into sequences of bits using either ASCII or UNICODE schemes. In binary files, numerical values are directly converted into sequences of bits using dedicated encoding schemes. The advantage of text files is that they can be opened by any editor and directly interpreted by the user. On the contrary, binary files require knowledge of the encoding/decoding scheme originally used to create them, in order to reconvert sequences of bits back into numbers.

The main disadvantages of text files are:
a) size: a dense point cloud may occupy a large amount of disk space, and be very inefficient to read and write;

b) accuracy: a choice must be made on how to convert a real number (for example a coordinate) into a sequence of characters of finite length; using too few characters may lead to truncation errors.

Binary files are on the contrary more compact and efficient to write and read, though dedicated software implementing the selected encoding/decoding scheme must be available, which reduces portability across different software platforms.

The same consideration can be made for mesh file formats, which allow to store information also related to the surface geometry of a 3D object (for instance number of triangle faces, connectivity between vertices and faces, face normal vectors, *etc.*). As for point cloud formats, the binary encoding is preferable. Common point cloud and mesh file formats are listed in Table 2.1.

Table 2.1 Common point cloud and mesh file formats

Filename extension	**Information encoding**	**File structure**	**Contents**	**Notes and references**
XYZ	text	Points List (lists of other elements, *i.e.,* RGB)	Non-standardised set of files based on x, y and z Cartesian coordinates	-
ASC	text	Points List (lists of other elements, *i.e.,* RGB)	Non-standardised set of files based on x, y and z Cartesian coordinates	-
PCD	binary	Version, Fields Size, Type Count Width, Height No. points Points List	Fields: x, y and z Cartesian coordinates and a series of user-selected properties	Point Cloud Data file format, used inside Point Cloud Library PCL [111]

LAS	binary	No. points Points List (lists of other elements, *i.e.*, RGB, NIR, GPS time)	x, y and z Cartesian coordinates and a series of user-selected properties	LiDAR Aerial Survey (LASer) format, specified by the American Society for Photogrammetry and Remote Sensing
PTX	text	No. rows No. columns Scanner position Scanner axes Transf. matrix Points List (lists of other elements, *i.e.*, RGB)	The header contains the scanner location and any matrices to transform multiple scans into one coordinate system; this is followed by x, y and z data, and RGB info	Typically, from LIDAR scanners and Leica Cyclone (Plain Text)
PTS	text	No. points Points List (lists of other elements, *i.e.*, RGB, intensity)	The first line gives the number of points to follow. Each subsequent line has 7 values: the first three are the x, y and z coordinates, the fourth is an intensity value, and the last three are the RGB info	Typically, from LIDAR scanners and Leica Cyclone (Laser scan plain data format)
E57	binary	Header Binary sections (encoding the point data or images) XML section	x, y and z Cartesian coordinates and a series of user-selected properties, such as normals, colours and scalar field intensity	Suitable for storing images and metadata produced by laser scanners and other 3D imaging systems (ASTM E57 Committee on 3D Imaging Systems [119])
PLY	text and binary	Header Points List Face List	x, y and z Cartesian coordinates and a series of user-selected properties	Designed either to handle triangle meshes and to store point clouds (Polygon File

		(lists of other elements, *i.e.*, RGB, normals)		Format or Stanford Triangle Format [120]
OBJ	text and binary	Geometric vertices Texture vertices Vertex normals Face List	x, y and z Cartesian coordinates and a series of user-selected properties, such as texture, normals, faces; OBJ coordinates have no units, but OBJ files can contain scale information	Wavefront technologies; suitable for 3D geometries; an OBJ file may contain vertex data, elements, freeform curve/surface body statements and connectivity, grouping and display/render attribute information
STL	text and binary	Header No. of triangles For each triangle: Normal vector Vertex 1 Vertex 2 Vertex 3 Vertex-to-Vertex Rule: each triangle must share two vertices with each adjacent triangle	x, y and z Cartesian coordinates of the vertices of a triangle, and index describing the orientation of the surface normal vector (both text and binary encode the information in the same way); counter clockwise vertex orientation for each triangle	STereoLithography Interface Format created by 3D Systems; it is widely used for rapid prototyping, 3D printing and computer-aided manufacturing. This file format describes only the surface of an object approximated to a series of triangle facets, without attribute information (such as colours, texture, *etc.*)
Others: FLS FBX	(FARO Cloud) binary text and binary			

2.2.1.3 Face and vertex normals of a triangle mesh

As previously discussed in Section 2.2.1.1, triangle meshes are typically defined by a set of vertices, and edges, which form a continuous structure of connected triangular faces. The majority of mesh file formats are typically designed in order to store information such as indexed faces and vertices, including a connectivity list, and additional elements such as vertex and face normal (Section 2.2.1.2). Typically, the aforementioned information is available and easily accessible in the 3D file, without the need to be computed.

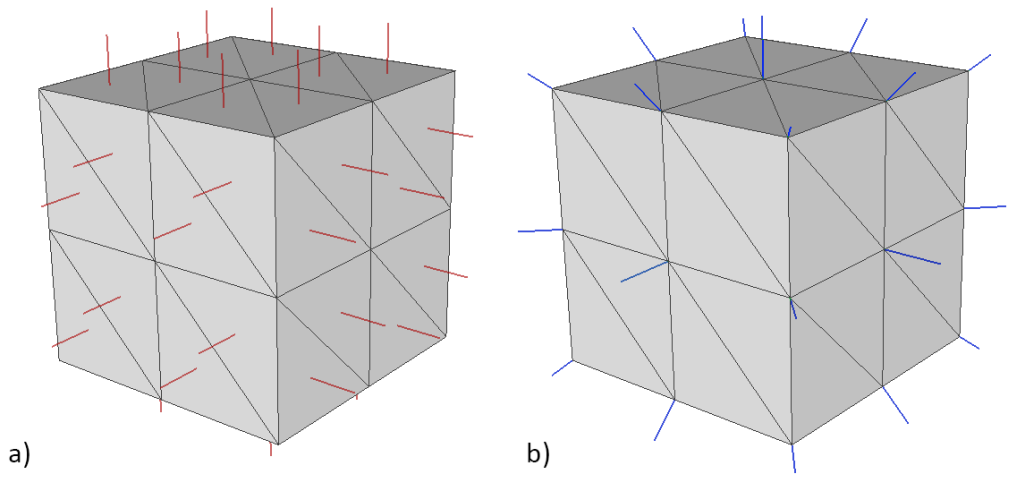

Figure 2.9 Example of triangle mesh cube normal vectors. a) Normal vectors per triangle facet (face normals in red), b) normal vectors (vertex normals in blue) per each vertex of triangle facet

A face normal (also known as surface normal) corresponds to the vector perpendicular to the plane defined by the three vertices of a triangle. A normal vector to a triangle facet (at a point randomly located onto the surface of the triangle) is the same for the entire face. Face normals allow to quickly evaluate

the orientation of each triangle composing the mesh. Commonly, the convention is that the normals face outwards, in case the triangle mesh defines the boundary of a solid object. A vertex normal (*i.e.,* directional vector associated with a vertex in the mesh) is computed as the normalised average of the surface normals of the triangle facets that contain the vertex. Mesh normals (face and vertex normals) computed on a triangle mesh are shown in Figure 2.9.

2.2.1.4 Point cloud transformations

Point cloud transformations fall into two categories: rigid and non-rigid transformations. Rigid transformations result in translations and/or rotations of the point cloud with respect to the local coordinate system, or equivalently, in changes of coordinate system. Non-rigid transformations instead imply a change in shape/size of the cloud, *i.e.,* a change in relative positions between points [84,121]. Examples of non-rigid transformations include bending or stretching of a point cloud or changing its scale (Figure 2.10).

Rigid and non-rigid transformations are typically represented by using a 4×4 matrix, meant to be pre-multiplied or post-multiplied (depending on the convention) with each point in the point cloud, where points are expressed in homogeneous coordinates. The transformation, in the pre-multiplication format, can be written in vector form

$$\boldsymbol{q}_i = \mathbf{M}\,\boldsymbol{p}_i, \tag{2.2}$$

and in scalar form:

$$[x^q{}_i \quad y^q{}_i \quad z^q{}_i \quad 1] = \begin{bmatrix} m_{11} & m_{12} & m_{13} & m_{14} \\ m_{21} & m_{22} & m_{23} & m_{24} \\ m_{31} & m_{32} & m_{33} & m_{34} \\ m_{41} & m_{42} & m_{43} & m_{44} \end{bmatrix} \cdot [x^p{}_i \quad y^p{}_i \quad z^p{}_i \quad 1]^T, \tag{2.3}$$

where $\boldsymbol{q}_i = [x^q{}_i \quad y^q{}_i \quad z^q{}_i]$ is the i^{th} point after the transformation, $\boldsymbol{p}_i = [x^p{}_i \quad y^p{}_i \quad z^p{}_i]$ is the original i^{th} point (*i.e.,* before the transformation) and $\mathbf{M}$ is the 4×4 transformation matrix. In the case that the transform is rigid (rotation and translation), the 4×4 transformation matrix $\mathbf{M}$ is typically expressed as

$$\begin{bmatrix} r_{11} & r_{12} & r_{13} & t_x \\ r_{21} & r_{22} & r_{23} & t_y \\ r_{31} & r_{32} & r_{33} & t_z \\ 0 & 0 & 0 & 1 \end{bmatrix}, \tag{2.4}$$

where r_{ij} are the components of the 3×3 rotation matrix and t_x, t_y, t_z are the components of a 3×1 translation vector. In the case of rigid transformations, another common notation is the following

$$\boldsymbol{q}_i = \mathbf{R}\,\boldsymbol{p}_i + \boldsymbol{t}, \tag{2.5}$$

where the rotation matrix and translation vector embedded in the transformation matrix in equation (2.4) are separated so that the $\mathbf{R}$ is a 3×3 rotation matrix, $\boldsymbol{t}$ is a 1×3 translation vector and point $\boldsymbol{p}_i$ (before) and $\boldsymbol{q}_i$ (after the transformation) do not need to be expressed in homogeneous coordinates.

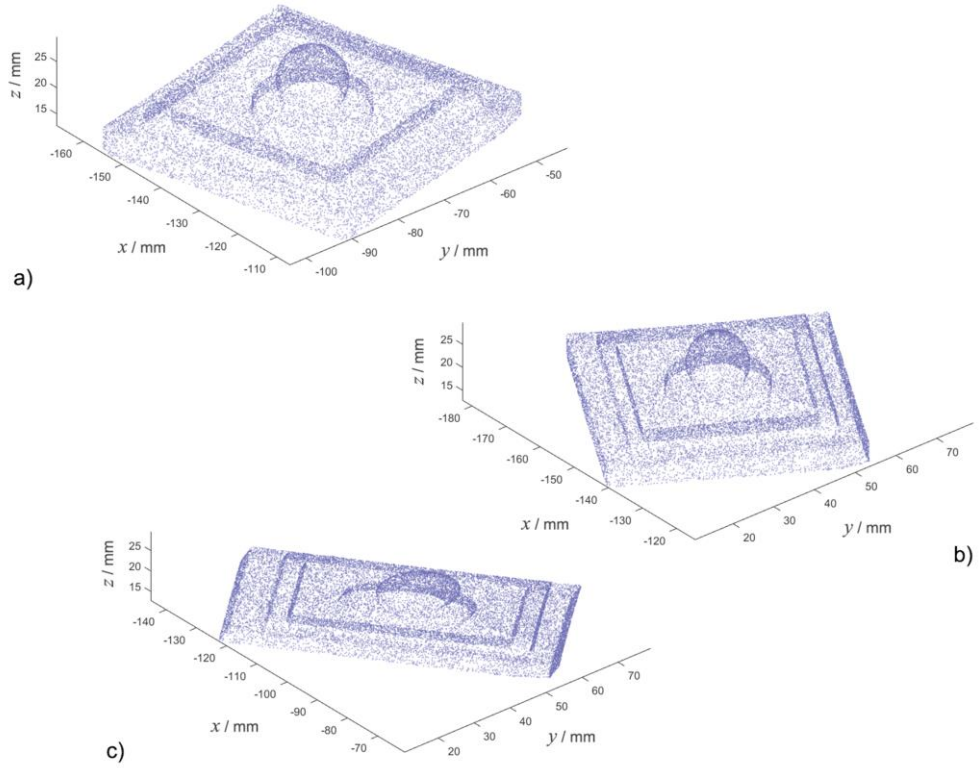

Figure 2.10 Example of rigid and non-rigid transformations applied to a point cloud representing a test artefact (Manufacturing Metrology Team, University of Nottingham): a) original cloud, b) transformed by rotation of 45 degrees along the z axis (rigid transformation), c) stretched along the x axis by selective rescaling of the x coordinates (non-rigid transformation)

In industrial measurement applications, point coordinates are the result of a measurement process, thus any transformation must be considered with care in relation to how it may alter the measurement results. Rigid transformations are primarily required when the point cloud needs to be referred to a different coordinate system, or equivalently, when the point cloud needs to be aligned to another geometric object, typically another point cloud (see Section 2.2.6 for point cloud registration). Non-rigid transformations may instead be applied to correct scaling error, or to compensate for measurement-induced distortion.

2.2.2 Extracting properties and organising information in point clouds

Several methods exist to analyse point clouds and extract their salient properties. The challenges of navigating a topologically unstructured set, such as a point cloud, can be eased by introducing organisation, for example through spatial grouping by proximity, or by computing geometric properties mapped to subsets (regions) of the cloud. Efforts to add organisation and structure to point clouds lead to easier navigation, easier and quicker searching, and retrieval of points with specific properties, easier and quicker processing (filtering, aligning) and more effective comparison when multiple point clouds are involved.

2.2.2.1 Convex hull and bounding boxes

The computation of convex hull and bounding boxes is used to obtain a quick estimate of spatial occupancy and boundaries of a point cloud. A set of points in a Euclidean space (*i.e.,* a point cloud) is defined to be convex if it contains the line segments connecting each pair of its points. The convex hull of a point cloud $\mathbf{P}$ (convex or not) is the smallest convex set containing all the points, mathematically the intersection of all convex sets containing the points.

In computational geometry, given a set $\mathbf{P}$ of n points $\boldsymbol{p}_i, \forall i \in \{1,..,n\}$, the linear combination of the points is given by equation (2.6) and is called a convex combination [122]

$$\sum_{i=1}^{n} \lambda_i \boldsymbol{p}_i, \tag{2.6}$$

where λ_i satisfies the conditions $\lambda_i \geq 0 \; \forall i$ and $\sum_{i=1}^{n} \lambda_i = 1$. The convex hull of a set of points is exactly the set of all possible convex combinations of the points.

The convex hull of a finite point set $\mathbf{P} \subset \mathbf{R}^d$ forms a convex polygon when $d = 2$ and a convex polyhedron when $d = 3$. A convex polygon (or polyhedron) is specified by the sets of its vertices and the edges connecting them. In 3D space, the convex hull is the boundary of a closed convex surface generated by applying Delaunay triangulations with the outer points, vertices of the smallest possible convex bounding volume identified by a triangle mesh (Figure 2.11).

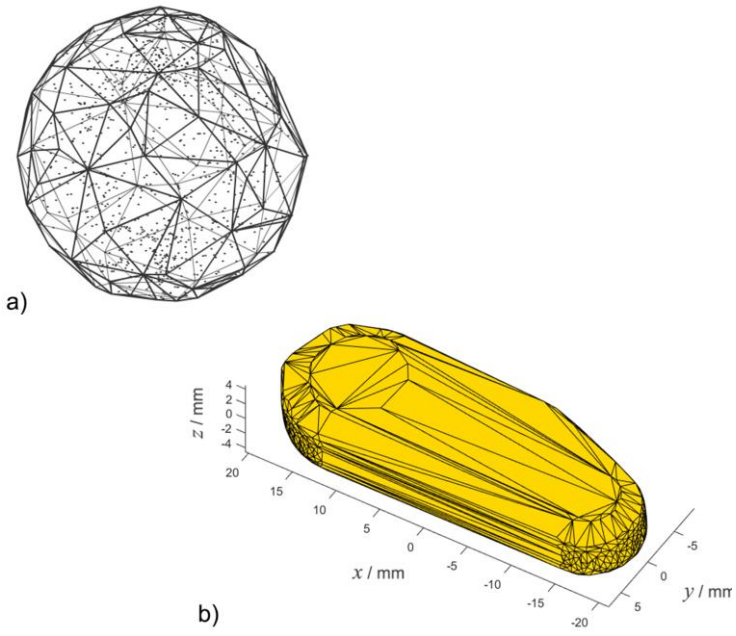

Figure 2.11 Convex hulls obtained by Delaunay triangulation: a) for a random set of points, and b) for the roof bracket part

A bounding box is a parallelepiped in 3D, or a rectangle in 2D space, enclosing a geometric object. When the box is aligned with the axes of the coordinate system, it is then known as an axis-aligned bounding box (AABB – see example in Figure 2.12).

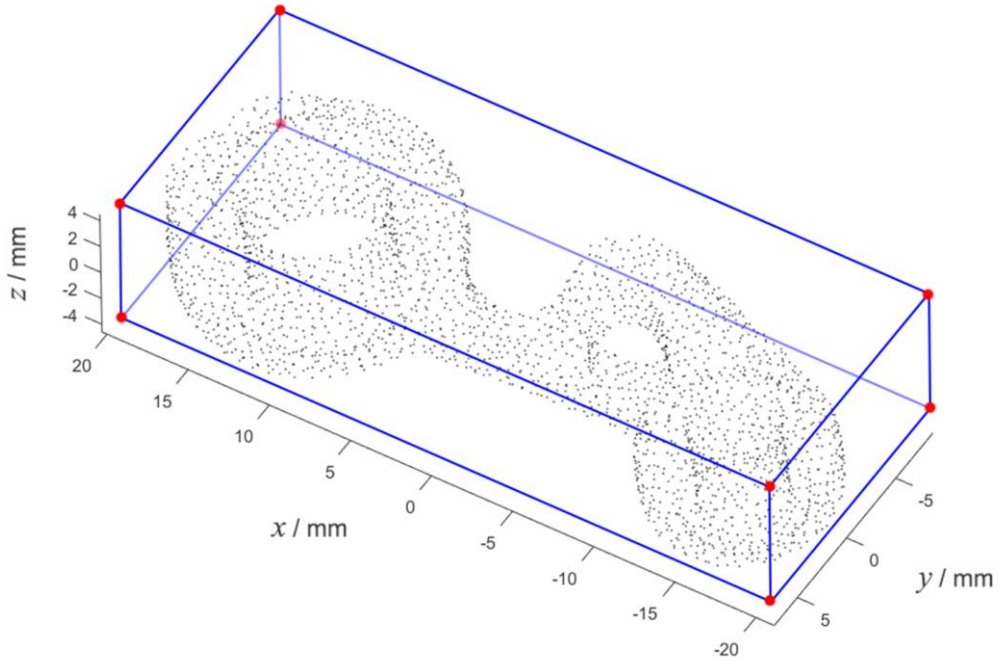

Figure 2.12 Axis-aligned bounding box, enclosing a point cloud (simplified cloud from measurement of the roof bracket)

To distinguish an arbitrarily oriented bounding box from an AABB, the former is called an oriented bounding box (OBB) [123]. The minimum or smallest bounding box for a point set **P** is the box with the smallest measure (area, volume or hypervolume in higher dimensions) within which all the points of **P** lie. The minimum bounding box of a point set is the same as the minimum bounding box of its convex hull.

2.2.2.2 Centroid and principal axes of a point cloud

The centroid $\boldsymbol{c}$ of a point cloud $\mathbf{P}$ (in 2D or 3D) is a point whose coordinates are defined as the arithmetic mean of the coordinates of all the points of the cloud [124]. The centroid is often used as a first, coarse indicator of point cloud localisation in space (central tendency).

In addition to knowing a point cloud localisation, it is important to determine how points are dispersed (*i.e.,* scattered) in space about the centroid. Dispersion can be measured along any arbitrary axis passing through the centroid. However, it is generally convenient to evaluate dispersion along specific directions known as principal axes (Figure 2.13).

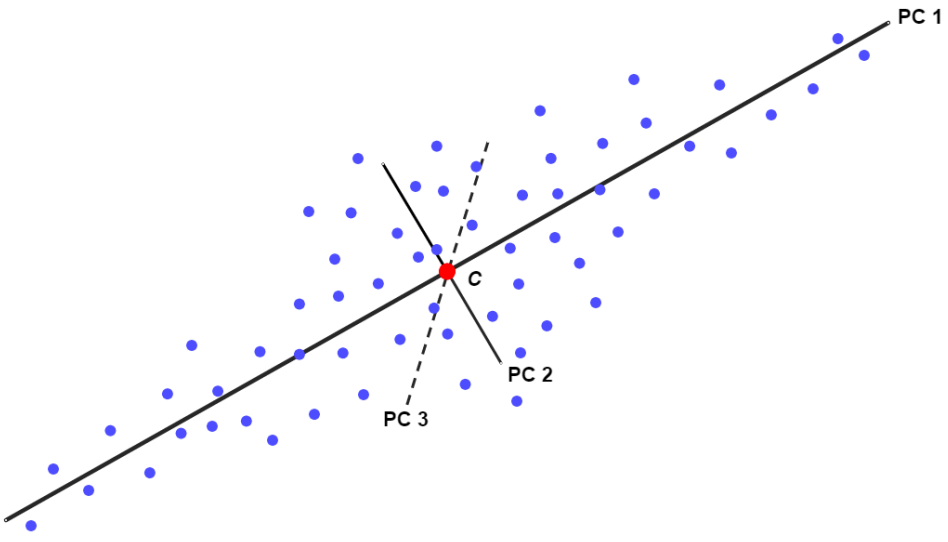

Figure 2.13 Example result of principal component analysis for a point cloud; centroid $\boldsymbol{c}$ (red) and first (PC1), second (PC2), third (PC3) principal axes (black) for an example point cloud (blue)

The principal axes are defined as orthogonal directions (two in 2D space or three in 3D space) where the largest, intermediate and smallest dispersion of the points can be observed respectively [121,125]. Principal axes are typically found by running principal component analysis (PCA) [126]. In statistical analysis, PCA is used to simplify random variables of high dimensionality by identifying a smaller set of new dimensions (linear combinations of the original ones) capable of encapsulating most of the variance for the original set. In geometric modelling, PCA can be computed on a point cloud by considering each point as a realisation of a trivariate random variable (bivariate if in 2D space). The principal components, found from the eigenvectors and eigenvalues of the covariance matrix, correspond to axes in space (2D or 3D) passing through the centroid, and are called principal axes.

Given a set of points $\{p_1, \ldots, p_n\}$ with centroid $\boldsymbol{c}$, the covariance matrix $\mathbf{C}$ is built as follows

$$\mathbf{C} = \mathbf{P} \times \mathbf{P}^{\mathrm{T}}, \tag{2.7}$$

where $\mathbf{P}$ is expressed as

$$\mathbf{P} = \begin{bmatrix} p_{1_x} - c_x & p_{2_x} - c_x & \ldots & p_{n_x} - c_x \\ p_{1_y} - c_y & p_{2_y} - c_y & \ldots & p_{n_y} - c_y \\ p_{1_z} - c_z & p_{2_z} - c_z & \ldots & p_{n_z} - c_z \end{bmatrix}, \tag{2.8}$$

whose i^{th} column is the vector $\boldsymbol{p}_i - \boldsymbol{c}$.

Centroid and principal axes are often used as coarse descriptors of localisation and orientation of a point cloud and are, therefore, often used as the starting point to solve alignment problems involving multiple point clouds (see Section 2.2.6.3). In addition, if the point cloud is representative of a portion of surface with uniform spatial orientation (for example, a plane or a surface with small curvature), principal axes can be used to identify the orientation of the local surface normal, corresponding to the principal axis capturing the least variance (see Section 2.2.4.1). Since PCA also allows computation of the amount of dispersion along the principal axes through the eigenvalues of the covariance matrix, information about the cloud aspect-ratio can also be obtained (for example, rate of elongation with respect to one or two principal axes) paving the way for methods for shape classification and comparison.

2.2.2.3 Spatial subdivision of point clouds

A way to add organisation to a topologically unstructured set of points is to subdivide the set into groups of points that occupy similar positions in space [122,123]. Spatial subdivision is an efficient way for enabling fast search and retrieval of points (for example, to find the closest points to a given geometric reference – point, plane, another point cloud, *etc.*). Many spatial subdivision methods are hierarchical, meaning that subdivision is performed recursively, leading to the generation of nested volumes (or areas in 2D) of increasingly smaller occupancy, each containing points from the original point cloud. Hierarchical subdivisions give origin to graph-like structures (trees), where nodes contain the description of each subset generated by the subdivision,

including the points they contain. Hierarchical subdivision trees can be navigated across levels (an operation known as "tree traversal"), typically performing recursive searchers starting from coarse subdivisions and moving towards finer ones, in order to retrieve points. Most of the hierarchical, recursive subdivision methods discussed in this section can be adapted to operate on other geometric primitives in addition to points, for example triangle meshes. Also, most analytical definitions for recursive spatial subdivisions work in d-dimensional spaces, meaning that they have identical formulations in 2D, 3D or any space of higher dimensionality.

AABB trees, binary space partitioning and kd-trees

AABB trees [127] adopt a hierarchical, recursive decomposition where each generated convex subset of space is an axis aligned bounding box (AABB, as discussed in Section 2.2.2.1). A multitude of different AABB trees can be implemented depending on the method adopted to partition space, how many partitions are generated per decomposition level, whether partitions are overlapping or not, and whether partitions contain only points. The freedom in the decomposition procedure makes AABB trees particularly convenient in applications involving collision detection of complex geometries, because custom trees can be built to address specific requirements of specific regions in the geometry.

Binary space partitioning (BSP) encompasses a family of recursive decomposition techniques where the common denominator is that each subdivision is strictly binary, meaning that it divides the d-dimensional space into two partitions only, known as half-spaces [128], and the partitions are

non-intersecting. The subdivision is typically performed by a hyperplane, whose position and orientation depends on type of BSP. At each level, the partitioning is binary, therefore, in the resulting tree, each node (corresponding to a partition) generates only two children ("leaves" - the result of the binary subdivision of the partition). The most popular type of BSP is the kd-tree [129–131]. An example of kd-tree computed on a triangle mesh is shown in Figure 2.14.

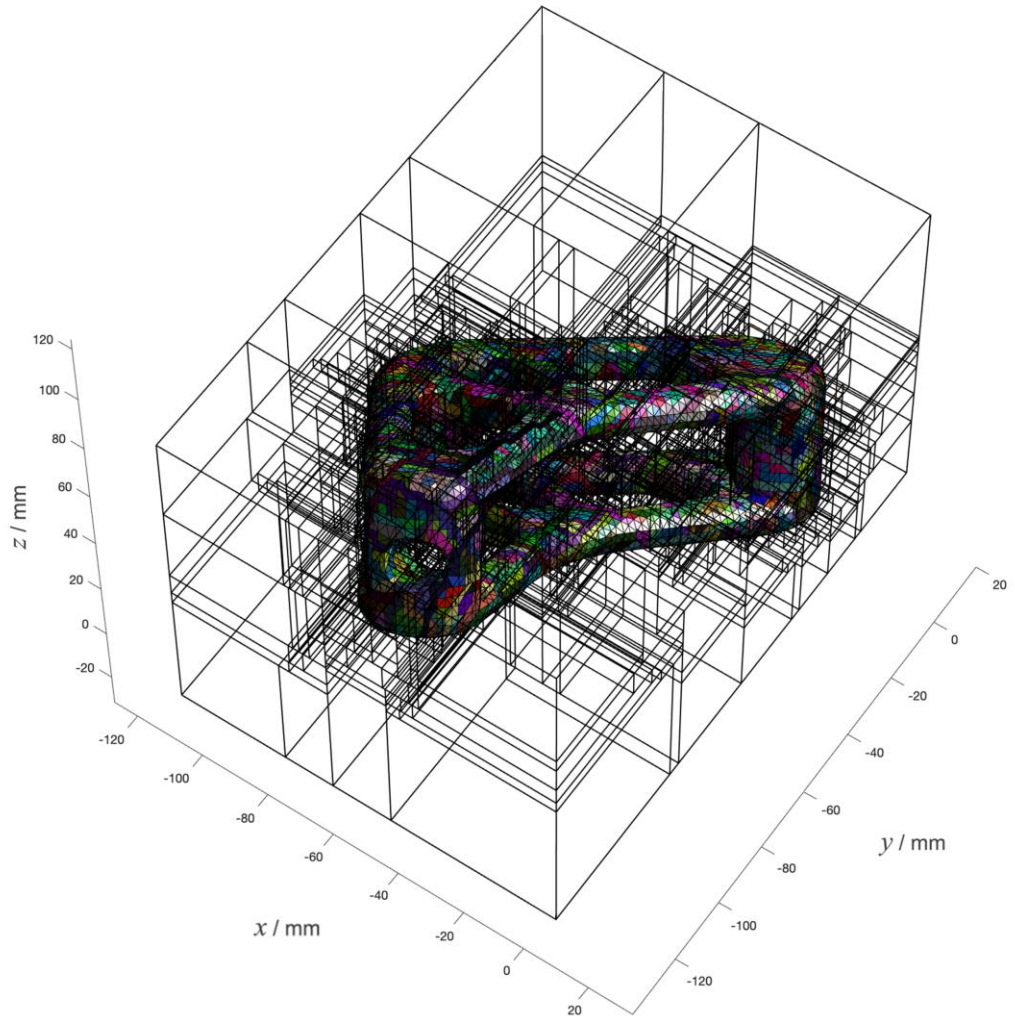

Figure 2.14 Example of kd-tree decomposition applied to a triangle mesh; the mesh has been artificially generated and is representative of typical hollow structures which could be produced by additive manufacturing

The kd-tree is the result of a very specific type of recursive spatial partitioning where:

a) the partitioning at each decomposition level is binary (*i.e.,* the decomposition is a type of BSP);

b) the generated partitions are AABBs (*i.e.,* the generated tree is a AABB tree);

c) the position of the partitioning hyperplane is decided by very specific criteria, described in the following.

In kd-tree decomposition for each convex AABB set to be partitioned, a hyperplane is created aligned to one of the three main axes (x, y or z), usually the one corresponding to maximum point dispersion within the partition. Then, the position of the hyperplane is set as coincident to the median value of the coordinates of the points along the same axis. This default partitioning behaviour generates balanced kd-trees (balanced: each point is reachable by traversing approximately the same number of nodes starting from the root). However, different hyperplane positioning strategies can be implemented depending on the application.

Octree decomposition

Another popular hierarchical subdivision method is known as octree decomposition [122,123,132]. In octree decomposition, each spatial partition is described as a 3D cuboid (again a type of AABB). Recursive partitioning consists of subdividing the cuboid into eight equal parts (also cuboids) known as octants. Note that cuboids degenerate into cubes if the root AABB has the same sizes along the three main axes. Analogously to kd-trees, octree

decompositions use hyperplanes and create convex, non-intersecting partitions. However, eight new partitions are generated from each decomposed AABB (creating a tree with eight leaves per node) and the position of the hyperplanes cannot be optimised due to the requirement for generating eight equal cuboids. Due to the generation of octants, octree decompositions are applicable to 3D geometries only. The 2D equivalent of an octree decomposition is known as quadtree decomposition. In this case, each partition is a 2D AABB shaped as a rectangle (or cube if the sizes are equal), and each decomposition generates four equal rectangles, known as quadrants (*i.e.,* four leaves per node). The same considerations formulated when comparing octree decompositions to kd-trees apply to quadtree decompositions, compared to 2D kd-trees.

Cell decompositions

In cell decompositions, the point cloud (or other geometrical object) is subdivided into a set of 3D cells (in 3D space) or 2D cells (in 2D space) of equal volume/area. There is no recursive subdivision and cells are immediately generated at their final size [133]. Each cell is filled with the points located within the occupied region. In the most common case, cells are cubic. In such cases, they are referred to as voxels, and cell decomposition is called voxelisation. The use of cubic cells brings several advantages, the main one being that cells can be organised in a uniform 2D or 3D grid. In the grid, cells are indexed and can be easily navigated, for example paving the way to the use of data manipulation technologies derived from image processing, though in three dimensions. Voxelisations are very simple to obtain: the most

common approach is to create a uniform grid of the desired size on top of the cloud, and then iterate through the cells in order to identify the points falling within each cell [134]. Voxelisations have the main advantage of creating a topological infrastructure associated with the point cloud, because adjacency between points can be inferred directly from voxel indices in the grid. However, the decomposition is often inefficient: voxels that are too large may contain many points, resulting in an excessively coarse decompositions; on the contrary, very small cells may contain no points in low density regions of the point cloud, leading to a waste of memory and computational challenges in search/retrieval. Abandoning constant voxel size in favour of variable-sized cells means losing the advantages of dealing with uniform grids and thus is seldom implemented.

Point search and retrieval using spatial subdivisions

The main reason to perform spatial subdivision of a point cloud is related to the generation of a structured organisation in an otherwise topologically unstructured dataset. The organisation into a structure facilitates and accelerates search and retrieval operations, which ultimately consist of finding the nearest points to a given set of coordinates, either in the same point cloud, or in an external entity [135]. In other words, given a set of points $\mathbf{P}$ and a query point $\boldsymbol{q}$, which may or may not belong to $\mathbf{P}$, the problem is to find a subset of $\mathbf{P}$ containing either the k closest points to $\boldsymbol{q}$ (Figure 2.15.a), or all the points whose Euclidean distance to $\boldsymbol{q}$ is smaller than a given radial distance $\boldsymbol{r}$ (Figure 2.15.b).

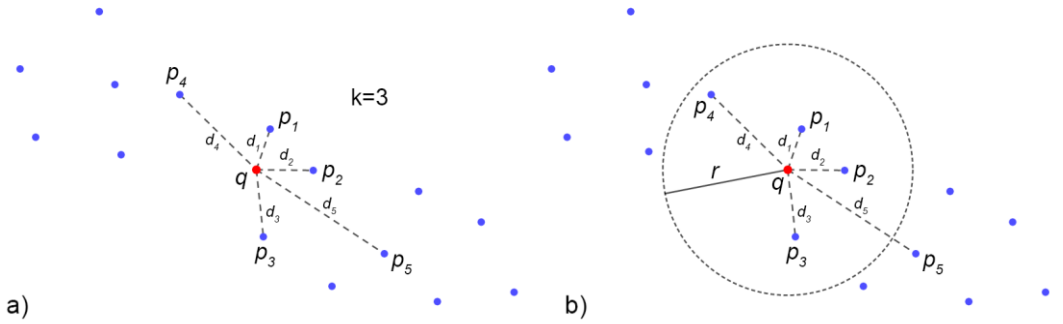

Figure 2.15 Schematic representation of the two most typical point search and retrieval problems: a) find the k nearest neighbours of a given point $\boldsymbol{q}$; b) find all the points that lay within a radius $\boldsymbol{r}$ from $\boldsymbol{q}$

In absence of a spatial subdivision, the only way to solve the aforementioned tasks is by brute force, computing the Euclidean distances of all the points in $\mathbf{P}$ to the query point $\boldsymbol{q}$. This is done, for example, by the most popular search and retrieval algorithm for point clouds, known as the k-nearest neighbours algorithm (k-NN). In k-NN, once the Euclidean distances to three query points are known, points can be ranked on increasing distance so that the k nearest ones can be returned [135,136]. A similar approach is adopted to identify points at a maximum distance $\boldsymbol{r}$ from the query point $\boldsymbol{q}$. Again, once all the Euclidean distances to $\boldsymbol{q}$ are computed, the selection is driven by thresholding on the given radial distance $\boldsymbol{r}$.

On the contrary, if a spatial subdivision is available, the same procedures to retrieve the k nearest points or all the points within a given radial distance $\boldsymbol{r}$ can be applied on much smaller sets of points, identified from selected nodes in the subdivision tree (the node selection procedure depends on the type of

subdivision, but essentially consists of traversing the tree until some conditions are met).

Spatial subdivision can also be used to navigate across points of a point set using the Euclidean minimum spanning tree (EMST) method [96]. In the EMST method, a path is automatically found to connect any two arbitrarily chosen points of a set. The path is formed by finding a sequence of points to be connected by segments, so that the total path length is minimised. Each segment represents the Euclidean distance between the pair of points it connects. Spatial subdivision methods greatly help to speed up the identification of which points to connect in the EMST.

2.2.3 Point cloud pre-processing

Many industrial coordinate measurement technologies produce high-density point clouds. In the context of inspection and verification, high-density implies high-resolution spatial sampling, and thus potentially richer information available to assess whether the part conforms to dimensional and geometric specification requirements, in particular for smaller-sized features. Nevertheless, several issues typically affect the quality of high-density point clouds obtained by measurement: part coverage may be suboptimal, with some surfaces being suitably represented by truly high-density sampling, while other surfaces may be less covered, or not represented at all (for example, if the surface is not within line-of-sight of an optical instrument, or unreachable by a contact probe). On the other hand, some surfaces may be subjected to excess/redundant sampling. Excess sampling may occur, for example, in

correspondence to regions that have been sampled multiple times as a result of partially overlapping fields of view. Other problems affecting high-density point clouds, in addition to sampling coverage, are related to measurement error leading to point misplacement: typical examples are high-spatial frequency "noise", usually widespread on the entire point cloud, or isolated points significantly differing from their neighbours (often also a product of measurement error, and typically referred to as "outliers" because of the way they can be algorithmically detected, see Section 2.2.3.2).

Several point cloud pre-processing operations are available to help compensate problems related to non-uniform coverage and measurement error. Some operations are dedicated to reducing noise or removing isolated points, while others are applied to improve the uniformity of sampling density (uniformity of point spacing). In the following sections, an overview of the most common pre-processing operations is presented.

2.2.3.1 Point cloud simplification, decimation and resampling

Point cloud simplification is the process of reducing the number of points in a cloud. The operation can be performed to reduce the computational complexity in the subsequent analysis operations, to reduce memory occupation, or to remove unwanted points, such as isolated points, overlapping points or points falling on surfaces other than the measurand ones (Figure 2.16). An operation to reduce the overall number of points in a cloud is frequently performed at the beginning of the point cloud analysis process, given the high sampling densities commonly achieved by most coordinate measurement technologies.

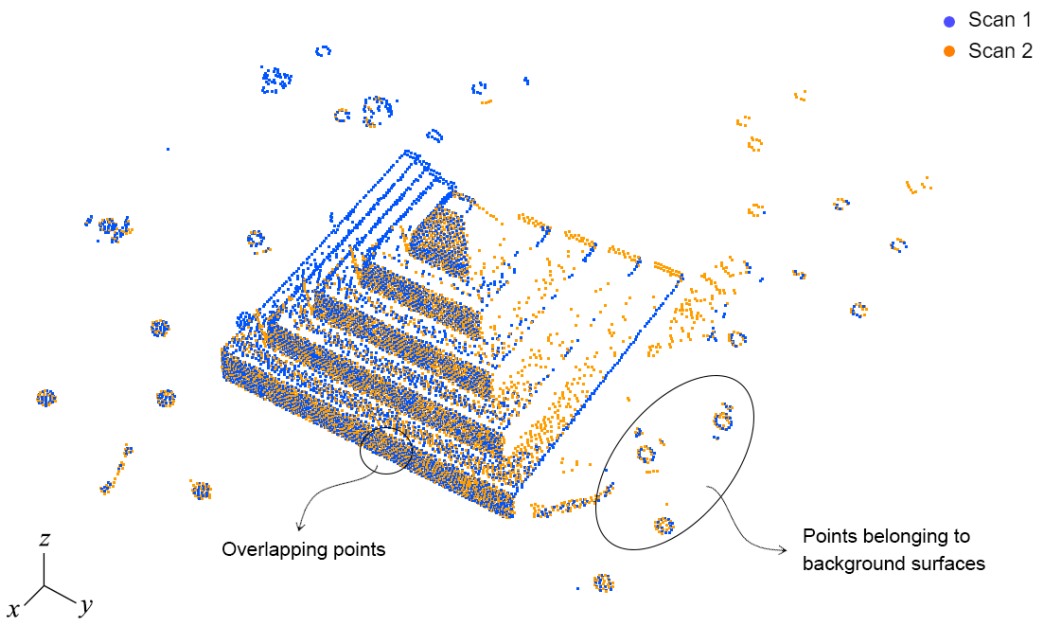

Figure 2.16 Example scenario involving clouds with excess points and requiring simplification. Two point clouds (blue and orange) obtained from different measuring the same test artefact for two different directions of observation. The clouds have been registered (*i.e.*, co-localised in space, see Section 2.2.6) so that they can be merged into a single dataset. Regions captured by both the point clouds feature excess points; additional, isolated clusters of points are also present, representative of background surfaces that have been accidentally captured (pyramid artefact designed by Manufacturing Metrology Team, University of Nottingham)

Point cloud simplification may be performed by deletion of selected points, a process also known as decimation, or by replacing a set of existing points with a smaller-sized set of new points, usually obtained by some form of interpolation or other aggregation mechanism starting from the original set. The replacement operation is typically referred to as "point cloud resampling", to evoke the idea that points are the result of sampling on a continuous surface. It is worth pointing out that resampling in general may not necessarily imply a reduction in size of the point cloud and it may also be found in contexts different to point cloud simplification. In the specific case

of dataset simplification, resampling is applied when the goal is to reduce the total number of points while at the same time obtaining a more uniform sampling density, if a simple decimation process does not suffice.

In general, operations involving the reduction of size of a point cloud (either by decimation or by resampling) imply reduction of spatial density, with a consequent loss of detail. Particularly in relation to the smaller-scale geometric features, an aggressive reduction may lead to the loss of definition of the underlying geometry and, therefore, to the loss of quality in the inspection result [137]. An additional risk of simplification based on resampling is related to the introduction of interpolated (*i.e.,* non-measured) points.

In the literature, a large variety of simplification, decimation and resampling methods are discussed. Simplification methods have been introduced, for example, by Linsen [138] and Pauly et al. [139], who developed algorithms to create simplified point clouds as true subsets of the original point set, extending Taubin [140]'s Laplacian operator method (originally developed for triangle meshes) to point clouds. An overview of simplification methods is given by Xiaohui et al. [141], in which sampling methods are divided into three categories: resampling, iterative simplification and clustering. The resampling category includes methods for the computation of a new sampled point cloud, considering specific features from the original dataset as key factors, that lead to a reduction of the number of points. The iterative simplification collapses pairs of points into a single data point, preserving the density of the point cloud. Clustering methods are often used to reduce the complexity of 3D point clouds, subdividing the bounding box

into grid cells and replacing the original points that fall into the same cell by a common representative (see previous Section 2.2.2.3).

2.2.3.2 Elimination of isolated points and noise reduction

A point in a point cloud is identified as isolated when it is significantly distant from its neighbours. The assessment of significance for distance is typically based on some global or local threshold (see later in this section). Isolated points are classified as:

- isolated points due to distance measured orthogonal to a local surface fitted to the neighbours (*i.e.,* isolated points away from the surface – see Figure 2.17.a);
- isolated points that still approximately lie on the locally fitted surface, but are too distant from their neighbours, as measured on the surface itself (*i.e.,* isolated points on the surface – see Figure 2.17.b).

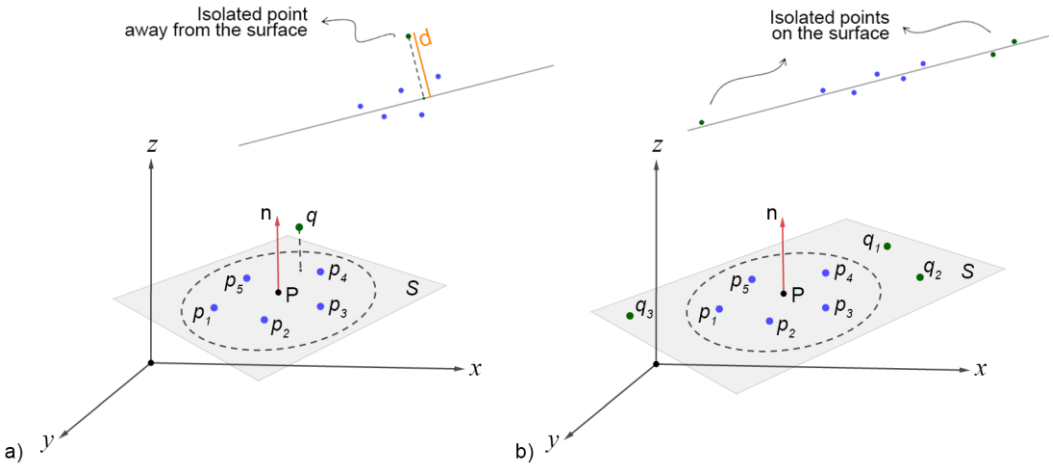

Figure 2.17 Types of isolated points: a) isolated point away from the surface - isolation of point $\boldsymbol{q}$ is due to anomalous distance of the point to the fitted plane or surface $\boldsymbol{S}$; b) isolated point on the surface - isolation of point $\boldsymbol{q}$ is due to anomalous distance of the point to its closest neighbours, even though $\boldsymbol{q}$ approximately lies on the fitted plane or surface $\boldsymbol{S}$

Isolated points on the surface are perceived as related to a local decrease of density or to the presence of "void" regions: they can be either eliminated or they can be filled by resampling, as previously discussed in Section 2.2.3.1 (for example, by clustering based on cell decomposition). Isolated points detected away from the locally fitted surface may not necessarily imply a local decrease of density and are typically perceived as "spikes" with respect to the surrounding points. Points away from the surface can be either eliminated, creating a local void, or replaced by points located closer to the surface. In most cases, the identification of a threshold of significance for distance is based on outlier statistics [142–144]. For example, the typical method for detecting whether the query point $\boldsymbol{q} \in \mathbf{P}$ is a "spike" works as follows [145,146]:

a) a surface (plane, low-order polynomial or spline) is locally fitted to a set of k points $\boldsymbol{p_k}$ selected as neighbours of $\boldsymbol{q}$ (in an alternative to fitting, PCA can be used to determine the orientation of the local plane. In the fitting process, $\boldsymbol{q}$ is excluded);

b) the local normal to the fitted plane or surface is computed, at the location identified by $\boldsymbol{q}$;

c) the distances of all the $\boldsymbol{p_k}$ points to the fitted plane or surface are computed, measured along the direction of the local normal, and used to build a probability distribution;

d) the distance of the query point $\boldsymbol{q}$ to the fitted surface, also computed along the local normal, is tested against the distribution of distances obtained for the neighbouring points, to see whether it must be considered as an inlier or an outlier, using one of the many available outlier testing methods from statistical analysis.

For example, assuming that the distribution of distances can be modelled by a Gaussian function with a mean μ_k and a standard deviation σ_k, an outlier can be defined as any value whose difference from the mean is larger than a given multiple of the standard deviation (for example, $\mu_k \pm 3\sigma_k$). A similar formulation for outliers can be adopted to recognise isolated points on the surface, as long as the probability distribution is built on distances between neighbours on the fitted surface (*i.e.,* not orthogonal to it). Finally, again, the same formulation can be adopted to detect isolated points in any direction, by considering the local probability distribution of distances considered in 3D.

Removal of noise from point clouds is typically implemented following methods similar to those illustrated for spikes. Noise is typically seen as high (spatial) frequency disturbances of point placement, measured orthogonally to the locally fitted surface and distributed over the cloud. Moving windows whose orientation follows the local normal can be implemented that, akin to signal processing, apply kernels based on mean or median filtering operations. As for spikes, local fitting can be replaced by local PCA depending on needs. Because of the parallelism with signal processing, noise removal and spikes removal operations are frequently referred to as point cloud "filtering" operations. A comprehensive analysis of the state-of-the-art methods for filtering point clouds can be found in Han et al. [147].

2.2.3.3 Point cloud conversion to/from triangle meshes

Another pre-processing operation which is often implemented for point cloud analysis is conversion to or from triangle meshes. The conversion from a

triangle mesh to a point cloud is typically trivial, as the vertices of the mesh can simply be converted into the points of the point cloud. The conversion from mesh to cloud is used when only vertices are needed for subsequent steps of the analysis, for example, when a specific property needs to be assessed which solely depends on points in a dataset.

However, the inverse task, *i.e.,* converting a point cloud into a mesh, is challenging. At first glance, the points of a point cloud could be directly used as vertices of the mesh. This is in principle correct. However, a triangle mesh also consists of the connectivity between vertices (to/from edges and then triangles), and the generation of a connectivity map is far from straightforward. Typically, in measurement, the points are considered as the result of sampling a continuous surface. The conversion to a triangle mesh (*i.e.,* the generation of connectivity) would, therefore, somewhat restore the continuity of the surface from which the points were originally sampled. However, without any further knowledge on the measurand surface, there is no robust way of knowing whether two points really belong to the same portion of locally continuous surface, even if they appear very close to each other in space. For example, points sampled from two opposite surfaces of a very thin wall may still appear close to each other, yet they should not be considered as connected because they belong to different surfaces.

One of the most popular methods for reconstructing a triangle mesh from a point cloud is the application of Delaunay triangulation (DT) [148]. In a 2D space, the DT for a given set $\mathbf{P}$ of points is a triangulation DT($\mathbf{P}$), such that no point in $\mathbf{P}$ lies inside the circumcircle of any triangle in DT($\mathbf{P}$). The 2D form is preferred for point clouds that do not feature re-entrant parts and

can, therefore, be projected onto a plane where the triangulation takes place. Once the 2D triangles have been generated, the 3D geometry can be reconstructed by adding back the coordinate along the direction of projection. A natively 3D form of the DT also exists that can be applied to any point cloud; however, it generates tetrahedra, meaning that the final triangles must be extracted at a later step by identifying the outer faces of the tetrahedra, *i.e.,* faces that are not shared by more than one tetrahedron [122]. The general problem with DT (2D or 3D) is that connectivity is established following criteria driven by the desire to obtain triangles that conform to specific geometric properties (no point of the original cloud may lie inside any given triangle or tetrahedron). Such geometric properties may not necessarily guarantee that the connectivity is correct for the underlying surface that the method is trying to reconstruct. Many other methods to establish connectivity and create a triangle mesh from a point cloud exist [149–152]. The problem of converting a point cloud into a triangle mesh is a special case of a more general problem known as "surface reconstruction", where the goal is to start from a point cloud and obtain a continuous surface expressed in some analytical form, from which the cloud might have been sampled. The problem of surface reconstruction can be addressed considering any type of continuous geometry, including polynomial surfaces and parametric surfaces (splines, b-splines, non-uniform rational basis splines - NURBS). Reconstruction into a triangle mesh is, therefore, seen as a special case of reconstruction where the surface is defined in a very simple way (a set of connected triangles). The conversion of point clouds into triangle meshes is of primary importance, given the large diffusion of triangle meshes in many applications dealing with 3D

geometries [115]. In the context of coordinate metrology and the themes covered by this chapter, evidently the possibility of reconstructing a surface in the form of a triangle mesh may provide significant benefit to all the other pre-processing and point cloud analysis methods discussed. This is primarily because a triangle mesh allows for a significantly more robust selection of the true neighbours of any given query point, whilst without connectivity, only selecting points based on distances cannot be relied upon.

2.2.4 Point features and partitioning

In point cloud analysis, a cloud feature is a property/attribute that describes the entire cloud. The dimensions of an AABB encompassing the whole cloud are examples of cloud features. The centroid and the aspect ratio between the principal axes computed on the point cloud are other examples of cloud features. Conversely, a point feature is any property/attribute that can be associated to each individual point of a point cloud. Examples of point features may be colour, local orientation or local curvature. The position of a point is a point feature itself, and it is the only feature that must be mandatorily defined for every point in the point cloud. Unless point features are directly available from measurement (for example, colour information, if the measuring system provides the option to capture it), most point features must be computed, and necessitate point neighbour information in order for the computation to take place. The local normal, for example, needs knowledge of point neighbours in order to identify a local, reference plane (see next Section 2.2.4.1). Local curvature also needs neighbour information (see

Section 2.2.4.2). Because of the need for neighbours, many point features essentially capture properties related to the local "shape" of the surface (as approximated by the point itself and its immediate neighbours) and are, therefore, often referred to as local shape descriptors. A survey on point features for 3D point clouds is reported in Han et al. [153].

Cloud features and associated similarity/difference metrics can be used to compare point clouds, recognising those that are similar to each other, or different based on size, position, aspect ratio, *etc.* Analogously, point features and associated similarity/difference metrics can be used to compare points, recognising those that are more similar or different from each other, based on any attribute that can be computed as a point feature.

2.2.4.1 Point normals

The estimation of the local normal to a query point $\boldsymbol{q}$ (Figure 2.18.a) is usually performed by fitting a plane $\boldsymbol{T}$ (a low-order polynomial surface or a spline) to $\boldsymbol{q}$ and its closest neighbours $\boldsymbol{p}_k$, found using the k-NN algorithm. Then, the point normal $\boldsymbol{n}$ is identified by the normal to the fitted plane [96]. Alternatively (Figure 2.18.b), once the local subsets of neighbouring points have been selected via the k-NN algorithm, PCA can be performed [139,154].

The PCA is computed on the union of the query point $\boldsymbol{q}$ and its $\boldsymbol{p}_k$ neighbours (see Section 2.2.2.2 for PCA general formulation on entire dataset $\mathbf{P}$). The covariance matrix $\mathbf{C}$ shows how subsets of neighbouring points locally vary from their centroids $\boldsymbol{c}$. Given $\boldsymbol{v}_j$ the eigenvectors, and λ_j the corresponding eigenvalues with $j \in \{0, 1, 2\}$

$$\mathbf{C} \cdot \boldsymbol{v}_j = \lambda_j \cdot \boldsymbol{v}_j \,. \tag{2.9}$$

If $\lambda_0 \leq \lambda_1 \leq \lambda_2$, the eigenvector $\boldsymbol{v}_0$ with the smallest eigenvalue λ_0 identifies the normal vector to the fitted tangent plane T, geometrically perpendicular to the eigenvector $\boldsymbol{v}_2$ with the greatest eigenvalue λ_2, in the direction of the principal variation.

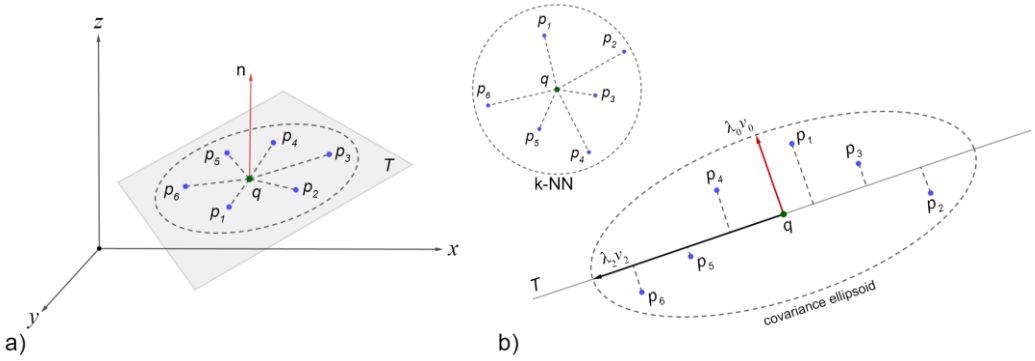

Figure 2.18 Point normal estimation approaches: a) fitted plane T to a query point $\boldsymbol{q}$ and its neighbours $\boldsymbol{p}_k$; $\boldsymbol{n}$ to the point $\boldsymbol{q}$ is identified by the normal vector to the fitted plane. b) Once the neighbouring points are found using k-NN, the normal estimation can be found via PCA; given the covariance matrix built with the coordinates of local points, the eigenvector $\boldsymbol{v}_0$ with the smallest eigenvalue λ_0 corresponds to the normal vector $\boldsymbol{n}$

In many operations for point cloud processing, point normals are required to be consistently oriented: the normals must all be directed inwards or outwards with respect to a hypothetical surface, which ideally encloses the geometric object from which the points have been sampled. As a convention, normals associated to the surface of a geometric object are typically assumed as pointing outwards (Figure 2.19). However, the methods illustrated above

for computing point normals do not guarantee consistent orientation, thus some type of post-processing operation must be typically applied.

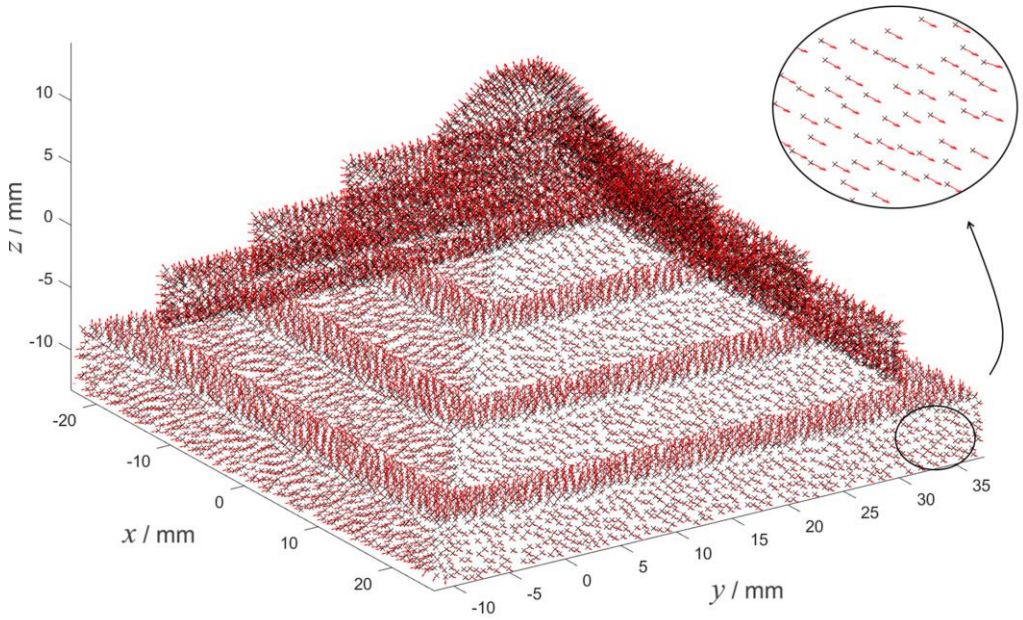

Figure 2.19 Point vector normals consistently oriented pointing outwards, shown on pyramid artefact designed by Manufacturing Metrology Team, University of Nottingham

A method to compute a consistent orientation of the normal vectors is based on using Euclidean minimum spanning trees (EMST [96]). Starting from a subset $\mathbf{Q} \subset \mathbf{P}$ of points whose normals are assumed as correctly oriented, EMST is used to reach neighbours located within a region of increasing radius. The normal $\boldsymbol{n}_j$ of each new neighbour $\boldsymbol{p}_j$ is checked against the (correct) normal $\boldsymbol{n}_i$ of the previous (correct) point $\boldsymbol{p}_i$, and flipped if inconsistent using:

$$\boldsymbol{n}_i \cdot \boldsymbol{n}_j < 0 \rightarrow \boldsymbol{n}_j = -\boldsymbol{n}_i \,. \tag{2.10}$$

2.2.4.2 Point curvatures

In differential geometry, k_1 and k_2 are the maximum and minimum local curvatures of the planar curves formed by intersecting a normal plane with the surface itself [155]. The principal curvatures can be used as local shape descriptors [156,157].

Surface curvature estimation has been studied extensively over the past decades, though mostly dedicated to continuous surfaces. For point clouds, methods for computing curvatures rely on locally fitting the point and its neighbours to a continuous surface onto which the curvatures are computed, or rely on using a triangle mesh as a substitute for the continuous surface [158,159]. More recently, methods have been proposed for curvature computation directly on point clouds [160]. An example method consists of running a PCA on the local normals (*i.e.,* not on the point coordinates) belonging to the neighbours of $\boldsymbol{q}$, and estimating the principal curvatures using the eigenvectors and eigenvalues of the resulting covariance matrix.

Two additional types of curvature, often computed on point clouds, are the Gaussian curvature K and the mean curvature H [161]. These can be estimated from the principal curvatures k_1 and k_2 as follows

$$K = k_1 \cdot k_2 , \tag{2.11}$$

$$H = \frac{(k_1 + k_2)}{2} . \tag{2.12}$$

In Figure 2.20, mean and Gaussian curvature values are mapped to a colour scale for visualisation purposes. Mean and Gaussian curvature can be used as local shape descriptors, for the purpose of segmentation, classification, comparison of shapes and registration (see further discussion in Section 2.2.6.1).

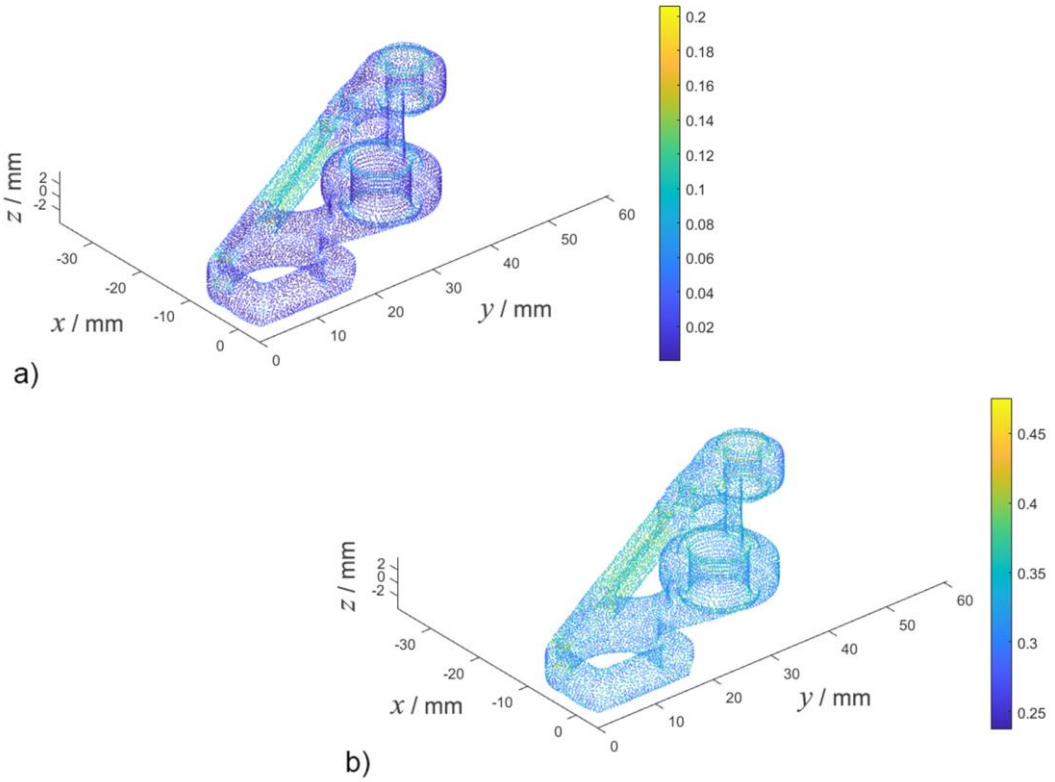

Figure 2.20 Local curvature values estimation on point cloud (roof bracket), converted into a colour map representation: a) Gaussian curvature K, and b) mean curvature H

2.2.4.3 Fast Point Feature Histograms

Local point feature similarities/differences may not be sufficiently discriminative, for example when different surface shapes show very similar curvature values. For this reason, more powerful local shape descriptors are

often preferable over curvatures to achieve correct segmentation, classification and registration results. An example solution is given by the Fast Point Feature Histograms (FPFH) descriptor, proposed by Rusu et al. [162] as a simplified and optimised alternative to Point Feature Histograms (PFH – local descriptors which encode the local geometric information of a point feature) [163].

PFH and FPFH are pose-invariant local feature descriptors (*i.e.,* shape descriptors that are not affected by the pose variation of an object) which represent the properties of the underlying surface model at a point $\boldsymbol{p}$. Their computation is based on the geometrical relationship between the point $\boldsymbol{p}$ and its k closest neighbours. With the same power of PFH, FPFH encode the geometric information of point features, incorporating the x, y, z 3D point coordinates with surface normal vectors (n_x, n_y, n_z). Instead of considering pair of points in the neighbourhood of $\boldsymbol{p}$ as in the PFH construction, the process is simplified by computing three angular features $(\alpha, \varphi, \theta)$ for each point $\boldsymbol{p}$ between itself and its $\boldsymbol{p}_k$ neighbours (Figure 2.21), as follows:

$$\alpha = v \cdot \boldsymbol{n}_k,$$

$$\varphi = u \cdot \frac{(\boldsymbol{p}_k - \boldsymbol{p})}{d}, \tag{2.13}$$

$$\theta = \arctan(w \cdot \boldsymbol{n}_k, u \cdot \boldsymbol{n}_k),$$

where $\boldsymbol{d}$ is the distance between $\boldsymbol{p}$ and its $\boldsymbol{p}_k$ neighbours, and having previously defined a Darboux uvw frame at $\boldsymbol{p}$:

$$u = \boldsymbol{n},$$

$$v = u \times \frac{(\boldsymbol{p}_k - \boldsymbol{p})}{\|\boldsymbol{p}_k - \boldsymbol{p}\|_2}, \tag{2.14}$$

$$w = u \times v.$$

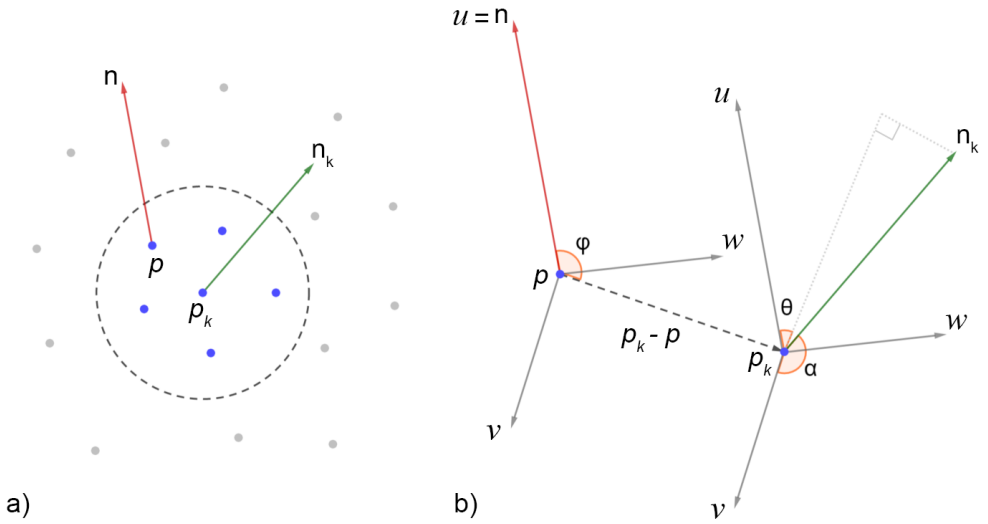

Figure 2.21 Fixed coordinate frame and angular features computed for a pair of points. a) Identification of point $\boldsymbol{p}$ and its $\boldsymbol{p}_k$ neighbours with normal vectors $\boldsymbol{n}$ and $\boldsymbol{n}_k$ respectively; b) definition of the Darboux frame and computation of $(\alpha, \varphi, \theta)$ angular features

The optimisation leads to the construction of a Simplified Point Feature Histogram (SPFH). For each point $\boldsymbol{p}$, its k neighbours are re-determined, and the neighbouring SPFH values are used to weight the final FPFH as follows:

$$FPFH(\boldsymbol{p}) = SPFH(\boldsymbol{p}) + \frac{1}{k}\sum_{i=1}^{k}\frac{1}{\omega_k} \cdot SPFH(\boldsymbol{p}_k), \tag{2.15}$$

where ω_k represents a distance between the point $\boldsymbol{p}$ and a neighbouring point $\boldsymbol{p}_k$, scoring the pairs $(\boldsymbol{p}, \boldsymbol{p}_k)$.

For a point $\boldsymbol{p}$ the algorithm first estimates its SPFH values by creating unique pairs between $\boldsymbol{p}$ and its neighbours. This is repeated for all the points in the cloud, followed by a re-weighting of the SPFH values of $\boldsymbol{p}$ using the SPFH values of its neighbours, thus creating the FPFH for $\boldsymbol{p}$.

FPFH local descriptors can be used in applications such as point cloud registration (see Section 2.2.6).

2.2.4.4 Partitioning and segmentation

By using point features, for example normals, curvature values, and local descriptors as illustrated in the previous sections, points can be classified, *i.e.,* mapped to a discrete and countable number of classes. Classification can be implemented in multiple ways:

a) by threshold-based rules (by explicitly setting a maximum degree of similarity for point features to belong to the same class);

b) by statistical clustering, *i.e.,* automated identification of thresholds to produce groups of similar point features;

c) by region growing (a combination of thresholding and clustering, starting from points of known classification and expanding the result via incorporation of consistent neighbours).

Regardless of the classification method, any classification operation results in a partitioning, *i.e.,* generation of subsets of points, corresponding to the identified classes. If the partitioning operation leads to subsets containing

points that are also topologically adjacent (assuming that the topological relationships can be reconstructed - see Section 2.2.3.3), then such subsets are called segments. In parallel with digital image processing, a segment is in fact a set of adjacent pixels classified as belonging to the same class [164]. A classification operation on point features leading to segments is called a point cloud segmentation [165].

Point cloud segmentation paves the way for shape representations that rely on decomposition, favouring the implementation of shape-based automated reasoning solutions powered by machine learning [166] and supporting applications where semantic interpretation of regions is needed (for example, decomposition of a teapot model to identify its handle). Reviews of the most common segmentation methods for point clouds can be found elsewhere [111,165,167,168].

Partitioning of point clouds based on k-means and hierarchical clustering

Clustering-based approaches (for example, k-means and hierarchical clustering) applied to point clouds generate partitions/clusters where each cluster gathers points with similar point feature values. Similarity/difference can be computed in multiple ways, for example by using Euclidean or city-block distance, depending on the dimensionality of the feature (for example, a scalar or a n-dimensional vector) [125].

In point cloud k-means clustering, a final number of clusters (k) must be decided in advance. The method starts with an initial random assignment of points to clusters, then it proceeds by iteratively refining the assignments using considerations based on similarity/difference. Clusters are updated at

each iteration, so that point assignment evolves dynamically until the last point has been classified. An example application of k-means clustering is shown in Figure 2.22.a, where points are assigned to one of five clusters ($k = 5$) based on Gaussian curvature. Note how points belonging to the same cluster may not necessarily be adjacent to each other; that is, partitioning by k-means clustering is not a segmentation method.

Hierarchical clustering of points in point clouds is an alternative to k-means that does not involve the specification of the number of clusters needed. Instead, the most similar points (where similarity is computed on point features) are grouped into proto-clusters, then iteratively aggregated into larger ones, following between-cluster similarity measures. The iterative aggregation process is described as a tree-like graph known as "dendrogram", which invariably terminates with a single cluster incorporating all points of the point cloud. Criteria can be set to stop the recursive aggregation once specified criteria are met (for example, the maximum difference between clusters that still allows their aggregation). An example application of hierarchical clustering for point cloud partitioning is shown in Figure 2.22.b, again using Gaussian curvature as the point feature driving the classification.

As for k-means, the partitioning result is not a segmentation, because points may belong to the same cluster even if they are far apart from each other. Clustering is often used to isolate subsets of points whose point features are extremal in value, for example, to isolate points with the highest curvature values. Such points may act as landmarks for subsequent registration processes, as illustrated in Section 2.2.6.1.

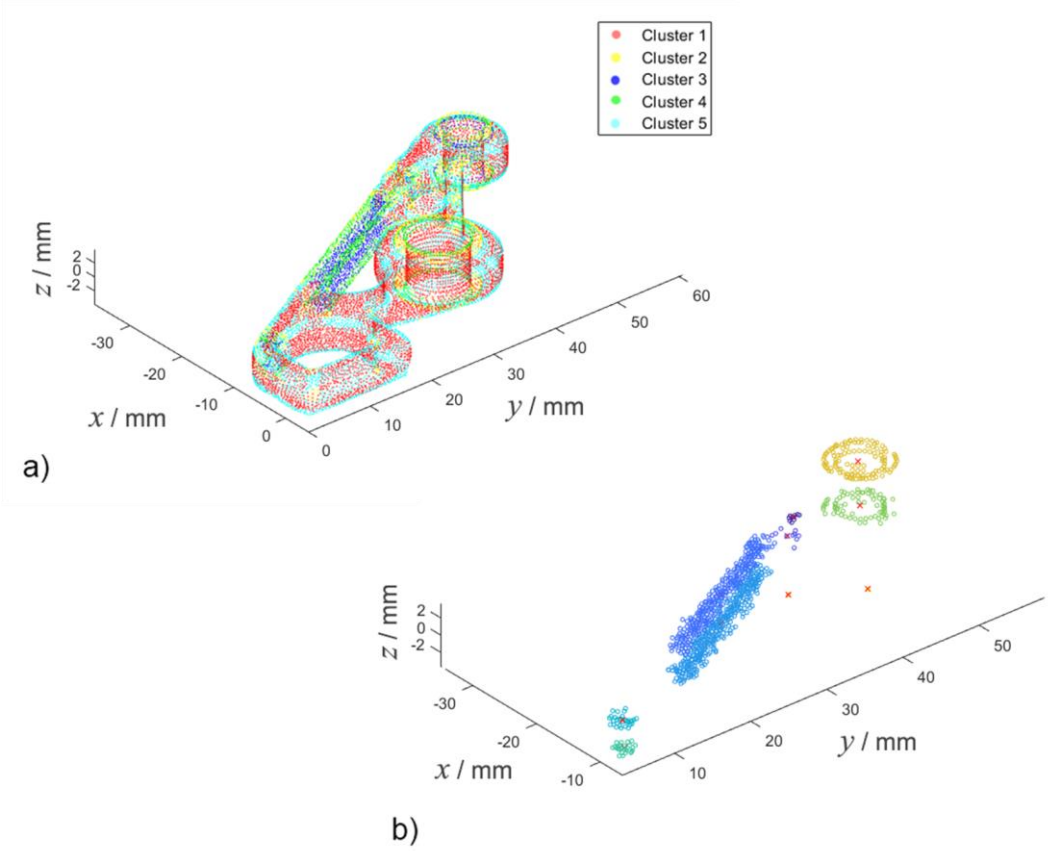

Figure 2.22 Point cloud partitioning methods: a) k-means clustering on Gaussian curvature (points are assigned to one of five clusters ($k = 5$)); cluster 3 refers to the points with the highest curvature values. b) Hierarchical clustering on Gaussian curvature and cluster centroids. The points taken into account are the ones with the highest curvature values

2.2.5 Point cloud fitting

Point cloud fitting is defined as the process of identifying a geometric surface model that best describes the point cloud [169,170]. In layman's terms, fitting means finding a geometric model whose surfaces are sufficiently close to the points of a set to support the assumption that such points might have been sampled from that geometry.

Point cloud fitting is commonly used for a variety of reasons, such as replacing a point cloud with a continuous, mathematically defined geometry; investigating local properties of the point cloud by approximating a local cloud subset to a more "readable" geometric entity (for example, fit a local subset of points to a plane to obtain the local normal); obtaining reference geometric datums to perform further computation of distances, lengths, *etc.*; and finally, for comparing a point cloud (assumed from measurement) to a nominal reference (the fitted geometric model). A point cloud fitting process is comprised of two steps:

a) choosing a geometric model to fit the point cloud to;

b) choosing a fitting method.

The geometric model to fit to is called a "substitute feature". The choice of substitute feature influences the type and number of geometric modifications that the fitting process can apply to the feature itself, in order to make it a better fit to the point cloud; for example, a parametric, cylindrical surface could be altered by operating on the length and diameter (parameters) to obtain a cylinder that better fits a given point cloud. A polynomial surface may be fit to the point cloud by changing the orders of the underlying polynomials. The substitute feature may also be a triangle mesh. In this latter case though, the transformations imposed by fitting may be limited to a change of scale, or more frequently to a single rigid transform (translation and rotation), which turns the fitting problem into a registration problem [121] - see Section 2.2.6. In coordinate metrology, fitting to a triangle mesh is commonly used to perform a coarse comparison between a nominal geometry (the triangle mesh) and the result of a measurement (the point cloud). More

challenging is the choice of a substitute feature when fitting involves clouds sampled to freeform or otherwise complex surfaces. This is a frequent issue with additively manufactured parts [170].

The second step of fitting is the choice of the mathematical process through which the chosen analytical geometric model (substitute feature) is adapted to the point cloud. In general terms, fitting is usually implemented as some type of minimisation involving the distances of the points to the best-fit geometric model. In the following sections, the most common fitting methods are presented.

2.2.5.1 Fitting methods

The geometric model (substitute feature) can be assumed as a mathematically defined, continuous surface. In general, this can be expressed by the parametric function $\boldsymbol{f(u;b)}$ where $\boldsymbol{b}$ is known as the shape vector [171] which changes depending on the type of mathematical representation adopted, and $\boldsymbol{u}$ is a vector of parameters to navigate across the continuous surface (a generalisation of surface coordinates). Most fitting methods are based on the L_p norm, given by

$$L_p \doteq \left[\frac{1}{N}\sum_{i=1}^{N}|e_i|^p\right]^{1/p}, \tag{2.16}$$

where N is the number of points in the cloud, e_i is the shortest Euclidean distance between the i^{th} point of the cloud and the nearest point on the continuous surface defined by the substitute feature. The best-fit feature is

the one that minimises L_p. Since this is a minimisation problem, $1/N$ and the exponent $1/p$ can be omitted, leading to the following expression to be minimised

$$E_p \doteq \sum_{i=1}^{N} |e_i|^p, \tag{2.17}$$

where E_p is a measure of cumulative "error" between the point cloud and the substitute feature.

Least-sum-of-distances fitting

When $p = 1$, equation (2.17) becomes

$$E_1 = \sum_{i=1}^{N} |e_i|, \tag{2.18}$$

where E_1 is a sum of absolute distances. The minimisation of E_1 is called least-sum-of-distances fitting. The minimisation problem can be solved using a number of optimisation methods [171].

Total-least-squares fitting

When $p = 2$, equation (2.17) becomes

$$E_2 = \sum_{i=1}^{N} |e_i|^2 = \sum_{i=1}^{N} {e_i}^2, \tag{2.19}$$

where E_2 is called the sum of squared distances, and the minimisation problem is known as total-least-squares (TLS) fitting, also referred to as orthogonal distance regression [172,173]. Note that, as stated previously, e_i is the Euclidean distance between point $\boldsymbol{p}_i$ and the corresponding closest point on the geometric model. Assuming that such a closest point can be found using the value $\boldsymbol{u}_i$ for the parameter vector $\boldsymbol{u}$, the minimisation of the sum of squared distances is expressed as

$$\min_{b}\left(\sum_{i=1}^{N}|\boldsymbol{p}_i - f(\boldsymbol{u}_i;\boldsymbol{b})|^2\right). \tag{2.20}$$

Equation (2.20) describes the minimisation problem as the problem of finding the optimal values for the components of the shape vector $\boldsymbol{b}$ so that E_2 is minimised. The minimisation problem is in general non-linear and must be solved via iterative methods (for instance, Gauss-Newton or Levenberg-Marquardt), though the risk of converging to local minima must be taken into account. In general, TLS fitting is the most frequently applied fitting method for point clouds. However, least-sum-of-distance fitting is also applied, in particular as it is slightly more robust to outlier points.

Ordinary-least-squares fitting

In some cases, when the nature of the point cloud allows it, fitting could be done to a function of type: $z = f(x, y;\ \boldsymbol{b})$. In this formulation, the substitute feature is described by a dependent variable (z) function of the variables x, y, which define the location and essentially replace the vector of parameters $\boldsymbol{u}$,

and $\boldsymbol{b}$ is still the shape vector of the surface, the usual independent variable in the minimisation problem. When this formulation is possible, the L_p norm can be modified by defining the Euclidean distance between each point and its closest neighbour in the substitute feature (e_i) as a simple difference in z coordinates. For the $p = 2$ case (least-squares), the minimisation problem is expressed as

$$\min_{b}\left(\sum_{i=1}^{N}|z_i - f(x_i, y_i; \boldsymbol{b})|^2\right), \tag{2.21}$$

which is an example of ordinary-least-squares (OLS) formulation as opposed to TLS. The OLS problem is computationally simpler, and in some cases, it admits closed-form solution. For example, when considering the OLS fitting of a point cloud to a plane, equation (2.21) becomes

$$\min_{b}\left(\sum_{i=1}^{N}|z_i - (Ax_i + By_i + C)|^2\right), \tag{2.22}$$

where parameters A, B and C are the components of the shape vector $\boldsymbol{b}$ that must be found in order for the expression to be minimised. Turning a point cloud fitting problem into the OLS problem defined by equation (2.22) is appealing as the formulation admits closed-form solution. However, the field of applicability of equation (2.22) is limited by the requirement of the point

cloud being representable by $z = f(x_i, y_i; \boldsymbol{b})$, which automatically excludes re-entrant surfaces or full-3D geometries.

The difference between solving the OLS problem or the TLS problem is visually exemplified in Figure 2.23, where a 2D point cloud is fit to a line.

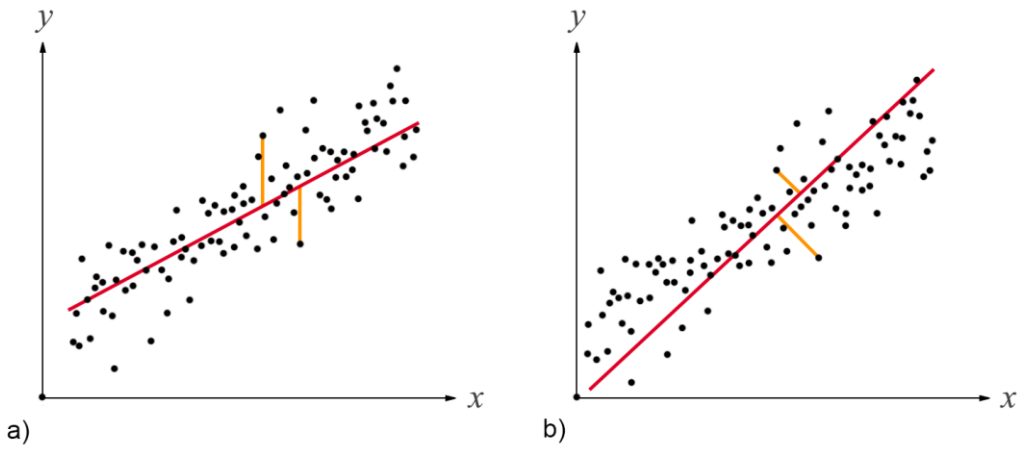

Figure 2.23 2D representation of point cloud fitted to a line. Difference between a) ordinary-least-squares (OLS) fitting, and b) total-least-squares (TLS) fitting

Two-sided and one-sided minmax fitting

Two-sided minmax fitting consists of the minimisation of the L_p norm when $p = \infty$. When $p = \infty$, it can be demonstrated that

$$L_\infty = \lim_{p \to \infty} L_p = \max_{1 \leq i \leq N} |e_i|. \tag{2.23}$$

In other words, L_∞ is the maximum distance of the points in the cloud computed on both sides of the geometric surface model. The minimisation of L_∞ is expressed as

$$\min_{b}\left(\max_{1\le i\le N}|e_i|\right), \tag{2.24}$$

which means that at the end of the fitting process, the maximum signed e_i will be reduced to its minimum possible value, or in other words, that the maximum signed distance of the sampled data points and the geometric model is minimal on both sides. Because of this effect, the minimisation is called "two-sided minmax fitting".

With two-sided minmax fitting, the fitted model will lie approximately in the centre of the data points, in a visually similar manner to the results of a TLS fitting (though the two methods solve slightly different minimisation problems). In some circumstances, however, a fitting problem must be solved to identify a substitute feature that lays entirely on one side of the point cloud. A typical example is fitting to the minimum circumscribed circle or to the maximum inscribed circle. Another example is the identification of the lowest plane "touching" the cloud from above, and the highest plane touching it from below. Geometric tolerances are typically assessed solving these types of problem. Minmax fitting can be used to solve these problems as long as the minimisation is accompanied by a constraint on the sign of the errors (e_i) that can be involved in the minimisation. For instance, if only the minimisation of the positive e_i is considered

$$\min_{b}\left(\max_{1\le i\le N}|e_i|\right), \qquad e_i \ge 0, \quad \forall i = 1,\cdots,N. \tag{2.25}$$

A two-sized minmax fitting, where minimisation is constrained on the sign of e_i, is called "one-sided minmax fitting". Note that one-side minmax fitting is not the only method available to solve one-sided fitting problems and to identify datums for tolerances, for example see Moroni and Petrò [174] for a survey on minimum-zone fitting.

RANSAC fitting

Random sample consensus (RANSAC) is a general framework for model fitting in the presence of a large number of outliers. Introduced by Fischler and Bolles [175], RANSAC is a robust iterative algorithm used to estimate parameters of mathematical features (for example lines or circles) from a set of observations that contains outliers. The name comes from the actual algorithm functionality of randomly selecting a sampled group of data points in datasets containing both inliers and outliers, and being able to consider only the points classified as inliers to perform the optimal fitting. The set of inliers obtained for the fitting is called the consensus set. RANSAC algorithms achieve their goals by iteratively repeating the steps that follow [175]:

- select a random subset of N points of the original dataset **P**. This subset is identified as a group of hypothetical inliers;
- fit a model x to the set of hypothetical inliers;

- test the rest of the data against the fitted model; the points that fit the estimated model well are considered as part of the consensus set K, within a user-given threshold;
- if a sufficient number of points is classified as part of the consensus set, the estimated model $\boldsymbol{x}$ is reasonably good and the process terminates; otherwise start a new iteration with another random subset.

The iterative procedure is repeated until the consensus set is large enough, and/or until a predefined number of iterations is reached. Reaching the latter condition may mean that a proper fitting has not been obtained. However, the advantages with respect to other methods, such as total or ordinary least-squares fitting, is that with RANSAC fitting it is possible to take outliers into better account, whilst in least-squares methods, all points are accounted for in the same manner (unless weighted formulations are adopted).

Because of its intrinsic robustness to outliers, RANSAC is often applied to solve point cloud-related problems other than fitting. For example, RANSAC is used as an outlier detection method [176], for automatic identification and extraction of shape primitives [177] and for registration [121,166] (see also Section 2.2.6.4).

2.2.6 Registration of point clouds

A point cloud produced by measurement is defined within a local coordinate system created by the measurement instrument itself. When multiple measurements are taken from the same object, for example from different

viewpoints or using different instruments, each point cloud has its own coordinate system and in principle there is no explicit information that indicates how point clouds are spatially related to each other. Registration is the process that brings multiple point clouds taken from observations of the same scene in their correct, relative position within a shared coordinate system.

From a mathematical standpoint, registration implies the application of a transformation to each point cloud consisting of a rotation and a translation (see previous Section 2.2.1.4). Such transformation is called "rigid" as it does not alter the shape of each point cloud (only its position and orientation), and the registration process is, therefore, called "rigid registration". There are also registration processes where transformations are allowed to slightly alter the shape of the cloud, for example by changing its scale, or by deforming the cloud to compensate for specific types of aberration introduced by measurement. When this happens, the registration process is called "non-rigid registration". In coordinate metrology, non-rigid registration is particularly challenging, because it could introduce additional errors to the already present measurement errors. In this section, rigid registration strategies will be the primary focus.

In optical measurement, rigid registration allows for multiple high-density point clouds to be aggregated from measurements taken at different viewpoints, in order to increase the part coverage. This process is known as point cloud stitching (Figure 2.24).

In coordinate metrology, rigid registration can also be used to localise multiple point clouds taken from the same surface region, so that later

aggregation can be used to reduce the random component of measurement error. Registration of point clouds acquired using multiple instruments can be used to compare the performances of the instruments themselves. Finally, registration of point clouds obtained by measuring different parts can be used to study geometric differences between the parts.

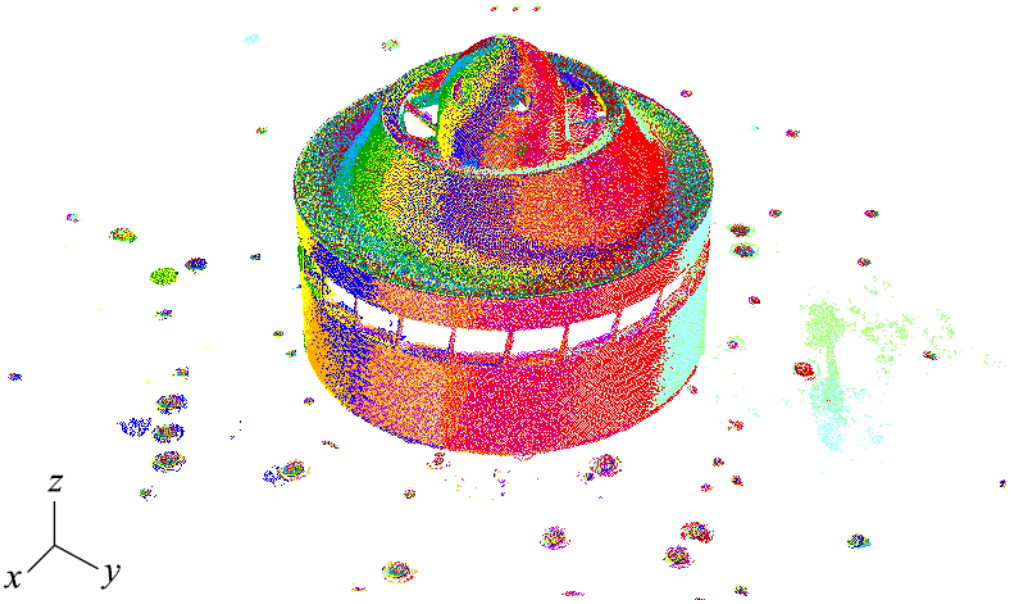

Figure 2.24 Example of point cloud stitching. High-density point set acquired with an optical system from multiple viewpoints (represented with different colours) are registered together, in order to maximise the part coverage

Registration may also be applied to localise triangle meshes, continuous surface representations and any hybrid combination of the previous types. Registration of point clouds to continuous surfaces or triangle meshes in particular can be used to compare a measured geometry to a nominal geometry (Figure 2.25), or to find a mathematical geometry that is representative of the cloud itself and can be used in substitution of the cloud.

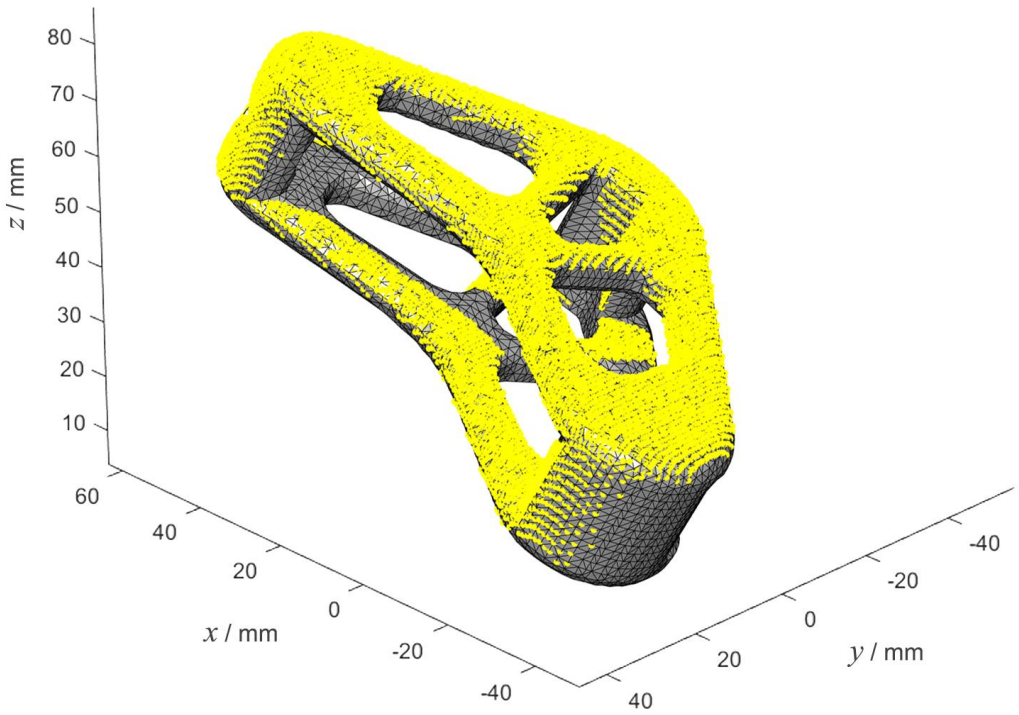

Figure 2.25 Example of registration between a point cloud to a continuous surface (*i.e.*, triangle mesh). The point cloud simulates a unidirectional single shot optical measurement of an industrial part

In this latter scenario, registration becomes a type of fitting (discussed in Section 2.2.5). Rigid registration is equivalent to a fitting process where only rigid transformations are allowed. Non-rigid registration methods can be adopted to tackle some fitting problems that involve modification of parameters of the substitute feature (for example, the scale). However, non-rigid registration methods in general do not cover an equivalently wide set of cases as other more general fitting methods (see Section 2.2.5.1).

Finally, registration processes may be defined where localisation involves more heterogeneous datasets, for instance 3D point clouds with digital 2D images, or 3D point clouds with 3D voxel data. These types of registration

processes are emerging in coordinate metrology but will not be covered in this section. The methods illustrated in the following always presume that at least one dataset to be registered is a point cloud, ideally but not necessarily produced by measurement.

An overview of most of the registration methods illustrated in this section can be found elsewhere [121]. Most registration methods only operate on two datasets at a time (point clouds or meshes); one typically being left in its original state while the other is transformed to achieve localisation in the coordinate system of the first. When multiple datasets must be registered, methods operating on pairs must proceed sequentially, either by registering each new dataset to the same reference one, or by registering each new dataset to the merged dataset obtained at the previous registration step, therefore, chaining new datasets in sequence. The chaining approach carries a larger risk of error accumulation, particularly when attempting to "close the loop" on point clouds chain-stitched all around a measured object. Finally, as opposed to proceeding with pairs, multi-view registration methods are capable of processing all the datasets simultaneously. Further details on registration methods based on pairs or operating on all datasets at the same time can be found elsewhere [86,172,178–181].

2.2.6.1 Registration based on external references or based on matching landmarks

When either the part being measured or the measurement system can be mounted onto a robotic arm, contact CMSs or other moveable, indexed devices (for example, a part placed on a rotary stage), relative positioning can

be recorded from encoders and can be used to perform the registration of multiple point clouds taken within the same setup. The accuracy and precision of measurement is usually superior to that of the positioning system thus, registration results should usually be subjected to further refinement, using methods later described in Section 2.2.6.5.

However, information on relative positioning is often not present or may be inadequate. For example, in additive manufacturing, mass customisation typical of layer-based processes, often does not make it feasible or economically convenient to prepare dedicated fixtures, so even if using a rotary stage or other controlled positioning axes, small displacements between the part and the measurement point may occur.

When information on relative positioning is absent or not sufficiently reliable, the only option is to search for "hints" in the point clouds themselves. For example, if measurements are taken from slightly different viewpoints but cover at least in part the same portion of surface, region similarities between point clouds may be searched for, as potentially representative of sampling from the same area. The approach of searching for similarities is known as the "search for correspondences", or "search for corresponding landmarks". Once corresponding landmarks are found, the point clouds can be rotated and translated until the landmarks are overlaid, providing a best estimate of the registration result.

With the search for corresponding landmarks, the registration problem is turned into a problem of landmark identification, followed by their geometric overlay, the latter process often being referred to as geometric alignment. Geometric alignment of landmarks implies minimisation of their

relative distances, which mathematically is not dissimilar to the problems dealt with by fitting. The main limitation of registration based on aligning matching landmarks is the impossibility to apply this approach to point clouds which do not contain regions sampled from the same surface.

2.2.6.2 The absolute orientation problem

At the heart of many registration methods based on landmark alignment lies the absolute orientation problem. The absolute orientation problem has a closed-form solution and is, therefore, extremely fast, not requiring iterations, and is guaranteed to deliver an optimal solution. In the absolute orientation problem [182,183], two point clouds are considered, one moving $\mathbf{P} = \{p_1, p_2, \dots, p_n\}$, and the other fixed $\mathbf{Q} = \{q_1, q_2, \dots, q_m\}$, not necessarily containing the same number of points ($m \neq n$). A number k of pairwise correspondences has been pre-defined; those correspondences are known as pairwise matches, involving k points per cloud ($k < \min(m, n)$). In the context of landmark-based registration, individual points act as landmarks, and pairwise matches identify the unique aligned correspondences. Solving the absolute orientation problem means finding a transformation to be applied to the moving point cloud so that the Euclidean distances between pairwise matched points are minimised. The general transformation for $\mathbf{P}$ includes a rotation matrix $\mathbf{R}$, a translation vector $\boldsymbol{t}$ and a global scaling coefficient s, that is

$$\min_{s,\mathbf{R},\boldsymbol{t}} \left(\frac{1}{k} \sum_{i=1}^{k} \| \boldsymbol{q}_i - (s\mathbf{R}\,\boldsymbol{p}_i + \boldsymbol{t}) \|^2 \right), \tag{2.26}$$

where $\boldsymbol{p}_i$, $\boldsymbol{q}_i$ is the pair of points belonging to the i^{th} pairwise match. A simplified formulation that removes the scaling coefficient ($s = 1$) is commonly adopted, so that the absolute orientation problem can be embedded in rigid registration approaches, *i.e.*,

$$\min_{\mathbf{R},\boldsymbol{t}} \left(\frac{1}{k} \sum_{i=1}^{k} \| \boldsymbol{q}_i - (\mathbf{R}\,\boldsymbol{p}_i + \boldsymbol{t}) \|^2 \right). \tag{2.27}$$

The above minimisation problem has a closed-form solution which has been found following multiple approaches [182,184,185]. Resolution methods are compared and discussed elsewhere [186]. An analogous problem has been solved in statistical shape analysis under the name of "Procrustes analysis" [187].

2.2.6.3 Alignment by means of principal component analysis

PCA (see Section 2.2.2.2) can be used to perform alignment between multiple datasets. In this case, landmarks are not identified as subsets of existing points from the original point clouds; instead they are new geometric entities automatically generated by the PCA on each point cloud, namely the centroid and principal axes. Alignment by PCA [126] is always a rigid transformation unless the corresponding principal axes are scaled, in order to obtain a match in length. The rigid version of the procedure is tackled as follows (Figure 2.26):

- the centroids of the datasets are overlaid by translation applied to the moving point cloud **P**;

- a rotation is applied in order to align the first, second and third principal axes of the datasets.

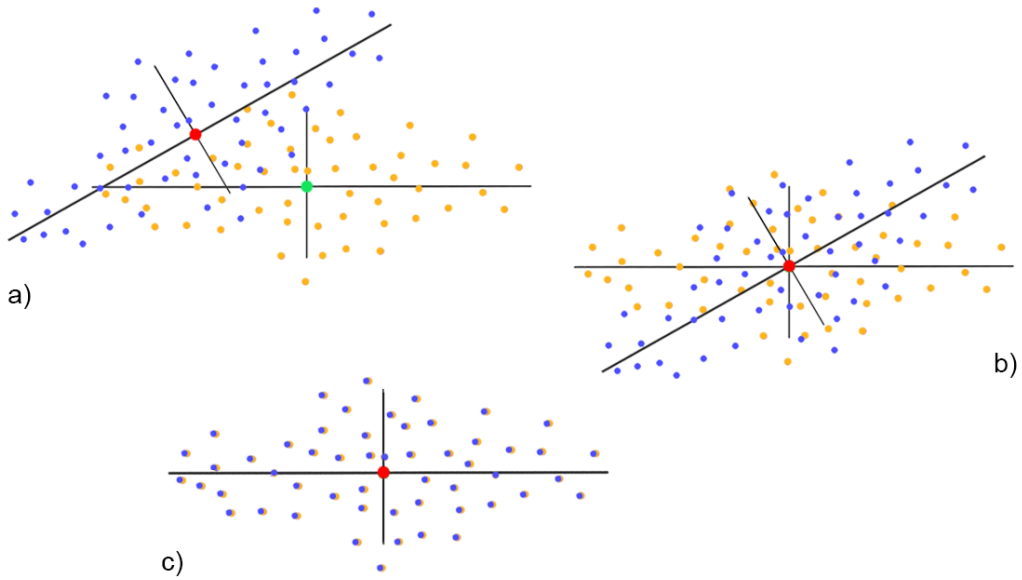

Figure 2.26 Point clouds alignment via PCA. a) Two sets of points (blue and orange respectively) in their initial configuration, b) centroid (red) of first point cloud is translated in order to coincide with centroid (green) of the second point cloud, and c) a rotation is applied in order to align the first, second (and third if 3D representation) principal axes of the datasets

Alignment performed via PCA can always be applied to any pair of point clouds, even when they do not feature any apparent similarity [180]. The downsides are related to the intrinsic properties of PCA: if the principal axes are very similar in length (*i.e.,* have similar eigenvalues), the wrong axes may be paired. Even when the pairing is correct, there are two valid solutions for each axis (either the positive directions along the axis are matched or a positive is matched to a negative) leading to 180° rotations that are equally valid PCA results (Figure 2.27).

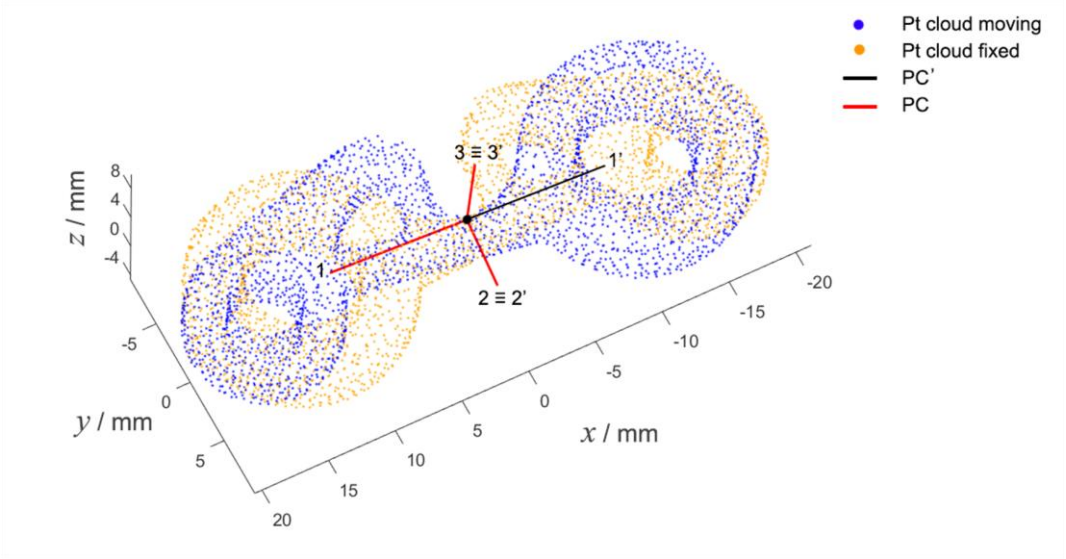

Figure 2.27 Example of wrong PCA alignment: the principal axis PC1' (black) of the moving point cloud (blue) is matched correctly with PC1 (red) of the fixed point cloud (orange). However, the directions are opposite (negative and positive respectively)

The use of alignment by PCA is, therefore, confined to obtaining very crude initial approximated localisation of point clouds in space, to pave the way for the subsequent application of better performing methods.

2.2.6.4 RANSAC alignment

Recalling the absolute orientation problem as the core method to mathematically solve the alignment problem (see Section 2.2.6.2), the challenge remains for the identification of correspondences between points (best pairwise matches), needed to solve the absolute orientation problem. Two solutions can be adopted:

a) the best matching points are those that can be better aligned, regardless of any other consideration about the nature of the selected points;

b) the best matching points are those that are the most similar, according to some metric defined using the points themselves and (usually) their immediate neighbours, regardless of whether such matches can be optimally aligned or not.

The most popular approaches which implement the first solution (best pairwise matches are those leading to optimal alignment) are known as RANSAC, and iterative closest points (ICP) alignments. RANSAC alignment is discussed here, while ICP will be illustrated in Section 2.2.6.5. Alignment methods based on similarity matches between landmarks are discussed in Section 2.2.6.6.

The RANSAC alignment algorithm is conceptually very similar to RANSAC fitting, discussed in Section 2.2.5.1 - see also [175]. The general idea in RANSAC alignment is to iteratively create random pairwise matches until a configuration is found that brings the majority of the points belonging to a moving point cloud **P** into alignment with a fixed point cloud **Q**. In detail, at each iteration, a set of random matches between **P** and **Q** is created involving only a core subset of the two point clouds. These matches are used to solve the absolute orientation problem, leading to the transformation of the entire **P** point cloud. Further pairwise matches are then constructed between the points not belonging to the core subset and evaluated for goodness of alignment (using the same equation (2.26) to solve the absolute orientation problem). If a sufficient number of pairs are found in good alignment (*i.e.,* there is a sufficient consensus), then the iterations terminate, and the alignment is considered valid. On the contrary, if too few pairs show good alignment, the procedure is repeated, starting from a new random core subset.

Figure 2.28 Paired of correspondences (squares and circles) identified in two point clouds (red and orange respectively) are matched via RANSAC alignment

The advantage of RANSAC alignment is its simplicity of implementation and speed, as it relies on closed-form solution of the absolute orientation problem. The downside is that there is no guarantee that an optimal alignment is found, due to the inherent randomness of the method and due to the need to set the controlling parameters of the method in a trial and error fashion. An example of coarse alignment between two datasets, matching correspondences via RANSAC, is shown in Figure 2.28.

2.2.6.5 Alignment by iterative closest points

The disadvantage of RANSAC alignment is that there is no learning, no evolution of the alignment result towards an increasingly better solution. In RANSAC alignment, if the consensus is not reached at any given iteration,

the search restarts from the beginning, from an entirely new set of randomly selected, tentative correspondences. The iterative closest point (ICP) method [188] circumvents this problem by introducing a different type of iteration, based instead on refinement of the previous result. There is actually a multitude of variants of ICP [189], so in the following section, only the most characteristic aspects are discussed.

As with RANSAC, the ICP method begins by creating a set of tentative matches, typically by selecting a random core subset of points in the moving $\mathbf{P}$ and fixed $\mathbf{Q}$ point clouds. The absolute orientation problem is solved, and $\mathbf{P}$ is brought into the best possible alignment for the given set of correspondences. Differently from RANSAC, after absolute orientation is solved, the correspondences in the core set are broken, and an entirely new set is formed by searching for the nearest neighbour $\boldsymbol{q}$ of each point $\boldsymbol{p}_i$. When the new correspondences are established, the absolute orientation problem is solved again, and the moving point cloud $\mathbf{P}$ is displaced once more. The process continues iteratively, with new correspondences being formed and a new absolute orientation problem being solved at each step. The termination criterion is usually related to the algorithm having reached a maximum number of iterations, or to the detection of the interruption of motion of the moving point cloud, meaning that final correspondences have been found and stabilised, so no further change is required.

Because of the intrinsic nature of the ICP iterative loop, the most significant displacement of the moving point cloud $\mathbf{P}$ occurs at the first iteration step, when the absolute orientation problem is solved the first time. After the first step, $\mathbf{P}$ can only shift by small amounts, corresponding to small

changes in the set of correspondences, and soon reaches a stop when the method is unable to evolve the correspondences any further. ICP is, therefore, very likely to quickly converge to a local minimum, with little capability of exploring the search space any further. ICP performance is strongly dependent on the initial position of **P**, and thus is typically adopted as a refinement of a previous, coarse alignment step (typically performed by landmark matching, see Section 2.2.6.6).

Several researchers have studied ways to increase the exploration power of ICP. For example, the use of an additional step to forcibly displace the moving point cloud by a small amount after resolution of the absolute orientation problem has been suggested to promote the exploration of new correspondences [188]. The creation of new, temporary points in the fixed cloud **Q** has also been proposed, again as a means to facilitate further motion of **P** after the first iteration step. Temporary points can be created by interpolation on **Q** [188,189] or on tangent planes defined locally on the fixed surface [190,191]. If **Q** is comprised of vertices of a triangle mesh, temporary points can be created by interpolating directly on the triangle mesh (see Figure 2.29).

In some circumstances, ICP may fail to converge: geometries that do not have enough constraints for good convergence are identified as unstable [192]. It follows that further challenges must be tackled to make ICP capable of detecting failure to obtain a stable result. Another challenge with ICP is related to processing speed, as the search for closest neighbours to establish correspondences at each step is slow and computationally expensive. In addition to point cloud partitioning methods dedicated to accelerating point

search, such as k-NN (discussed in Section 2.2.2.3), methods specifically dedicated to ICP have been developed, for example the projective association method [193].

A recent overview of ICP variants is given elsewhere [194]. ICP variants, for example, introduce different ways to identify the initial random core subset for the first alignment iteration, adopt different distance metrics to equation (2.26), present different methods to remove outlier points from the computation of distance at each iteration, or propose weighing methods to give different relative importance to specific correspondences.

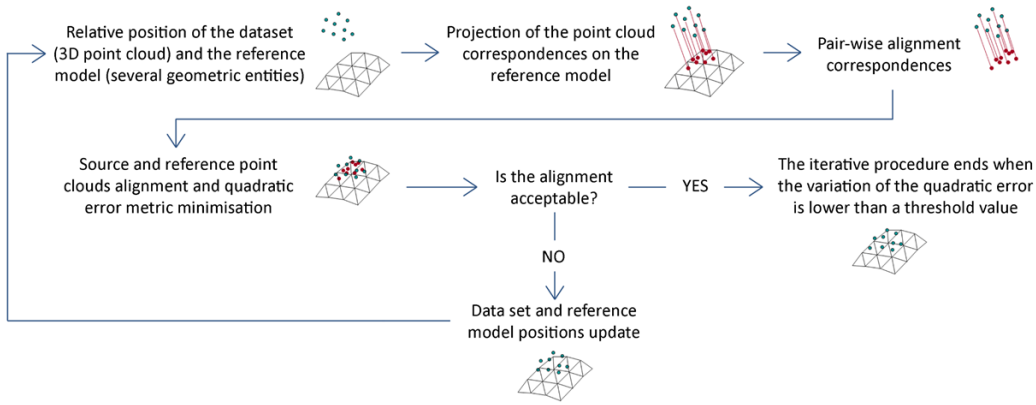

Figure 2.29 The iterative workflow of the ICP scheme: registration between a point cloud and a triangle surface

2.2.6.6 Landmark matching and alignment using similarity metrics

As introduced in Section 2.2.6.4, there are two fundamental concepts that can be adopted to identify correspondences and solve the alignment problem. The first concept is that the best matching points are those that can be better aligned, regardless of any other consideration about the nature of the selected points. Both RANSAC alignment and ICP alignment fundamentally follow this concept. The second concept is that the best matching points are those that are representative of similar regions, regardless of whether such matches can be optimally aligned or not. Alignment methods adopting the second concept require:

a) the definition of criteria to locate "interesting" regions in the point cloud; interesting because they could host candidate landmarks;
b) the development of solutions to mathematically encode the shape-related information associated to such regions/landmarks;
c) the development of solutions to quantitatively assess the degree of similarity (or difference) or paired regions/landmarks [153,195,196].

When correspondences between landmarks have been established following the second concept, once again the alignment is typically achieved by resolution of the absolute orientation problem (for example, using the centroids of the paired landmark regions) [164]. There is a large variety of alignment methods that rely on the identification of matched landmarks. Any local shape descriptor, such as those described in Section 2.2.4, for example local curvature, may be used to search for landmarks, and later for pairwise

matches based on similarity. Finally, it is worth pointing out that alignment methods may actually implement a hybrid combination of the two concepts.

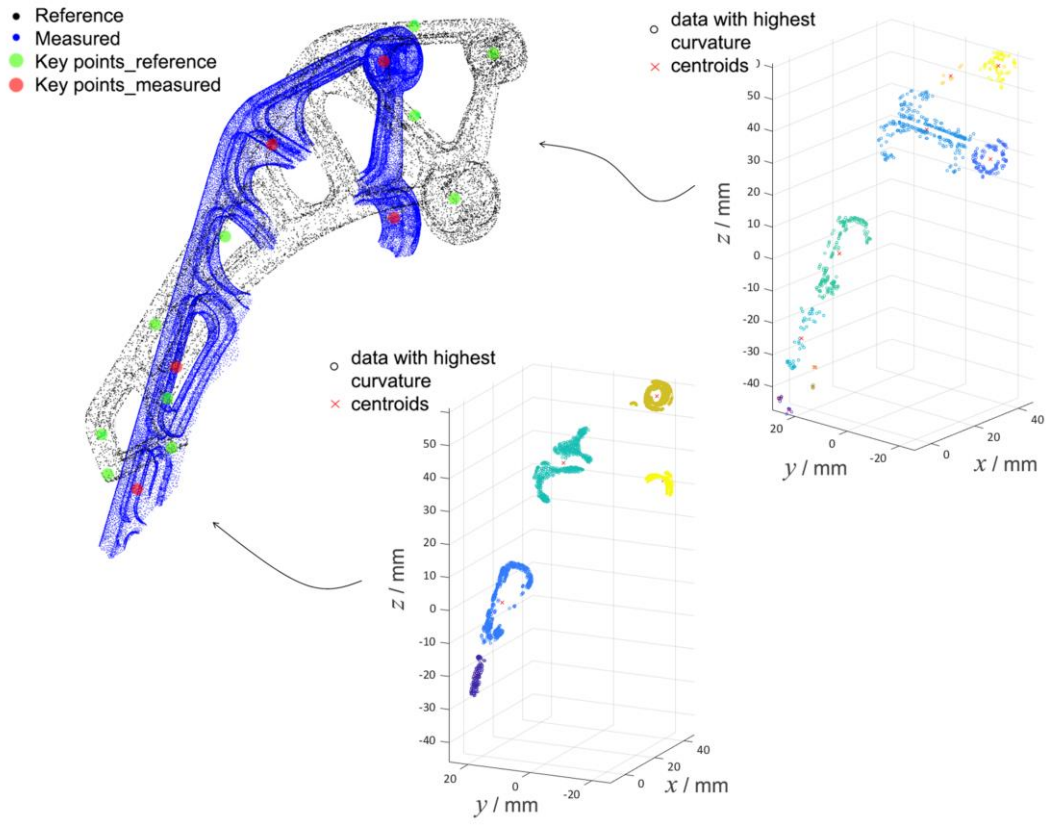

Figure 2.30 Data, divided into clusters, represent the points in the cloud with the highest Gaussian curvature values. The centroids of those subsets are matched via RANSAC

For example, as it is shown in Figure 2.30, candidate landmarks are identified by computing local surface curvatures. Because curvature similarity alone does not have sufficient discriminative power to allow robust identification of the strongest matches (different local surface shapes may have very similar curvature), the candidates have been processed using a RANSAC alignment procedure and refined with ICP [166].

2.2.6.7 Distance metrics

Two of the most commonly used distance metrics for point correspondences evaluation [197] are reported in this section. As previously discussed in Section 2.2.6.2, given an identified subset of n points $\mathbf{P'}$ and $\mathbf{Q'}$ selected respectively from dataset **P and Q**, the goal is to find for each $\boldsymbol{p}_i \in \mathbf{P'}$ the best matching points $\boldsymbol{q}_i \in \mathbf{Q'}$ (*i.e.,* finding optimal correspondences).

The *coordinate root mean squared error* (cRMSE) is the measure of the distance between two sets of points with known correspondences. cRMSE measures how close each point $\boldsymbol{p}_i$ is to each corresponding point $\boldsymbol{q}_i$ after a rigid alignment transformation is globally computed for the entire set of correspondences. This is a problem of absolute orientation (see Section 2.2.6.2) in rigid registration approaches, *i.e.,* minimisation problem reported in equation (2.27), thus

$$\mathrm{cRMSE}^2(\mathbf{P'}, \mathbf{Q'}) = \min_{\mathbf{R},\boldsymbol{t}} \left(\frac{1}{n} \sum_{i=1}^{n} \|\mathbf{R}\,\boldsymbol{p}_i + \boldsymbol{t} - \boldsymbol{q}_i\|^2 \right), \tag{2.28}$$

where $\mathbf{R}$ is a rotation matrix and $\boldsymbol{t}$ is a translation vector. The cRMSE distance metric is broadly employed to measure the residual error in registration algorithms.

Alternatively, the *distance root mean squared error* (dRMSE) is computed by comparing all pairwise distance combinations of the two correspondence sets, and is defined as

$$\mathrm{dRMSE}^2(\mathbf{P}', \mathbf{Q}') = \frac{1}{n^2}\sum_{i=1}^{n}\sum_{j=1}^{n}(\| \boldsymbol{p}_i - \boldsymbol{p}_j\| - \| \boldsymbol{q}_i - \boldsymbol{q}_j\|)^2. \tag{2.29}$$

The main difference between the aforementioned distance metrics resides in the computation of the roto-translation alignment transformation [197]. In other words, cRMSE requires the computation of the alignment transformation prior evaluation of the quality of the pairwise correspondences obtained. On the other hand, dRMSE compares the internal pairwise distances of each pointset, meaning that the pairwise distance matrix computed for $\mathbf{P}'$ is compared to the pairwise distance matrices of the potential correspondence set $\mathbf{Q}'$, without taking into account the global transformation matrix.

2.2.7 Point cloud to mesh comparison

Registration and consequent comparison of measured point clouds to reference surfaces are key aspects useful to the inspection and verification of manufactured parts, which commonly present deformations due to thermal effects, stress, as well as inherent material properties, and several defects due to the manufacturing process [5]. The comparison of scanned point clouds with existing nominal geometries (such as CAD and triangle meshes) gives information on how much a fabricated AM part deviates from a reference, capturing the shape variation and quantifying the geometric displacement of the points in the cloud with respect to the aligned surfaces of the reference

model. Several authors have addressed the issue, developing theoretical and computational frameworks to compare two or more geometric entities [198–200]. A common method is to compute the signed distances between a measured point cloud and its registered reference surface. The observed differences are considered as an acceptable approximation of the difference between nominal and real geometry, not taking into account the presence of multiple error sources. Cloud-to-cloud and cloud-to-mesh comparison techniques based on distance metrics are reviewed elsewhere [201–203]. Comparison strategies lead to a unique association between tagged points with regions of interest in triangle meshes, for instance surfaces with specific measurement requirements. For example, the associations enable measurement systems to identify regions unsuccessfully or insufficiently acquired, guiding them to perform further measurement actions (more details on cloud-to-mesh association are discussed in Chapter 4). In the following sections the mathematical formulation to determine the Euclidean distances between two points and a point and a triangle in 3D space are discussed.

2.2.7.1 Distance between two points in 3D space

Given two points $\boldsymbol{p}_1$ and $\boldsymbol{p}_2$ in a 3D space, their Euclidean distance $\boldsymbol{d}$ is simply given by

$$d(\boldsymbol{p}_1, \boldsymbol{p}_2) = \sqrt{|\boldsymbol{p}_2 - \boldsymbol{p}_1|^2}. \tag{2.30}$$

The distance between two points in 3D space is therefore the square root of the sum of the squares of the differences between corresponding point coordinates $\boldsymbol{p}_1 = \{x_1, y_1, z_1\}$ and $\boldsymbol{p}_2 = \{x_2, y_2, z_2\}$

$$d(\boldsymbol{p}_1, \boldsymbol{p}_2) = \sqrt{(x_2 - x_1)^2 + (y_2 - y_1)^2 + (z_2 - z_1)^2}. \quad (2.31)$$

2.2.7.2 Distance between a point and triangle in 3D space

The geometrical problem of finding the distance from a point $\boldsymbol{p}$ in 3D space to a triangle (or in general the distance from a point cloud to a triangle mesh) can be addressed following two approaches [204,205], the first in 3D and the second in 2D. The point $\boldsymbol{p}$ is orthogonally projected onto the plane that contains triangle T (Figure 2.31).

Given $\boldsymbol{p}' = \{x', y', z'\}$ the projection of $\boldsymbol{p} = \{x, y, z\}$, the distance pp' can be found considering the angle α between the normal vector of T and pp''

$$|pp'| = |pp''| \cos \alpha. \quad (2.32)$$

If $\boldsymbol{p}'$ falls outside the triangle, the distance to the closest edge or vertex to $\boldsymbol{p}$ is given by pp'', with $\boldsymbol{p}'' = \{x'', y'', z''\}$ being the nearest point on T (Figure 2.31.a); if $\boldsymbol{p}'$ lays within the triangle, pp' would be the actual distance of $\boldsymbol{p}$ to T (Figure 2.31.b). The distance is signed according to the face normal vector to identify on which side of the surface the query point resides.

The second approach converts the 3D method into a 2D problem. Each triangle in the mesh is rotated and translated so that one vertex of the triangle lies on the origin, one lies on the z axis, and the third lies in the yz plane. The query point $\boldsymbol{p}$ is therefore transformed into $\boldsymbol{p'}$, projected directly on the plane containing T by ignoring the x coordinate. If $\boldsymbol{p'}$ appears to be inside T, the distance point-to-triangle is simply the x coordinate of $\boldsymbol{p}$.

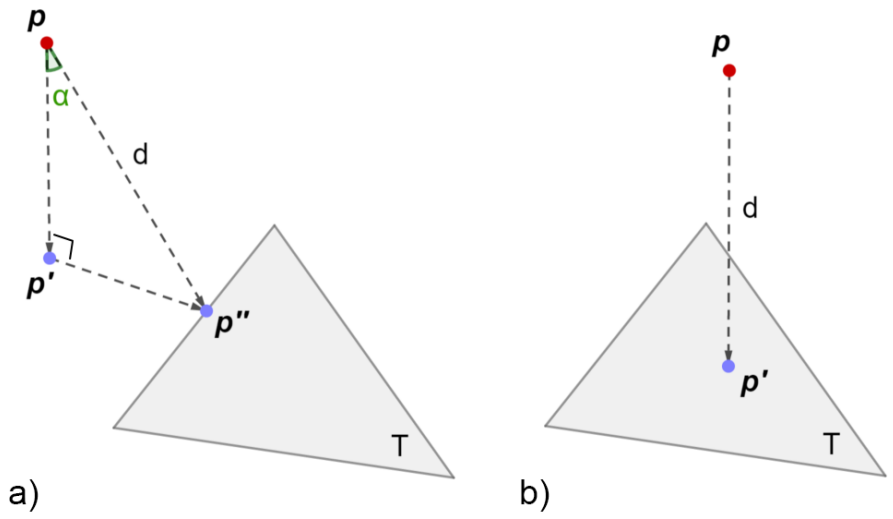

Figure 2.31 Distance from a point $\boldsymbol{p}$ and a triangle: d is the minimum distance from point $\boldsymbol{p}$ to any point on triangle T. a) The projected point $\boldsymbol{p'}$ is outside the triangle T; the minimum distance d is $\boldsymbol{pp''}$, where $\boldsymbol{p''}$ is the nearest point on T. b) The projected point $\boldsymbol{p'}$ is inside the triangle T; the minimum distance d is given by $\boldsymbol{pp'}$

2.2.8 Measurement uncertainty in point cloud surface data

Most current technologies for the inspection and verification of coordinate metrology are centred around the measurement and manipulation of point

cloud surface data [206,207]. The problem of correctly quantifying measurement uncertainty for a given measurement process, or more generally, for any given measurement system, is still an open research question.

The term measurement uncertainty and its specific definition are previously introduced in Section 2.1.1. In layman's terms, measurement uncertainty addresses our lack of knowledge of a real quantity value (distance, length, area, volume, *etc.*) due to measurement error, and defines an interval, centred on the result of a measurement, within which the real quantity value is supposed to be located. When dealing with measurement uncertainty, the central role of point cloud surface data is often overlooked. However, clearly each digital point is the result of a chain of events and physical phenomena that define the measurement process and which result in some form of associated positional uncertainty (*i.e.,* uncertainty on where the point should be actually located in absence of measurement error [208]). Analogously, any dimensional or geometric assessment deriving from point cloud analysis and manipulation should be associated to an uncertainty that comes from the propagation of point positional uncertainty and additional error sources introduced by the processing methods and algorithms [209]. A proper reconstruction of the chain of events that lead to the propagation of point positional uncertainty into a final inspection/verification result, for example the assessment of a feature of size, or a tolerance interval, would play a relevant role contributing towards a better understanding of the measurement error.

2.2.8.1 Uncertainty associated with point clouds

Despite optical measurement technologies involve the generation and processing of point cloud surface data, few approaches devoted to estimate uncertainty in optical measurement are fully dedicated at the understanding and modelling of the uncertainty associated with the individual points of the point cloud. Such uncertainty, referred to as positional uncertainty, is the result of a chain of physical events taking place in the measurement process, and its in-depth investigation would allow for better understanding of how measurement error propagates through the data processing pipeline influencing simplification, filtering, partitioning and datum fitting, and ultimately affecting the results of the characterisation process [210]. As an example, the relationship between measurement uncertainty and fitting has been investigated [170,211,212] as a means to determine the uncertainty in the characterisation of form error.

Point positional uncertainty has been addressed by multiple authors in different scientific contexts. Research on how to describe the spatial placement of points of a cloud in probabilistic terms has been carried out in relation to skin models in the field of geometric tolerancing [213–215]. A skin model is a surface model capable of representing geometric variability across manufactured instances of the same part. For skin models, the idea of using random variables to describe the coordinates of each point has been explored.

As shown in Figure 2.32, in some cases, a random variable is only associated with a displacement in the direction defined by the local surface normal, in other cases, a full 3D probability ellipsoid (tri-variate random variable) is associated with each point. Univariate random variables

associated with local surface normals have been explored for example in Thompson et al. [216], specifically as a means of addressing measurement uncertainty. Random variables may be defined as independent between points or spatial dependency can be captured by modelling co-variance [214].

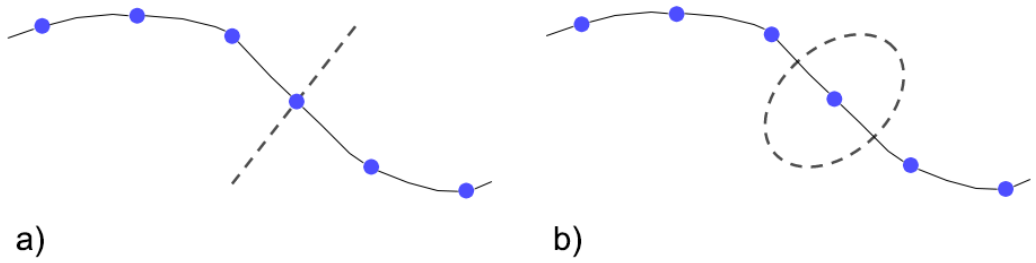

Figure 2.32 Models of point positional uncertainty: a) random variable associated to a displacement in the direction defined by the local surface normal, b) full three-dimensional probability ellipsoid (tri-variate random variable) associated to each point

Typically, statistical point cloud models for addressing measurement uncertainty are constructed by aggregating repeated measurements; however, statistical models can also be obtained by fitting an individual measurement (single point cloud), as long as specific assumptions are made. For example, Evans [217] has demonstrated how standard deviation maps computed from repeated height observations can be propagated into the assessment of peak-to-valley form error for a flat surface, using Monte Carlo simulation. Standard deviation maps obtained from measurement repeats are also useful for calibration and more general tasks related to uncertainty assessment [218,219]. In Moroni et al. [220], a statistical model is obtained by fitting the point cloud to a Gaussian field using a shift-invariant model for covariance

defined using a co-variogram. The use of spatial statistics based on Gaussian fields, in particular kriging, has been investigated [221], where a method to directly derive form error from the kriging model was presented, and the relationships with point-based sampling investigated. More recently, kriging models have been used to estimate uncertainty and calibrate non-contact CMSs [222]. A variety of other approaches have been presented to represent point clouds in probabilistic terms [223–228]. For example, Pauly et al. [223] consider the problem of surface reconstruction from a point cloud, assuming the point cloud as a finite set of noisy samples that provide incomplete information about the underlying surface. To capture uncertainty about the surface, they introduce a statistical representation that quantifies for each point in space the likelihood that a surface fitting the data passes through that point. This likelihood map is constructed by aggregating local linear extrapolators computed from weighted least-squares fits. The quality of fit of these extrapolators is combined into a corresponding confidence map that quantifies the quality of local tangent estimates.

The advantage of having a statistical model for a point cloud, is that many new "virtual" observations of the cloud can be obtained by simulation, and error propagation through the data processing pipeline can be investigated without the need for analytical models. This is typically carried out using Monte Carlo simulation [220] or Markov chain Monte Carlo simulation [213].

2.3 Discussion

The computational pipeline that starts from the point cloud and leads to the result of an inspection or verification task is complex and often comprised of numerous steps, such as point cloud simplification, resampling, elimination of isolated points, noise reduction, segmentation and partitioning, fitting, registration, and more. From the literature, it has emerged that the mathematical methods and algorithms underlying the aforementioned point cloud tasks are numerous and subject of active research. Some of them have not been comprehensively investigated yet, particularly those related to the assessment of quality in measurement and the incorporation of measurement error into the point cloud processing pipeline, or, more specifically, the evaluation of point cloud positional uncertainty. In parallel, in the context of the 4^{th} industrial revolution smart processes, combined with integrated *a priori* knowledge, have spread rapidly through industry, guiding machines in decisional tasks for automated quality control obtainable in real-time. However, the actual implementation of knowledge-driven processes into physical instruments for measurement optimisation and their application into the production line is characterised by numerous challenges. As a result, there is definitely a research need in the development of flexible approaches for the assessment of measurement performance, especially in the context of complex additively manufactured products.

Through the review of the state-of-the-art, the following key findings in relation to the aims and objectives of the thesis can be found:

- optical instruments for the measurement of form are increasingly employed in industry for surface and coordinate measurement, but the traceability and uncertainty infrastructure are missing, especially due to the complex nature of the shapes and surfaces fabricated via advanced manufacturing technologies;
- performance monitoring and indicators of quality assessment are indispensable means needed in order to improve the performances of the manufacturing shop floor. Nevertheless, examples of developed metrics for point cloud quality assessment that can be readily implemented into measuring instruments are still too few;
- for what concerns the evaluation of uncertainty associated to point clouds, conventional approaches (such as starting from first principle) are not ideally applicable, due to the multitude of potential error sources and the complexity of their interactions. The most common methods found in literature to describe point positional variability (*i.e.*, positional uncertainty in point clouds) are expressed in probabilistic terms. However, the related on-going research is still in its infancy.

2.4 Summary

In the last few decades, in particular in the context of non-contact measurement technologies, increasingly denser point clouds have begun to be available in coordinate metrology. This provides the possibility of investigating the geometrical properties of manufactured parts at an

unprecedented range of scales, thus providing a competitive advantage in the inspection of complex geometries, typical in AM. However, the adoption of digital technologies in advanced manufacturing processes is currently hindered by a lack of confidence in the data that is captured and managed within those processes. In tandem, smart point cloud data processing algorithms and intelligent measurement strategies enriched by available sources of information play an increasingly important role in industrial inspections, representing the starting point for a more comprehensive understanding of the behaviour and performance of coordinate measurements, and potential solutions for the assessment of quality under broader perspectives.

The contents reviewed in this background chapter will be used through the thesis, contributing to the development of the project, motivating towards the achievement of the research objectives, and providing an overall methodological integrity of the proposed study. More specifically, a set of algorithmic solutions for computing unique indicators of measurement performance and uncertainty will be illustrated, based on the knowledge of measured point clouds and their underlying registered CAD geometry. As part of the thesis contribution

- as registration represents the core of the measurement pipeline for the inspection and verification of a measured part, an alignment strategy will be illustrated in Chapter 3, defining the assessment of the pose between a point cloud and a reference geometry adopting some of the well-established methods discussed in the literature;
- a set of novel performance indicators will be defined and illustrated (see Chapter 4 and [97]), aiming at autonomously assessing quality in

measurement results via addressing coverage and density attributes, and contributing towards future development of intelligent optical measuring instruments. The words "quality" and "performance" related to the indicators will be used interchangeably throughout the thesis;

- a novel method based on fitting Gaussian random fields (GRFs) to high-density point clouds produced by measurement repeats will be proposed (see Chapter 5 and [210]). The fitted GRFs deliver a depiction of the spatial distribution of random measurement error over a part geometry, and can incorporate local bias information through further measurement or with the use of an external model to obtain a complete, spatial uncertainty map.

The conceptual flow of this Ph.D. thesis is shown in Figure 2.33.

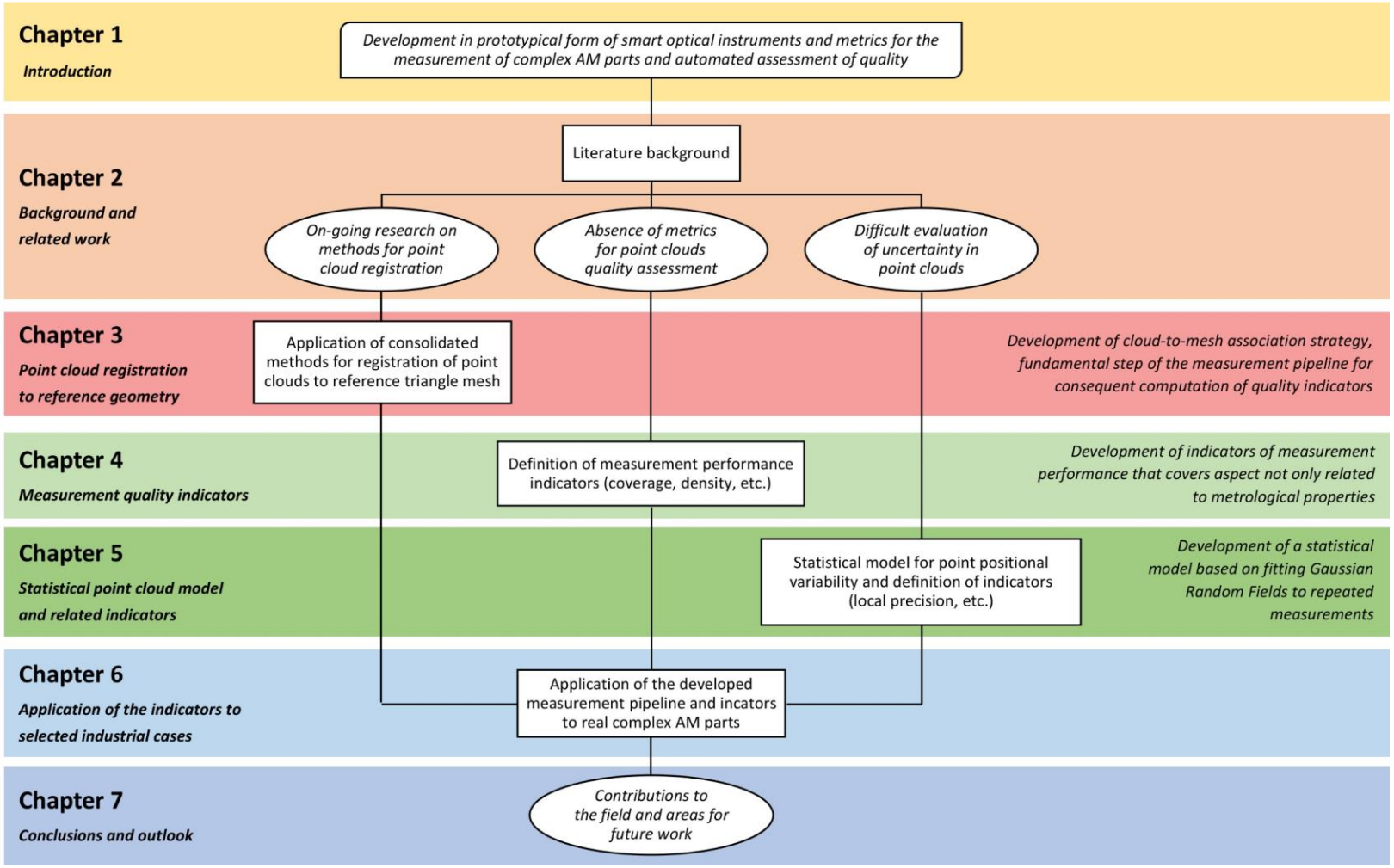

Figure 2.33 Ph.D. thesis outline and conceptual flow

Chapter 3

Point cloud registration to reference geometry

3.1 Overview

A strategy defined for the registration process and the consequent assessment of the pose between a point cloud and a reference model is discussed in this chapter, based on the knowledge acquired of well-established methods comprehensively presented in Chapter 2 (see in particular Section 2.2.6). In this thesis, pose assessment is defined as the estimation of the position in three-dimensional (3D) space of a measured point cloud of initial unknown pose with respect to a reference geometry kept fixed, assumed as the final registration target location. Therefore, the *a priori* knowledge of the CAD

model featuring the part available in form of triangle mesh (see previous discussion in Section 2.1.3.1) represents in this thesis the reference used to perform registration of the measured point clouds. Registration is defined in ISO 10360 part 13 [229] as the "transformation(s) of coordinate systems that brings single-view coordinates into a unified coordinate system", noting that each single-view (or measurement) holds its own coordinate system and requires a transformation (in terms of linear homogeneous transformation or rigid roto-translation) to the unified coordinate system (*i.e.,* considered in this thesis as the CAD model coordinate system).

Registration determines a key aspect of the measurement pipeline previously illustrated in Chapter 1 and it is required in order to identify and select subsets of points corresponding to specific regions of a part surface, and define criteria for the assessment of the quality of measurement results. In other words, in this thesis the correct registration of the measured point clouds to the reference model is fundamental for the definition of the quality indicators, especially those related to part coverage (later defined in Chapter 4) and those that derive from the statistical point cloud model (later discussed in Chapter 5), given the need for the estimation of the unique associations between each point in the cloud – or groups of points - and each triangle facet belonging to the reference mesh geometry.

This chapter begins with a discussion of the methods and techniques employed to perform registration, followed by the identification of selected industrial cases featuring metal components of different shape complexity fabricated via additive manufacturing (AM) technologies. The three samples have been selected in order to test the registration strategy presented in this

chapter. Additionally, two of them have been chosen for the application of the performance indicators, as later documented in Chapters 4 to 6.

The results obtained from the application on one of the selected industrial cases of the registration approach described in this chapter have been presented at the *34th Annual Meeting of the American Society for Precision Engineering (ASPE)* in Pittsburgh (US), attended during the course of the Ph.D. [166].

3.2 The registration pipeline

The approach presented in this chapter for the registration of measured point clouds into the coordinate frame of the reference geometry is based on the computation and detection of point features (*i.e.,* any property/attribute that can be associated to each individual point of a point cloud, as it is defined in Section 2.2.4) in the available datasets (CAD model in form of triangle mesh - fixed reference dataset; measured point cloud - moving dataset). For the reference geometry, the computation of point features is performed considering the mesh as a "cloud of vertices" or, in other words, performing the computation on the extracted vertices composing the triangle mesh. Registration is then achieved via clustering of groups or regions of point features (and associated similarity/difference metrics) in all datasets, and subsequently performing a rigid transformation in terms of translation and/or rotation of the moving datasets with respect to the local coordinate system of the fixed one. The result obtained from the transformation represents an

initial coarse guess of the point cloud position with respect to the reference geometry. Groups or regions of point features presenting similar properties or attributes will be identified in this chapter and throughout the thesis as "landmarks" or "correspondences".

As it is discussed in the literature (see Section 2.2.6.6), any point feature or local shape descriptor for point clouds (respectively point normals and curvatures, or Point Feature Histograms (PFH) and Fast Point Feature Histograms (FPFH) to cite a few – see Section 2.2.4 and Han et al. [153] review on local shape descriptors) may be used in applications such as landmarks recognition and registration of pairwise matches based on found similarity. Since local point feature (such as local curvatures) may not be sufficiently discriminative in correspondence to specific regions of the shape of a part (*i.e.,* when different surfaces in a shape show very similar curvature values) [230], in this thesis, in addition to local normals and local curvatures, a more powerful local shape descriptor (*i.e.,* FPFH) has been selected to test registration. Discussions on local normals, local curvatures and FPFHs descriptors are previously illustrated in Sections 2.2.4.1 to 2.2.4.3 respectively.

The registration approach adopted and described in this chapter is shown in Figure 3.1 and outlined as follows:

a) local normals are computed on the point clouds and on the vertices of the triangle mesh using principal component analysis (PCA – see Section 2.2.2.2 for general formulation) (Figure 3.1.a);
b) common landmarks (properties/features such as local curvatures or other 3D shape descriptors that show some kind of similarities – see

Section 2.2.4) are computed and identified both in the measured point cloud and in the vertices of the triangle mesh (Figure 3.1.b);

c) clustering-based segmentation approaches (specifically k-means and hierarchical clustering in this thesis – see Section 2.2.4.4) are applied to the datasets in order to generate partitions/clusters of points based on similar attributes (Figure 3.1.c);

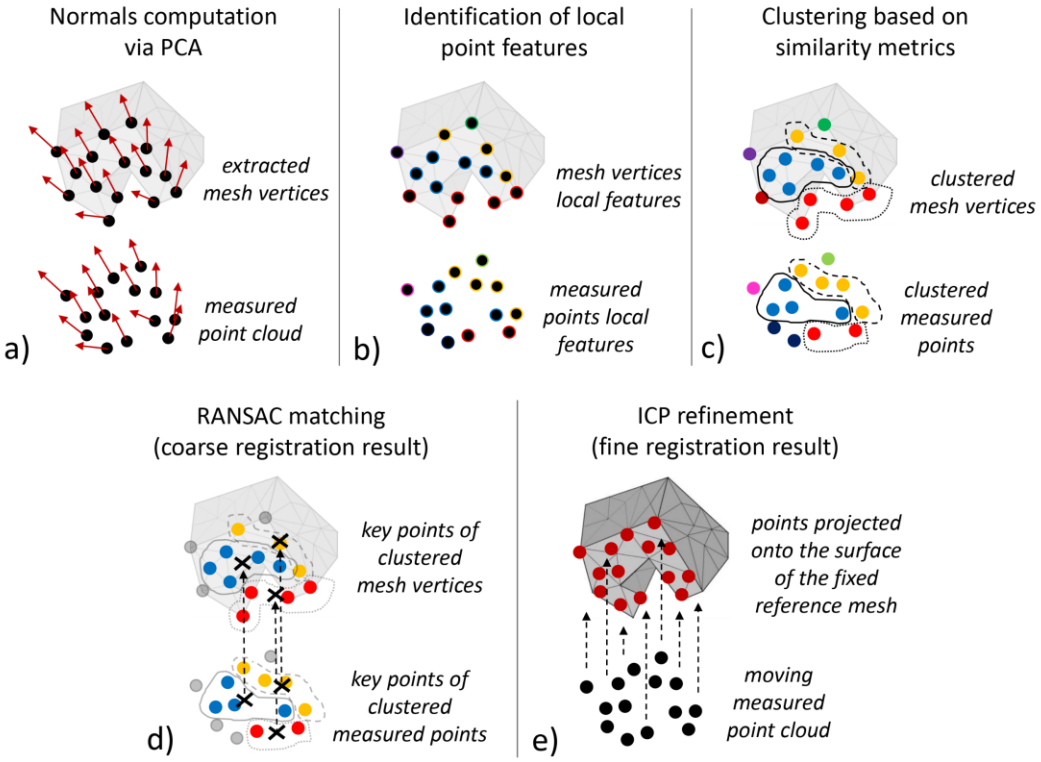

Figure 3.1 The registration pipeline based on landmark matching between a fixed dataset (represented by the vertices extracted from a mesh geometry) set as target, and a moving point cloud (measured points). a) Computation of point normal vectors, b) local identification of point features (*i.e.,* properties, metrics extracted from the datasets), c) clustering-based approach for feature partitioning (*i.e.,* points with similar attributes are clustered in separate regions) and identification of correspondences between datasets, d) first registration phase (coarse registration) characterised by iterative matching of the identified correspondences via RANSAC algorithm, and e) second registration phase (fine registration) done using ICP algorithm, refining the previously obtained coarse transformation iteratively minimising the distance between the fixed and moving datasets

d) a first registration phase (identified as coarse registration, shown in Figure 3.1.d) is applied to the identified features (see Section 2.2.6.6), pruning correspondences between datasets via Random Sample Consensus (RANSAC) algorithm (see Section 2.2.6.4);

e) a second registration phase (identified as fine registration, shown in Figure 3.1.e) refines the transformation obtained from the coarse phase via application of the iterative closest point (ICP) algorithm (see Section 2.2.6.5).

The computation of the normal vectors is estimated using PCA on local subsets of neighbouring points. The neighbouring points are found via the k-nearest neighbour (k-NN) algorithm in combination with a spatial subdivision structure kd-tree (see Section 2.2.2.3). k nearest points (with $k = 6$ in this chapter) are retrieved in correspondence to nodes in the subdivision tree, enabling a faster computation of the normal vectors. Given the covariance matrix built with the coordinates of local points, each normal vector is represented by the eigenvector with the smallest eigenvalue (see Section 2.2.4.1). In order to ensure a correct orientation of the normal vectors (*i.e.,* conventionally pointing outwards from the hypothetical geometry underlying the point cloud), the Euclidean minimum spanning tree (EMST) method is applied as it is discussed at the end of Section 2.2.4.1. The correct computation of the local normals is a relevant aspect of the measurement pipeline as it will be extensively demonstrated throughout this thesis (for instance for the computation of quality indicators – see Chapter 4 – and for the definition of the statistical point cloud model and derived indicators – see Chapter 5).

Once the local normals are correctly computed on all datasets, the principal local curvatures at each point are assessed running again PCA on the normal vectors belonging to the neighbours of each query point within a fixed radius. The search radius is defined depending on the average distance between adjacent points. The principal curvatures $\boldsymbol{k_1}$ and $\boldsymbol{k_2}$ correspond to the eigenvectors and eigenvalues of the resulting covariance matrix (see Section 2.2.4.2). From the principal curvatures, the Gaussian curvature K and mean curvature H are computed from equations (2.11) and (2.12) respectively, as it is discussed in Section 2.2.4.2.

As it is previously illustrated in Section 2.2.4.4, points can be classified into a discrete and countable number of classes according to the identification of similarity metrics in point features. Following the approach presented in this chapter, clusters of points with similar curvature values are partitioned using at first a k-means clustering process (see Section 2.2.4.4), used to identify k-classes of curvature values. The number of k clusters is chosen for each dataset using the elbow method [231]. The method consists of plotting the explained variation (*i.e.,* the proportion to which a mathematical model accounts for the dispersion of a given data set) as a function of the number of clusters. In particular, the resultant optimal k represents the cluster number corresponding to 90% of the explained variation [231].

The points belonging to the class with the highest-curvature values are then isolated and subjected to a second clustering process, this time aimed at isolating spatially distant subsets of points with high-curvature values. The second clustering is, therefore, hierarchical and based on Euclidean distances between points (see Section 2.2.4.4).

The matching of the clustered curvature landmarks belonging both to the fixed and the moving datasets and the consequent coarse alignment of the latter with respect to the former using similarity metrics is achieved via resolution of the absolute orientation problem (see Section 2.2.6.2). The absolute orientation problem is solved by applying a transformation to the moving point cloud so that the Euclidean distances between best pairwise matches of the moving and the fixed datasets are minimised. For the registration approach presented in this chapter and used throughout this thesis, the centroids of the clustered regions of points with high curvature values represent the correspondences (*i.e.,* key points) needed to solve the absolute orientation problem. The best pairwise matches are pruned iteratively using RANSAC (see Section 2.2.6.4). The method consists in creating random pairs between points belonging respectively to the moving and the fixed datasets, up to a reference number of pairs previously defined. Procrustes algorithm [187] is solved on the selected pairs, identifying as good matches those resulting in a spatial alignment that minimises the sum of squared distances between matched points. A threshold value based on Euclidean distance between paired points (*i.e.,* maximum Euclidean distance still considered acceptable in order to obtain a good alignment) is set in order to discriminate between pairs computed across the iterations. Once the iterative procedure is completed, the attempt resulted in the best score (*i.e.,* consensus, highest number of paired points closer than the distance threshold) is selected, the set of random pairs corresponding to the best score is retrieved, and the transformation associated to it is returned. In this work, the discriminative threshold value for too distant pairs was set as a fraction of

the size of the reference mesh, considering the maximum dimension of its bounding box (see Section 2.2.2.1).

The registration based on FPFH matching (see Section 2.2.4.3 and [163]) is expressed by the extraction of FPFH descriptors both from the measured point clouds (both partial and complete) and mesh cloud of vertices. Local geometric information of point features is encoded incorporating the points coordinates and associated normal vectors, in correspondence of each key point and its closest neighbours. The method for finding the neighbouring points is based on radius search (see Section 2.2.2.3); the radius is defined depending on the average distance between adjacent points for each separate dataset. Once the FPFH features are extracted, the identified valid correspondences are again pruned and best-matched iteratively via RANSAC (see Section 2.2.6.4). The iterative procedure terminates when a meaningful number of matched features is obtained for each paired dataset, resulting in good alignment.

The coarse alignment results obtained from the feature matching strategies (both based on curvature and FPFH computations) are refined using the iterative closest point (ICP) algorithm (see Section 2.2.6.5), which revises the obtained transformations based on a rigid roto-translation by iteratively reducing the distances from the measured moving dataset to the fixed reference until the variation of the squared error is minimised [188].

The registration results of both coarse and fine phases obtained using different feature matching strategies are firstly evaluated by immediate visualisation of the applied transformations to the datasets, and then quantitatively assessed calculating the registration error, using the distance

metric minimisation formula (2.28) previously introduced in Section 2.2.6.7. Specifically, the *coordinate root mean squared error* (cRMSE) – simply indicated with RMSE in this chapter – of the corresponding sets of points is returned, defined as the square root of the mean of the sum of squared Euclidean distances between points in the cloud and its paired closest neighbours located on the surface of the triangular mesh facet (*i.e.,* points projected onto the closest mesh surface). The RMSE [189] is defined as

$$\mathrm{RMSE} = \sqrt{\frac{\sum_{i=1}^{n}(\mathbf{R}\,\boldsymbol{p}_i + \boldsymbol{t} - \boldsymbol{q}_i)^2}{n}}, \tag{3.1}$$

where $\boldsymbol{p}_i$ correspond to the points belonging to the moving dataset (*i.e.,* measured point cloud $\mathbf{P}$) and $\boldsymbol{q}_i$ identify the set of points projected onto the surface of the fixed triangle mesh $\mathbf{Q}$, paired with $\boldsymbol{p}_i$; n is the number of paired correspondences. The smaller the RMSE, the better the two datasets are aligned (*i.e.,* in terms of registration, the closer the RMSE is to zero – is minimised – the better is the registration result obtained).

3.3 Application of registration pipeline on selected industrial cases

In the following sections, the registration pipeline showed in Figure 3.1 and discussed in Section 3.2 is applied to selected industrial cases fabricated with AM technologies.

3.3.1 Identification of the test samples

The choice of the samples (indicated interchangeably with the words "sample", "test case", and "test part" through the thesis) was made in order to test the advantages and limitations of the adopted registration strategy, and, more specifically, to later investigate measurement quality in relation with critical areas and features of the measured surfaces, such as high slope angles, hollow features, freeform geometries, which characterise AM parts. The descriptions and images of the selected samples are presented hereafter:

- Sample A - roof bracket (Figure 3.2): the part is a bracket of approximately (120 × 38 × 35) mm total volume featuring a freeform, hollow AM geometry. The part was designed, fabricated and kindly provided by BMW Group (Munich), made in Al-Si-10Mg using the laser powder bed fusion (LPBF) AM process. The sample is asymmetric along the three axes and it presents highly complex geometric features. The test part is used as example application for the measurement quality indicators defined in Chapter 4 and documented in Chapter 6.

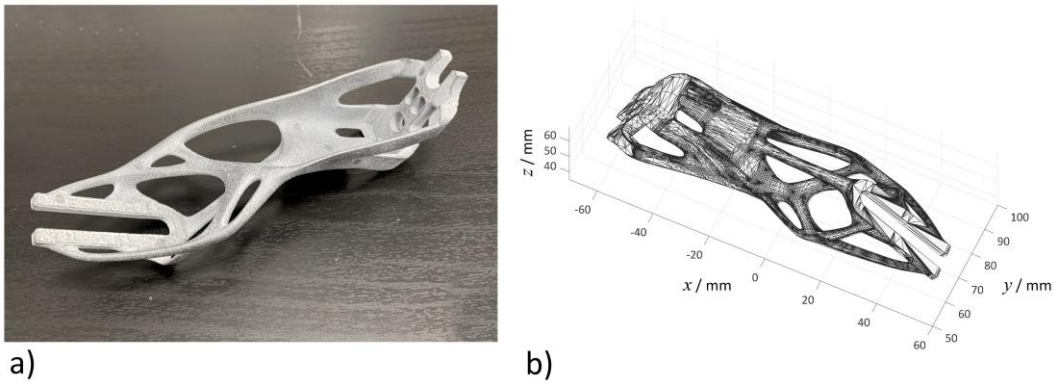

Figure 3.2 Sample A: roof bracket (120 × 38 × 35) mm fabricated by LPBF. a) Picture of the part, b) nominal geometry of the test part available in form of STL triangle mesh (64,958 face count), designed and provided by the manufacturer BMW Group

- Sample B - pyramid (Figure 3.3): a metal AM sample with the size of an enclosing envelope of (50 × 50 × 28) mm was designed at the University of Nottingham [51] and manufactured in Ti6Al4V using LPBF, based on a previous design made by the National Institute of Standards and Technology (NIST) [232].

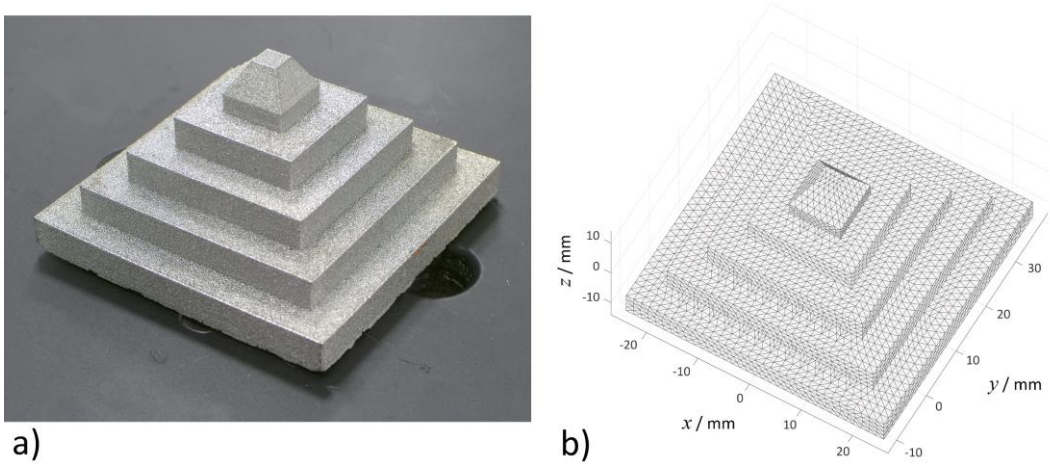

Figure 3.3 Sample B: pyramid (50 × 50 × 28) mm fabricated by LPBF. a) Picture of the part, b) nominal geometry of the test part available in form of STL triangle mesh (9,344 face count), designed by the Manufacturing Metrology Team at Nottingham

For this sample presenting four nominally identical sides, pose assessment will only pertain to the accurate identification of the angular orientation of the visible corner in the measured point clouds. The sample is used as example application for the indicators derived from statistical point cloud model defined in Chapter 5 and documented in Chapter 6.

- Sample C - arm bracket (Figure 3.4): the metal sample of approximate dimensions of (125 × 45 × 8) mm (size of the enclosing envelope) was fabricated at the University of Nottingham by LPBF using stainless steel 316L. The test part is symmetric with respect to the axis corresponding to the shape maximum dimension.

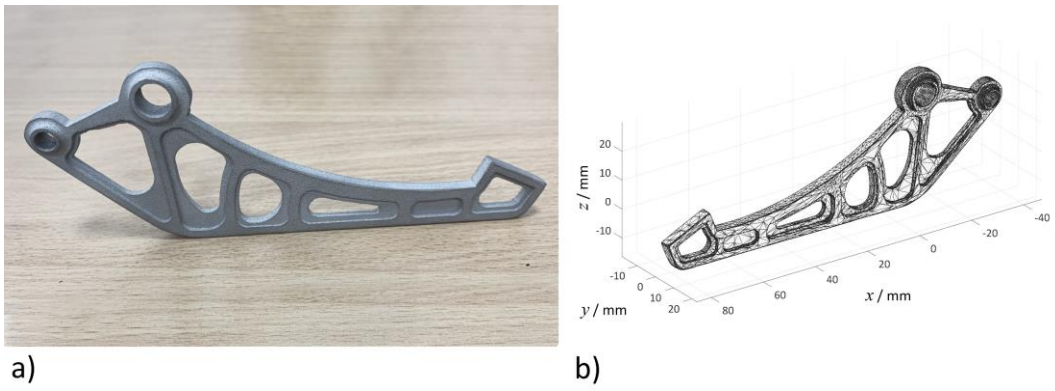

Figure 3.4 Sample C: arm bracket (125 × 45 × 8) mm fabricated by LPBF. a) Picture of the part, b) nominal geometry of the test part available in form of STL triangle mesh (44,652 face count), designed by the Centre for Additive Manufacturing at Nottingham

3.3.2 Measurement conditions, experimental set-up and initial data processing

The experimental set-up for the measurement of each part is based on a combination of a commercial measurement fringe projection system (blue-light technology GOM ATOS Core 300 [233]) and algorithms developed in MATLAB [234]. Measurements were made in the Manufacturing Metrology Team (MMT) laboratory at the University of Nottingham, where temperature was set at (20 ± 0.5) °C. The samples were placed on a rotary table one at the time (example of the measurement set-up and sample C shown in Figure 3.5).

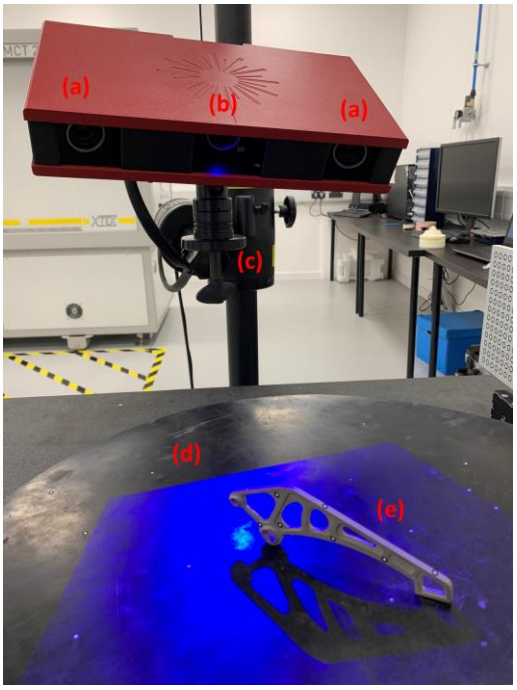

Figure 3.5 Example of measurement set-up: GOM ATOS Core 300 fringe projection system while measuring one of the samples. Reference point markers (0.4 mm) are sticked onto the surface of the part in order to support the stitching of multiple acquisition into one complete measurement. (a) Pair of cameras, (b) blue light projector, (c) tripod, (d) rotary table, (e) sample C

The fringe projection GOM ATOS Core 300 system is mounted on a tripod and consists of a blue light projector of fringes and a pair of cameras, placed respectively at equal distances to the right and left sides of the projector. The position of the pair of cameras allows the measurements within a field of view of (300 × 230) mm and a minimal measuring point distance of 0.12 mm, as stated by the manufacturer [233]. The same instrument will be one of the systems used in this thesis to test and apply the later illustrated developed performance indicators on selected industrial cases (see later in Chapter 6). The measuring acquisitions of each sample were obtained by firstly capturing a unidirectional single-shot measurement of the selected part, and then, without moving it, by scanning the entire surface of the sample at 360°. For the latter case, the acquired data was stitched in real-time into complete 3D point clouds in the GOM Scan software [235], with the support of reference point markers of 0.4 mm sticked onto the surfaces of each sample. The measurements were performed in the aforementioned manner in order to test the robustness of the registration approach to density variation (*i.e.,* "resolution" of the data in terms of point count) and completeness (*i.e.,* if no obvious or significantly large portion of data are missing) of the measured point clouds. More specifically, the measurements represent two particular scenario: the measurement is available as a partially acquired point cloud (*i.e.,* the measuring instrument is not able to acquire most of the features and surfaces of the part geometry because out of its line-of-sight, or multiple single-views present different locations and orientations in the coordinate space), or the point cloud is accessible as a complete measurement (*i.e.,* multiple point clouds are automatically stitched together in the same

coordinate frame directly on the instrument software in real-time while the sensor is measuring).

The acquired datasets were cleaned by the application of a noise filter based on outlier detection, and deletion of isolated points (see Section 2.2.3.2). Isolated points were removed by fitting a plane locally around each data point using its six closest neighbours found with the k-nearest neighbour (k-NN) algorithm (see Section 2.2.2.3); points resulting too far away from the fitted plane were removed. In addition, a threshold radius of 1 mm between the selected query point and its neighbours allowed removal of isolated points with less than three neighbours within the specified radius. The number of neighbours and the threshold radius were chosen for each dataset according to the mean spacing value between points (a method for computing the average point-to-point spacing is later discussed in Section 4.2.2, and defined as a measurement quality indicator).

3.3.3 Results on sample A

Unidirectional single-view measurement, complete point cloud acquisition, and extracted mesh vertices of freeform sample A are shown on the left-hand side panels of Figure 3.6 (a, b and c respectively). As previously discussed, the vertices of the triangle mesh were extracted and defined as fixed reference for registration. Computed normal vectors at each point of all datasets are shown on the right-hand side panels of Figure 3.6 (d, e and f respectively). Normal vectors were computed as illustrated in Section 3.2, needed to then calculate Gaussian and mean curvature local values using PCA.

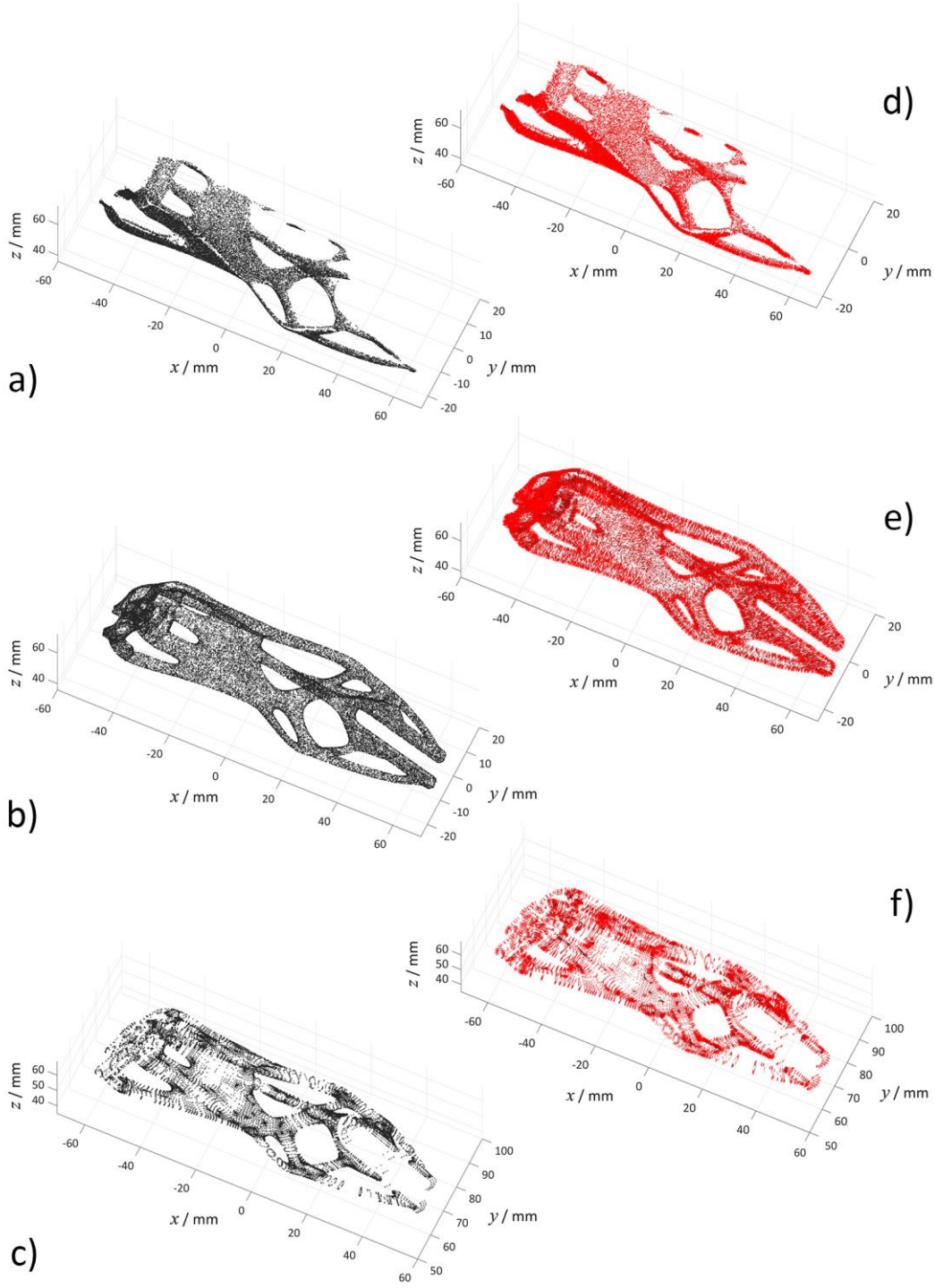

Figure 3.6 Datasets of sample A (in black). a) Single-shot measurement (30,272 point count), b) complete point cloud (50,502 point count), c) triangle mesh extracted vertices (32,451 point count). Point vector normals consistently oriented pointing outwards (in red). d) Single-shot measurement, e) complete point cloud, f) triangle mesh vertices

3.3.3.1 Gaussian curvature for registration of sample A

Local Gaussian curvature values are shown in Figure 3.7 in normalised form and mapped to a colour scale for visualisation purposes. The values were normalised by division with the maximum local Gaussian curvature value recorded across the three datasets. The radius used for neighbours search and consequent principal curvatures computation was chosen based on the average distance between adjacent points, and it was set to 1.5 mm for the point clouds measured with the fringe projection system (both partial and complete) and to 3 mm for the extracted vertices from the triangle mesh.

The first clustering procedure for the partitioning of the datasets was based on k-means method applied to the Gaussian curvature values, as it is shown on the left-hand side panels of Figure 3.8 (a, b, and c for partial point cloud, complete acquisition and mesh vertices respectively). The number of clusters was chosen using the elbow method (previously discussed in Section 3.2), resulting in an optimal number of k clusters equal to three. Cluster 2 resulted in the points with the highest Gaussian curvature values.

The second clustering method was applied to the points that resulted with the highest curvature values (Cluster 2) after the previous application of k-means. The points were clustered based on Euclidean distance as it is shown on the right-hand side panels of Figure 3.8 (d, e, and f for partial point cloud, complete acquisition and mesh vertices respectively). The number of maximum clusters was set to 10. The centroids of the clusters represented the key points (correspondences) needed in order to solve the absolute orientation problem for coarse registration.

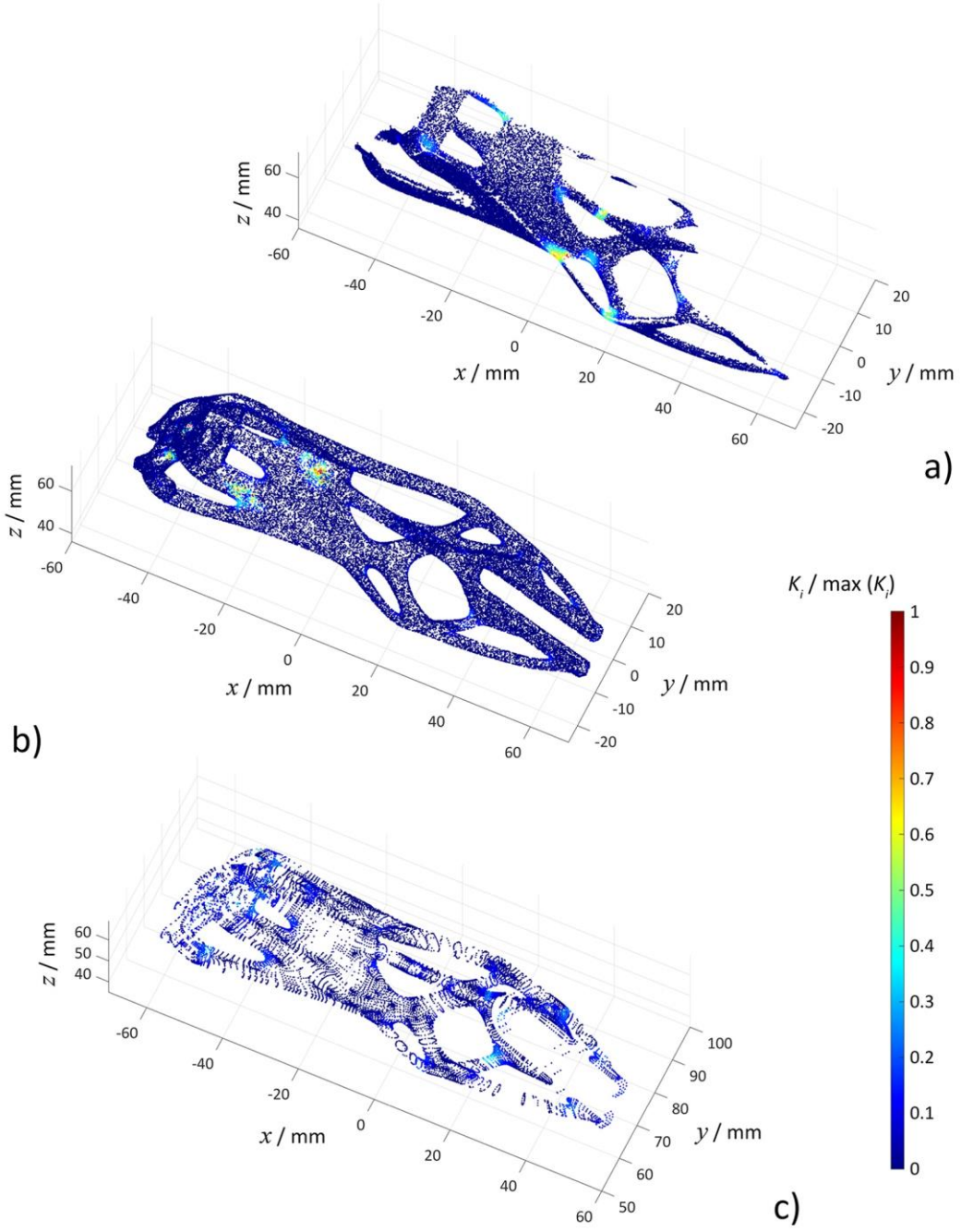

Figure 3.7 Local Gaussian curvature K values estimation on point cloud (sample A), converted into colour map representations. a) Single-shot measurement, b) complete point cloud, c) triangle mesh vertices

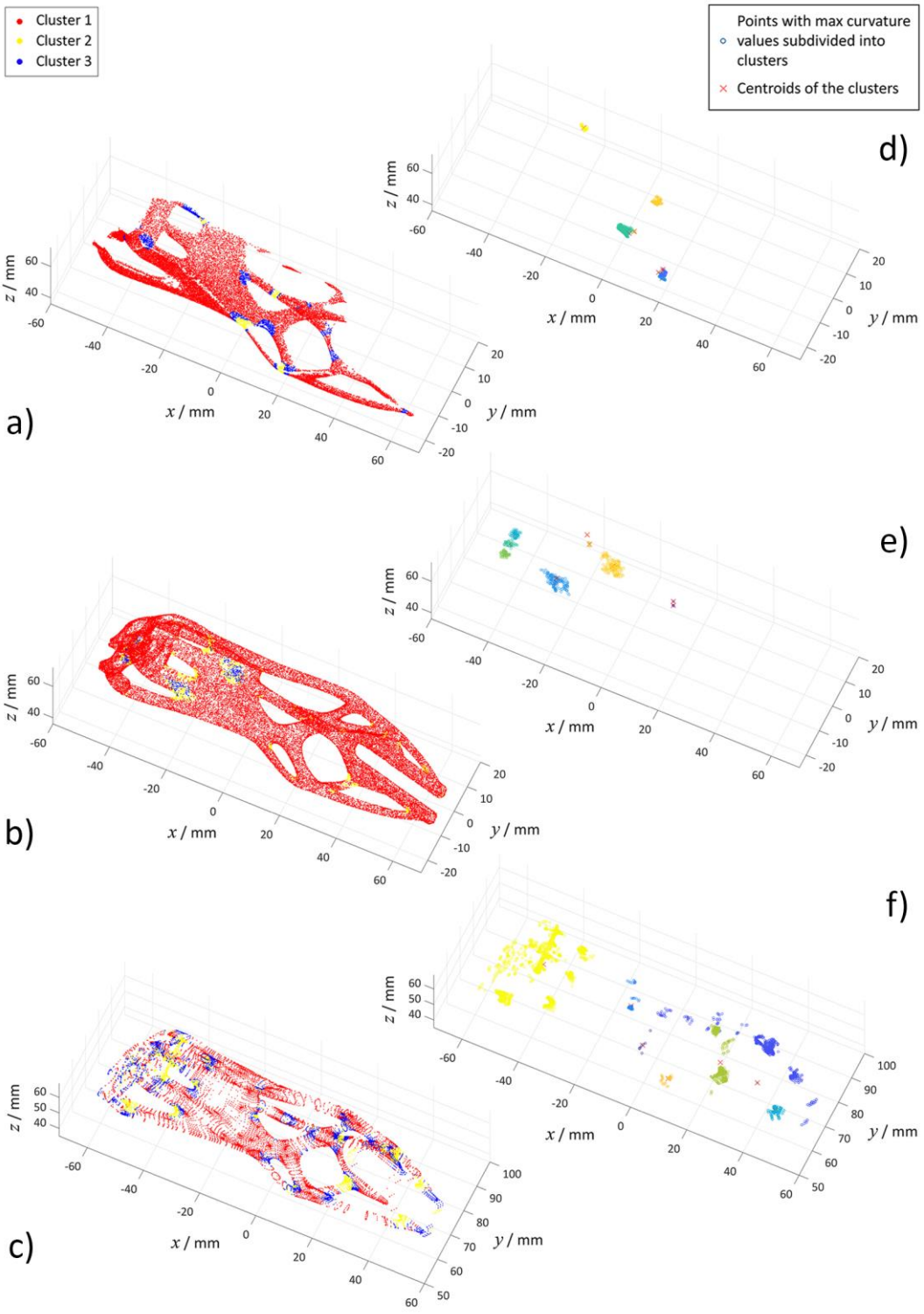

Figure 3.8 Point cloud partitioning on Gaussian curvature for sample A: k-means clustering (points are assigned to one of three clusters ($k = 3$)). a) Single-shot, b) complete point cloud, c) mesh vertices. Hierarchical clustering and cluster centroids (total number of clusters set to ten). d) Single-shot, e) complete point cloud, f) mesh vertices

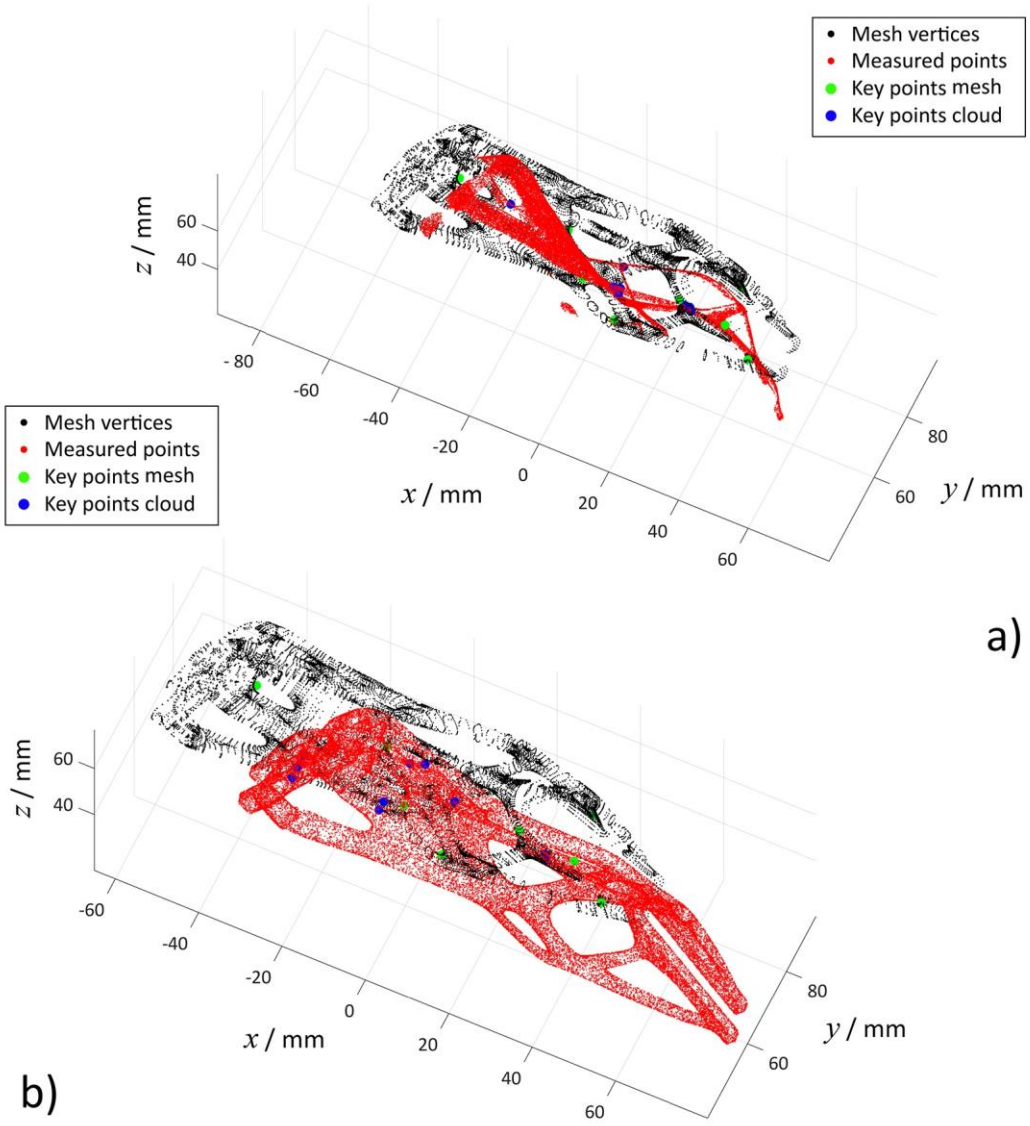

Figure 3.9 Paired centroids of Gaussian curvature clusters (key points in green and blue) identified in the mesh vertices and measured point clouds (in black and red respectively) of sample A, matched via RANSAC after 1,000 iterations. a) Single-shot measurement coarse registration result, b) complete point cloud coarse registration result

Figure 3.9 shows the transformation results of the identified key points belonging to the moving datasets (partial in Figure 3.9.a and complete point clouds in Figure 3.9.b) iteratively pruned and best-matched using RANSAC

to the paired key points in the reference dataset (mesh vertices), kept fixed. The minimum number of meaningful correspondences needed in order to obtain an acceptable transformation was set to five, resulting after the iterative procedure in a successful number of matches equal to 80% for the partial point cloud and 60% for the complete dataset (with a total number of key points equal to ten, *i.e.,* cluster centroids).

3.3.3.2 Mean curvature for registration of sample A

Local mean curvature values are shown in normalised form and mapped to a colour scale for visualisation purposes in Figure 3.10 (values normalised by division with the maximum mean curvature value recorded across the datasets). The radii for neighbours search were set to 1.5 mm for the measured point clouds and to 3 mm for the mesh vertices.

k-means clustering applied to the mean curvature values is shown on the left-hand side panels of Figure 3.11 (a, b, and c for partial point cloud, complete acquisition and mesh vertices respectively). The optimal number of clusters computed with the elbow method resulted in $k = 3$. Cluster 2 resulted in the points with the highest mean curvature values.

The second clustering applied to the points belonging to Cluster 2 (resulted in the highest mean curvature values) is shown on the right-hand side panels of Figure 3.11 (d, e, and f for partial point cloud, complete acquisition and mesh vertices respectively). The total number of clusters was set equal to ten.

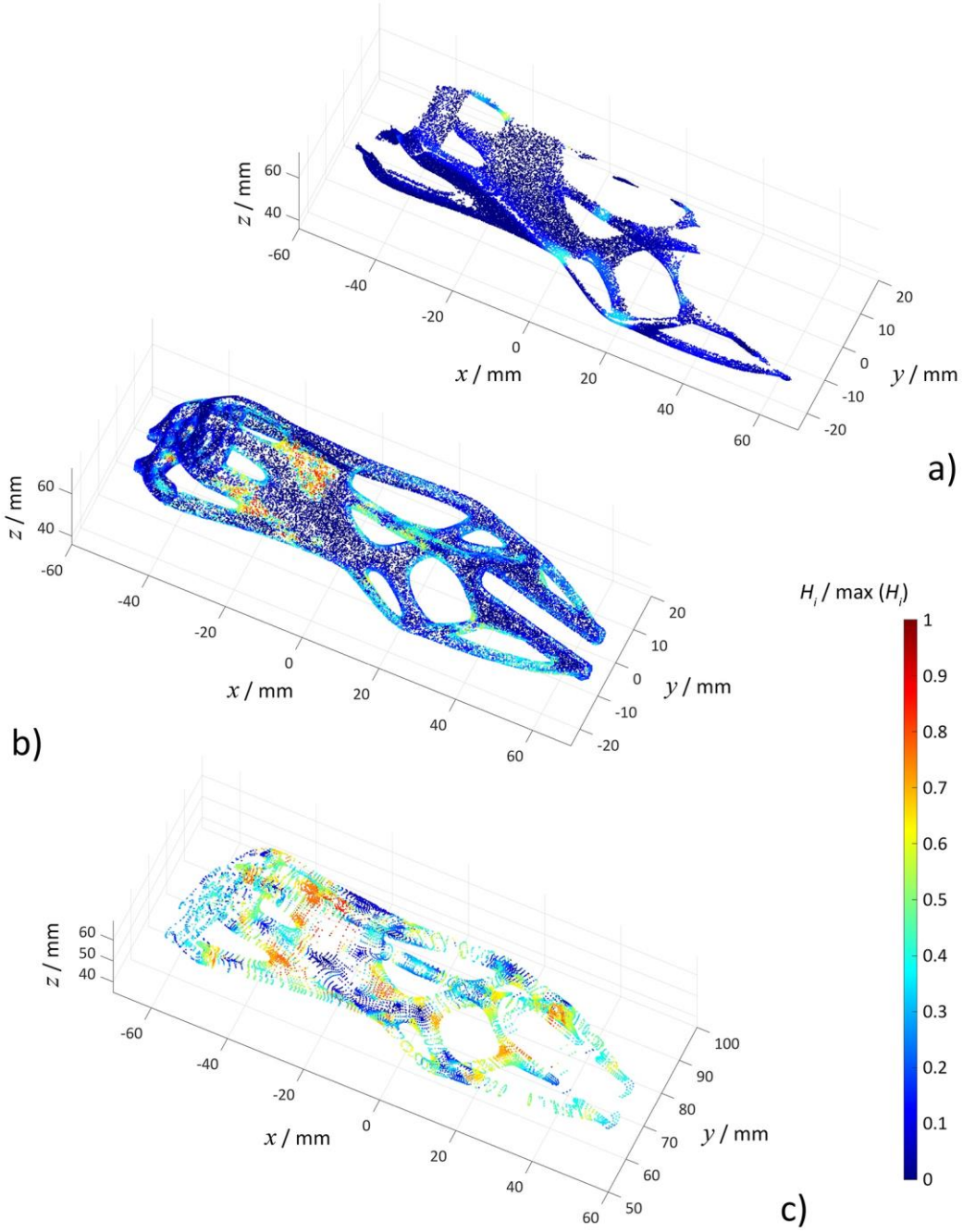

Figure 3.10 Local mean curvature H values estimation on point cloud (sample A), converted into colour map representations. a) Single-shot measurement, b) complete point cloud, c) triangle mesh vertices

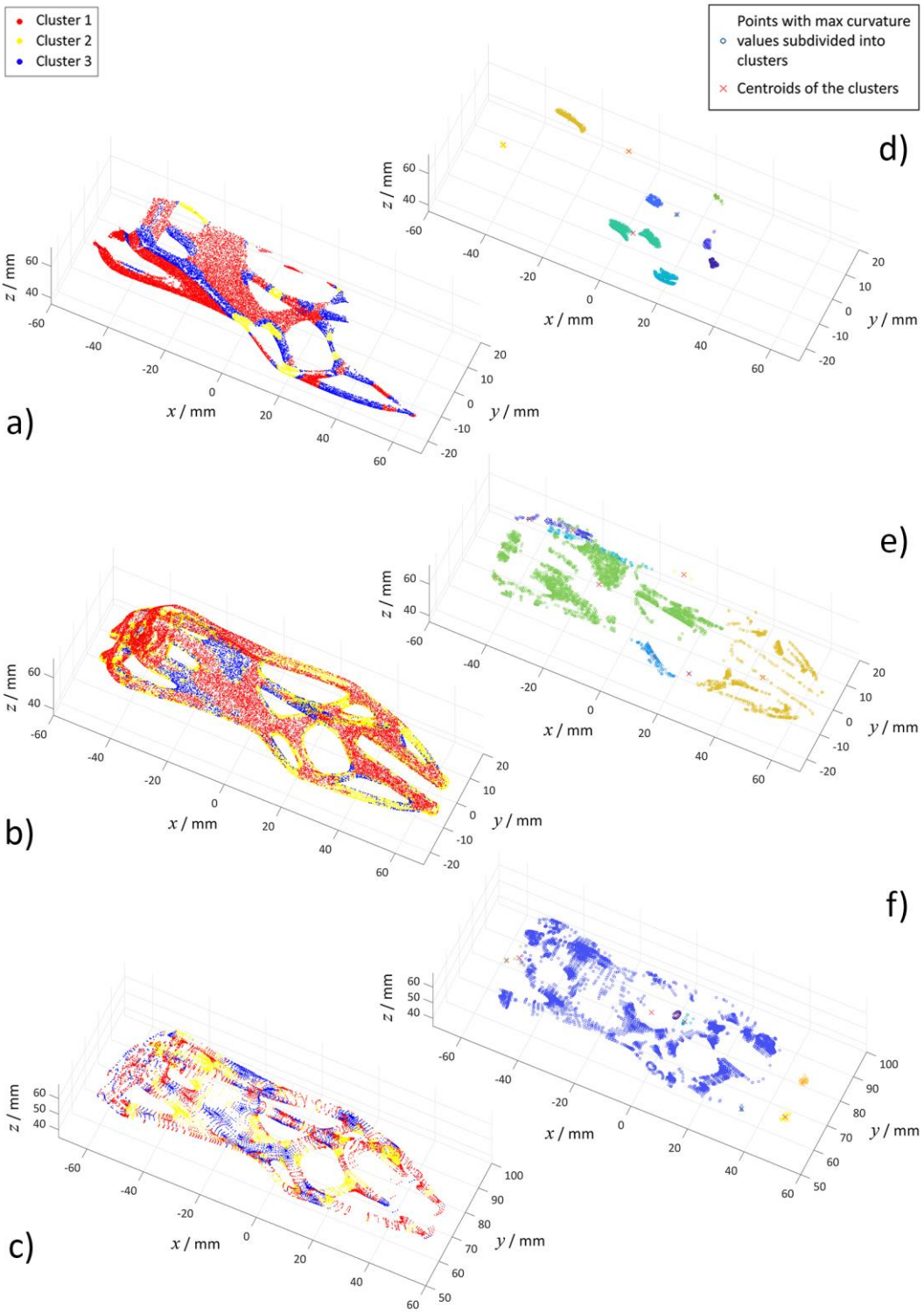

Figure 3.11 Point cloud partitioning on mean curvature for sample A: k-means clustering (points are assigned to one of three clusters ($\boldsymbol{k} = 3$)). a) Single-shot, b) complete point cloud, c) mesh vertices. Hierarchical clustering and cluster centroids (total number of clusters set to ten). d) Single-shot, e) complete point cloud, f) mesh vertices

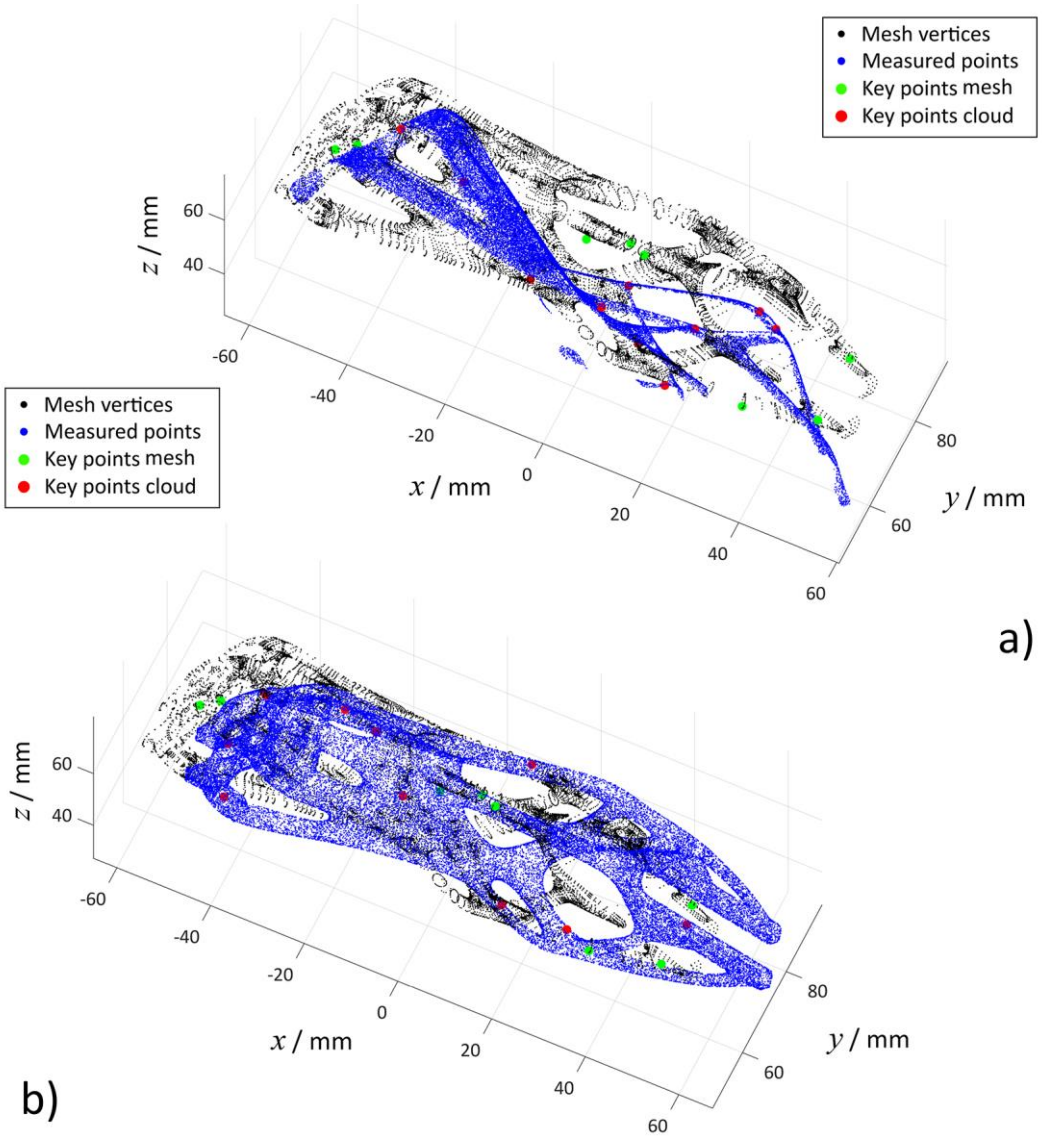

Figure 3.12 Paired centroids of mean curvature clusters (key points in green and red) identified in the mesh vertices and measured point clouds (in black and blue respectively) of sample A, matched via RANSAC after 1,000 iterations. a) Single-shot measurement coarse registration result, b) complete point cloud coarse registration result

The results of the coarse registration are shown in Figure 3.12. The key points found in all datasets were iteratively pruned and paired matched using RANSAC. After 1,000 iterations the successful number of matching correspondences resulted in a successful number of matches equal to 60% for

the partial point cloud and 80% for the complete dataset. The minimum number of meaningful correspondences needed in order to obtain an acceptable transformation was set to five.

3.3.3.3 FPFH feature descriptors for registration of sample A

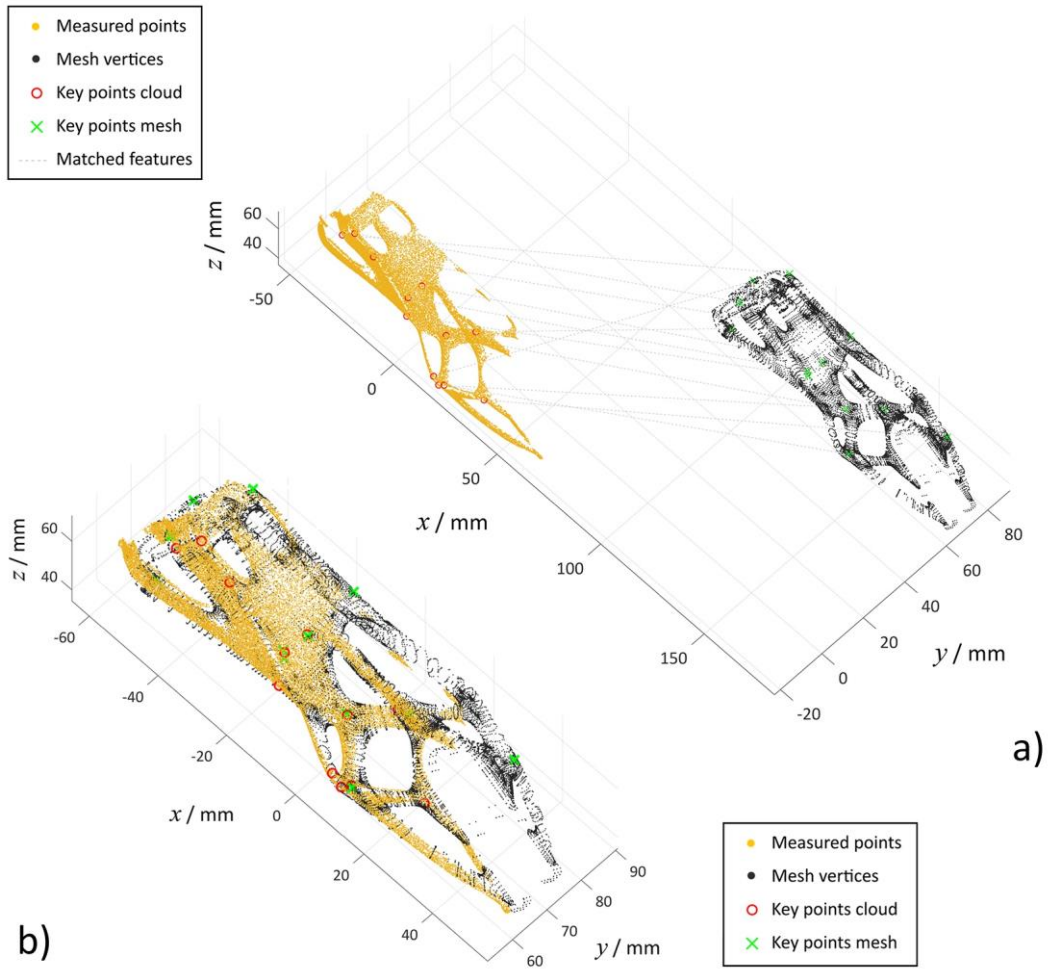

Figure 3.13 Paired FPFH features (total number of successful matched features: 12 pairs) identified in the mesh vertices and measured single-shot point cloud (in black and yellow respectively) of sample A, matched via RANSAC after 1,000 iterations. a) Datasets in their initial configuration (grey lines represent the coarse correspondence sets), b) coarse registration result after RANSAC

Figure 3.13 and Figure 3.14 show the identification of FPFH features in the mesh vertices and measured point clouds. The successful number of matched pairs were identified via RANSAC after 1,000 iterations, resulting in 12 and 29 pairs of successful correspondences for the partial point cloud and the complete measurement respectively.

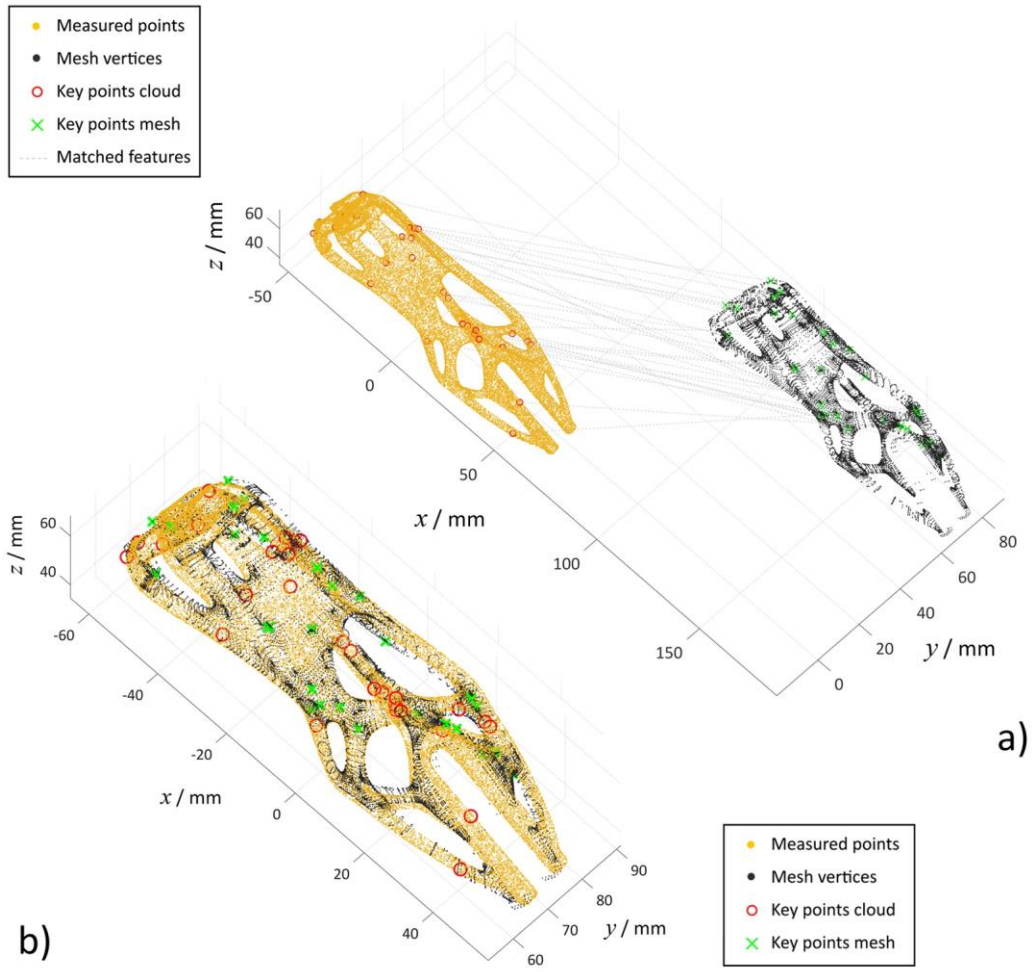

Figure 3.14 Paired FPFH features (total number of successful matched features: 29 pairs) identified in the mesh vertices and complete point cloud acquisition (in black and yellow respectively) of sample A, matched via RANSAC after 1,000 iterations. a) Datasets in their initial configuration (grey lines represent the coarse correspondence sets), b) coarse registration result after RANSAC

3.3.3.4 Summary of the coarse registration results and ICP refinement on sample A

To verify the effectiveness of the registration strategy (in particular the coarse registration phase based on feature matching), the results obtained from the application of the three types of point features (Gaussian curvature, mean curvature and FPFH descriptors) onto two sets of measured data (partial and complete point clouds) are illustrated and compared in this section. The registration results were quantitatively assessed calculating the RMSE between corresponding points. Specifically, the RMSE values were recorded for the datasets in their initial coordinate frame (*i.e.,* initial input positions), at the updated mutual positions after the coarse registration, and at their final refined ICP configurations. From the coarse registration results previously obtained via feature matching, the registration error between the datasets was further minimised by refining the obtained coarse transformations using ICP algorithm. The graphical results of the refined transformations for a single unidirectional point cloud and a complete measurement registered to the reference geometry using different point features (*i.e.,* final poses assessed) are shown in Figure 3.15. Figure 3.16 shows the differences of the recorded RMSEs for partial and complete point clouds across the registration stages, while employing different local point features (Gaussian curvature in Figure 3.16.a, mean curvature in Figure 3.16.b and FPFH descriptors in Figure 3.16.c). The RMSEs recorded at the coarse and fine registration stages are additionally reported in Figure 3.17.

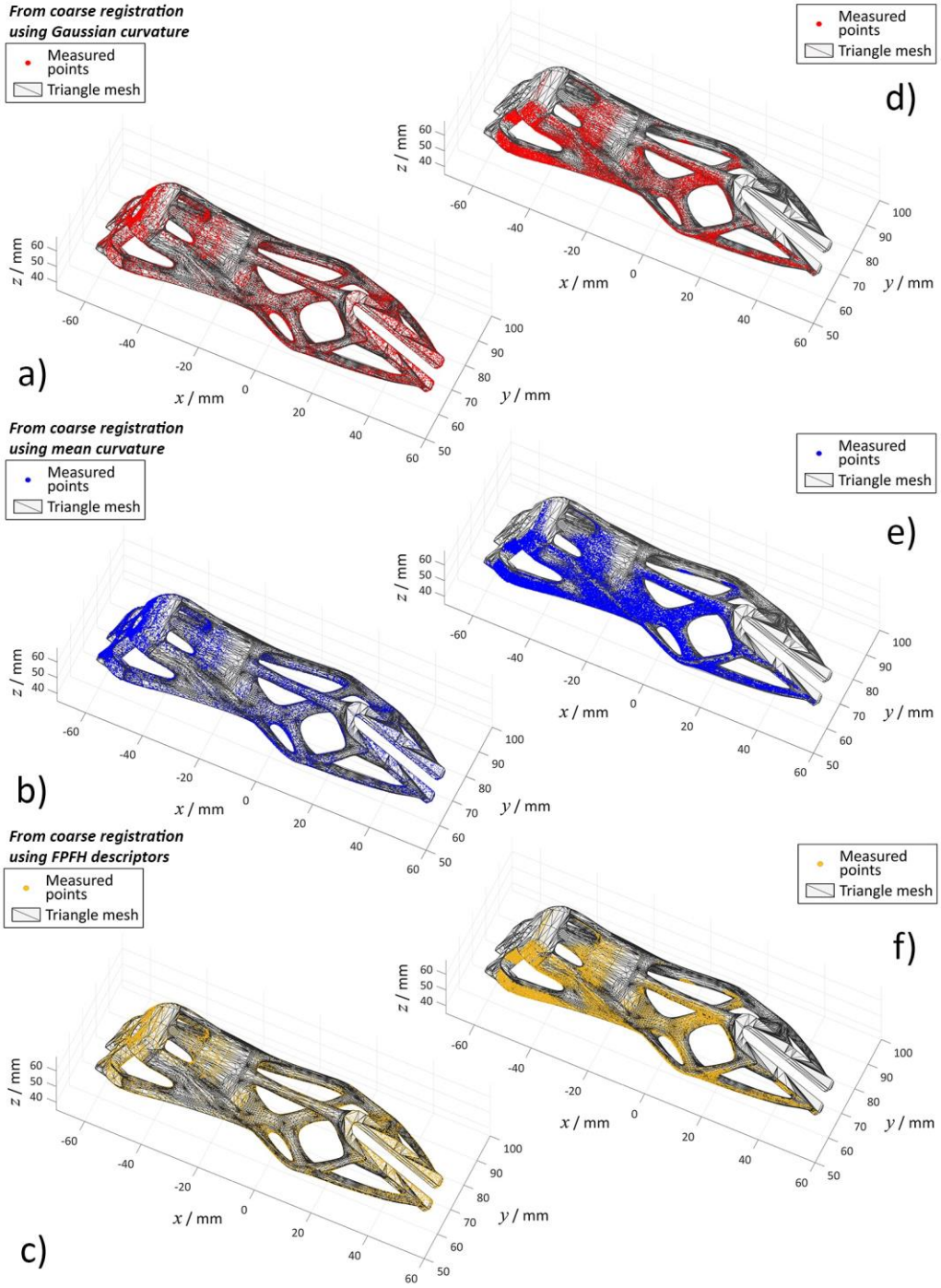

Figure 3.15 Registration results of coarse transformation based on landmark matching refined using ICP (1,000 iterations) for sample A. Complete point cloud a) Gaussian curvature, b) mean curvature, c) FPFH descriptors; single-shot measurement d) Gaussian curvature, e) mean curvature, f) FPFH descriptors

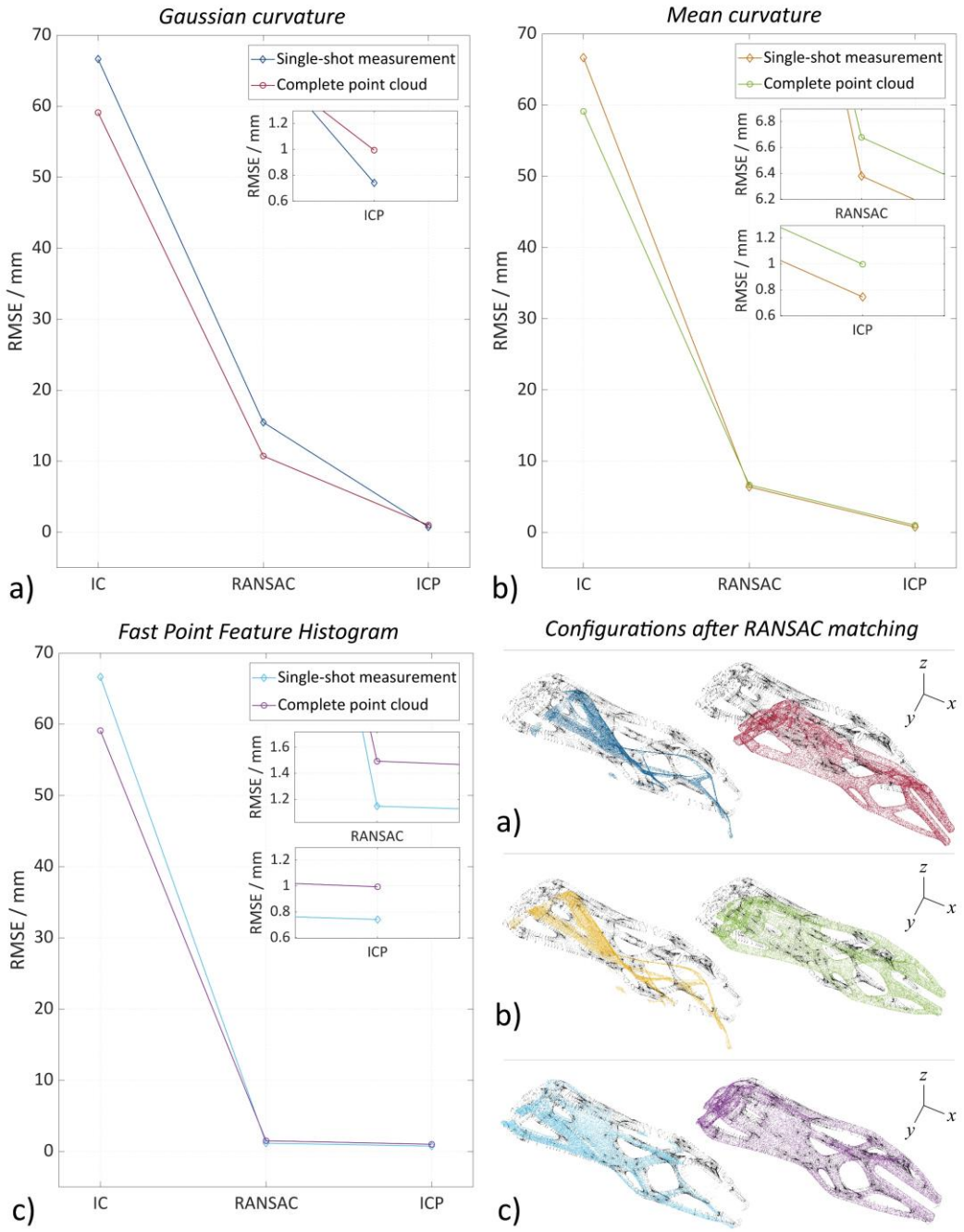

Figure 3.16 Registration results of sample A using different features descriptors for partial and complete point clouds (indicated with different colours). From left to right in each graph, the RMSE is recorded in different registration stages: RMSE recorded between the datasets at their initial configuration (*i.e.,* initial positions of the input data – indicated with IC), RMSE recorded in the coarse registration phase (indicated with RANSAC), and RMSE recorded in the fine registration (indicated with ICP). RMSE graphs and point clouds visual results obtained using a) Gaussian curvature K, b) mean curvature H, and c) FPFH as landmarks for registration

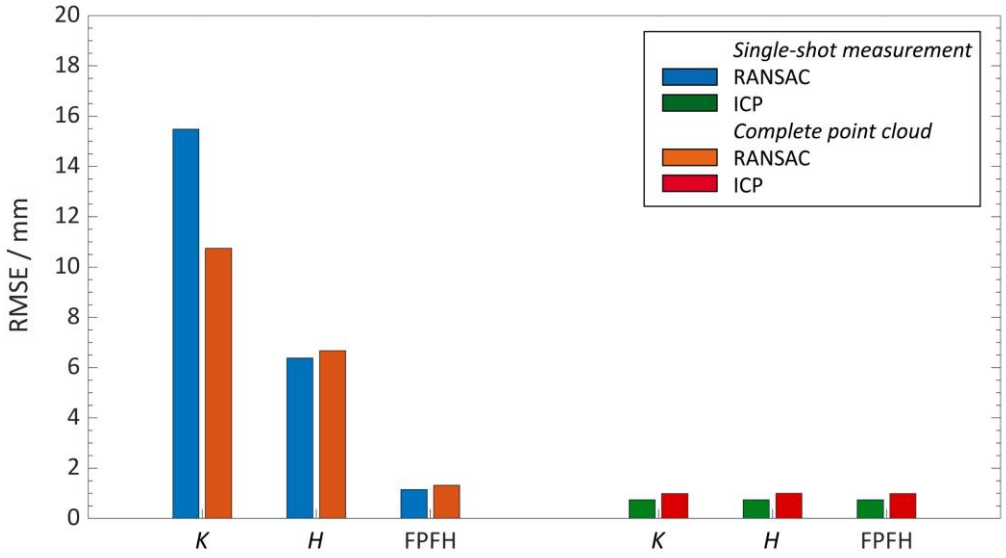

Figure 3.17 Histograms of RMSE of coarse and fine registration for partial and complete point clouds of sample A using different point features/descriptors (Gaussian curvature K, mean curvature H and FPFH reported on the x axis). The absolute values recorded of RMSE for the coarse registration are reported on the left hand-side of the graph (indicated in blue and orange RANSAC for partial and complete measurements respectively); on the right hand-side the RMSE for the fine registration are reported (indicated in green and red ICP for partial and complete measurements respectively)

The results presented in Figure 3.16 show a rapid decrease in the registration error for all datasets immediately after the first registration phase was carried out, regardless the local point features chosen. The results illustrate a significant agreement for both partial and complete point clouds when selecting FPFH descriptors as landmarks for registration, as it is shown in Figure 3.17 (refer also to Figure 3.13, Figure 3.14 and bottom right-hand side in Figure 3.16). On the contrary, the results obtained from local Gaussian and mean curvatures present higher RMSEs for both partial and complete point clouds, with a slight improvement in the mean curvature error results.

The freeform shape of sample A would suggest an easy identification of similar attributes within the landmark features locally computed, especially in correspondence of complex geometric elements [192,236]. However, both Gaussian and mean curvature results show that the paired correspondences returned by RANSAC were still severely contaminated by incorrect matches (Figure 3.9, Figure 3.12 and bottom right-hand side in Figure 3.16) compared to the ones obtained from FPFHs. In order to ensure an efficient matching, local point features should present high discriminative power in terms of similarity/difference metrics [230]. For instance, point curvatures approximate the neighbourhood information with single scalar values and most points might show the same or very similar curvature values, thus reducing the selected local feature informative characteristics [197,237]. This explains the reason why the FPFH results present the lowest RMSE values, due to the capability of these descriptors to encode neighbourhood's geometrical properties more extensively than curvatures, providing overall scale and pose invariant multi-value features [162].

The RMSE values recorded for the fine registration phase (Figure 3.17) show results within the same order of magnitude for both partial and complete datasets regardless the choice made for the employed features, meaning that all methods could bring the moving point clouds fairly close to the target fixed model for the ICP algorithm to work efficiently (see 3D representation in Figure 3.15).

3.3.4 Results on sample B

Before discussing the results of the registration obtained on sample B, it is worth mentioning that symmetrical shapes and featureless surfaces could cause geometric instability during registration (*i.e.,* absence of enough constraints to reach a good convergence; a geometry is "unstable" when it is characterised by regions that do not contain enough information to fully constrain a transformation [192]), meaning that the applied registration algorithms might fail and return poor alignment results. In addition, for this sample presenting four nominally identical sides, it is not possible to assess for certain with which of the four sides in the reference CAD the point clouds will be aligned.

Aware of the aforementioned issues that could be potentially caused by the selected sample, it is important to highlight that the registration process is needed in this thesis primarily for the identification of a global coordinate frame of reference (specifically the coordinate system of the reference CAD), which is then shared by the measured point clouds. The localisation of measured points and reference CAD will then lead to the further computation of performance indicators, later introduced in this thesis. Therefore, for this sample pose assessment results will only pertain to the accurate identification of the angular orientation of the visible corner in the measured point clouds, as previously mentioned in Section 3.3.1.

Unidirectional single-view measurement, complete point cloud, and extracted mesh vertices are shown in Figure 3.18, along with computed normal vectors.

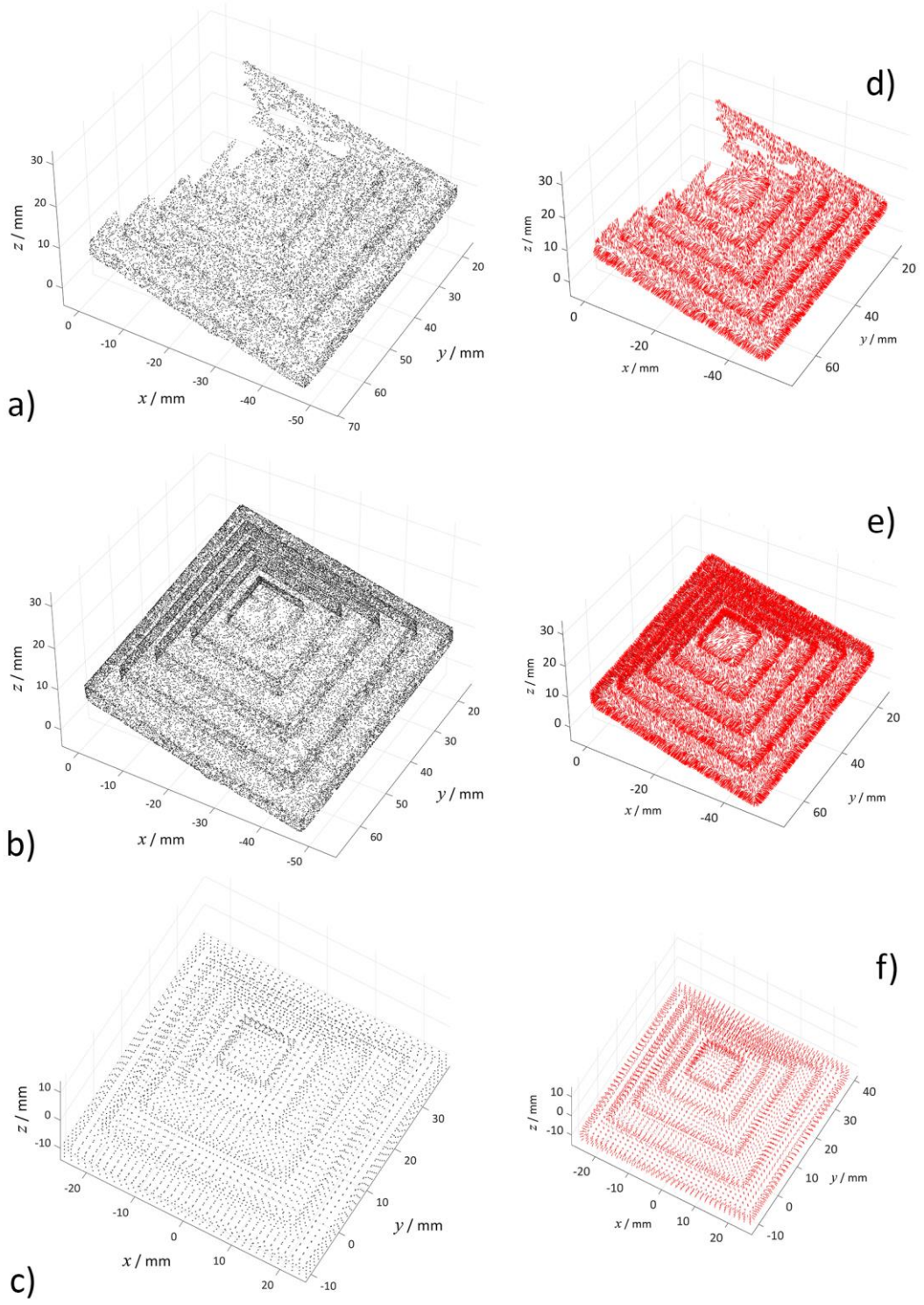

Figure 3.18 Datasets of sample B (in black). a) Single-shot measurement (17,078 point count), b) complete point cloud (38,489 point count), c) triangle mesh extracted vertices (6,481 point count). Point vector normals consistently oriented pointing outwards (in red). d) Single-shot measurement, e) complete point cloud, f) triangle mesh vertices

3.3.4.1 Gaussian curvature for registration of sample B

Local Gaussian curvature values are mapped to a colour scale for visualisation purposes (Figure 3.19, shown in normalised form). The radius used for neighbours search and consequent principal curvatures computation was chosen based on average point-to-point distance (set to 1.5 mm for both point clouds and to 2.5 mm for mesh vertices).

The first clustering method for the partitioning of all datasets based on k-means was applied to the Gaussian curvature values (Figure 3.20 on the left-hand side panels a, b and c). Once again, the number of clusters was chosen using the elbow method, resulting in k equal to five. Cluster 4, which resulted in the cluster of points with the highest Gaussian curvature values recorded, was sub-clustered a second time based on Euclidean distance (hierarchical clustering method) as it is shown on the right-hand side panels of Figure 3.20 (d, e and f) for all datasets. The centroids of the clusters represented the correspondences needed to perform the first registration coarse step and solve the absolute orientation problem.

The results of the initial transformation between the key points of the moving datasets (partial and complete point clouds) and those of the reference dataset (mesh vertices) are shown in Figure 3.21. The correspondences were iteratively pruned and best-matched using RANSAC, setting the minimum number of meaningful correspondences to five. After 1,000 iterations, 50% of successful matches (total number of key points previously defined in the second clustering stage equal to ten) resulted in both partial and complete datasets matching with the fixed reference.

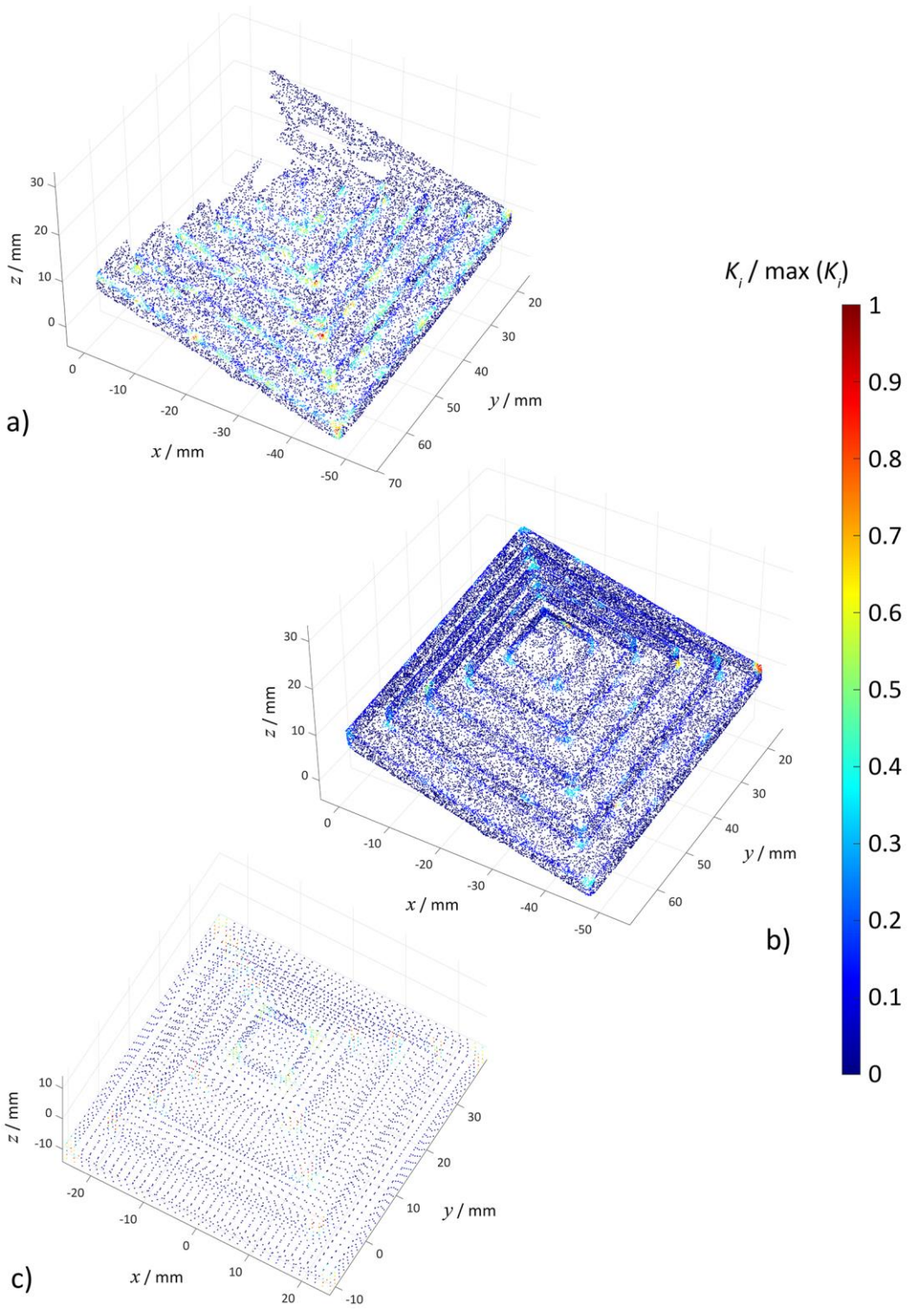

Figure 3.19 Local Gaussian curvature K values estimation on point cloud (sample B), converted into colour map representations. a) Single-shot measurement, b) complete point cloud, c) triangle mesh vertices

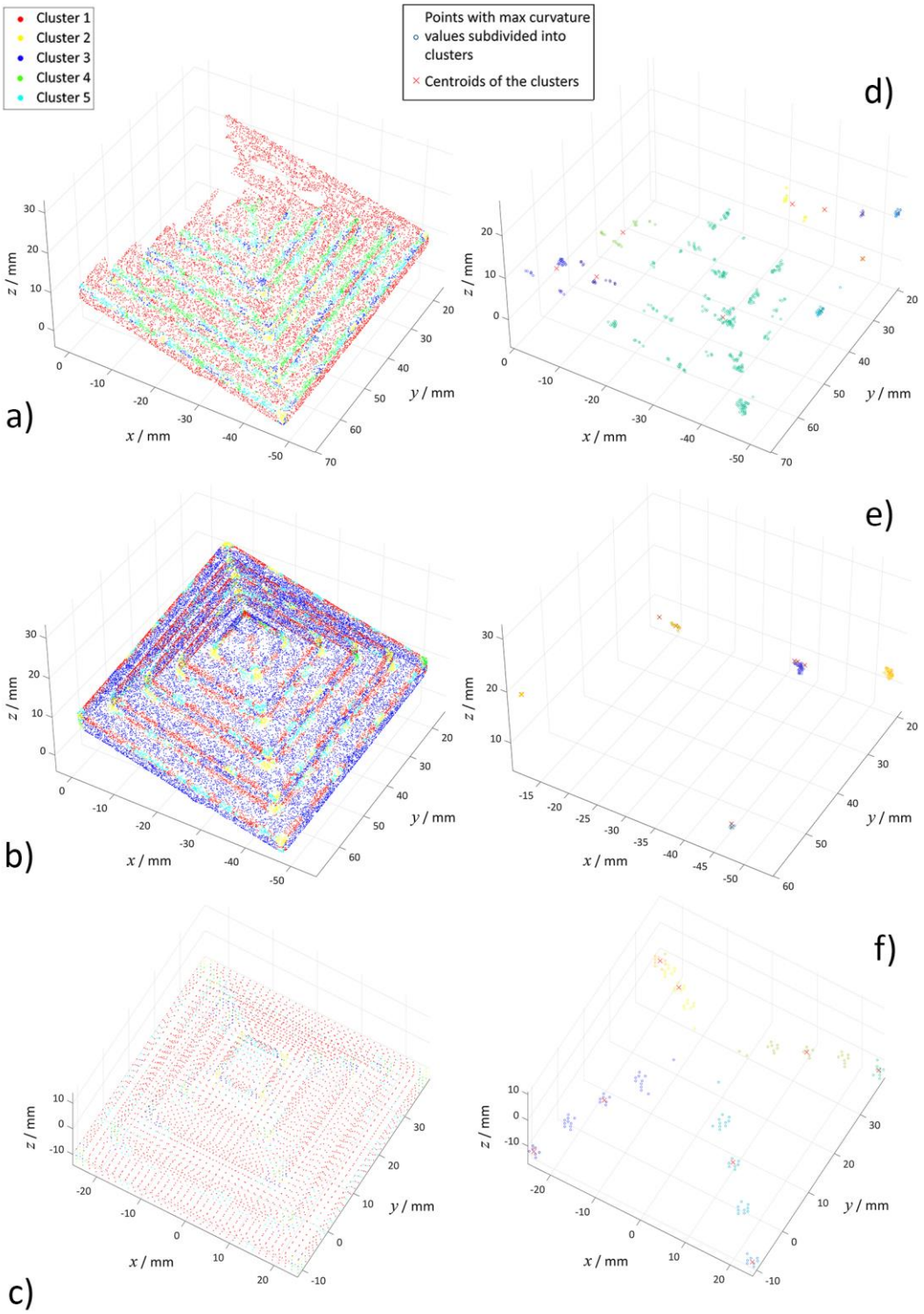

Figure 3.20 Point cloud partitioning on Gaussian curvature for sample B: k-means clustering (points are assigned to one of three clusters ($k = 5$)). a) Single-shot, b) complete point cloud, c) mesh vertices. Hierarchical clustering and cluster centroids (total number of clusters set to ten). d) Single-shot, e) complete point cloud, f) mesh vertices

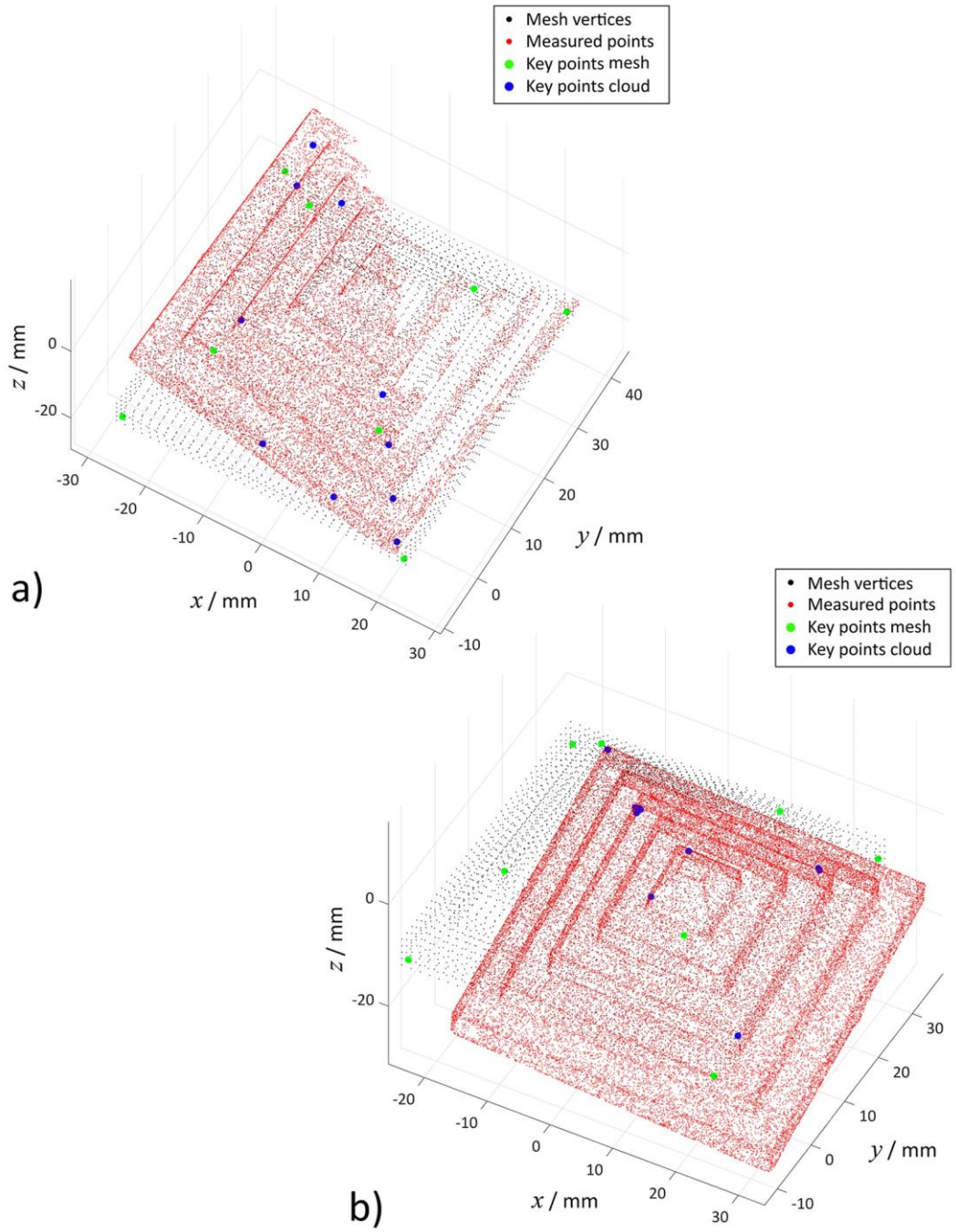

Figure 3.21 Paired centroids of Gaussian curvature clusters (key points in green and blue) identified in the mesh vertices and measured point clouds (in black and red respectively) of sample B, matched via RANSAC after 1,000 iterations. a) Single-shot measurement coarse registration result, b) complete point cloud coarse registration result

3.3.4.2 Mean curvature for registration of sample B

Local mean curvature values are shown in normalised form in Figure 3.22, mapped on all datasets to a colour scale for visualisation purposes. The radii for neighbours search in order to compute PCA on the normal vectors and assess the local curvature values were set to 1.5 mm for the measured point clouds and to 2.5 mm for the vertices of the mesh.

Figure 3.23 shows the application of the first clustering method (k-means clustering on the left-hand side panels a, b and c) to the computed mean curvature values. The number of clusters was chosen once again using the elbow method, returning k equal to five as the optimal number of clusters. Cluster 3 resulted in the points with the highest mean curvature values recorded.

The second clustering method (hierarchical on the right-hand side panels d, e and f of Figure 3.23) was based on subdivision depending on Euclidean distance between the regions of points resulting with the highest mean curvature values recorded (Cluster 3). The centroids of the clusters (set to 10) represented the key points needed for registration, pruned and matched with RANSAC between the fixed reference and the moving datasets (as it shown in Figure 3.24). The minimum number of meaningful correspondences needed to obtain the coarse transformation was set to five, resulting after 1,000 iteration in a successful number of paired correspondences equal to 60% for the partial point cloud and again 60% for the complete dataset (ten is the total number of key points, *i.e.,* cluster centroids).

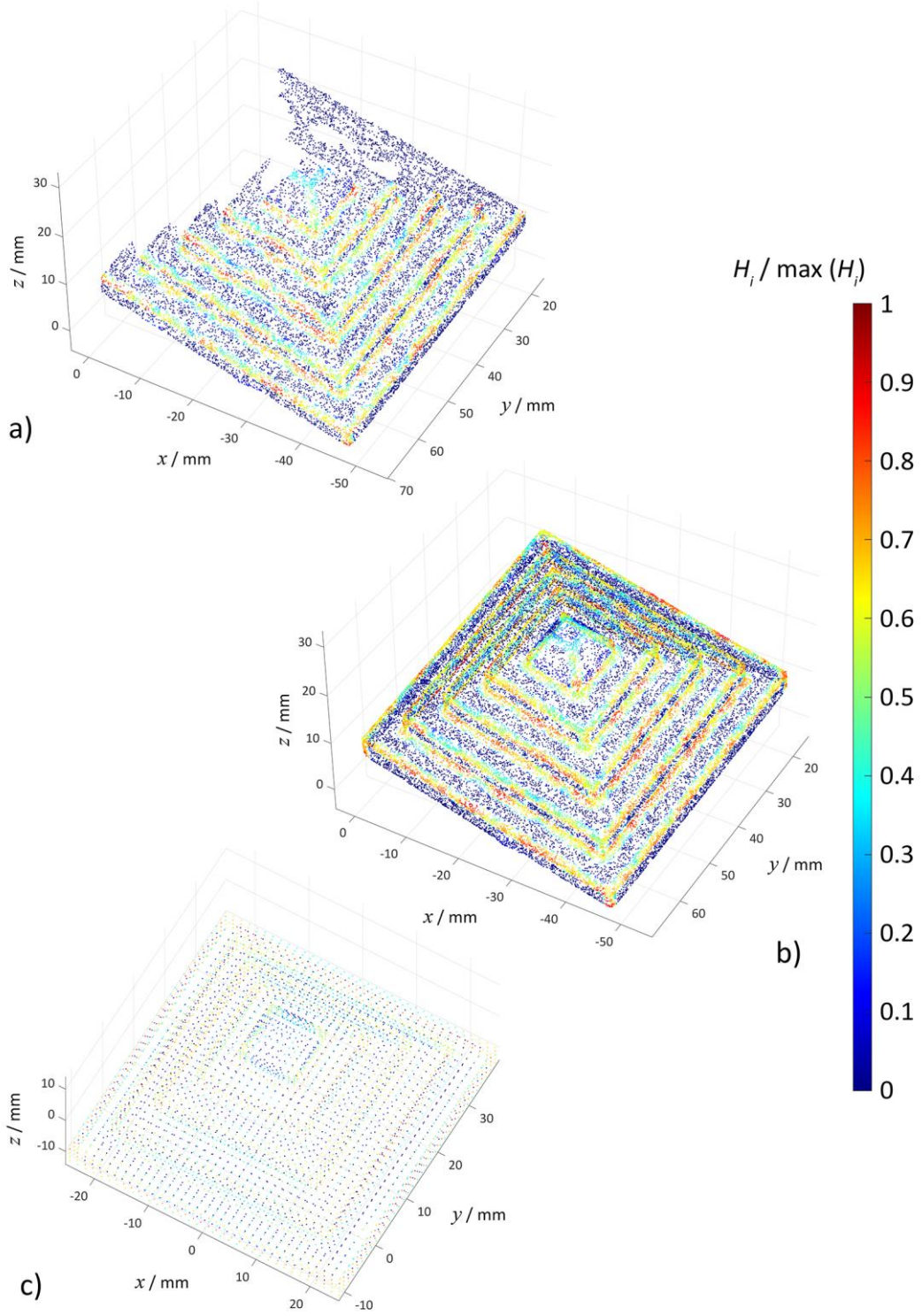

Figure 3.22 Local mean curvature H values estimation on point cloud (sample B), converted into colour map representations. a) Single-shot measurement, b) complete point cloud, c) triangle mesh vertices

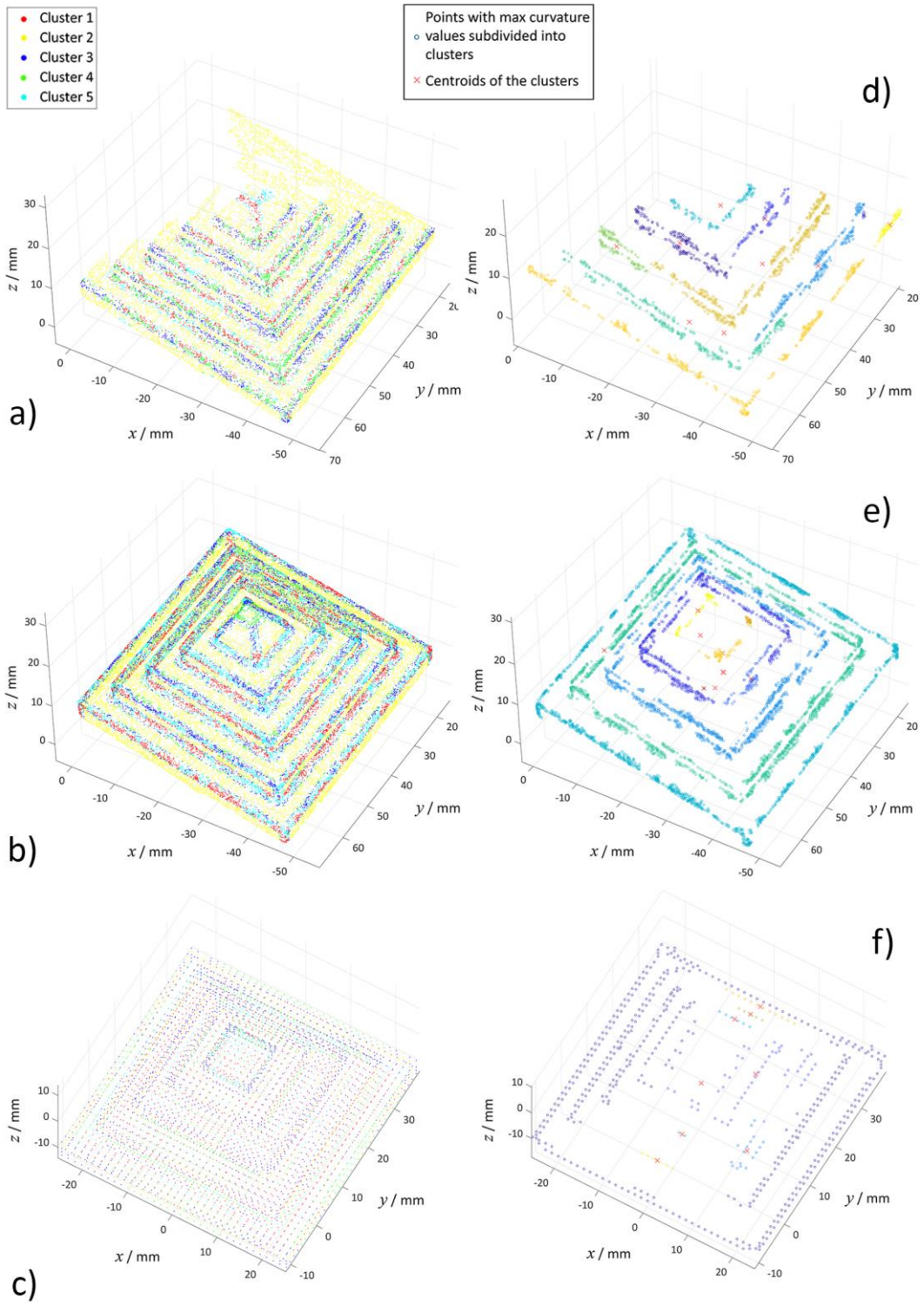

Figure 3.23 Point cloud partitioning on mean curvature for sample B: k-means clustering (points are assigned to one of three clusters ($k = 5$)). a) Single-shot, b) complete point cloud, c) mesh vertices. Hierarchical clustering and cluster centroids (total number of clusters set to ten). d) Single-shot, e) complete point cloud, f) mesh vertices

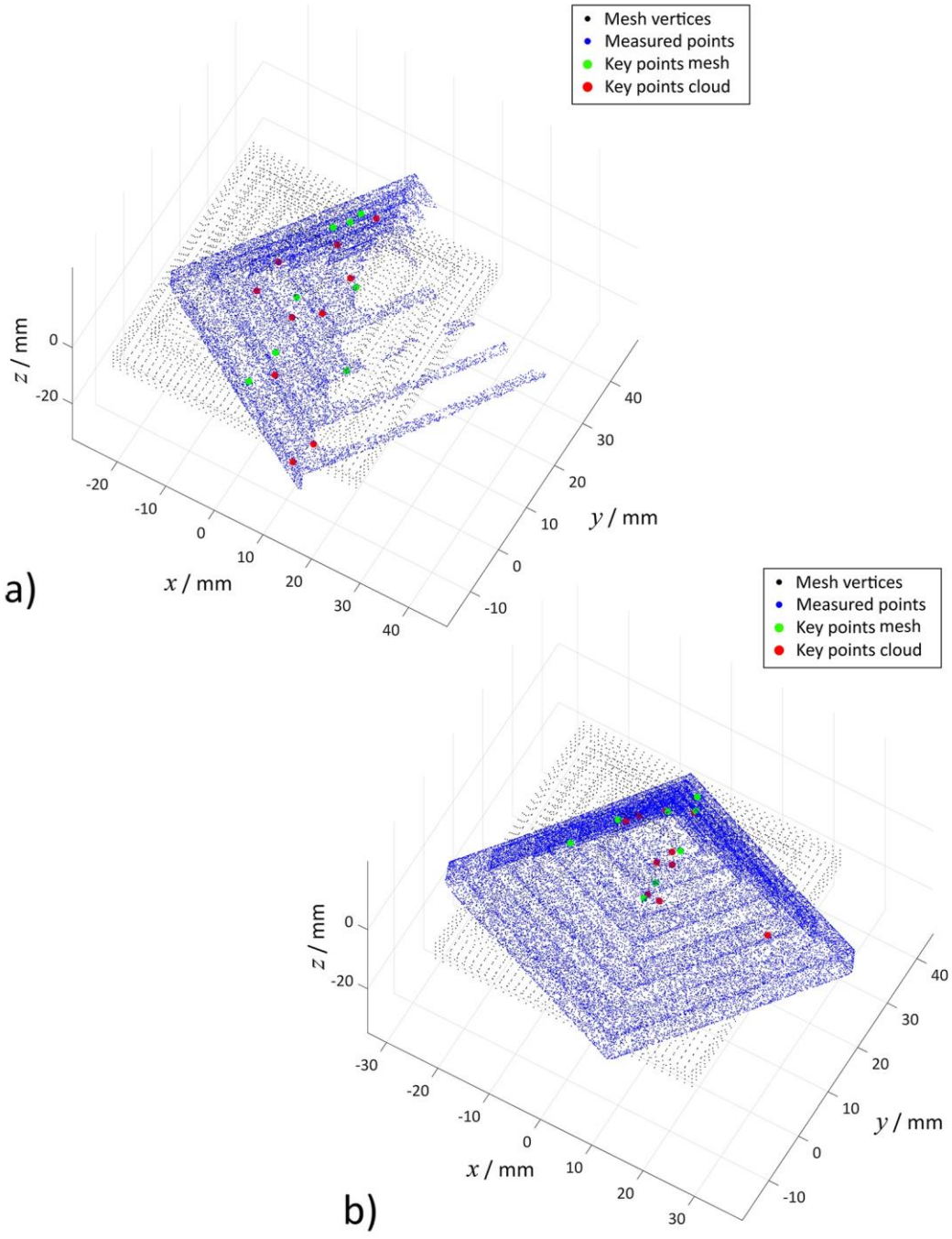

Figure 3.24 Paired centroids of mean curvature clusters (key points in green and red) identified in the mesh vertices and measured point clouds (in black and blue respectively) of sample B, matched via RANSAC after 1,000 iterations. a) Single-shot measurement coarse registration result, b) complete point cloud coarse registration result

3.3.4.3 FPFH feature descriptors for registration of sample B

FPFH features computation and matching via RANSAC are shown in Figure 3.25 and Figure 3.26. After 1,000 iterations, RANSAC established a successful number of paired correspondences between datasets equal to 21 and 38 matches for the partial and the complete point clouds respectively.

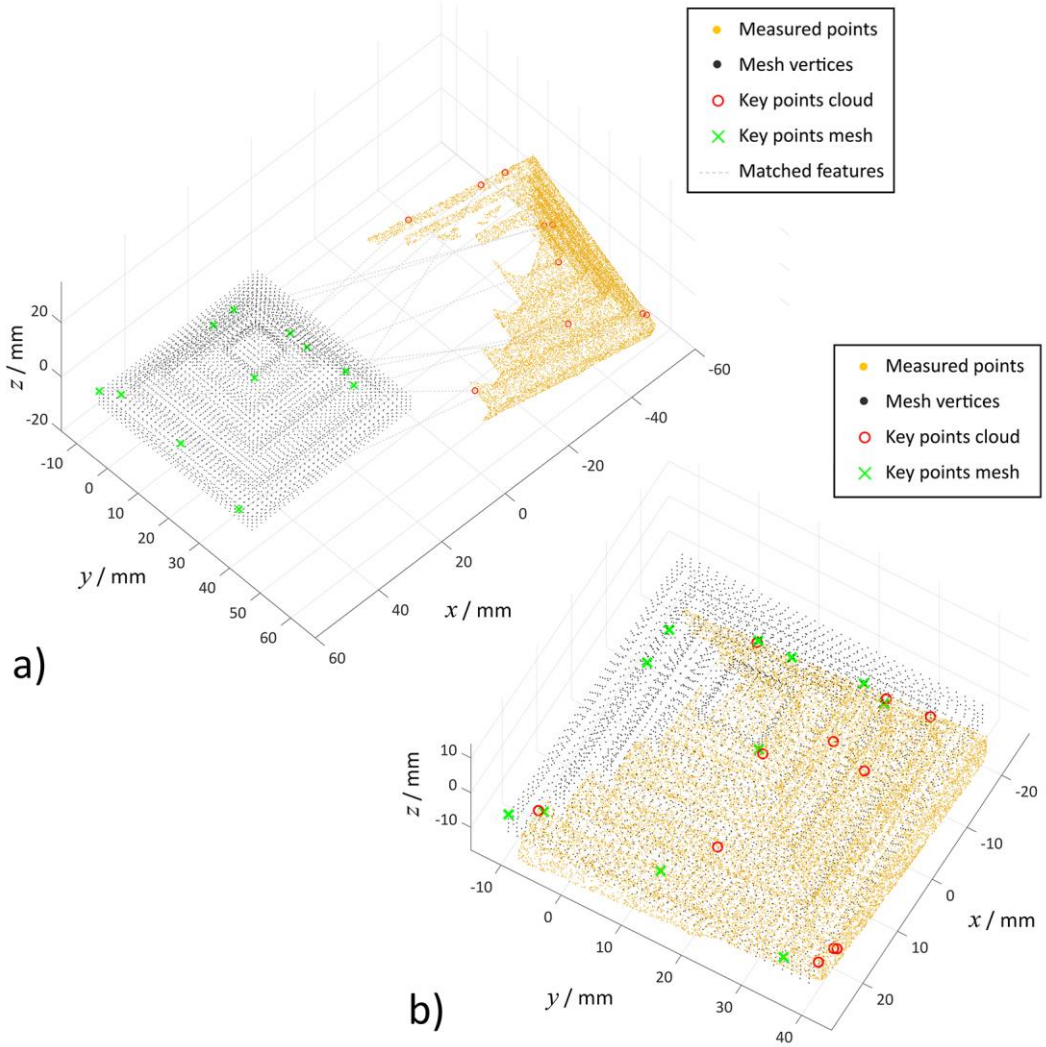

Figure 3.25 Paired FPFH features (total number of successful matched features: 21 pairs) identified in the mesh vertices and measured single-shot point cloud (in black and yellow respectively) of sample B, matched via RANSAC after 1,000 iterations. a) Datasets in their initial configuration (grey lines represent the coarse correspondence sets), b) coarse registration result after RANSAC

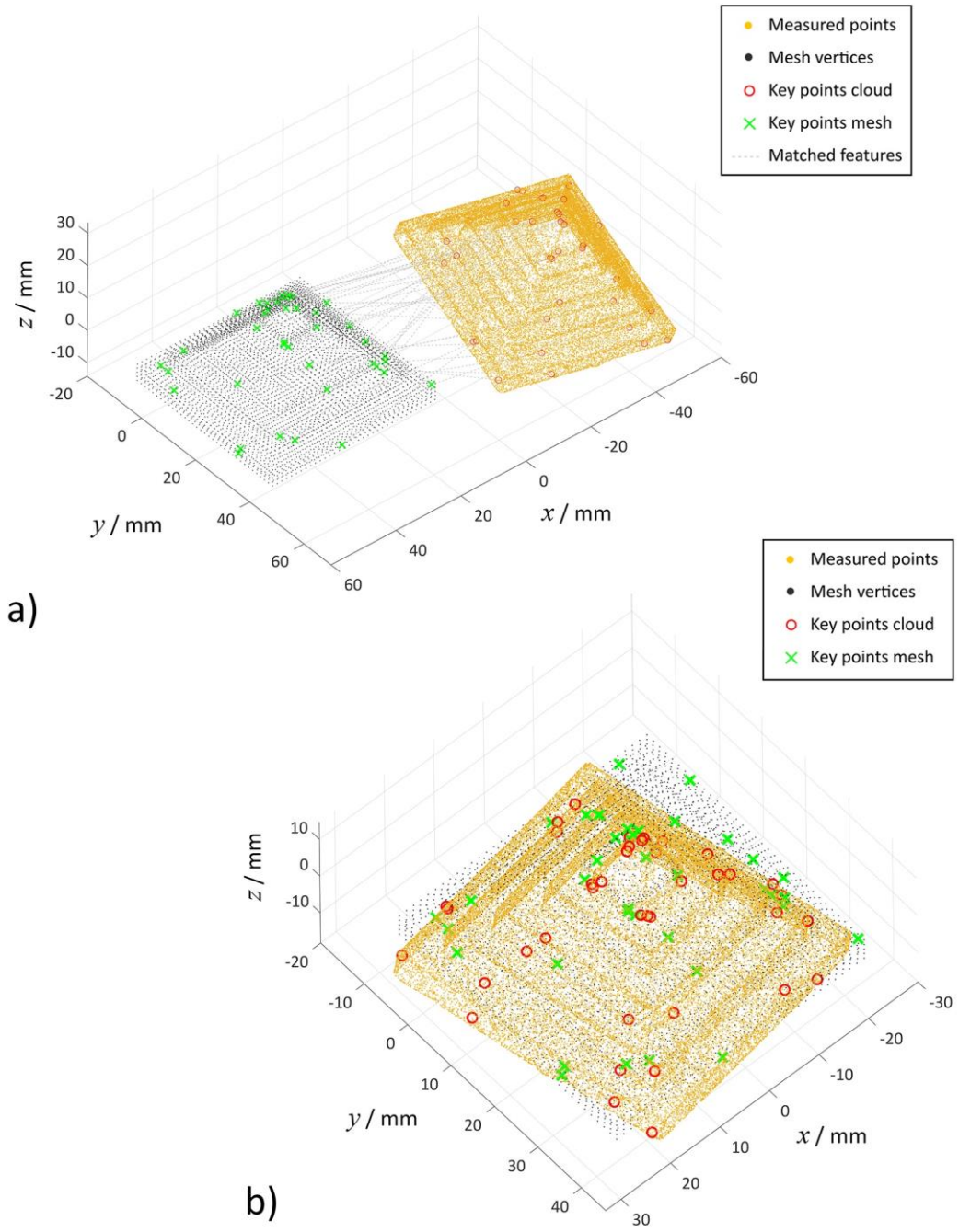

Figure 3.26 Paired FPFH features (total number of successful matched features: 38 pairs) identified in the mesh vertices and complete point cloud acquisition (in black and yellow respectively) of sample B, matched via RANSAC after 1,000 iterations. a) Datasets in their initial configuration (grey lines represent the coarse correspondence sets), b) coarse registration result after RANSAC

3.3.4.4 Summary of the coarse registration results and ICP refinement on sample B

In this section, the registration results obtained using different point features applied to the measurements of sample B are discussed. The registration results were quantitatively assessed calculating the error metrics recorded for the measured datasets in their initial configuration with respect to the fixed mesh model, as well as for their configurations after coarse and fine registrations, as it was done for sample A (see Section 3.3.3.4).

The results of the ICP algorithm for the refined registration phase are illustrated in Figure 3.27, after 1,000 iterations of distance metric minimisation between fixed and moving datasets. Figure 3.28 shows the differences of the recorded RMSEs for partial and complete point clouds across the registration stages, while employing different local point features (Gaussian curvature in Figure 3.28.a, mean curvature in Figure 3.28.b and FPFH descriptors in Figure 3.28.c). The RMSEs recorded at the coarse and fine registration stages are additionally reported in Figure 3.29. Similar to the results shown for sample A, the registration error decreased rapidly for all datasets of sample B immediately after the coarse registration was carried out, as it is shown in Figure 3.28. The best performances were recorded for the FPFH descriptors, especially when applied to the complete point cloud (see also Figure 3.26). With the exception of the local Gaussian curvature K which showed a better RMSE result for the partial measurement, the dependency of point-based feature candidates on the level of density variation and completeness was again proven [192,197], even if in a less significant level as for sample A.

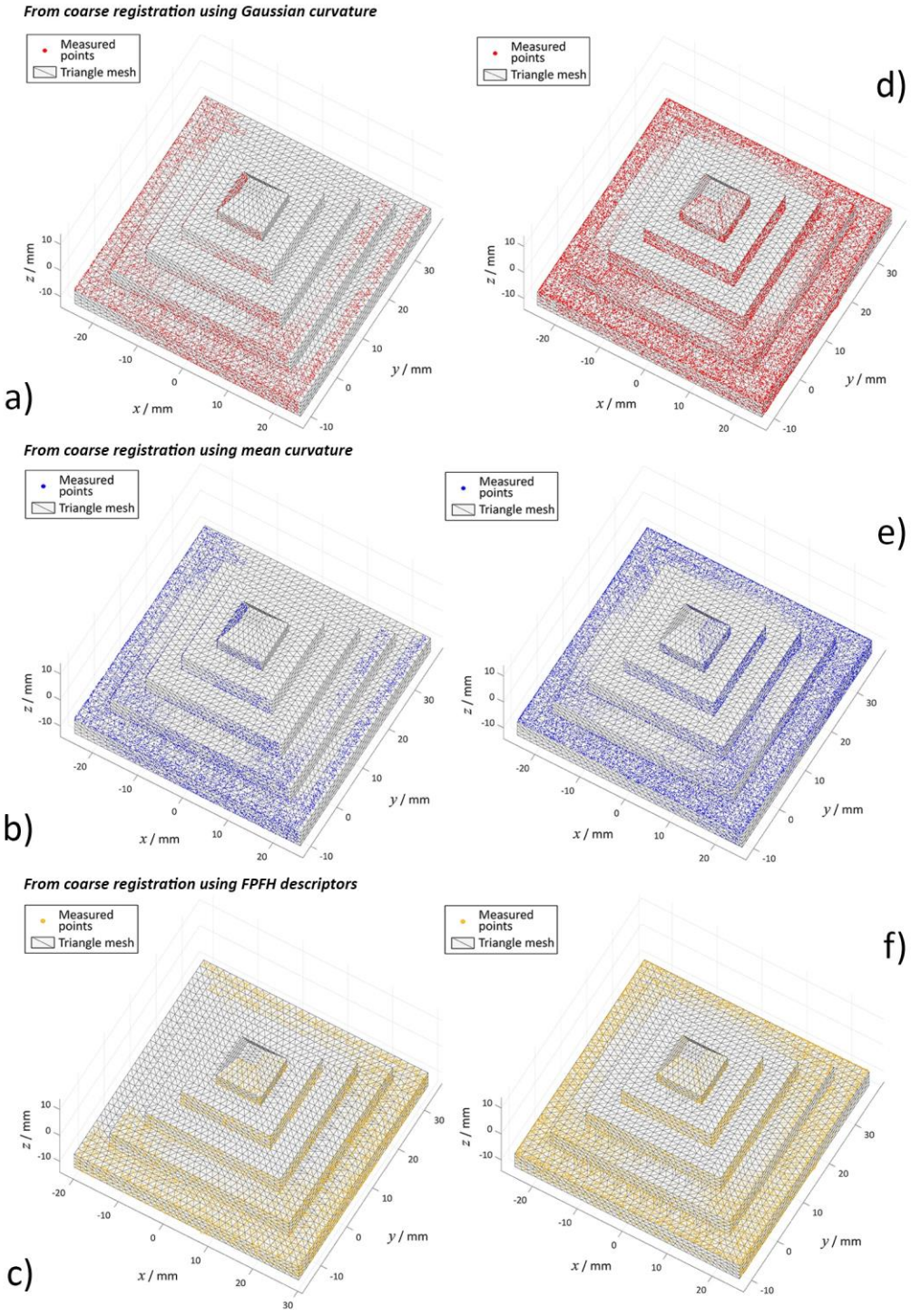

Figure 3.27 Registration results of coarse transformation based on landmark matching refined using ICP (1,000 iterations) for sample B. Single-shot measurement a) Gaussian curvature, b) mean curvature, c) FPFH descriptors; complete point cloud d) Gaussian curvature, e) mean curvature, f) FPFH descriptors

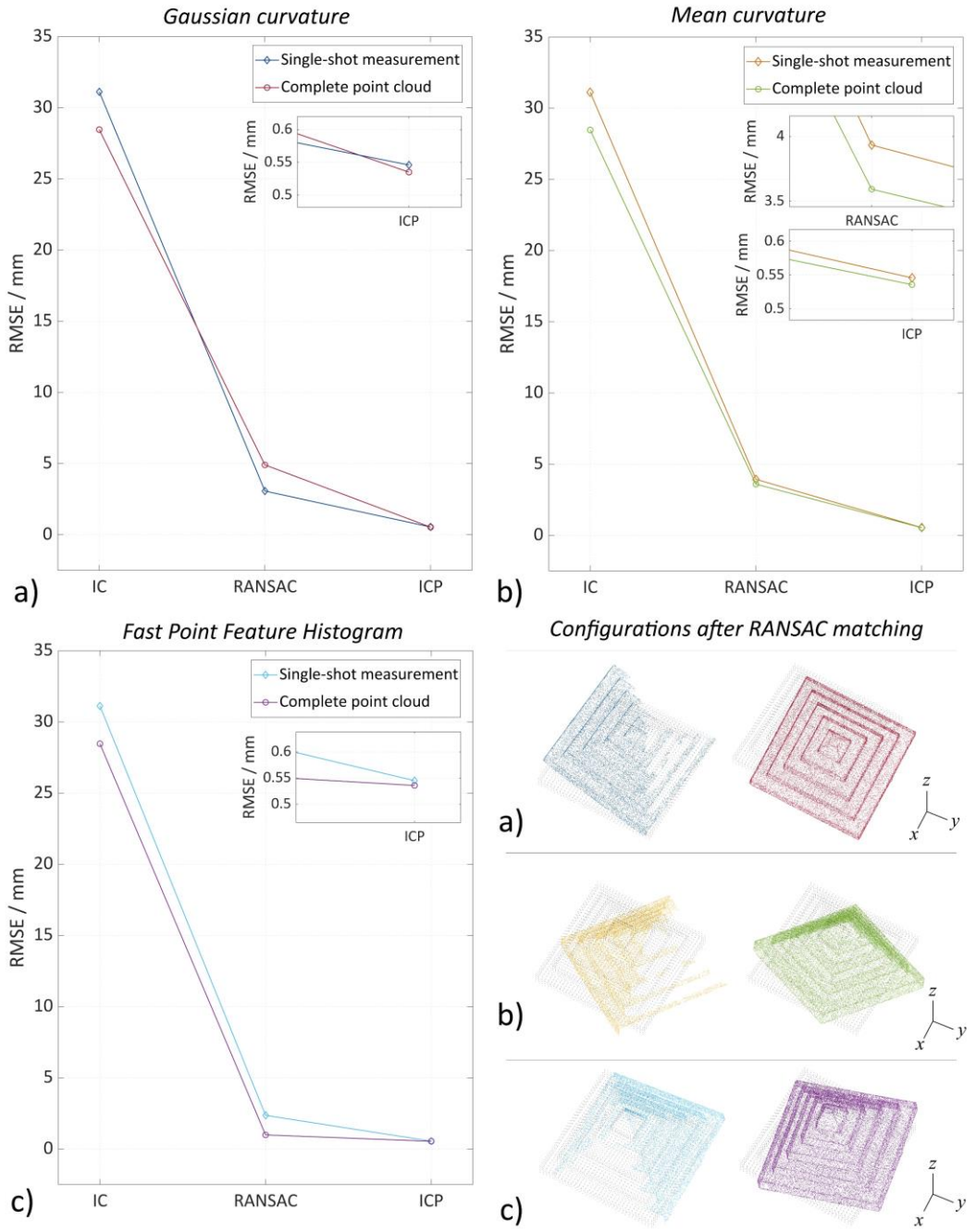

Figure 3.28 Registration results of sample B using different features descriptors for partial and complete point clouds (indicated with different colours). From left to right, the RMSE is recorded in different registration stages: RMSE recorded between the datasets at their initial configuration (*i.e.*, initial positions of the input data – indicated with IC), RMSE recorded in the coarse registration phase (indicated with RANSAC), and RMSE recorded in the fine registration (indicated with ICP). RMSE graphs and point clouds visual results obtained using a) Gaussian curvature K, b) mean curvature H, and c) FPFH as landmarks for registration

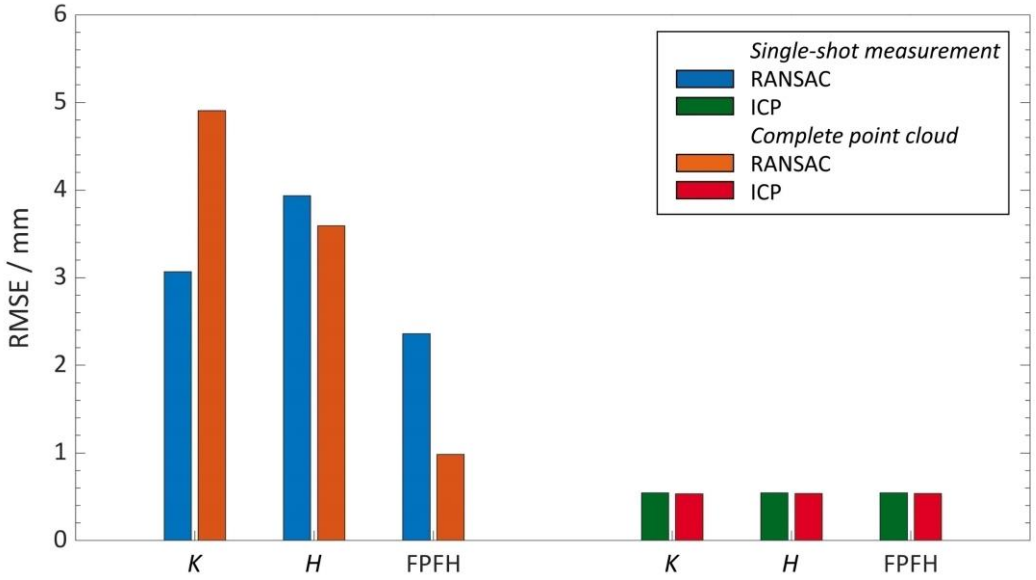

Figure 3.29 Histograms of RMSE of coarse and fine registration for partial and complete point clouds of sample B using different point features/descriptors (Gaussian curvature $\boldsymbol{K}$, mean curvature $\boldsymbol{H}$ and FPFH reported on the x axis). The absolute values recorded of RMSE for the coarse registration are reported on the left hand-side of the graph (indicated in blue and orange RANSAC for partial and complete measurements respectively); on the right hand-side the RMSE for the fine registration are reported (indicated in green and red ICP for partial and complete measurements respectively)

The results showed that the paired correspondences returned by RANSAC were contaminated by incorrect matches in all cases, as it can be immediately seen from the configurations shown in Figure 3.21, Figure 3.24, Figure 3.25 and Figure 3.26. The symmetric shape of sample B and the presence of extensive featureless regions (such as flat and spherical regions) surely contributed to the unsuccessful matching of correct correspondences, given the presence several areas of the object surface with similar local point features (in particular very similar curvature values) [192], showing problems of geometric instability, as discussed at the beginning of Section 3.3.4.

Despite the low robustness of the coarse registration results, the RMSE values recorded for the fine registration phase showed significantly minimised results for both partial and complete datasets, meaning that all coarse positions of the moving point clouds allowed the ICP algorithm to work efficiently (see Figure 3.27) and achieve an acceptable convergence. The noticeable bias between the surfaces of the CAD and the measured points (*i.e.,* the points in the cloud appear to be heavily negatively biased with respect to the top surfaces of the CAD, while the points registered at the bottom of the pyramid appear instead as correctly registered and slightly positively biased) could suggest a potential warping in the printed object, as a consequence of known shape bending often observed in Ti6Al4V parts fabricated by laser-powder bed fusion [238]. To conclude, the ICP algorithm is a global alignment method, which might further justify the fine registration results and consequent biases obtained: regions in a point cloud containing a greater number of points lead and constrain the registration process [188].

3.3.5 Results on sample C

The same registration process as for samples A and B has been applied to a third selected AM part featuring a hollow complex shape. The obtained results are illustrated in the following sections.

The initial datasets of sample C are shown in Figure 3.30 (single-view, complete point cloud, and mesh vertices on the left-hand side panels a, b and c respectively). Computed normals consistently oriented pointing outwards are shown on the same figure (right-hand side panels d, e and f respectively).

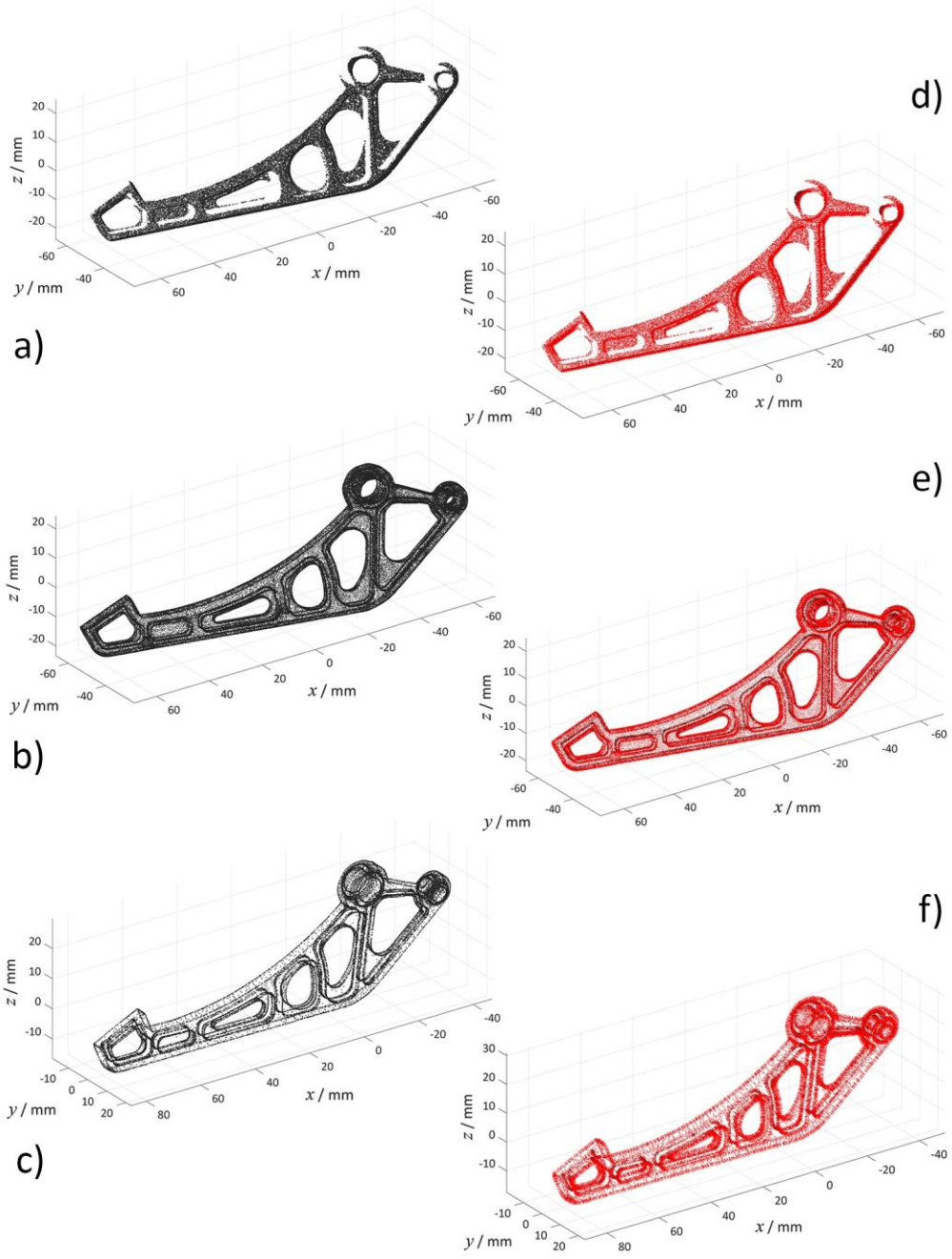

Figure 3.30 Datasets of sample C (in black). a) Single-shot measurement (42,790 point count), b) complete point cloud (72,468 point count), c) triangle mesh extracted vertices (22,314 point count). Point vector normals consistently oriented pointing outwards (in red). d) Single-shot measurement, e) complete point cloud, f) triangle mesh vertices

3.3.5.1 Gaussian curvature for registration of sample C

Figure 3.31 shows the local Gaussian curvature values mapped to each dataset and reported in normalised form (*i.e.,* normalised by division with respect to the maximum Gaussian curvature value recorded across the datasets).

The neighbours search radius for principal curvatures computation was set to 1.5 mm for the measured point clouds (both partial and complete) and to 2.5 mm for the extracted vertices from the triangle mesh.

Figure 3.32 shows the methods for points partitioning applied to sample C, respectively k-means and hierarchical clustering. For the former, the points were subdivided into five clusters ($k = 5$, resulting from the elbow method) based on Gaussian curvature values. Cluster 2 resulted in the points with the highest recorded values. The latter was instead hierarchical and based on Euclidean distance between regions of points belonging to Cluster 2. The centroids of the clusters (set to ten) represented the correspondences needed to perform the coarse registration based on landmark matching.

The correspondences (key points shown in Figure 3.33) were iteratively pruned and best-matched using RANSAC, defining the number of meaningful correspondences as a minimum of five. After 1,000 iterations, 50% of matches resulted successful for the partial point cloud, and 90% for the complete dataset (ten is the total number of key points, *i.e.,* cluster centroids).

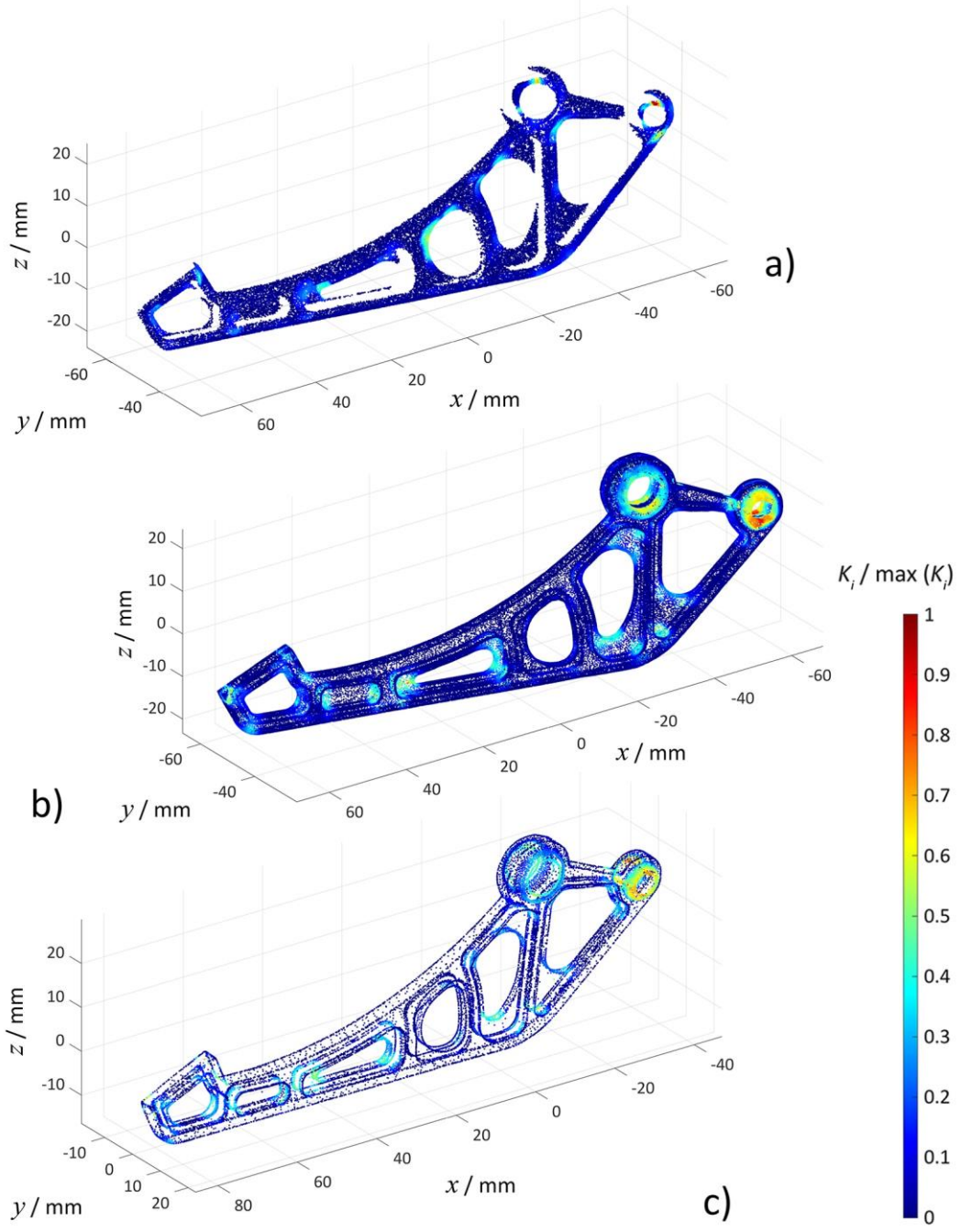

Figure 3.31 Local Gaussian curvature K values estimation on point cloud (sample C), converted into colour map representations. a) Single-shot measurement, b) complete point cloud, c) triangle mesh vertices

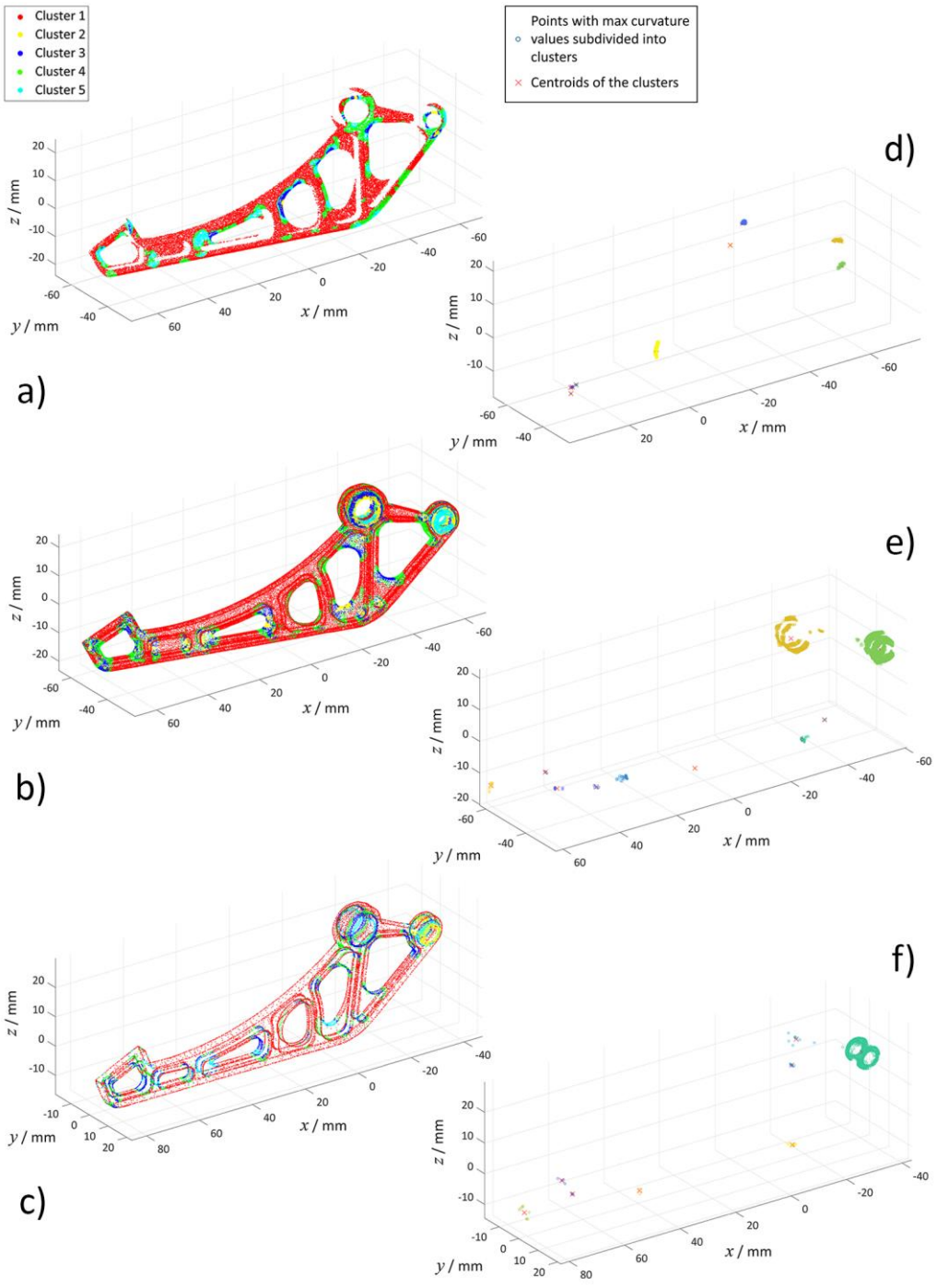

Figure 3.32 Point cloud partitioning on Gaussian curvature for sample C: k-means clustering (points are assigned to one of three clusters ($\boldsymbol{k} = 5$)). a) Single-shot, b) complete point cloud, c) mesh vertices. Hierarchical clustering and cluster centroids (total number of clusters set to ten). d) Single-shot, e) complete point cloud, f) mesh vertices

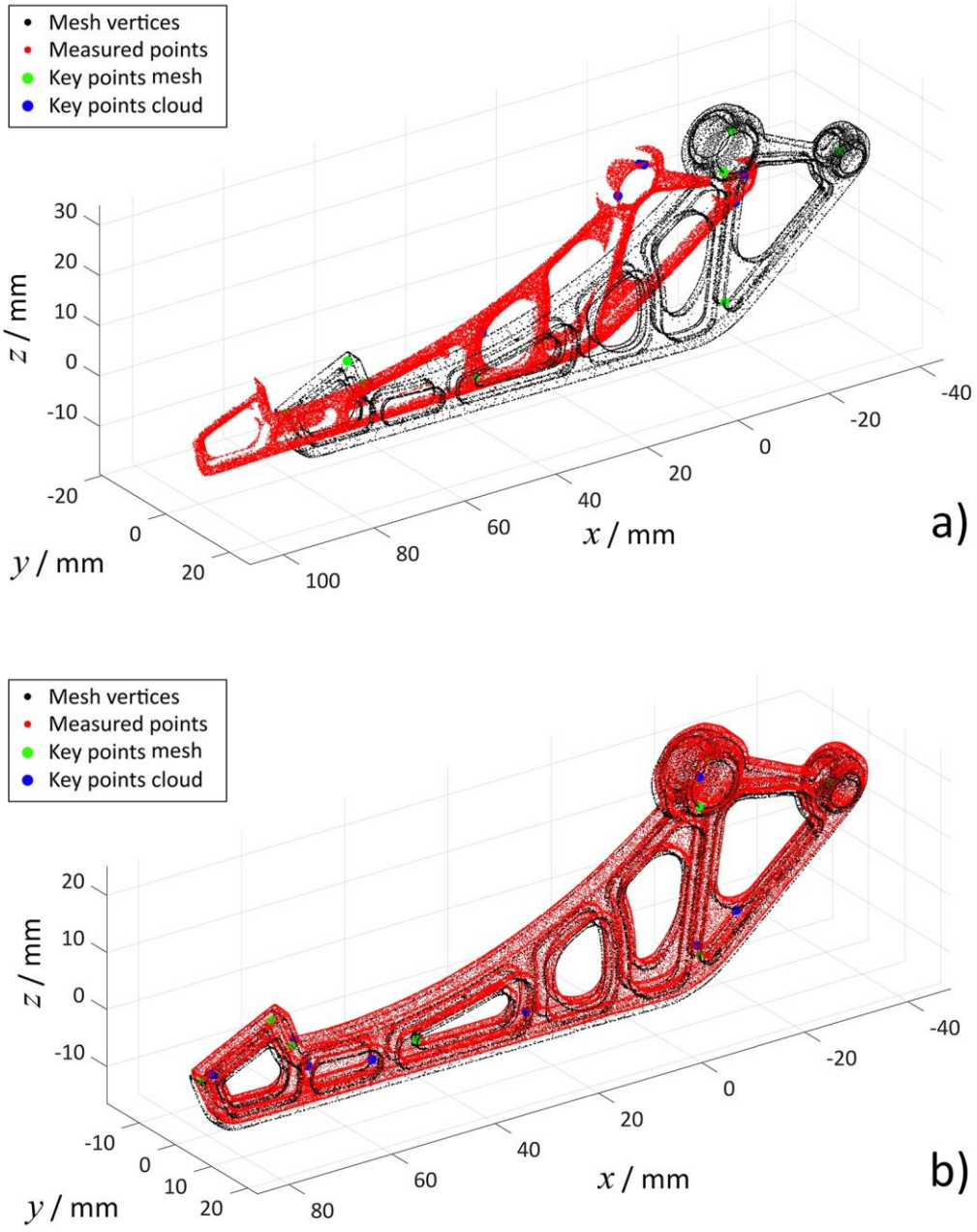

Figure 3.33 Paired centroids of Gaussian curvature clusters (key points in green and blue) identified in the mesh vertices and measured point clouds (in black and red respectively) of sample C, matched via RANSAC after 1,000 iterations. a) Single-shot measurement coarse registration result, b) complete point cloud coarse registration result

3.3.5.2 Mean curvature for registration of sample C

Figure 3.34 shows the local mean curvature values in normalised form mapped to a colour scale for visualisation purposes to all datasets. The radius for neighbours search used to compute the principal curvatures were set to 1.5 mm for the measured point clouds and to 2.5 mm for the mesh vertices.

The two partitioning methods applied to the obtained mean curvature values are shown in Figure 3.35. For k-means the points were subdivided into five clusters ($k = 5$ resulting again from the elbow method). Cluster 2 resulted in the points with the highest mean curvature values. The second clustering was applied to the points belonging to Cluster 2, subdividing them into ten sub-regions based on Euclidean distance. The correspondences needed to solve the absolute orientation problem were found in the centroids of the identified clusters.

In order to perform registration based on landmark matching, the centroids of the clusters were pruned and matched via RANSAC as it is shown in Figure 3.36. The minimum number of meaningful correspondences needed to obtain the coarse transformation was set to five, resulting after 1,000 iteration in 70% successful number of paired correspondences for the partial point cloud and 90% for the complete dataset (ten is the total number of key points, *i.e.,* cluster centroids).

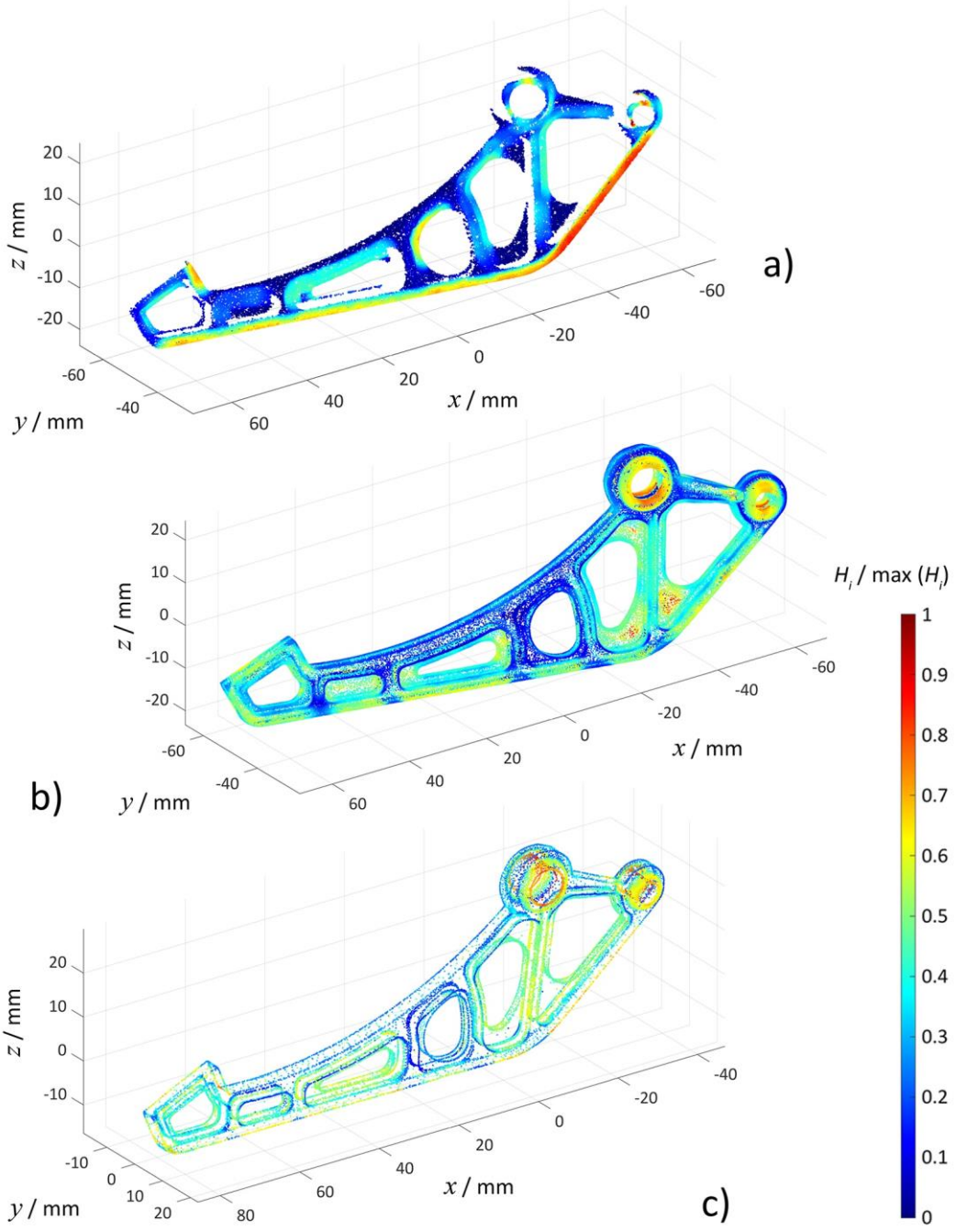

Figure 3.34 Local mean curvature H values estimation on point cloud (sample C), converted into colour map representations. a) Single-shot measurement, b) complete point cloud, c) triangle mesh vertices

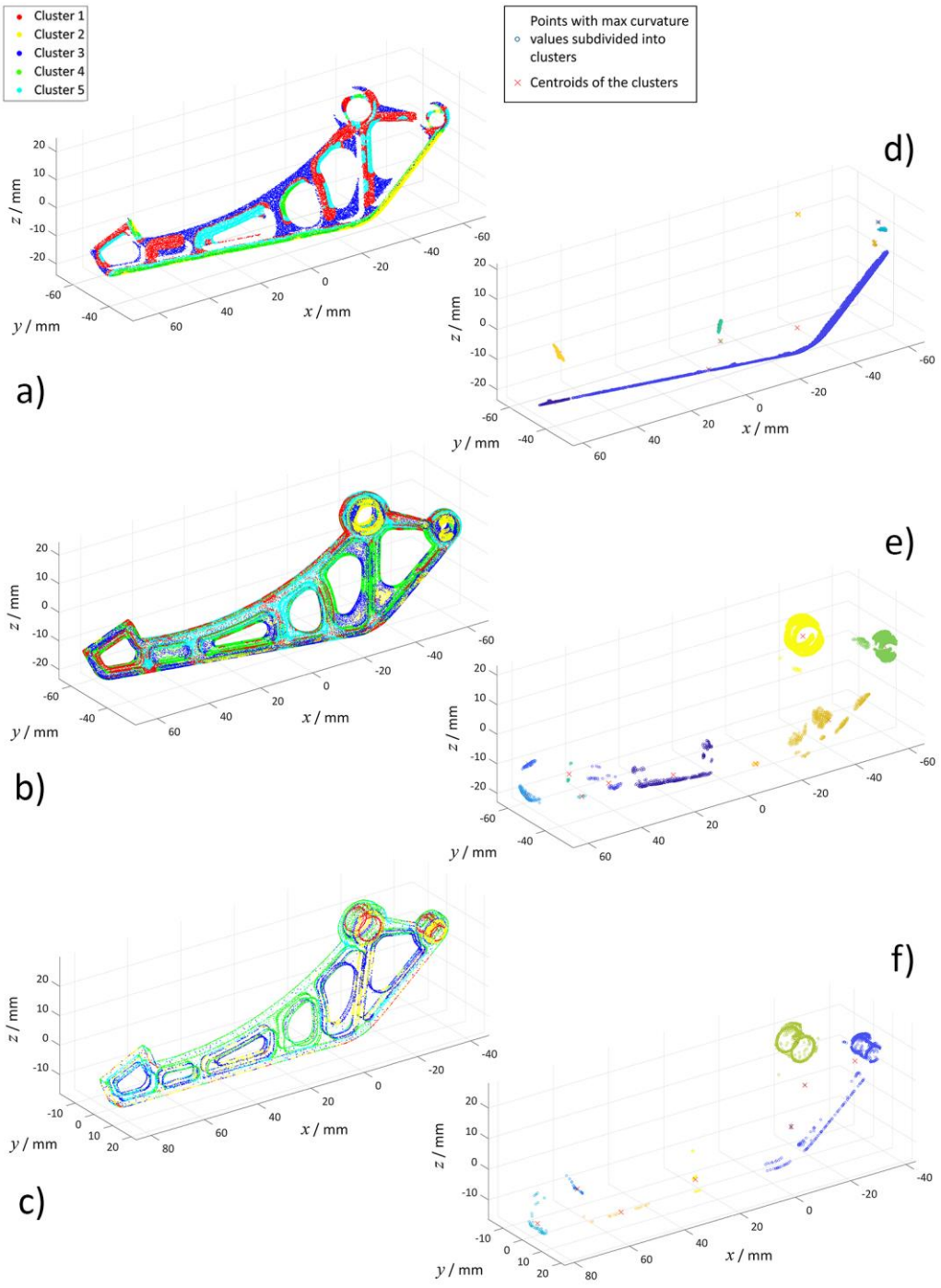

Figure 3.35 Point cloud partitioning on mean curvature for sample C: k-means clustering (points are assigned to one of three clusters ($k = 5$)). a) Single-shot, b) complete point cloud, c) mesh vertices. Hierarchical clustering and cluster centroids (total number of clusters set to ten). d) Single-shot, e) complete point cloud, f) mesh vertices

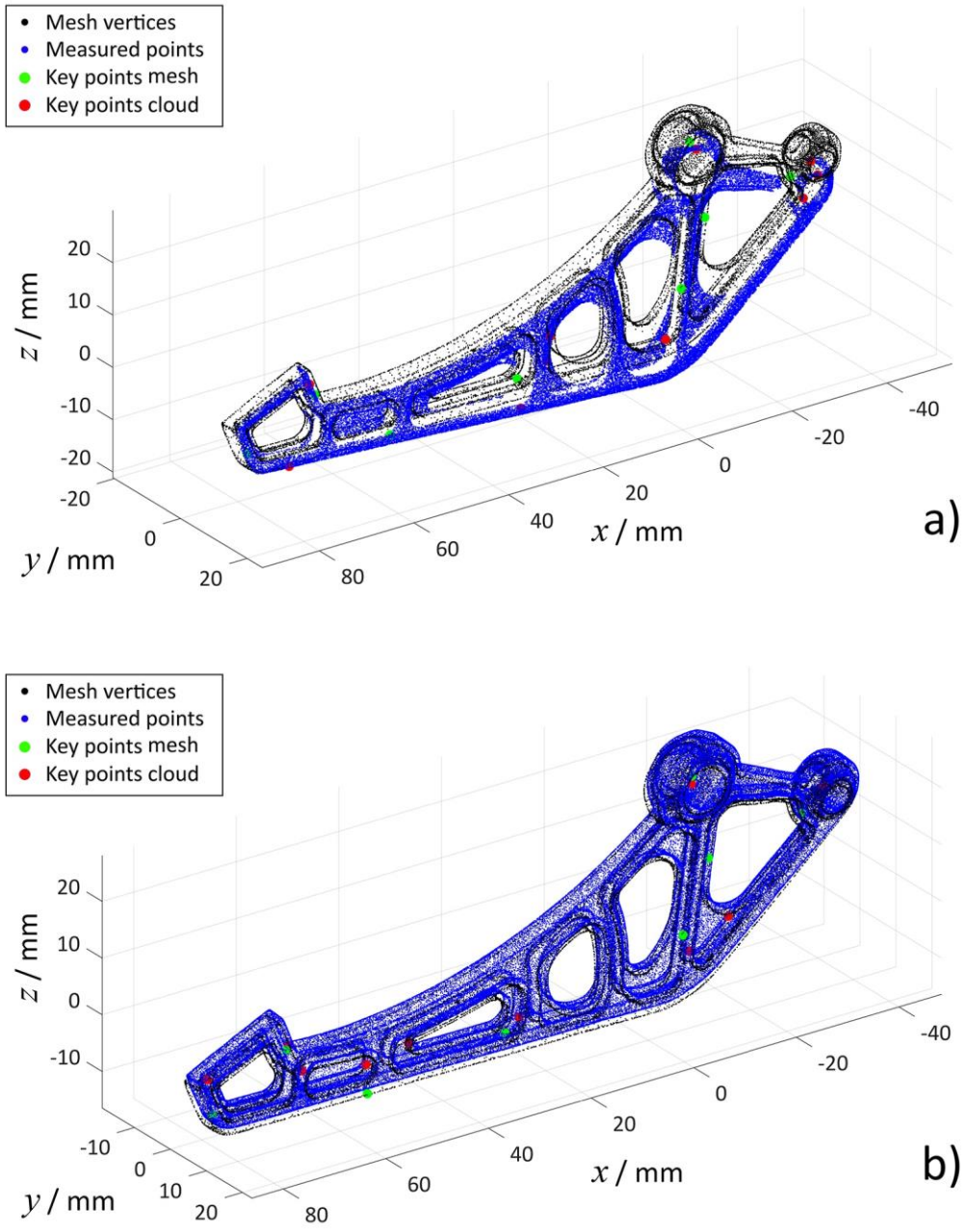

Figure 3.36 Paired centroids of mean curvature clusters (key points in green and red) identified in the mesh vertices and measured point clouds (in black and blue respectively) of sample C, matched via RANSAC after 1,000 iterations. a) Single-shot measurement coarse registration result, b) complete point cloud coarse registration result

3.3.5.3 FPFH feature descriptors for registration of sample C

The identification of FPFH features in the mesh vertices and partial and complete measured point clouds are shown in Figure 3.37 and Figure 3.38 respectively. After 1,000 iterations the successful number of matched pairs were identified via RANSAC, resulting for the partial point cloud and the complete measurement respectively in 11 and 39 pairs of successful correspondences.

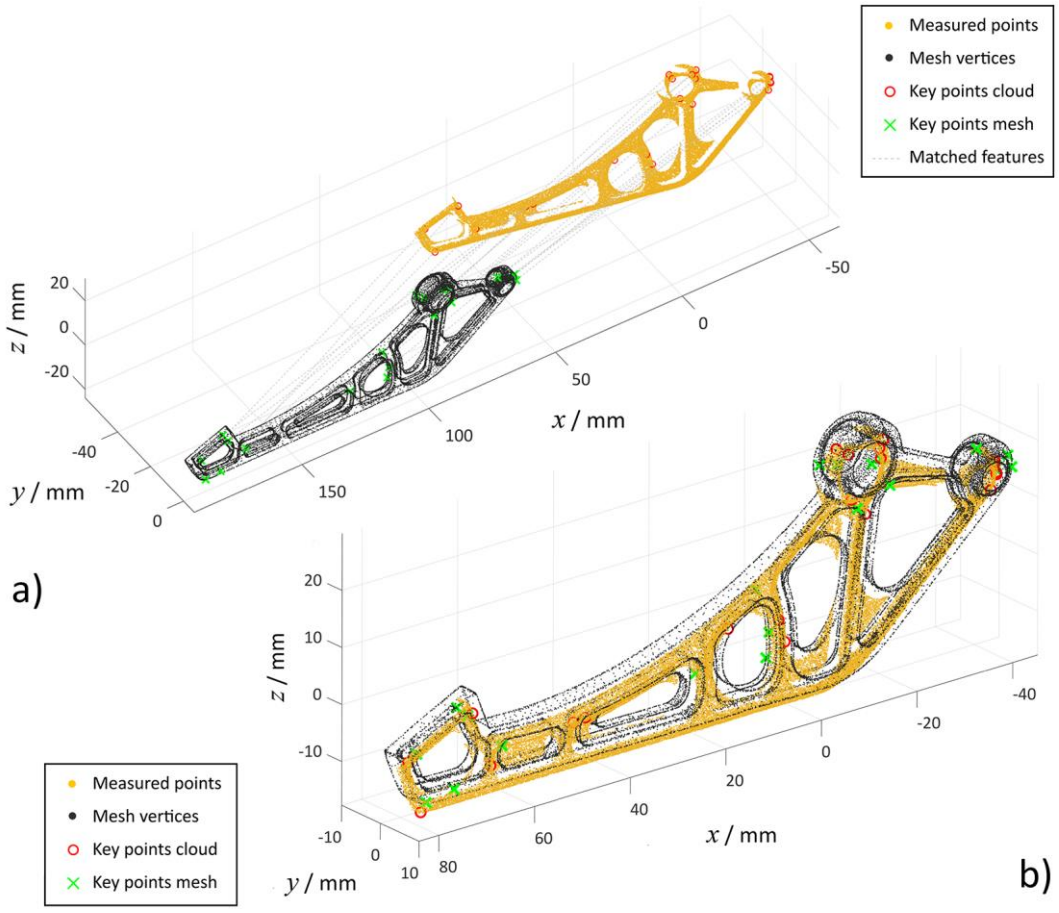

Figure 3.37 Paired FPFH features (total number of successful matched features: 11 pairs) identified in the mesh vertices and measured single-shot point cloud (in black and yellow respectively) of sample C, matched via RANSAC after 1,000 iterations. a) Datasets in their initial configuration (grey lines represent the coarse correspondence sets), b) coarse registration result after RANSAC

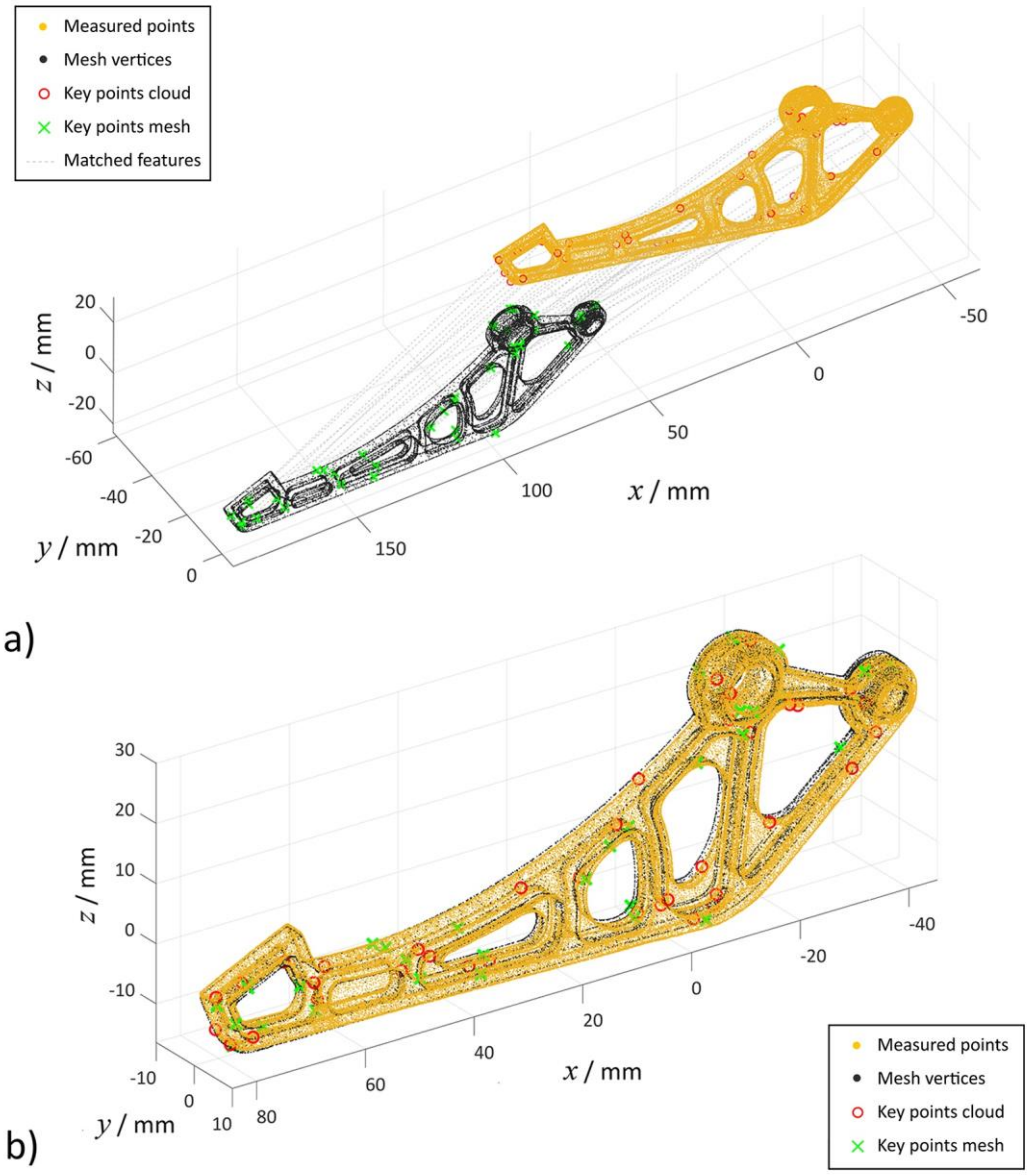

Figure 3.38 Paired FPFH features (total number of successful matched features: 39 pairs) identified in the mesh vertices and complete point cloud acquisition (in black and yellow respectively) of sample C, matched via RANSAC after 1,000 iterations. a) Datasets in their initial configuration (grey lines represent the coarse correspondence sets), b) coarse registration result after RANSAC

3.3.5.4 Summary of the registration results on sample C

The results obtained for registration using different point features (Gaussian curvature, mean curvature and FPFH descriptors) applied to the measurements of sample C and to the underlying triangle mesh geometry are discussed in this section. As for sample A and B previously illustrated in Sections 3.3.3.4 and 3.3.4.4 respectively, the registration results on sample C were quantitatively assessed calculating the root mean square error recorded for the measured datasets in their initial configuration with respect to the fixed model, as well as for their configurations after coarse and fine registrations.

From the coarse registration results previously obtained via feature matching, the registration error between the datasets was further minimised refining the obtained coarse transformations using ICP algorithm. The results of the refined transformations after 1,000 iterations for a single unidirectional point cloud and complete measurement registered to the reference geometry are shown in Figure 3.39.

The RMSEs recorded for partial and complete point clouds feature matching registrations (RANSAC with Gaussian curvature K, mean curvature H and FPFH descriptors respectively) and the final RMSEs recorded after fine registration (using ICP) with respect to the reference mesh local point features are shown in Figure 3.40 and Figure 3.41.

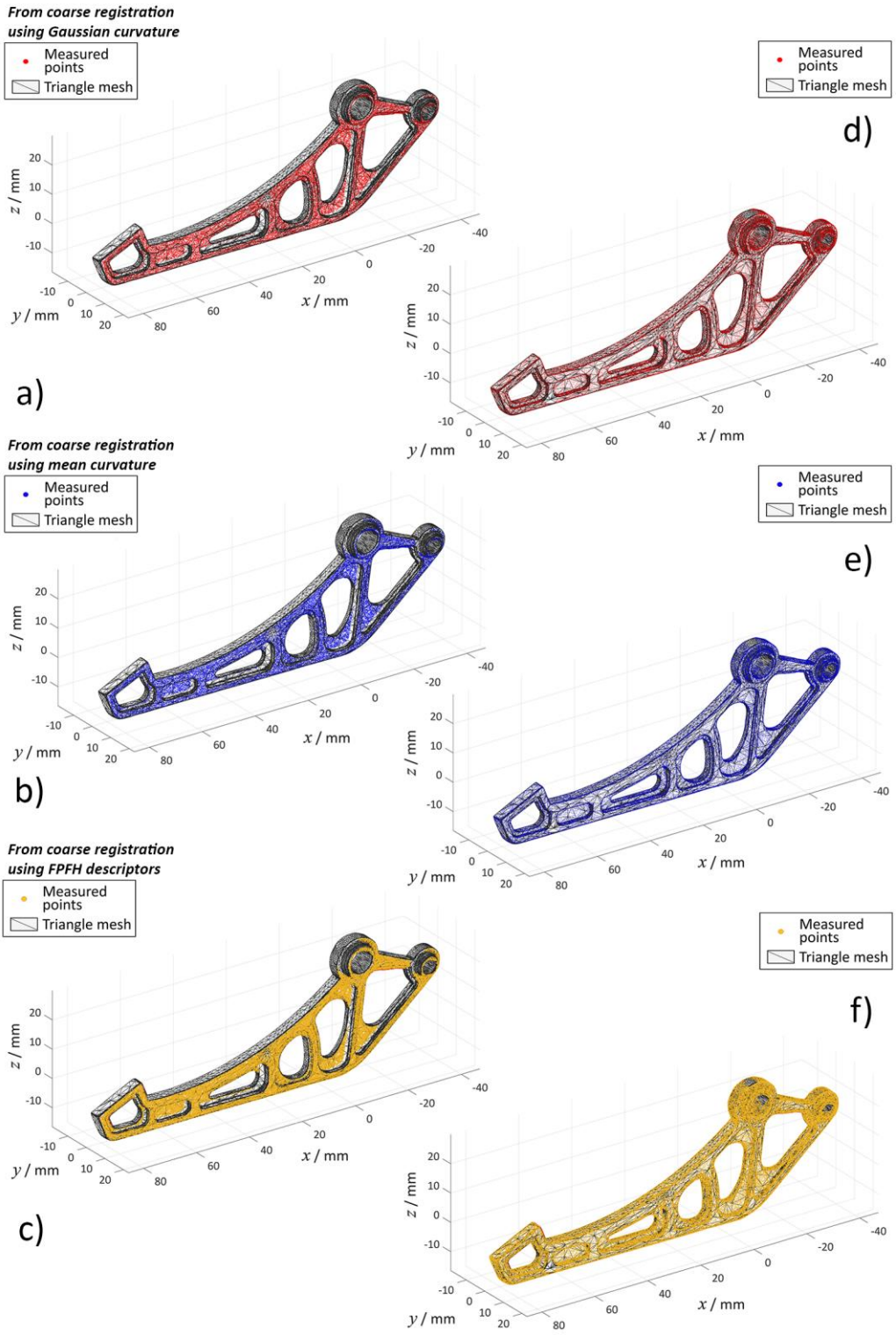

Figure 3.39 Registration results of coarse transformation based on landmark matching refined using ICP (1,000 iterations) for sample C. Complete point cloud a) Gaussian curvature, b) mean curvature, c) FPFH descriptors; single-shot measurement d) Gaussian curvature, e) mean curvature, f) FPFH descriptors

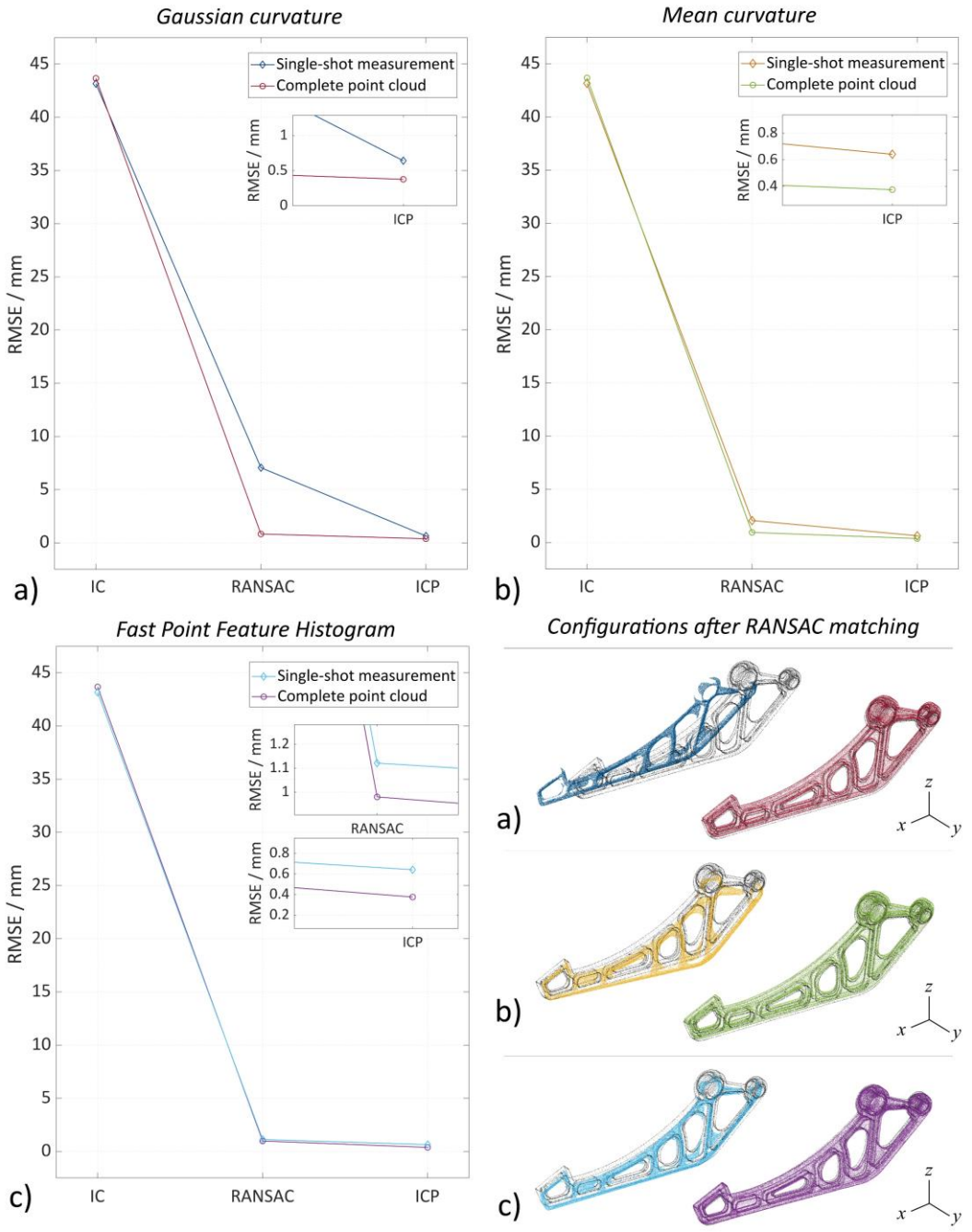

Figure 3.40 Registration results of sample C using different features descriptors for partial and complete point clouds (indicated with different colours). From left to right, the RMSE is recorded in different registration stages: RMSE recorded between the datasets at their initial configuration (*i.e.*, initial positions of the input data – indicated with IC), RMSE recorded in the coarse registration phase (indicated with RANSAC), and RMSE recorded in the fine registration (indicated with ICP). RMSE graphs and point clouds visual results obtained using a) Gaussian curvature K, b) mean curvature H, and c) FPFH as landmarks for registration

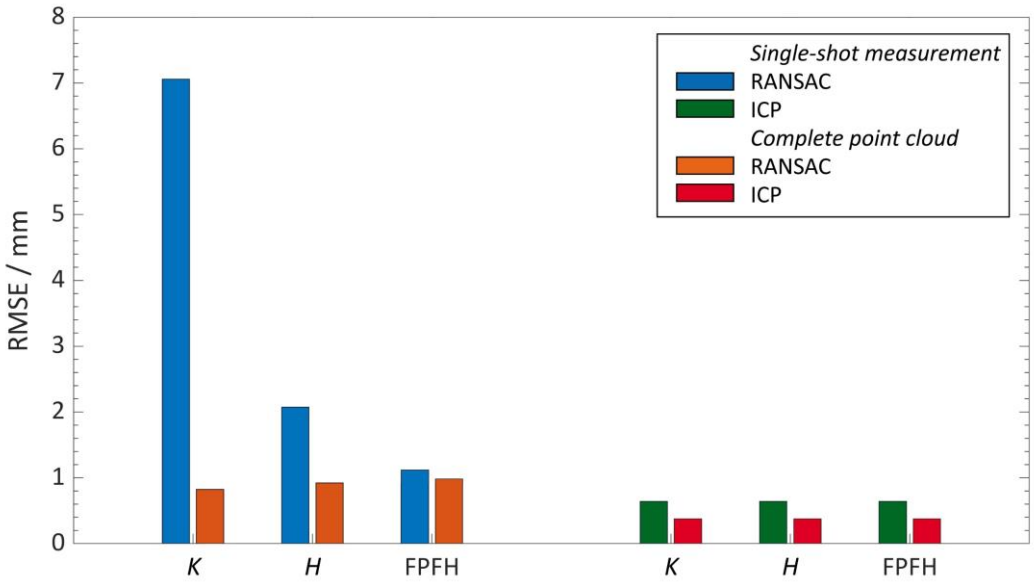

Figure 3.41 Histograms of RMSE of coarse and fine registration for partial and complete point clouds of sample C using different point features/descriptors (Gaussian curvature K, mean curvature H and FPFH reported on the x axis). The absolute values recorded of RMSE for the coarse registration are reported on the left hand-side of the graph (indicated in blue and orange RANSAC for partial and complete measurements respectively); on the right hand-side the RMSE for the fine registration are reported (indicated in green and red ICP for partial and complete measurements respectively)

Differently from the results obtained for the registrations of sample A and B (Sections 3.3.3.4 and 3.3.4.4 respectively), which showed higher RMSE values recorded after the first coarse registration phase based on feature matching, the results obtained for sample C resulted in smaller registration errors and less contamination of incorrect matches (see Figure 3.36, Figure 3.37, Figure 3.38), with the exception of Gaussian curvatures matching for the single-shot measurement (Figure 3.33.a). In particular, feature matching for the complete datasets returned correct paired correspondences (pruned by RANSAC) as it is clearly illustrated by the graphical representations of the position configurations and RMSE results (Figure 3.40). This strongly confirms once again the dependency to density variation and completeness of

the data [192,197] for the accomplishment of a correct feature correspondence process. Overall, the coarse correspondence sets for FPFH showed the best results for the single-shot point cloud.

The symmetric shape of sample C along the axis corresponding to the longest dimension of the part would suggest a potential lack of stability in the registration process [192], as it was clearly demonstrated for sample B (see Section 3.3.4.4). However, the presence of distinct and significant geometric elements (for example hollow shapes, recesses, sharp edges, slot-holes, *etc.*), far more frequent than those characterising the shapes of sample A and B, contributed to the identification of point features and successful matching [197,236,239].

Final RMSE values recorded after the fine registration phase returned slightly better results for the complete dataset regardless the landmark features chosen to perform alignment.

3.4 Chapter conclusions

A registration strategy for the automated pose assessment of the measured point cloud with respect to a reference geometry was illustrated in this chapter. Based on the knowledge acquired from the literature on currently employed registration methods, this chapter began with the definition of a complete registration pipeline characterised by several defined phases, adopting the alignment method of landmark matching using similarity/difference metrics (see Section 2.2.6.6). Candidate landmarks were

identified by computing local features such as local point normal vectors, local surface curvatures (Gaussian and mean), and local shape descriptors (FPFH) on measured point clouds and on the vertices of the underlying reference mesh geometry.

The registration pipeline was therefore applied to selected industrial cases featuring AM components of different shape complexity measured with fringe projection. In order to test the robustness of the adopted registration approach to density and completeness of the available point clouds, single-shot and multiple-scan measurements of the samples were performed, featuring different measuring scenario (*i.e.,* the measurement is available as partially acquired point cloud or it is accessible as complete measurement). No prior knowledge about the initial position of the datasets was required for the development of the registration strategy presented in this chapter. In addition, registration was performed in a fully automated way, requiring human intervention only in the setting of control parameters for the algorithms (for example distance threshold, neighbouring search radius, maximum number of acceptable correspondences, *etc.*).

The results obtained from the registration of each sample were evaluated and compared based firstly on visualisation of the registered moving-target dataset configurations, and then quantitatively assessed using the root mean square error between corresponding points identified in both moving and target datasets. From the results obtained the following observations can be made:

a) density variation in terms of point count and completeness of the available data have both a significant weight in the registration process,

especially in the point-to-point correspondences matching process. This means that computed point features or descriptors should be robust and sufficiently discriminative, as it was demonstrated for instance by FPFHs, which were able to encode point neighbourhood geometrical properties more extensively than Gaussian and mean curvature local features;

b) the presence of multiple geometric elements characterising the surface of a sample (for example hollow shapes, recesses, sharp edges, slot-holes) contributed to the identification of distinct attributes (*i.e.,* local point features or regions with similar properties) needed for registration. In the specific case of sample C, the aforementioned geometric information represented a significant advantage to the achievement of successful matching with the reference targets;

c) symmetry in shape and large featureless surfaces (*i.e.,* large flat or spherical regions) characterising the sample can cause problems and lead the registration algorithm towards convergence failure, as it was for instance demonstrated for sample B. Even in the case of a completely asymmetrical shape (for instance Sample A) the presence of poor geometric information to fully constrain the transformation might fail the registration process.

In order to localise, identify and select subsets of points corresponding to specific regions of a part surface, the correct registration of a measured point cloud with the underlying reference 3D model must be accomplished. Regions of the measured part will be associated to a finely registered reference datum, aiming at creating a detailed map of the performances of the

measurement and highlighting which areas are the most critical to measure (for instance, regions of the part hidden from the instrument line-of-sight). In conclusion, the achievement of a good registration result is a fundamental aspect of the measurement pipeline. The registration pipeline described in this chapter will define the strategy developed for the definition of a set of original indicators of measurement performance presented in Chapter 4.

Chapter 4

Measurement quality indicators

4.1 Overview

In Chapter 3, a registration strategy for the automated assessment of the position of the measured point cloud with respect to a reference geometry using landmark matching has been illustrated, determining a key aspect of the measurement pipeline described in Chapter 1. In order to achieve "pose assessment" (defined in Chapter 3), the measured point clouds were registered to a reference geometry in form of triangle mesh representing the part. Registration is required in order to identify and select subsets of points corresponding to specific regions of a part surface, and define criteria for the assessment of the quality of measurement results.

A set of original indicators defined in this thesis as "measurement quality indicators" is described in this chapter. The indicators are designed to capture the quality of a measurement result under multiple viewpoints, not only limited to the evaluation of conventional metrological criteria (for instance the uncertainty associated to features of size), but also performance and behaviour at the point cloud level (for example coverage, accessibility of hidden regions of the part surface, sampling representativeness, density, and spatial dispersion of the points with respect to the associated, reference surface). The ability to capture hidden surfaces of the part geometry, maximise the measurement coverage, and produce high-density point clouds represent increasingly challenging requirements that must be fulfilled by measuring instruments [14,15]. Therefore, in a context where the increased demand in manufacturing industries to deliver products of adequate quality and achieve optimised measurement results is strong, the integration at an algorithmic level into measuring instruments of new intelligent functionalities (defined in Chapter 1 and introduced in this thesis in form of performance indicators) plays a significant role into the measuring process [92,96].

Quantitative metrics are defined in the following sections, aimed at assessing the quality of individual high-density point clouds produced by optical technologies, and registered to the available *a priori* triangle mesh geometry. In order to define and evaluate the performances of the indicators, in this work measured points are assessed for quality by considering where they fall within the triangle mesh, specifically within individual triangle facets. Therefore, a point-to-triangle association strategy is illustrated, representing an essential aspect of the indicators' estimation method.

The definitions of the indicators and method developed to compute them are illustrated in this chapter as an extended version of a journal paper published in *Measurement* [97]. This work introduces the concept of quality indicators, performance measures designed to monitor fabrication processes and lead to the optimisation of production. The indicators presented in this chapter represent a novel contribution to the field, locally mapped to the measurand reference geometry (*i.e.,* triangle mesh), highlighting measurement behaviour in correspondence to diverse geometric features of the measured part. Implemented as built-in functions, performance indicators represent the primary means for developing intelligent measuring instruments, able to autonomously plan a measurement process and assess measurement performance while the inspection task is in progress.

4.2 Performance indicators definitions

The set of novel, formally defined indicators proposed in this chapter is designed to capture various aspects of measurement quality and instrument performance, addressing high-density optical measurements under multiple viewpoints. The proposed performance indicators are summarised in Table 4.1, and cover aspects related to: measurement effort (*i.e.,* time and resources needed for a complete measuring procedure, essential factor to consider when planning measurements); intrinsic properties of a point cloud (for example number of points, average point spacing); part coverage (*i.e.,* how much of the object surface is correctly acquired by the selected measuring instrument,

and, in addition, how effective the original measurement plan is); metrological performance of a measurement with respect to an associated geometry (for instance the Euclidean distance and dispersion of the distances of each point in the point cloud to their closest reference surface); the inspection of features of size using simple statistics (for dimensional characterisation, an indicator related to measurement bias is provided, using a more accurate measurement as reference).

Table 4.1 Single-cloud performance indicators

Covered aspect	**Intermediate computations**	**Performance indicator**
Measurement effort	-	• Acquisition time • Processing time
Intrinsic properties of the measured point cloud	-	• Number of points in the raw dataset • Number of points in the final point cloud • Point-to-point spacing
Part coverage	• Covered or uncovered triangles	• Sampling density (within each triangle) • Zero-coverage triangle • Coverage ratio • Coverage area ratio
Metrological performance	• Point-to-surface distance (within each triangle) • Statistics of the distribution of dispersion of signed distances to the triangle surface	• Dispersion of signed distances to the triangle surface
Features of size	-	• Standard and expanded uncertainty on features of size • Bias for features of size

Aside from measurement time, the proposed indicators are assessed at the point-cloud level, computed from a single measurement, and then locally mapped to the underlying registered geometry, assumed as available in form

of triangle mesh. The majority of the indicators allow for the generation of customised and detailed three-dimensional (3D) maps of measurement performance in correspondence to diverse surfaces of the part. Detailed definitions and further information on the indicators are illustrated in the following sections.

4.2.1 Measurement effort indicators

The measurement effort indicators capture the time and resources needed to carry out the measurements, from the acquisition of the original data as it is reproduced by the measuring instrument, to the achievement of the final point cloud, ready to be fed into the computational analysis pipeline adopted to implement inspection. The measurement effort indicators describe the performance of a complete measurement solution, including instrument utilised, measurement technology, operator, software, measurement set-up, data processing. The following indicators are defined:

acquisition time: time required to perform the measurement and obtain a point cloud. In this thesis, the terms "raw point cloud" or "raw dataset" indicate a point cloud that has not been processed in any way and it is considered "as-is", *i.e.,* as produced by the measurement instrument;

processing time: time required to perform processing on the raw point cloud to turn it into the "final point cloud", *i.e.,* a cloud suitable for form inspection and characterisation. Processing may include noise and isolated points removal (cleaning), deletion of anomalous points and removal of cloud regions capturing background surrounding the parts (for example for optical

technologies such as photogrammetry), utilising the methods described in the literature (see Section 2.2.3.2).

4.2.2 Indicators capturing intrinsic properties of the measured point cloud

These indicators capture properties of the point clouds that are independent of the geometry of the measured part, but dependent on the user's measurement planning and on the measurement technology employed. Different measuring instruments and technologies return data with different point counts (*i.e.,* number of points in the cloud, both in the original and in the processed point cloud) and average point-to-point spacing (*i.e.,* distance between two adjacent points). The following indicators are defined:

number of points in the raw dataset: number of points in the raw point cloud (*i.e.,* before any processing is applied);

number of points in the final point cloud: number of points in the cloud after processing (*i.e.,* cleaning, stitching and background removal);

point-to-point spacing: the average point spacing (PS) is defined as the mean distance between each point of the final point cloud and its closest neighbours, located within a sphere of radius r. The value of r is chosen in order to allow the selection of at least six neighbouring points within the specified limit (see Section 2.2.2.3 for neighbour search). If the point cloud is assumed as regularly distributed, PS is alternatively defined as the square root of the average area per point (*i.e.,* the area of a triangle in the mesh divided by the number of points it contains).

4.2.3 Indicators of part coverage

The part coverage indicators describe how much of the overall part surface is covered by the point cloud [166]. These indicators are designed to capture aspects such as the presence of occluded or otherwise unreachable surfaces, and/or the presence of differences in local point-sampling density across different surfaces of the part (lower local point density implies lesser coverage). For the computation of these indicators, the availability of a reference model in the form of triangle mesh is required (concept further discussed in Section 4.3.1). The following indicators are defined:

sampling density (within each triangle): density in point-based sampling defines the amount of data points per unit area (for example given for one square meter, hence unit $\mathrm{pts/m^2}$) at which the surface of an object is sampled. Therefore, sampling density SD_j per unit area simply describes the number of points n_{pts} associated with the j^{th} triangle (defined and indexed as $\mathrm{idx\_T}_j$) divided by the area A_j of the triangle itself, thus $\forall\, j : 1, \ldots, n_{\mathrm{tri}}$ with n_{tri} being the total number of triangles in the mesh

$$SD_j = \frac{n_{\mathrm{pts}}}{A_j}. \tag{4.1}$$

Considering the definition in Section 4.2.2 of PS point-to-point spacing, in case the point cloud is assumed as regularly distributed the relationship between SD and PS can be expressed as

$$PS = \sqrt{\frac{1}{(SD)}}. \tag{4.2}$$

Therefore, a highly dense point cloud will present small point-to-point spacing values. Point density does not represent the same concept as point-to-point spacing: the former is defined as points per square unit area, while the latter is expressed as a linear dimension;

covered or uncovered triangle: number of triangles whose sampling density is greater or equal to a given threshold value (indicated with n_{triC} covered) or less than the threshold (indicated with n_{triU} uncovered, including the number of triangles with zero sampling density n_{tri0}), where n_{tri} is the total number of triangles. An adequate threshold value is chosen by the user depending on application and measurement requirements. The classification of triangles into covered/uncovered area is used as an intermediate variable to compute coverage ratio and coverage area ratio (see following definitions);

zero-coverage triangle: triangle n_{tri0} with zero sampling density (*i.e.,* no measured points associated with the triangle);

coverage ratio: ratio between the number of covered triangles n_{triC} and the total number of triangles (*i.e.,* $n_{\mathrm{triC}} + n_{\mathrm{triU}}$) in the triangle mesh. Typically expressed as a percentage, thus

$$\kappa\% = \frac{n_{\mathrm{triC}}}{n_{\mathrm{triC}} + n_{\mathrm{triU}}} \cdot 100\,; \tag{4.3}$$

coverage area ratio: ratio between the total area of the covered triangles and the total area of all the triangles A_j with $j: 1, \ldots, n_{\mathrm{tri}}$ (*i.e.,* $n_{\mathrm{triC}} + n_{\mathrm{triU}}$) in the triangle mesh. Typically expressed as a percentage, thus

$$\kappa A\% = \frac{\sum \mathrm{A}_{n_{\mathrm{triC}}}}{\sum_{j=1}^{n_{\mathrm{tri}}} \mathrm{A}_j} \cdot 100\,. \tag{4.4}$$

4.2.4 Indicators of metrological performance making use of an associated triangle mesh

This class of indicators captures precision-related terms contributing to uncertainty (*i.e.,* dispersion-related terms, how close the measured values are from each other and how they differ from a fixed value, such as their average) of the measurement computed for each triangle facet. The suggested indicators act with respect to the surface of each triangle and their associated subsets of points, aiming to represent the local scatter (normal to each triangle facet) of values distributed around an average. The average distance values of all points from a triangle facet (to whom they are associated to) act as reference for dispersion computation, and represent a measure of the locations of the points with respect to the triangle itself. The following indicators are defined:

point-to-surface distance (within each triangle): signed or unsigned distance d_i between each point $\boldsymbol{p}_i$ with $i: 1, \ldots, n$ and its paired closest point $\boldsymbol{p}_i{}'$ on the associated triangle (see Section 2.2.7.2). In other words, in order to find the paired points, d_i is computed by: a) finding the closest point to $\boldsymbol{p}_i$ that lies on the triangle surface (identified with $\boldsymbol{p}_i{}'$), and b) computing the Euclidean distance between $\boldsymbol{p}_i$ and $\boldsymbol{p}_i{}'$. Point-to-surface distance is considered as an intermediate quantity needed to compute the indicators described thereafter;

dispersion of signed distances to the triangle surface: standard deviation of the signed point-to-surface distances computed on all the points associated with the triangle. This indicator describes the local precision of the measurement (single point cloud) within each individual triangle. Considering

x as the coordinate axis orthogonal to the triangle surface (normal to each triangle facet), x_i (equal to d_i) as the signed distance of each point $\boldsymbol{p}_i$ with respect to the triangle surface ($x = 0$), and n_{pts} the number of points associated with each triangle, dispersion (Figure 4.1) is defined as

$$s = \sqrt{\frac{1}{n_{\text{pts}} - 1} \sum (x_i - \bar{x})^2}, \tag{4.5}$$

where

$$\bar{x} = \frac{1}{n_{\text{pts}}} \sum x_i \tag{4.6}$$

is the mean distance to the triangle computed from all the points associated with the triangle itself;

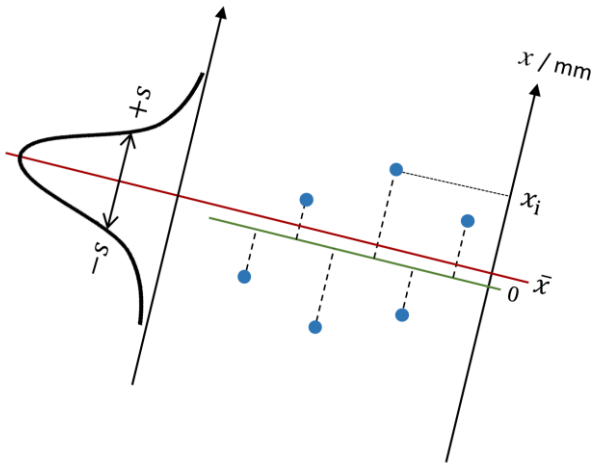

Figure 4.1 Dispersion of the signed point-to-surface distances to the triangle surface. x is the coordinate axis normal to the triangle facet, x_i is the signed distance of the i^{th} point (in blue) with respect to the triangle surface ($x = 0$, in green); $\bar{x}$ is the mean distance to the triangle computed from all points (in red)

statistics of the distribution of dispersion of signed distances to the triangle surface: the probability distribution is built with the dispersion of signed distance values computed for each triangle facet, *i.e.,* s_j for the j^{th} triangle, where s is defined by equation (4.5). The distribution is not an indicator per-se, but statistics computed on it are indicators, thus $\forall\, j : 1, \ldots, n_{\text{tri}}$

$$\text{mean}(s) = \frac{\sum_{j=1}^{n_{\text{tri}}} s_j}{n_{\text{tri}}}, \quad \text{mean of dispersion of signed distances over all triangles;} \tag{4.7}$$

$$\text{st.dev}(s) = \sqrt{\frac{1}{n_{\text{tri}}-1}\sum(s_j - \text{mean}(s))^2}, \quad \text{standard deviation of dispersion of signed distances over all triangles;} \tag{4.8}$$

$$\text{range}(s) = \left[\max(s_j), \min(s_j)\right], \quad \text{range of dispersion of signed distances over all triangles.} \tag{4.9}$$

4.2.5 Indicators for features of size

Geometric datums are used to infer geometric properties related to distance, length, parallelism, concentricity, *etc.* These datums are typically referred to as "features of size" [26]. The indicators described in this section are related to the inspection of those properties using simple statistics. For dimensional characterisation, an indicator related to measurement bias is provided, using tactile coordinate measuring system (CMS) as the reference (*i.e.,* more accurate measurement). The following indicators are defined:

standard and expanded uncertainty on features of size: the standard uncertainty on features of size [36] is defined here as the standard error of the mean computed on dimensions extracted by fitting point clouds to appropriate datums. Given N repeated measurements (point clouds) acquired with an optical measurement solution (indicated with M), and the N results for the feature of size dx indicated as $dx_1, dx_2, \ldots, dx_N$ computed from such point clouds, the standard uncertainty is defined as

$$u_{\mathrm{M}} = S_{\mu_{dx}} = \frac{s}{\sqrt{N}} \tag{4.10}$$

where $S_{\mu_{dx}}$ is the standard error of the mean and s is the sample standard deviation computed on the N repeats, *i.e.*,

$$s = \sqrt{\frac{1}{N-1}\sum\left(dx_i - \overline{dx}_{\mathrm{M}}\right)^2}. \tag{4.11}$$

The expanded uncertainty U_{M} is obtained by multiplying the standard uncertainty by a coverage factor k

$$U_{\mathrm{M}} = k \cdot u_{\mathrm{M}}\,, \tag{4.12}$$

where k provides a certain level of confidence (k is set to 2 in this thesis, providing a level of confidence of approximately 95%);

bias for features of size: as a consequence of the aforementioned definitions, the standard and expanded uncertainty on features of size indicators only capture the precision-related aspects of the measurement. For

the assessment of dimensional features, the bias term is computed by considering contact CMS values as more accurate references, thus

$$\text{bias}_{dx:(\text{M}-\text{CMS})} = (\overline{dx}_{\text{M}} \pm \tfrac{s}{\sqrt{N}}) - \overline{dx}_{\text{CMS}} \tag{4.13}$$

where $\text{bias}_{dx:(\text{M}-\text{CMS})}$ is the bias on the feature of size dx measured with measurement system M with respect to the reference contact CMS value, and $\overline{dx}_{\text{M}} \pm \frac{s}{\sqrt{N}}$ is the estimated population mean as obtained by considering N repeats with system M (*i.e.,* sample mean plus or minus standard error of the mean). In absence of a comprehensive metrological characterisation of the tactile CMS, maximum permissible error interval (±MPE) is used for a coarse estimation of the standard uncertainty for the contact CMS result, thus

$$\text{bias}_{dx:(\text{M}-\text{CMS})} = \left(\overline{dx}_{\text{M}} \pm \frac{s}{\sqrt{N}}\right) - \left(\overline{dx}_{\text{CMS}} \pm \text{MPE}\right). \tag{4.14}$$

Alternatively, it is possible to employ the definition as illustrated in ISO 22514-7 [240] for the estimation of the coarse standard uncertainty component, calculated as $u_{\text{MPE}} = \text{MPE}/\sqrt{3}$ for the tactile CMS (see later Section 5.3.2).

4.3 Indicators estimation method

The method developed for the estimation of the performance indicators is based on the analysis of individual high-density point clouds finely aligned to the underlying registered geometry in form of triangle mesh, following the registration process presented in Chapter 3. The proposed strategy allows to tag the point cloud in regions of interest that have specific measurement requirements (for example coverage, and precision of critical areas) in correspondence to associated triangles, exploiting the *a priori* knowledge of the available mesh model identified as reference datum.

In the following sections the characteristics and appearances of the datasets (*i.e.,* measured point cloud and triangle mesh) are described, in addition to the proposed association strategy of each registered point with its closest triangle facet.

4.3.1 Input datasets and initial indicators collection

Optical measurement solutions are able to produce multiple point clouds, for example when the acquisition of a part occurs from multiple probing directions. However, as a requirement of the proposed method, the measurement result of a scanning procedure needs to be available as a single point cloud. Therefore, the data are processed and stitched into a single set, cleaned from artefacts captured from the background of the scene and isolated points. Furthermore, particularly in correspondence of areas where two or

more scans have been stitched together, the final point cloud needs to be homogenised in terms of local density.

The time required for the aforementioned data processing actions is calculated and thus expressed by the measurement effort indicators, defined in Section 4.2.1. The number of points available pre and post processing are at this stage computed and compared (see definitions in Section 4.2.2).

As previously mentioned, the final point cloud is registered to a nominal part geometry, required for the definition of the indicators (in particular those related to part coverage and metrological performance, respectively defined in Sections 4.2.3 and 4.2.4) in the form of a triangle mesh. The choice of using a triangle mesh may appear as a limitation given the approximation of the form into triangles, especially in situations where the part to be measured is a freeform complex geometry. However, the method is designed to be applied to parts fabricated by additive manufacturing (AM) technologies, usually printed from already triangulated geometries, and computations which converge to results of continuous geometry can be achieved. In addition, the navigation of the topology of a part surface is easier if the latter is defined by triangles, given the information of faces connectivity stored in a mesh file format.

4.3.2 Cloud-to-mesh association strategy

Once the processing of the datasets (including their registration) is completed and the initial sets of performance indicators are collected (*i.e.,* those related to measurement effort and intrinsic properties of the point cloud), a cloud-to-

mesh association pipeline is defined, returning as a result the evaluation of which points in the point cloud refer (*i.e.,* are associated) to which triangle in the mesh. It is worth pointing out that in order to contain the computational complexity encountered during the estimation of the cloud-to-mesh associations and consequent later computation of the performance indicators (for instance of coverage and density), the number of triangles composing the original mesh might be reduced by simplification [140] (see specifically the example application shown in Chapter 6), decimating the number of triangle faces whereas maintaining at the same time unaltered the shape of the part This process is not yet integrated in the automated pipeline, it is done instead using the external software Blender [241] when required.

The procedure is shown in Figure 4.2 and outlined as follows:

- point cloud normals computation (Figure 4.2.a);
- point cloud normals intersections with triangle facets (ray casting, *i.e.,* projecting a grid or rays onto a triangle mesh - Figure 4.2.b);
- some of the intersections are flagged as invalid (*i.e.,* identification of points in the point cloud that lie within a certain distance from a triangle - Figure 4.2.c) following two criteria:
  1) distribution of the distances for outlier rejection (*i.e.,* the distance of the intersection is a statistical outlier ($\mu \pm 3\sigma$) with respect to the other distances – see Section 2.2.3.2);
  2) hardcoded rejection threshold (*i.e.,* the distance of the intersection is larger than a threshold value);

- storing information of the associations (including n_{pts} number of points associated with the j^{th} triangle, and its area A_j) and colour map representation of the associations (Figure 4.2.d).

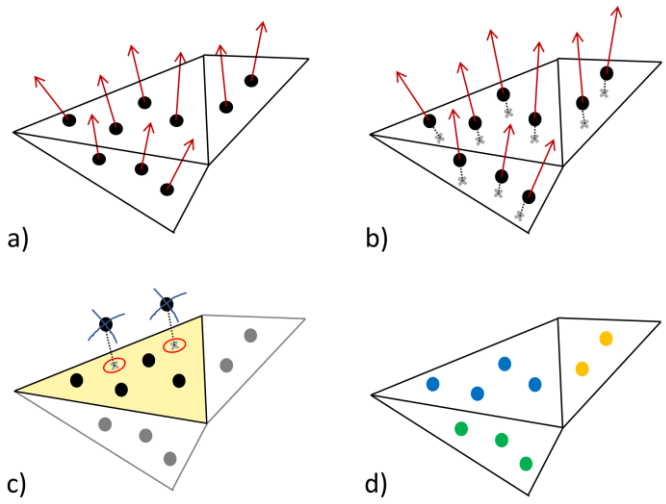

Figure 4.2 Cloud-to-mesh association pipeline: a) normal vectors (in red) computed to the points, b) ray casting technique and intersections (in grey, projections of points onto the surface of each triangle along the direction of the normal vectors) of points with their paired closest triangles, c) thresholding of points (crossed in blue) too distant from a selected triangle (in yellow) and their intersections with the triangle flagged as invalid (circled in red), d) valid intersections represented with different colours for points belonging to different triangles

From the registered point cloud, the normal vectors to each point is computed via principal component analysis (PCA), as shown in Figure 4.2.a. In order to apply PCA, for each point a local subset of neighbouring points is selected via the *k*-nearest neighbours (*k*-NN) algorithm, then PCA is performed as it is previously described in Section 2.2.4.1. The normal orientations are fixed by using the minimum spanning tree method, so that they all point towards the same direction (EMST, see Section 2.2.4.1).

Once the normals to the points are computed, their intersections with the triangle mesh are estimated using ray casting (Figure 4.2.b), known in 3D computer graphics [123,242]. Ray casting considers the computation of the intersections of rays (*i.e.,* identified by the local normal vectors from each point in a cloud) with each triangle facet in a mesh. The projection $\boldsymbol{p_i}'$ of a point $\boldsymbol{p_i}$ in a point cloud onto the surface of a triangle mesh (*i.e.,* the intersection point along the direction of the normal vector $\boldsymbol{n_i}$) could fall into the boundaries of a specific triangle, or lie outside and belong (*i.e.,* be associated and registered) to an adjacent triangle. In case of a complex geometric shape, the projection $\boldsymbol{p_i}'$ could intersect a triangle belonging to a different surface of the part that is in the direction of vector $\boldsymbol{n_i}$. On this account, a ray may intersect more than one triangle (known as collision detection problem of determining the first object intersected by a ray [243]); the algorithm identifies the first intersection of the query point to the closest triangle facet as the correct association. Some of the computed intersections can be considerable as invalid, for example in correspondence of floating-point approximations, or points affected by registration error. Therefore, a strategy to discriminate the false intersections is adopted following two criteria: initial thresholding based on outlier detection and hardcoded distance rejection (Figure 4.2.c).

In order to test if a ray intersects a triangle in the mesh, the algorithm tests each individual triangle against the ray. Therefore, the main issue in this procedure is given by the computational time, linearly dependent on the number of triangles in the 3D scene. As a support of the aforementioned issue, the algorithm calculates the points positions with respect to specific triangles

based on Euclidean distance (see Section 2.2.7.2). Registered points that are too distant from any triangle are classified as isolated and excluded. In addition, an acceleration structure is employed, encoding the mesh into an axis-aligned bounding box (AABB) tree (see Section 2.2.2.1), shown for example in Figure 4.3. Once the information of the associations point-to-triangle are correctly stored, a colour map representation of these associations can be rendered for verification purposes, tagging points belonging to different triangles with distinct colours (shown in schematic form in Figure 4.2.d and using a real mesh test case in Figure 4.4).

Table 4.2 shows how the algorithm stores the point-to-triangle associations information. From the associations, the computation of the number of points n_{pts} associated with each j^{th} triangle is therefore immediate, enumerating the amount of obtained point-to-triangle intersections.

Table 4.2 Point-to-triangle associations

Point in the point cloud	x_p	x coordinate of point $\boldsymbol{p}_i$
	y_p	y coordinate of point $\boldsymbol{p}_i$
	z_p	z coordinate of point $\boldsymbol{p}_i$
Associated triangle	idx_T_j	Closest indexed triangle facet to the query point $\boldsymbol{p}_i$ (the closest triangle intersected by the normal vector $\boldsymbol{n}_i$ to $\boldsymbol{p}_i$), with $j : 1, \dots, n_{\text{tri}}$ where n_{tri} is the total number of triangles
Distance point-to-triangle	d_i	Euclidean distance between point $\boldsymbol{p}_i$ and its closest triangle (if the distance is greater than a threshold value, the point is rejected), with $i : 1, \dots, n$
Intersection point (projected)	${x_p}'$	x coordinate of point ${\boldsymbol{p}_i}'$
	${y_p}'$	y coordinate of point ${\boldsymbol{p}_i}'$
	${z_p}'$	z coordinate of point ${\boldsymbol{p}_i}'$
Triangle area	A_j	Area of the associated triangle, $\forall\, j : 1, \dots, n_{\text{tri}}$
Number of intersections	n_{pts}	Number of points associated with each j^{th} triangle

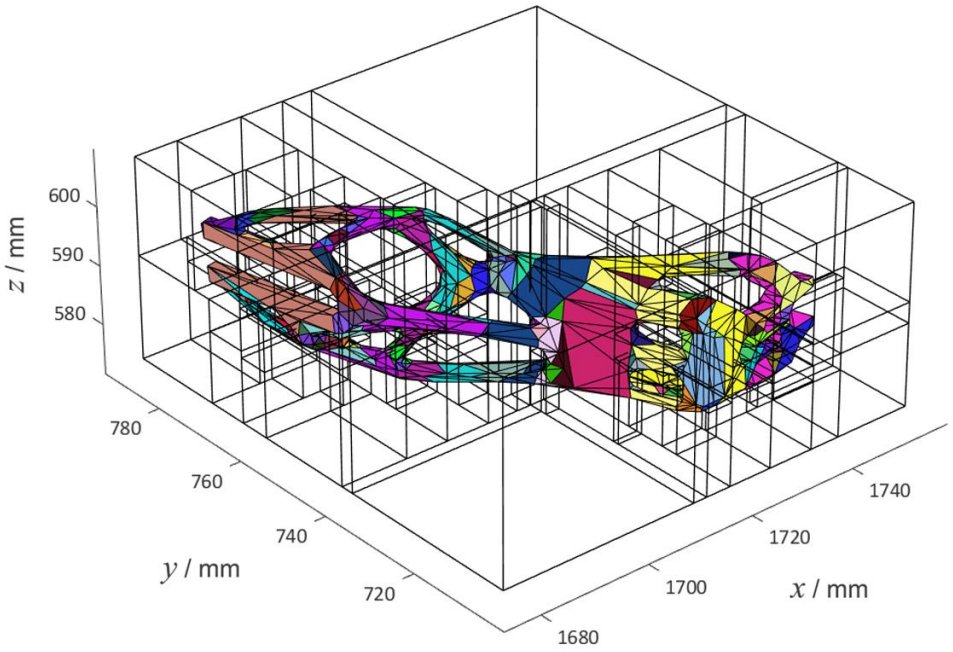

Figure 4.3 An example triangle mesh (roof bracket; part designed and kindly provided by BMW Group) is encoded into an AABB tree and decomposed into partitions; different colours correspond to different leaves of the tree

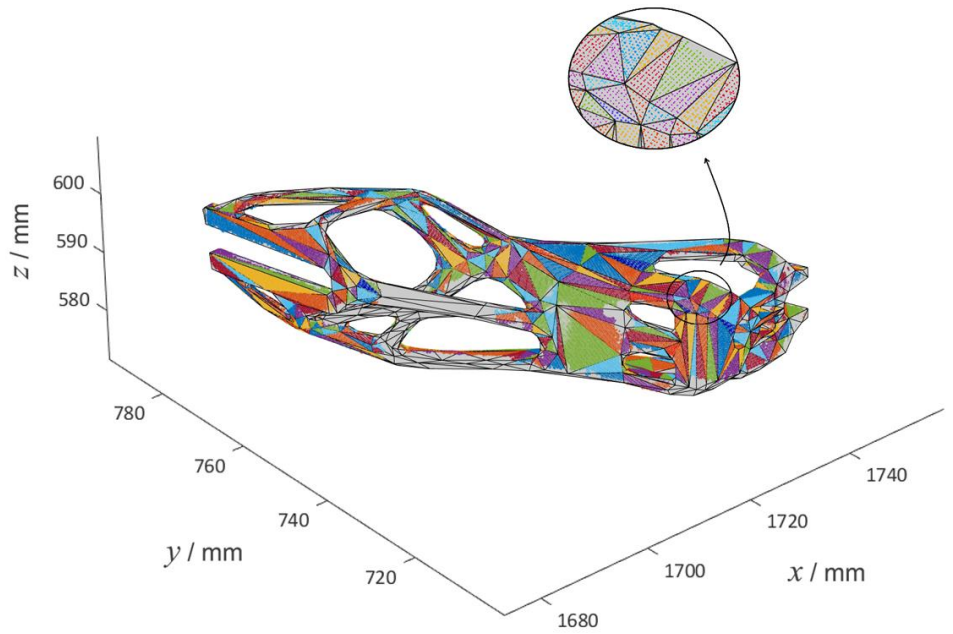

Figure 4.4 3D points associated to triangle mesh: from the colour map representation of the associations it is possible to visually identify and tag points belonging to specific triangles (different colour correspond to different associations)

Once the relevant information is obtained, the remaining performance indicators (*i.e.,* those of part coverage and metrological performance) can be computed and represented in graphical form through colour maps overlaid to the triangle mesh. Triangles are tagged with different colours according to the indicator selected. For instance, covered and uncovered triangles are indicated with a binary colouring representation, where green areas refer to triangles where the required point density has been achieved; red areas refer to regions with insufficient coverage (Figure 4.5).

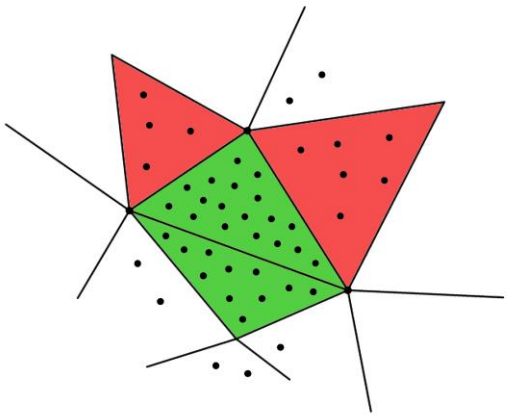

Figure 4.5 Schematic representation of a triangle mesh with overlaid colour map. Covered triangles (*i.e.,* with required point density and associated point) are indicated in green, while uncovered ones are indicated in red

4.4 Chapter conclusions

Measurement performance can be evaluated through multiple viewpoints, and not necessarily be limited to uncertainty assessment on dimensional results. As a contribution to the definition of measurement quality in its broader terms, the work illustrated in this chapter aimed at describing performance of

high-density optical form measurements through a series of custom-defined, quantitative performance indicators. These indicators could be computed algorithmically at a point cloud-level, starting from the measured dataset finely registered to the nominal geometry in form of triangle mesh. The association of data points with areas of the reference model acted as necessary element for the development of the method proposed for the estimation of the indicators.

Several aspects of measurement quality have been addressed: the measuring time and efforts needed for the acquisition and processing of the data (for example execution speed), and the intrinsic properties of the point cloud itself (for instance average point spacing and point count). Some of the designed indicators addressed coverage percentage, referring to extents of the surface regions covered by the point cloud, extents and positions of the neglected regions, sampling densities in the covered areas. In addition, some indicators were designed to cover aspects related to measurement error, though mostly related to precision, given that the computation relied solely on the measured dataset and the nominal geometric model. Indicators for the inspection and verification of features of size were defined, related to the computation of standard and expanded uncertainty. Furthermore, a bias term was defined considering the availability of a more accurate measurement that could act as reference.

The quality indicators proposed aim at allowing for planning more optimised, additional measurement processes, and can also be used as a starting point for the development of future intelligent measurement systems. By comparing the collected point clouds to the available mesh geometry, the

system will be able to analyse point by point the dispersion of the measurements, as well as return feedbacks of any extra scan views required, locating occlusions or areas needing more data to satisfy sampling density criteria. Furthermore, the original set of indicators represent a useful starting point for anyone wanting to compare measurement solutions under multiple viewpoints, performing quantitative comparisons.

Results and graphical representations of the indicators are later reported in Chapter 6 and Appendix A, applied to a selected industrial case (metal additively manufactured roof bracket previously illustrated in Chapter 3 as sample A, designed and kindly provided by BMW Group), measured using different optical technologies.

In the following chapter, a second set of indicators will be presented, aiming at investigating how measurement error is spatially distributed on different surfaces of a measured part. The indicators, derived from a novel statistical model of point positional uncertainty, will describe the local properties of a measurement, addressing the variability in the position of the points in a point cloud. As well as the indicators described in Chapter 4, the quality criteria discussed in Chapter 5 will be developed from the pre-defined registration strategy previously described in Chapter 3.

Chapter 5

Statistical point cloud model and related indicators

5.1 Overview

In Chapter 4, a set of quality indicators has been defined and computed on high-density point clouds, derived from single measurements. The indicators were designed to capture various aspects of the measurement pipeline including measurement time, surface coverage, density of point-based sampling, dispersion of the point-to-surface distances, and inspection of features of size.

As previously noted, the most common methods found in literature to describe point positional variability (*i.e.,* positional uncertainty in point

clouds) are expressed in probabilistic terms, but the research in these regards is at its beginning. Therefore, as a novel contribution to the metrology field, this chapter illustrates the development of a statistical point cloud model used to propose a novel approach for the investigation of the precision of measurements (*i.e.,* random error in repeatability/reproducibility conditions) based on fitting Gaussian Random Fields (GRFs) to high-density point clouds produced by optical measurement repeats. Then, a set of novel performance indicators are derived from the model.

The suggested approach focuses on the investigation of the positional uncertainty of each point in a point cloud. In this thesis, point clouds positional uncertainty refers to a lack of knowledge of where each point of the point cloud is located in three-dimensional (3D) space, with respect to where it should be assuming an ideal measurement (*i.e.,* a measurement without error). Differently from well-established methods used to evaluate measurement uncertainty (previously discussed in Section 2.1.1.1), the sources of error that compose a classical uncertainty budget, such as errors coming from the physics of the selected measuring instrument, or errors due to variations in the surrounding conditions of the measurement environment, are not investigated in this thesis. The method developed in this work covers:

a) the development of a statistical model built solely from measurement repeats (no modelling of error sources, nor from physics-related considerations);

b) the developed model addresses point clouds positional uncertainty and does not address the uncertainty on features of size or other geometric properties derived from the point cloud. However, the uncertainty of

features of size or other geometric properties can be procedurally derived from the model.

The indicators derived from the statistical point cloud model aim at proposing new means for the spatial mapping of measurement error, and can be implemented in a smart measurement system if the underlying measuring technology allows to acquire multiple measurement repeats effortlessly and fast. However, even when measurement repeats are not convenient (for example when day-to-day measurement operations are required), this set of indicators can represent useful means in preliminary experimental campaigns, and provide insights on the interaction between the measurement system and the measured part.

The material presented in this chapter is the result of a collaboration with Professor Nicola Senin from the Faculty of Engineering of the University of Perugia and it is illustrated in the journal publication [210] in *Precision Engineering*.

5.2 Statistical point cloud model

As indicated in the literature (see Section 2.2.8.1), uncertainty associated to point clouds is either defined in 3D around each point or associated to a displacement in the direction defined by the local surface normal. For the development of the mathematical model presented in this chapter, the positional uncertainty of each point is considered as following the latter

approach, modelling the uncertainty as a scalar quantity measured along a specific directional vector.

In planar datum fitting, point displacements orthogonal to the plane influence the fitting result more than displacements on the plane itself [171]. This consideration specifically applies to high-density point clouds, typical outputs from optical coordinate measuring systems (CMSs). On the contrary, if the point cloud was low-density, for example as measured by tactile CMS, then fewer points would be used to fit each geometric entity, and the position of individual points, as measured in all directions, would typically be more relevant for dimensional and geometric inspection and verification [211,212]. From these observations, it was decided to model positional uncertainty as a scalar value directed along the local normal vector to a point. The choice implies that the most relevant positional deviation of each point is assumed as the one measured orthogonally to the local surface fitted through that point. Therefore, as it is shown in Figure 5.1, positional uncertainty is expressed in this work as a unidimensional interval, and the distance of each real point with respect to its ideal counterpart (*i.e.,* that obtained with no measurement error) is expressed by a scalar value.

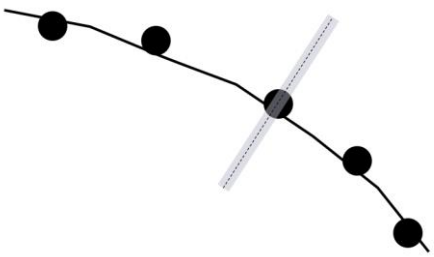

Figure 5.1 Positional uncertainty is expressed as a one-dimensional model: uncertainty modelled as a scalar value, directed along the surface local normal

As stated in Section 5.1, the mathematical model proposed in this chapter assumes the positional uncertainty of each point in the point cloud as solely caused by the measurement error. The measurement error at each point in a point cloud can be modelled as a random variable. The collection of the random variables corresponding to each point in a point cloud is called random field [244]. From a random field assumed as Gaussian (see later Section 5.2.1) and fitted to measurement repeats (see later Section 5.2.2) it is possible to derive the spatial distribution of the random components of the measurement error, and only those random components that are visible through measurement repeats, providing information of the local scatter of the points. Therefore, for each measurement a probability interval is computed in order to assess where each specific point will fall in space from a hypothetical mean value. Furthermore, the final model can incorporate an additional component representative of constant bias, introduced via the use of more accurate measurement or external mathematical models, in order to obtain a complete, spatial uncertainty map.

5.2.1 Definition of discrete Gaussian random fields

Each point in a point cloud is associated to a random variable. Since the points present finite spacing from each other, these random variables can be modelled as a (discrete) random field. N random variables for N points form a finite and countable set. As shown in Figure 5.2, each random variable Z_i in the random field (with i index of the point in the point cloud) is associated with an origin point $\boldsymbol{o}_i$ and to a directional vector (represented by the local

surface normal $\boldsymbol{n_i}$) that define a local coordinate system (z_{loc}). The origin point $\boldsymbol{o_i}$ acts as the location of the random variable in the 3D space, and is also needed to set a reference zero ($z_{loc} = 0$) in the local coordinate system. The position of the origin point $\boldsymbol{o_i}$ along the local normal is not necessarily meant to represent the result of an ideal measurement. The purpose of $\boldsymbol{o_i}$ and $\boldsymbol{n_i}$ is to map the scalar value of the random variable into a one-dimensional interval aligned to the direction along which the positional uncertainty of each point is supposed to be captured.

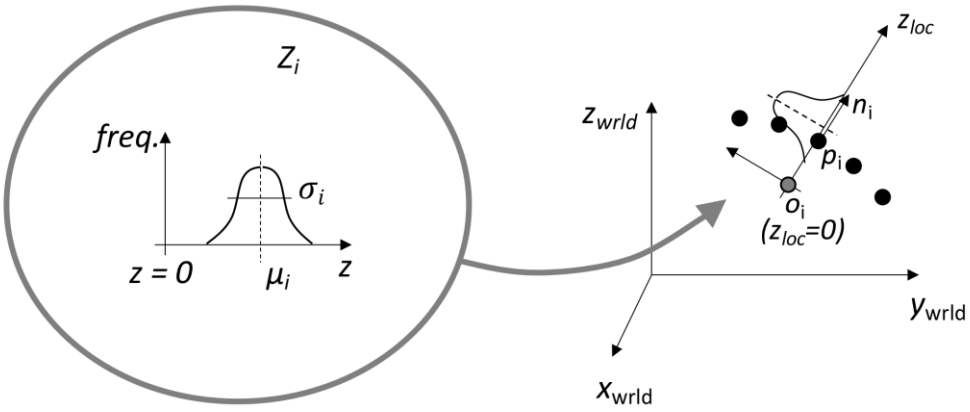

Figure 5.2 The i^{th} variable Z_i of the random field is associated to the point $\boldsymbol{p_i}$. The random scalar value is mapped to the 3D point cloud space through an origin point $\boldsymbol{o_i}$ (location) and an orientation vector defined by the local normal $\boldsymbol{n_i}$

The discrete random field is assumed as Gaussian. In a Gaussian random field (GRF), each random variable is defined by a normal distribution, and each subset of M random variables extracted from the field of N variables is also defined by a normal, multivariate (*i.e.,* M-dimensional) joint probability distribution. A Gaussian discrete random field of N variables $\{Z_1, Z_2, \cdots, Z_N\}$ is fully defined by a vector of mean values $\boldsymbol{\mu}$ (*i.e.,* N first order moments) and

a matrix $\mathbf{K}$ of covariance values (*i.e.,* $N \times N$ second order moments) covering all the pairwise associations between variables belonging to the field. The mean values $\boldsymbol{\mu}$ and the matrix $\mathbf{K}$ of covariance values are defined as follows

$$\boldsymbol{\mu} = \{\mu_1, \mu_2, \cdots, \mu_N\}, \tag{5.1}$$

$$\mathbf{K} = \begin{bmatrix} k_{1,1} & \cdots & k_{1,N} \\ \vdots & \ddots & \vdots \\ k_{N,1} & \cdots & k_{N,N} \end{bmatrix}, \tag{5.2}$$

where μ_i is the mean of Z_i, $k_{i,j}$ is the covariance of the pair Z_i, Z_j and $k_{i,i}$ is the variance of Z_i ($\mathbf{K}$ is symmetric, so $k_{i,j} = k_{j,i}$). The random field $\boldsymbol{Z(\mu, K)}$ can be associated to a point cloud of N points: $\{\boldsymbol{p}_1, \boldsymbol{p}_2, \cdots, \boldsymbol{p}_N\}$ and local normals $\{\boldsymbol{n}_1, \boldsymbol{n}_2, \cdots, \boldsymbol{n}_N\}$ through a series of origin points $\{\boldsymbol{o}_1, \boldsymbol{o}_2, \cdots, \boldsymbol{o}_N\}$ to set the zeros of the random variables. The formulation indicates that the positional uncertainty of each point $\boldsymbol{p}_i$ is described as a scalar quantity, and mapped to a vector field, defining the point position and orientation. Therefore, the local normals $\boldsymbol{n}_i$ and the origin points $\boldsymbol{o}_i$ define a spatial mapping between the scalar random field, representing local height (Z) as random variables over a flat space, and a full 3D surface defined by a series of points and their local normals. The set $\{\boldsymbol{o}_i, \boldsymbol{n}_i\}\ \forall i \in \{1, \ldots, N\}$ is therefore the vector field which allows mapping of a GRF of scalar quantities into the 3D space of the part. Figure 5.3 shows that the formulation defined above can be adopted for various geometric datasets, ranging from height/elevation maps (all heights defined along a single direction - Figure 5.3.a) to full 3D

point clouds or vertex meshes (Figure 5.3.b) where local heights are arbitrarily oriented in space.

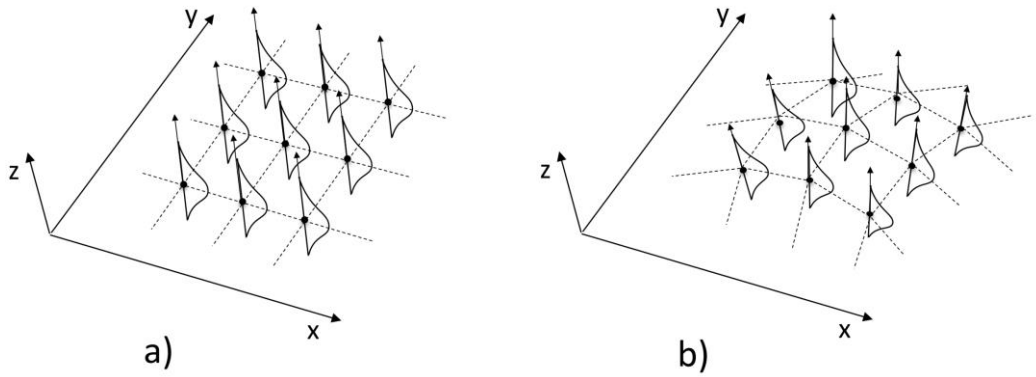

Figure 5.3 Discrete random field and its spatial mapping. Same formulation for a) height maps and b) 3D point clouds

Only one observation (point in the point cloud) for each random variable is obtained if only a single measurement is available. In this case, the available observational data is insufficient to fully determine the mean vector $\boldsymbol{\mu}$ and covariance matrix $\mathbf{K}$. In order to address the issue, typical assumptions are made (see the literature on Gaussian processes [244,245]), and for instance the concept of shift-invariance is used. Shift-invariance implies that the mean and variance are considered independent of position in space, and covariance is considered only dependent on the relative distance between the random variables [245]. Mean and variance are constant, and covariance is defined using kernel functions, only dependent on the relative distance between each pair of variables [246]. Shift-invariance typically implies that all the random variables have the same mean and same variance, so the local properties of the field are the same everywhere. Following this assumption, shift-invariance

reduces the complexity of the fitting problem, which can be solved, for example, via maximum likelihood estimation [245].

5.2.2 Gaussian random field fitting and generation of new point clouds

The approach proposed in order to solve the GRF fitting problem relies on the availability of measurement repeats: multiple point clouds obtained from the same surface result in multiple observations for any given location, as shown in Figure 5.4.a. Unfortunately, neither the existence of multiple points in correspondence to the same normal nor the alignment of local normals from different clouds can be achieved in practice (Figure 5.4.b), despite the high density of points. Given the aforementioned issues, the approach proposed in order to achieve a result similar to Figure 5.4.a relies on the following key factors:

- availability of a CAD model (for example, in form of an STL triangle mesh) to drive the alignment of the point clouds;
- use of one of the point clouds as the reference to define the resampling locations (*i.e.,* the locations at which the GRF is defined) and the local normals;
- resample the other point clouds at the intersections with the local normals using linear interpolation (Figure 5.4.c);
- intersect the local normals with the CAD surface; the intersections define the origin points to which the local z values of each random variable are referred.

Using this procedure, as many observations for the Z_i random variable are produced as the number of available measurement repeats (Figure 5.4.d).

The choice of assuming one of the point clouds as reference in terms of localisation and orientation is an element of arbitrariness of the proposed method, as any other point cloud could be used (including any other reference set, for example, sampled directly from the CAD surfaces). Furthermore, considering the points from the CAD surface as origin points does indeed convert all the other points into distances from the nominal surface. However, such distances are not meant to be considered as measurement error, since there is no information on how much the real surface deviates from the nominal one.

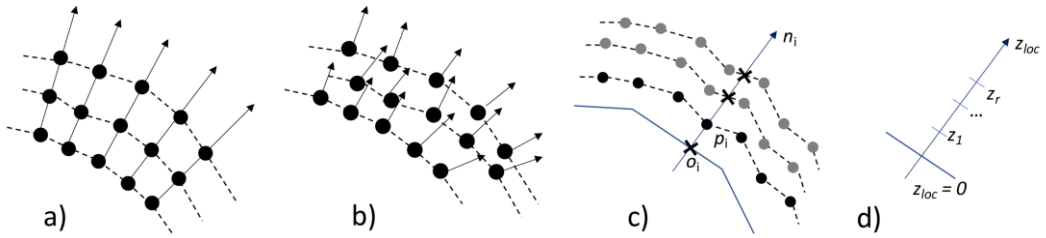

Figure 5.4 Portion of three measurement repeats used to create observations for each random variable Z_i (the points of each cloud are rendered as connected by an imaginary, dotted line). a) Ideal scenario: at any given location, observations from multiple clouds are natively available and all share the same local normal; b) real scenario: points from different repeats will not be aligned at shared locations, and each point may have a potentially different normal if computed using neighbours in the same cloud; c) proposed solution: the points of one cloud act as reference locations (*e.g.* $\boldsymbol{p}_i$); the local normal computed for $\boldsymbol{p}_i$ (*e.g.* $\boldsymbol{n}_i$) is used as reference direction; the other point clouds are resampled by interpolation at the intersections with the local normal; the intersection of the local normal with the CAD surface is assumed as the origin point $\boldsymbol{o}_i$; d) the computation produces multiple observations for the Z_i random variable in its local coordinate system z_{loc} (the entire process is repeated for each point of the reference point cloud)

After resampling is performed on R measurement repeats (point clouds), R observations $z_{i,r},\ \forall r \in \{1,\cdots,R\}$ are available for each random variable Z_i. These observations are referred to a local origin point $\boldsymbol{o}_{\mathrm{i}}$ ($z_{loc}=0$) on the CAD surface, and act as a random sample to describe Z_i, and there are as many samples as the number N of random variables in the GRF. If the random variables of the field can be considered as independent with each other, the full covariance matrix does not need to be solved, and the fitting problem is reduced to a determination of the mean vector $\boldsymbol{\mu}$ and the variance terms $k_{i,i}$ in the principal diagonal of the covariance matrix $\mathbf{K}$ (other covariance terms being zero). By adopting this approach each random variable can be estimated separately, starting from its first and second order moments, by simply using the observations available at each location [216]. In this situation, each sample mean

$$\bar{z}_i = \frac{\sum_{r=1}^{R} z_{i,r}}{R} \tag{5.3}$$

can be used as an estimator of the corresponding population mean μ_i in the vector $\boldsymbol{\mu}$. The covariance matrix $\mathbf{S}$ of the sample, defined by the terms $s_{i,j}$ for the pair of random variables Z_i, Z_j, is expressed as

$$s_{i,j} = \frac{\sum_{r=1}^{R}(z_{i,r}-\bar{z}_i)\cdot(z_{j,r}-\bar{z}_j)}{R}. \tag{5.4}$$

The covariance matrix $\mathbf{S}$ of the sample is not a good estimator for the covariance matrix $\mathbf{K}$ of the GRF (*i.e.*, each sample covariance term $s_{i,j}$ is not

a good estimator of the population covariance term $k_{i,j}$) because the number of dimensions in the random variables (*i.e.,* the number of points N in the field) is much larger than the number of observations R available for each point (*i.e.,* the number of repeats). Therefore, in this thesis $\mathbf{K}$ is estimated adopting the oracle shrinkage approximating estimator of the covariance, as detailed elsewhere [247].

The first use of the statistical model is to investigate how random measurement error is spatially distributed on the different surfaces of a part. Spatial maps representing the mean function and the variance as estimated by the statistical model can be obtained, as it is illustrated in simplified form in Figure 5.5. Variance describes local scatter of the measurement orthogonal to the underlying surface, taking into account any spatial dependency which may exist between neighbouring measured points. The mean function indicates central tendency of the measurement, *i.e.,* the most frequent localisation of the point cloud with respect to any specific surface region on the underlying CAD model. The interpretation of central tendency is particularly critical, because any non-zero displacement of the mean function with respect to the underlying CAD surface may be due to either measurement bias, or the real part being different from the nominal model (due to manufacturing error) or, most commonly, due to both aspects. Further discrimination is not possible because the statistical model is based on measurement repeats and, therefore, it cannot capture any error component that is invariant across repeats.

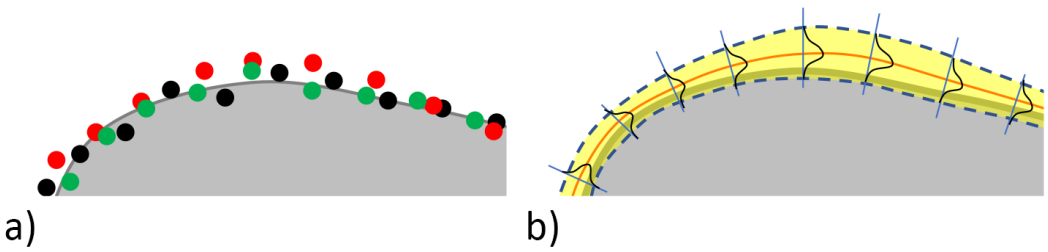

Figure 5.5 Schema of the type of information which can be obtained from the use of the proposed statistical modelling approach (simplified in two-dimensions). a) Original measurement repeats (point clouds, each repeat is shown in a different colour) in relation to the associated CAD model of the part (grey); b) spatial map of the mean (red line) and variance (yellow band) of the statistical model fitted on the point clouds. The yellow band is an interpolation of local $\pm 3\sigma$ values computed on the marginal probability distributions of the local random variables of the GRF

Another use of the proposed statistical modelling approach is to generate new "virtual" point clouds. Once the fitting of the GRF is concluded, a new set of values $\{z_1, z_2, \ldots, z_N\}$ for all the random variables in the field is generated (referred to as new realisation of the random field or new observation). These scalar values can be mapped back into 3D space and generate a new point cloud. The new realisation of the random field can be obtained by applying the Cholesky decomposition on the covariance matrix $\mathbf{K}$ [244]. The Cholesky decomposition of $\mathbf{K}$ (assumed Hermitian, positive-definite) leads to a lower triangular matrix $\mathbf{L}$ so that

$$\mathbf{K} = \mathbf{L}\mathbf{L}^{*} \tag{5.5}$$

where $\mathbf{L}^*$ is the conjugate transpose of $\mathbf{L}$. Assuming $\mathbf{K}$ is symmetric (which is the case for the variance-covariance matrix), then $\mathbf{L}^*$ is simply $\mathbf{L}^\mathbf{T}$, and because $\mathbf{K}$ is real-valued, $\mathbf{L}$ is also real. Then, each scalar value $z_{i,new}$ representing a component of the new realisation of the field, can be obtained as

$$z_{i,new} = \mu_i + N(0,1)\mathbf{L} \tag{5.6}$$

where μ_i is the i^{th} entry in the vector of means $\boldsymbol{\mu}$ and $N(0,1)$ is a new observation drawn from a standard normal (zero mean and unit variance).

Once all of the $z_{i,new}$ values have been obtained, the new point cloud, constructed from points $\{\boldsymbol{p}_{1,new}, \boldsymbol{p}_{2,new}, \dots, \boldsymbol{p}_{N,new}\}$, can be obtained by mapping each $z_{i,new}$ value back into the 3D space of the point cloud, *i.e.,*

$$\boldsymbol{p}_{i,new} = \boldsymbol{o}_i + z_{i,new} \cdot \boldsymbol{n}_i \tag{5.7}$$

where $\boldsymbol{o}_i$ is the i^{th} local origin point and $\boldsymbol{n}_i$ is the local normal.

5.3 Derived indicators

Definitions of performance indicators directly computed from the GRF and indicators derived from new observations generated from the GRF are discussed in the following sections. The indicators defined in this chapter rely on the availability of repeated high-density measurements (either real or simulated). The indicators are summarised in Table 5.1.

Table 5.1 Indicators derived from statistical point cloud model

Covered aspects	**Performance indicator**	**Notes**
GRF-derived indicators	• Local point dispersion • Local bias • Spatial maps of variance • Spatial maps of local bias	Class of indicators computed directly from the properties of the GRF. Most of these indicators (generated from the "field") are spatially mapped
Indicators based on new obs. generated from GRF	• Probability distribution of features of size • Bias for features of size	Indicators computed on new observations generated via Monte Carlo simulation from the GRF (*e.g.* computed on selected features of size)

5.3.1 GRF-derived indicators

This class of indicators is computed directly from the properties of the GRF defined in Section 5.2.1. The indicators refer to the local point scatter in the direction defined by the local reference normals capturing the dispersion of the points across measurement repeats, and to local bias, assuming the availability of a more accurate model or measurement to be considered as

reference. Additionally, spatial colour map indicators are defined consisting of a collection of values (*i.e.,* "map" of values) associated to spatial locations. Such map can be conveniently visualised using artificial colouring, in order to favour understanding via visualization and can be useful to investigate instrument behaviour and performance in correspondence to specific form features on the measured part. The following indicators are defined:

local point dispersion: this indicator is obtained directly from the fitted GRF on a series of measurement repeats. It captures the dispersion of the points (*i.e.,* measure of how close a set of values in a probability distribution are from each other), and therefore provides information about local point scatter in the direction defined by the local reference normals (*i.e.,* the extent to which a distribution is stretched or squeezed in the direction defined by the local reference normals, using the surface of the CAD as zero reference). Central tendency (*i.e.,* central value or average for a probability distribution) defined by the vector $\boldsymbol{\mu} = \{\mu_1, \mu_2, \cdots, \mu_N\}$ is expressed with reference to the vector of origin points $\mathbf{o} = \{o_1, o_2, \cdots, o_N\}$, typically computed from intersections with the CAD surface;

local bias: this indicator describes the local bias defined as the local distance between the GRF fitted to a series of measurement repeats and the GRF fitted to reference measurements identified as more accurate (*i.e.,* distance between the averages of two locally fitted GRFs). Alternatively, local bias can be computed using mathematical models, without the need for a second GRF. However, in absence of such mathematical models, bias with respect to an ideal measurement cannot be estimated starting from a single GRF, because central tendency as captured by $\boldsymbol{\mu}$ is referred to the nominal

model, and may not necessarily be representative of the real part that has been measured (for example, if the real part is warped with respect to the nominal geometry). In order to incorporate bias, two alternative routes can be followed:

a) a mathematical model capable of producing a bias value and associated uncertainty interval, mapped to each location of the part surface is available. The model may be produced using one of the approaches proposed in the literature (see Section 2.1.1.1);

b) an additional set of measurement repeats is obtained using a measurement solution recognised as more accurate and with an associated measurement uncertainty, typically using a traceable tactile CMS.

Therefore, using the same method described in Section 5.2.2, a second GRF can be constructed from the new set of measurement repeats. The original GRF obtained by optical data and the new one from a more accurate measurement are built using the same CAD model as reference, therefore co-localisation is assured. In order to assess bias, the Euclidean distance between the mean vectors of the two models can be used.

As previously discussed in Section 5.2.2, the same interpolation procedure can be used since the two GRFs do not present the same sample positions (Figure 5.6). Such an approach works better if the point clouds have similar densities, to reduce additional error potentially introduced by relying on interpolation.

The bias for the i^{th} point between two GRFs with associated uncertainty $\pm U$ is indicated in general as

$$bias = b_i \pm U; \tag{5.8}$$

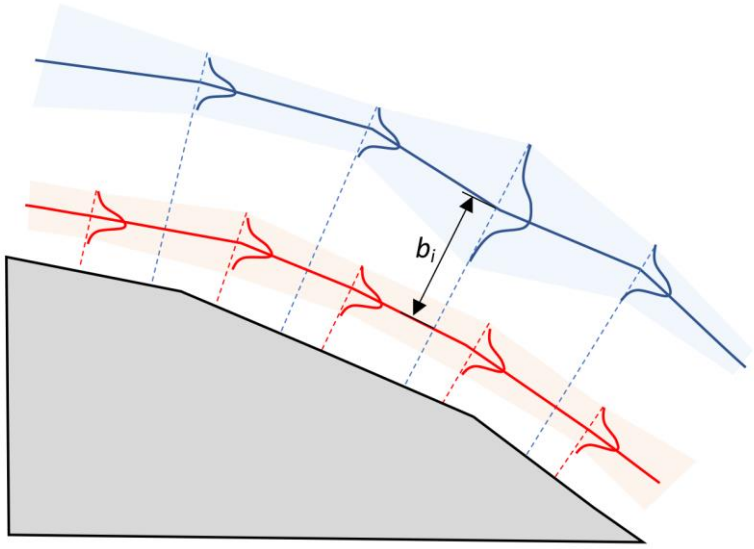

Figure 5.6 Procedure to assess bias between two GRFs. The original GRF is represented in blue, the second GRF (more accurate reference) is in red. The distances have been amplified for clarity. Local bias is computed starting from the mean function defined from first GRF, using the locations of the random variables in the first GRF and the related normals. The intersections with the mean function of the second GRF are found and used to determine bias (bias for the i^{th} point is shown in the figure). If the second GRF has an associated uncertainty $\pm U$, said uncertainty can be incorporated in the bias $(b_i \pm U)$

spatial maps of variance: information regarding the variance in correspondence to specific regions of the measured part is obtained and shown via the use of detailed spatial colour maps overlaid to the mean point cloud generated from the GRF;

spatial maps of bias: local bias information is shown via the use of colour maps, as long as either a reference measurement of stated uncertainty or a mathematical model with associated bias is available. The map is superimposed on the mean point cloud generated from the GRF with respect to a second GRF considered as reference.

5.3.2 Indicators based on new observations generated from the GRF

The GRF is used to reproduce new observations that act as "virtual" measurement repeats (*i.e.,* measurements that do not correspond to real measurements, but they present similarities with real ones) in combination with Monte Carlo (MC) simulations, in order to investigate how error propagates through the data processing pipeline, specifically how it affects the determination of features of size (extracted by fitting point clouds to appropriate datums) and the verification of conformance to specifications. The indicators describe the statistical distributions associated with the features of size assessed for central tendency and dispersion. In addition, an indicator related to bias for features of size is defined.

It is worth mentioning that the indicators defined in this section may as well be computed on original, real measurement repeats. However, the use of

a simplified approach based exclusively on real available measurements is costly and resource intensive in comparison with the generation of simulated data, since typically it is possible to afford the obtainment of only a few measurements. The estimation would be characterised by larger error, due to the small sample sizes available (for instance 3-5 to 10 repeats), typically much lower than the number of repeats obtainable from the GRF (for example 100-1,000 repeats). The restricted use of original repeats will cause the indicators to show a larger estimation error compared to the same indicators computed on simulated repeats and to be less reliable, as demonstrated in [210]. The following indicators are defined:

probability distribution of features of size: an arbitrary number of simulated observations can be generated from the GRF, in order to evaluate how error propagates in the point cloud processing pipeline for the evaluation of features of size using MC methods (Figure 5.7). New observations (point clouds) generated by the GRF, and any intermediate or final scalar result from the pipeline can be sampled into a probability distribution, which can later be assessed for central tendency and dispersion.

In coordinate metrology, a typical point cloud processing pipeline dedicated to the inspection and verification of shape and size consists of segmentation of the point cloud and fitting of different segments (subsets of neighbouring points) to datum surfaces [248]. The results of the pipeline refer to the observations extracted from the statistical model defined. Methods for point cloud segmentation and fitting are reported in Chapter 2 (see Sections 2.2.4.4 and 2.2.5.1 respectively);

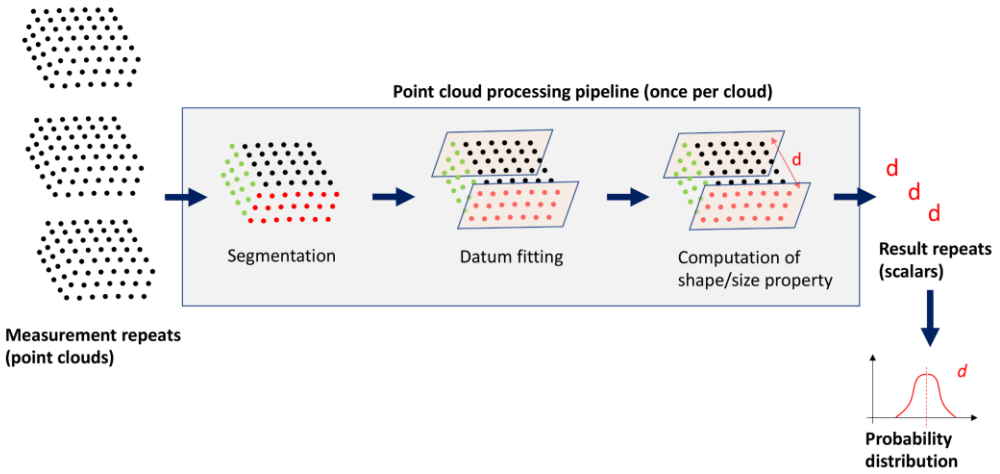

Figure 5.7 Overview of the process for error estimation of an example feature of size, via MC simulation and GRF (the GRF is used to generate new observations)

bias for features of size: given a feature of size dx, bias is defined both as signed distance and as signed percentage, as follows

$$\text{bias}_{dx:(\text{M}-\text{CMS})} = \overline{dx}_{\text{M}} - \overline{dx}_{\text{CMS}}, \tag{5.9}$$

$$\text{bias}\%_{dx:(\text{M}-\text{CMS})} = \frac{\overline{dx}_{\text{M}} - \overline{dx}_{\text{CMS}}}{\overline{dx}_{\text{CMS}}} \cdot 100, \tag{5.10}$$

where the bar indicates the arithmetic mean and the subscript indicates optical measurement (M) or contact measurement (CMS). Again, the results obtained from the pipeline refer to the observations extracted from the statistical model.

In absence of a comprehensive metrological characterisation of the tactile CMS, it is possible to rely on the maximum permissible error (MPE) [240] specified by the manufacturer to compute the standard uncertainty $u_{\mathrm{MPE}} = \mathrm{MPE}/\sqrt{3}$ for the tactile CMS.

Therefore, the formulation in equation (5.9) results in

$$\mathrm{bias}_{dx:(\mathrm{M-CMS})} = \left(\overline{dx}_{\mathrm{M}} - \overline{dx}_{\mathrm{CMS}} \pm \mathrm{MPE}/\sqrt{3}\right). \tag{5.11}$$

5.4 Validation and performance assessment

In this section a validation method based on simulation is proposed in order to compare with known target results the performance of the model and approach discussed in this chapter. The validation procedure covers the accuracy in the estimation of the random error component associated with a linear measurement, when the proposed statistical modelling approach is adopted to represent random variability in the point cloud across measurement repeats. The validation does not cover the accuracy of the method at estimating bias, thus the test data used in this validation does not contain any bias component. The method is illustrated in Figure 5.8.

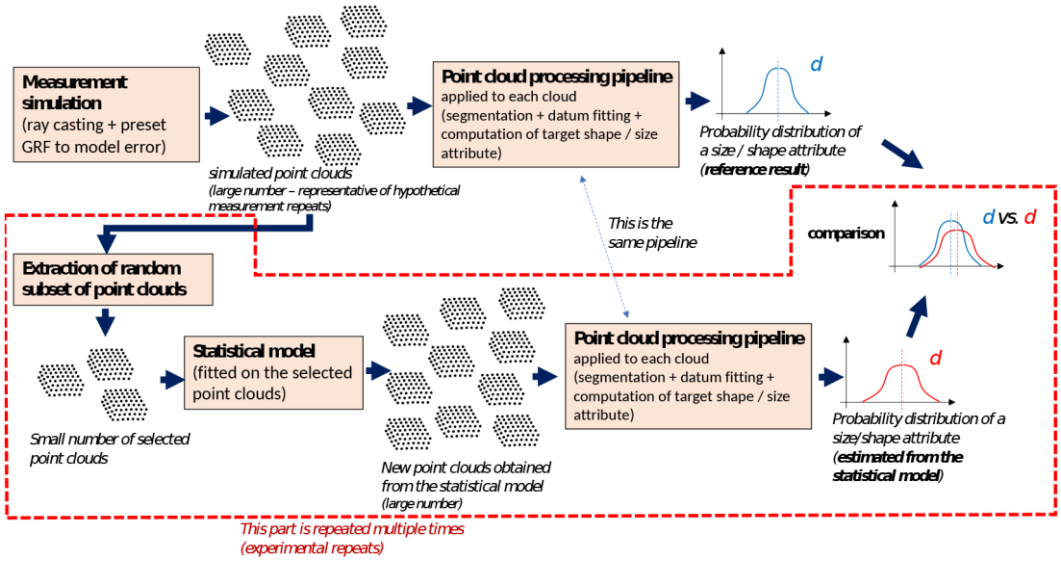

Figure 5.8 Validation procedure based on simulated measurements. The top row shows the process to obtain the reference result. The bottom row illustrates the estimation procedure implemented using statistical point cloud modelling

Simulated measurements (Figure 5.8 – top left) are performed on digital, test geometries by combining ray casting (*i.e.,* projecting a grid or rays onto a triangle mesh, as previously discussed in Chapter 4) and a GRF of known parameters to produce a large arbitrary number of point clouds, which incorporate known random measurement error. An arbitrarily high number of point clouds can be produced, representative of an ideal, but unrealistic scenario where one could perform a very large number (hundreds) of measurement repeats on the same test part. The point clouds are then processed (Figure 5.8 – top row) through a computational pipeline for shape/size inspection (as previously described in Section 5.3.2), applied to the entire set of virtually generated point clouds following the same procedure. Therefore, the probability distributions for each targeted attribute can be

obtained (Figure 5.8 – top right). Given the high number of point clouds used to model the probability distribution, the results of this simulation on a selected test case represent the ideal characterisation result that the proposed method aims to achieve (*i.e.,* representative of a reference result of the random error across repeats). The second stage of the validation procedure considers the random extraction of a much smaller subset of measurement repeats from the simulated overall set (Figure 5.8 – bottom left). Following the method discussed in Section 5.2.2, a new GRF is estimated from the selected subset (simulating a more realistic scenario where the user can only perform a limited number of measurement repeats and has no additional knowledge of measurement error), and new observations are generated. The same reference pipeline for dimensional inspection is now applied to all the new point clouds generated by the approximated GRF, leading (again by MC simulation) to estimated probability distributions for the selected size or shape attributes (Figure 5.8 – bottom right). The results obtained are compared with the ideal result (Figure 5.8 – middle right). From the comparison of the shape and statistics of the probability distributions it is possible to assess how closely the results of the proposed method match the ideal result. Selecting different random subsets of point clouds, the estimation procedure (Figure 5.8 – bottom row) is repeated multiple times, and the differences between the probability distributions of the estimated and reference results are assessed both via comparison of sample means and standard deviations, and via a nonparametric two-sample Kolmogorov-Smirnov (K-S) test [249]. The null hypothesis of the K-S test is that the two samples (in our case, the estimate and reference) belong to the same distribution. Hence, if the K-S test rejects

the null hypothesis we can conclude that the estimation did not perform well (*i.e.,* the estimated sample belongs to a distribution which is different from the "true" one). Finally, an investigation is carried out on how the choice of the number of repeats point clouds used to estimate the GRF in the proposed approach (Figure 5.8 – bottom left) affects the accuracy of the prediction (closeness between the results produced by the proposed approach and the reference results).

The proposed method is validated with the results obtained on simulated measurement repeats generated using simulated test geometries. These results are collected and illustrated in the journal publication [210] in *Precision Engineering*.

5.5 Chapter conclusions

A statistical model developed for the evaluation of point cloud positional uncertainty was presented in this chapter. The described approach implies the fitting of discrete Gaussian random fields (GRFs) to high-density point clouds. The developed model was built solely from measurement repeats, aiming at primary investigating the precision of the measurements (*i.e.,* random error in repeatability/reproducibility conditions). For each measurement a probability band was computed. In order to obtain a complete spatial uncertainty map, the defined statistical model would be eventually combined

with an additional component representative of constant bias, introduced via the use of more accurate measurement or external mathematical models.

From the properties of the fitted fields, a set of GRF-derived performance indicators was defined, covering aspects related to local point scatter in the direction defined by the local reference normals capturing the dispersion of the points across measurement repeats, and to local bias, assuming the availability of a more accurate model or measurement to be considered as reference. Also, spatial map indicators describing local properties of the measurement (for example local variance and local bias) were defined. A second set of indicators based on new "virtual" observations generated from the GRF in combination with MC simulations was illustrated, able to replicate the statistical properties of the original observations, saving the time and resources required in a real repeated measurement procedure. The indicators described the statistical distributions associated with the features of size. In addition, an indicator related to bias was defined.

As the quality metrics defined and described in Chapter 4, the developed statistical model and derived indicators can be implemented in a fully automated form. This paves the way for the development of "smart" measurement systems capable of performing self-assessment of measurement quality while in operation, and subsequently capable of autonomously performing corrective actions in order to improve the final quality of the measurement result. The use of the defined performance indicators and statistical point cloud model provides new means to investigate how measurement error is spatially mapped to all the regions of any given part, useful in the routine inspection of manufactured components in a production

scenario, as long as the execution of measurement repeats is viable, and as long as the interest is to characterise random error components visible across repeats. The developed procedure would be useful in research laboratory scenarios where the goal is to perform a more detailed investigation of the metrological performance and behaviour of coordinate measuring systems/measurement technologies applied to specific types of geometries, materials, aspect ratios, types of surface features (flat, curved, step-like, high aspect-ratio, smooth, irregular, *etc.*), suggesting new correlations that will allow a valid uncertainty budget to be established.

The results of the application of the indicators presented in this chapter and previously in Chapter 4 are reported as graphical representations in the following one, applied to selected industrial cases (metal additively manufactured roof bracket and pyramid artefact previously illustrated in Chapter 3 as samples A and B respectively, designed by the Manufacturing Metrology Team), measured using different optical technologies.

Chapter 6

Application of the indicators to selected industrial cases

6.1 Overview

Two series of original performance indicators, illustrated in Chapter 4 and Chapter 5 respectively, highlighted various aspects related to the intrinsic properties of measured point clouds and the quality of the measurement results. Measurement quality indicators described in Chapter 4 investigated the relationship between a measured point cloud and the reference geometry, addressing measurement performance under new viewpoints, encompassing elements connected to sampling density and surface coverage in relation to

individual regions of the part. The indicators defined in Chapter 5 investigated local dispersion of the point clouds, as well as local bias, by means of a statistical point cloud model fitted to optical measurement repeats, assessing metrological performance in repeatability and reproducibility conditions. The methods developed for the definitions of the two sets of performance indicators present clear differences in terms of contents. However, as previously discussed in Chapter 1, both sets of designed indicators aim at providing insights related to the intrinsic properties of a measurement, addressing quality under a broader metrological scenario. The solutions developed represent novel means for assessment of measurement performance for future integration into intelligent measuring systems.

In this chapter, the solutions developed are illustrated and validated through application to selected industrial cases of industrial relevance, two of the additively manufactured components previously described in Chapter 3. Whilst some results have already been reported as examples when illustrating the methods in the previous chapters, a complete summary of the findings obtained respectively on sample A (a freeform shaped metal roof bracket for the application of measurement quality indicators, illustrated in Section 3.3.1) and on sample B (a metal pyramid for the application of the indicators derived from the statistical point cloud model, illustrated in Section 3.3.1) measured using several optical instruments is here reported. The selection of the appropriate technologies for the measurement of the sample parts was defined as a result of the review of the most suitable current solutions in optical coordinate metrology for measurement applications in additive manufacturing (AM), illustrated in Section 2.1.2. Therefore, photogrammetry and structured

light are the optical technologies selected to perform the measurements, due to the advantages of producing highly dense point clouds, and performing multiple acquisitions achieving fast scanning rates [5,10]. Furthermore, measurements obtained from a tactile coordinate measurement system (CMS) are selected to act as nominally more accurate reference. The methods developed and the derived indicators rely on the availability of triangle mesh geometries underlying the selected part, as pre-existing knowledge used to guide several steps of the measurement pipeline (for example registration and point-to-triangle associations), resulting then in the computation of the indicators. The choice of the two samples has been made in order to specifically investigate measurement quality in relation with problematic features associated with the measurement of AM parts, for example steep slopes, hollow features, complex geometries, as it is previously mentioned in Section 2.1.2.

6.2 Application of measurement quality indicators on sample A

The application of the measurement quality indicators defined in Chapter 4 was demonstrated on sample A measured with a photogrammetry system (indicated in figures, tables, and results Section 6.2.2 as PG) developed by the Manufacturing Metrology Team (MMT) at the University of Nottingham (Figure 6.1.a), with the GOM ATOS Core 300 commercial fringe projection

system (indicated in figures, tables, and results Section 6.2.2 as FP) available at the MMT laboratory (Figure 6.1.b), and with the Artec Space Spider structured light pattern projection system (indicated in figures, tables, and results Section 6.2.2 as SL) available at the BMW Research and Development Centre in Munich (Figure 6.1.c). Five measurement repeats of the test artefact were performed for each instrument. In addition, selected features of the part were measured using a Mitutoyo Crysta Apex S7106 tactile coordinate measuring machine (indicated in figures, tables, and results Section 6.2.2 as CMS) with a 21 mm long, 1 mm diameter ball tipped stylus, available at the MMT laboratory (Figure 6.1.d). The contact CMS was selected in order to provide dimensional measurements that could act as reference for comparison.

The photogrammetry system relies on a camera to capture a series of images around the object, then applies reconstruction algorithms to obtain a dense three-dimensional (3D) point cloud [50,51]. A digital single-lens reflex (DSLR) camera (Nikon D3300, 24 MP sensor) was mounted on a translation stage and fixed within a distance from the part of 250 mm, providing a field-of-view that completely encapsulated the test sample at an elevation of approximately 45°. The translation stage is controlled via scripting to achieve the correct focal distance and/or to change magnification, providing pre-set elevation angles. An enclosure equipped with LED lighting designed in order to achieve uniform, diffuse illumination during the measurements contains the rotary stage where the part is located.

The fringe projection system employed [233] is the same previously introduced in Section 3.3.2 for the measurement of the datasets used to validate the registration strategy.

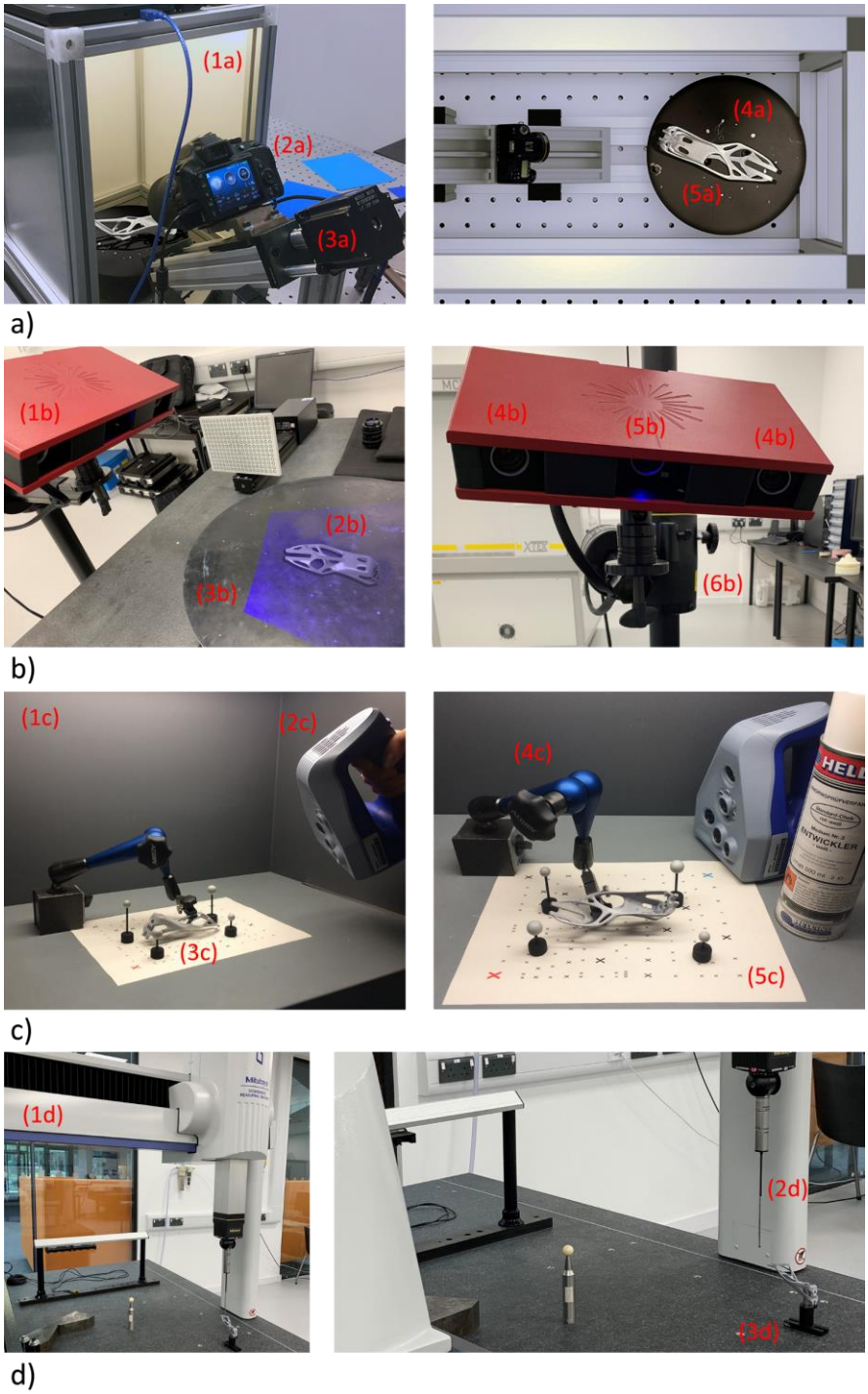

Figure 6.1 Measurement systems and setups selected for the test part. a) PG solution: (1a) enclosure with LED lighting, (2a) DSLR camera, (3a) translation stage, (4a) rotary table, (5a) sample A. b) FP solution: (1b) fringe projection system, (2b) sample A, (3b) rotary table, (4b) pair of cameras, (5b) blue light projector, (6b) tripod. c) SL solution: (1c) enclosure with LED lighting, (2c) structured light system, (3c) sample A, (4c) articulated measuring stand, (5c) artefacts and reference sheet with printed targets. d) Contact CMS: (1d) tactile CMS, (2d) ball tipped stylus, (3d) sample A

The instrument is mounted on a tripod and is composed of a pair of cameras and a blue light projector of fringes. The position of the pair of cameras allows the measurements within a field of view of (300 × 230) mm and measuring point distance of 0.12 mm, as stated by the manufacturer.

The handheld structured light system [250] featured an RGB camera surrounded by LED flash bulbs, a blue light speckle pattern projector and three sensors. The system measures up to one million points per second and produces images with a spatial resolution up to 0.1 mm with an accuracy over distance up to 0.03% over 100 cm, as reported by the manufacturer [250]. An enclosure opened on one side containing the part is designed with a strip of LEDs placed on the ceiling in order to provide a diffuse and uniform illumination during the measurements.

6.2.1 Data acquisition and processing

The photogrammetry measurements were performed in a temperature-controlled laboratory at (20 ± 0.5) °C. The full acquisition of the test part was obtained by automatically acquiring images, over a total of sixty rotation steps (top and bottom of the part, full scan of sixty images). For the test part, the camera settings were chosen to obtain optimal coverage of the measured sample and maximise the optical resolution. A 40 mm macro lens was used with F-stop of 11 to maximise the depth-of-field of the camera whilst ensuring the camera does not become diffraction limited. The 3D position of each measured data point was obtained by matching correspondences between the acquired images using the scale invariant feature transform (SIFT) method

[251]. The images were processed using commercial software (Agisoft Metashape [252]) to obtain the final reconstruction of the full 3D point cloud. Based on the estimated camera positions and orientation, the software calculates depth information for each point to be combined into a single dense point cloud.

The fringe projection measurements were performed in the same laboratory as the photogrammetry ones, and under the same measuring conditions. The acquisition of the test part was obtained by having the sample placed on a rotary stage and scanning it at 360°. The acquired data were directly processed and stitched into a single full 3D point cloud using the instrument software GOM Scan [235].

The structured light measurements were executed in a temperature-controlled laboratory at (20 ± 0.5) °C at the BMW Research and Development Centre in Munich. The acquisition of the test part was obtained by manually scanning one side of the object, followed by the acquisition of the part rotated by 180°. The raw data from both sides were converted into point clouds via the instrument software and stitched into a single full 3D point cloud using Polyworks Inspector [253].

Data processing for all the datasets involved removal of points belonging to the background surfaces surrounding the part, application of a noise filter based on outlier detection, and deletion of isolated points, applying the methods described in Chapter 2, in particular Section 2.2.3.2 for the application of a noise filter and elimination of isolated points. A plane was locally fitted around each data point using its six closest neighbours found with the k-nearest neighbour (k-NN) algorithm (see Section 2.2.2.3); points

resulting too far away from the fitted plane were removed. The number of neighbours was chosen for the specific test case, based on the point-to-point spacing indicator results. In addition, a threshold radius of 1 mm between the selected query point and its neighbours allowed the identification and removal of isolated points with less than three neighbours within the specified radius. Again, the threshold value was selected by considering the point-to-point spacing results. The computation of the normal vectors to the points in the point cloud was achieved via principal component analysis (PCA), as it is illustrated in Section 4.3.2 (see also literature in Section 2.2.4.1).

The reference model of the test sample was provided by the manufacturer in form of triangle mesh in STL format. The reference geometry is assumed as a common datum in order to provide a coordinate system shared by all measurement repeats, needed for the indicators computation. In order to contain the computational complexity of the developed indicators, in particular in the estimation of the cloud-to-mesh associations (see Section 4.3.2), the number of triangles composing the original mesh were reduced by simplification [140], as previously discussed in Section 4.3.2. For the assessment of the pose between the final point clouds and the reference model performed following the registration strategy presented in Chapter 3, and for the computation of the indicators for features of size, the mesh used was the one provided in its original configuration.

6.2.2 Results

The results presented in the following sections are evaluated based on a comparison of three optical technologies. The indicators operating at the point-cloud level developed at this stage do not intend to provide insights on the physics of the measurements, nor the relationships between such physics and the observed results. The complete set of illustrative results (*i.e.,* colour maps of the performance indicators) on sample A is given in Appendix A, the most significant examples of which are shown in this chapter.

6.2.2.1 Measurement effort and indicators capturing the intrinsic properties of the measured point clouds

Results for the indicators for measurement effort previously defined in Section 4.2.1 are summarised in Table 6.1 for the three measurement technologies.

Table 6.1 Indicators for measurement effort

	PG	**FP**	**SL**
Acquisition time	$<$ 2 s for a single shot; up to 30 min for full acquisition	$<$ 2 s for a single shot up to 30 min for full acquisition (calibration included)	$<$ 2 s for a single shot up to 30 min for full acquisition (calibration included)
Processing time	approx. between 2-4 hours	approx. 30 min	approx. 30 min

The acquisition times of the datasets produced by the optical technologies were found similar, with a duration of approximately 30 minutes per instrument for the acquisition of a single set of measurements (*i.e.,*

multiple views automatically stitched in a single point cloud). For FP and SL, the acquisition time included the calibration procedure of the instruments, which lasted approximately 30 minutes for both systems. The processing times were found instead significantly shorter for FP and SL than PG. This difference is due to the length of the reconstruction process required by the PG technology to obtain point cloud data from image data. Reconstruction can take from few minutes to several hours, determined by the number of images acquired and the level of details needed in the reconstructed output, depending on specific application requirements.

Results for the indicators related to the intrinsic properties of the measured point clouds previously defined in Section 4.2.2 are shown in Figure 6.2, using boxplots computed from five repeated measurements for each measuring technology. A one-way analysis of variance (ANOVA) for equal means performed separately on the three indicators resulted in the null hypothesis (PG, FP and SL having equal means) being rejected at the 0.05 significance level, with p-values: 1.67×10^{-17}, 3.81×10^{-13} and 3.22×10^{-15} (related to Figure 6.2.a, Figure 6.2.b and Figure 6.2.c respectively).

The PG measurement resulted in more populated raw point clouds (higher number of points, Figure 6.2.a). After processing (cleaning, filtering) the discrepancy in densities in the final point clouds was still significant (Figure 6.2.b). The result was reflected also by the point-to-point spacing indicator (Figure 6.2.c), highlighting the higher densities in the PG point clouds above all datasets.

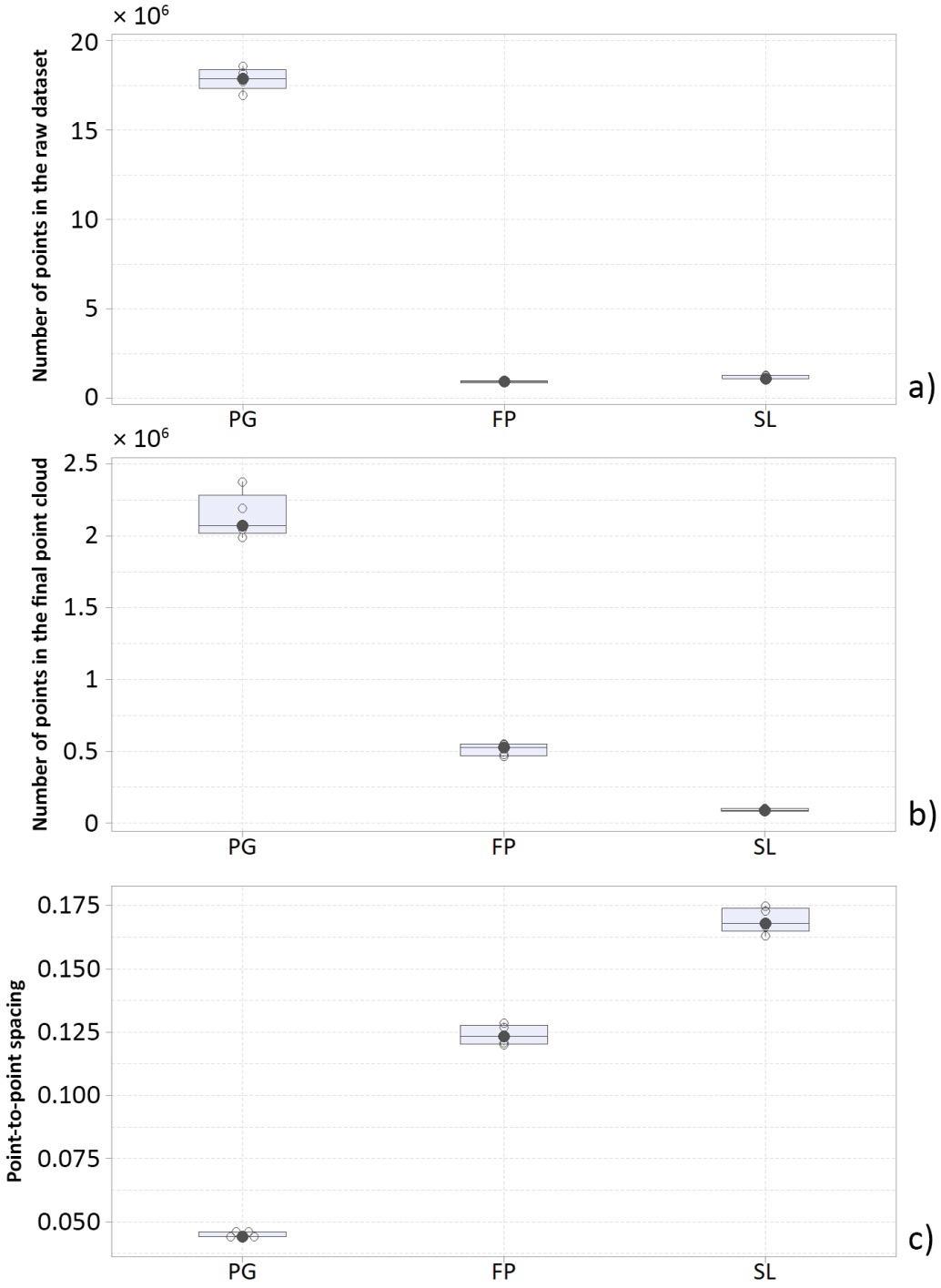

Figure 6.2 Indicators of intrinsic properties of the point clouds (boxplots from five measurement repeats). a) Number of points in the raw datasets, b) number of points in the final point cloud, and c) point-to-point spacing. In the boxplots, the boxes indicate the interquartile range (IQR), the black dot is the median value, the transparent circles are the individual observations

6.2.2.2 Indicators of part coverage

An example result of the coverage ratio indicator previously defined in Section 4.2.3 is shown in Figure 6.3. A complete reporting of the colour maps is illustrated in Appendix A.

As it is stated in Chapter 4, the threshold value for the computation of covered and uncovered triangles is application dependent and selected by the user according to related measurement requirements. As the number of covered/uncovered triangles is a parametric indicator (meaning that the results can change according to the chosen threshold), for this work the threshold value was selected as the 75% of the total detected density (*i.e.,* the total number of points in the point cloud over the total area of the triangle mesh, defined as *eps* in this thesis) for each individual point cloud, in order to show the functionality principles of the indicator.

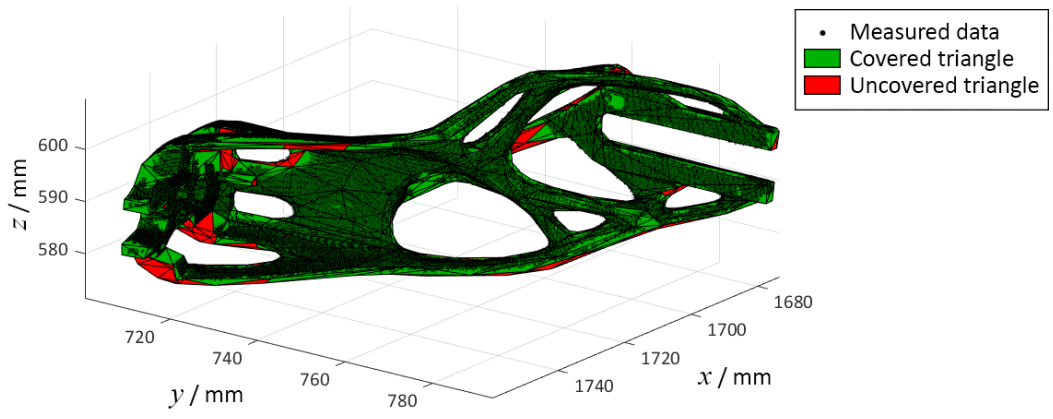

Figure 6.3 Example result of the coverage ratio indicator: covered and uncovered triangles are rendered using binary colouring (threshold at 75% of total detected density)

In Figure 6.4, boxplots for the coverage ratio and the coverage area ratio indicators are shown. ANOVA analysis for equal means performed separately on the two indicators resulted in the null hypothesis (PG, FP and SL having equal means) being rejected at the 0.05 significance level, with p-values: 7.58×10^{-9} and 6×10^{-3} (related to Figure 6.4.a and Figure 6.4.b respectively).

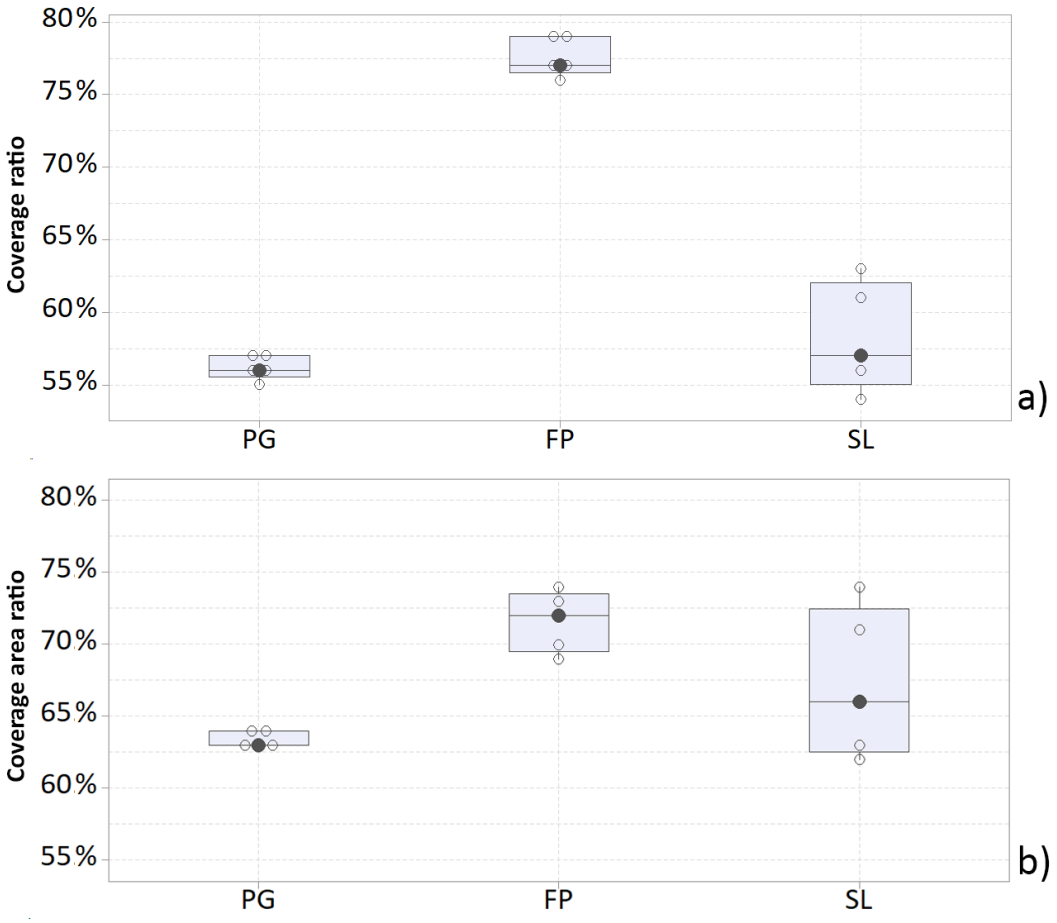

Figure 6.4 Indicators of part coverage (boxplots from five measurement repeats). a) Coverage ratio, and b) coverage area ratio

The results show repeatability issues in part coverage for the SL measurements. The sample was kept in a fixed position for all measurements performed with the three systems. However, because of the handheld configuration of the SL system, higher pose variability across measurement acquisitions resulted in higher variability of coverage, compared to the configurations of the PG and FP systems, which consist of fixed positions for both instruments (camera mounted on a stage for PG and pair of cameras and projector mounted on a tripod for FP) and rotary tables. Also, in terms of coverage, fewer internal surfaces were acquired by PG and SL, whilst the FP measurements proved no significant difficulties despite line-of-sight issues and the high complexity of the part. Overall, for FP measurements 78% of the triangles (extracted from the reference triangle mesh) were sufficiently covered (coverage ratio) and 71% of the part area was sufficiently covered (coverage area ratio), compared to the PG measurement, which scored 56% coverage ratio and 63% coverage area ratio, and SL with 58% and 67% respectively.

Example colour maps of sampling density indicator previously defined in Section 4.2.2 are shown in Figure 6.5. In order to obtain a visually clearer distribution of the results across the geometry, the values recorded for the sampling densities have been normalised by division with the maximum value recorded across all datasets. The colour maps clearly show the significant difference of the density values overlaid to the mesh geometry across the measurements acquired with different systems. The PG result shown in Figure

6.5.a (front and back views) for one measurement repeat illustrates high density values, except in correspondence of internal regions and critical areas where the values of sampling density decrease greatly towards zero (*i.e.,* triangles identified as zero-coverage). The FP and, in particular, the SL sampling density representations show lower rates of density, but a more homogeneous distribution compared to the PG measurements. Bar plots proportional to sampling density for PG, FP and SL measurements are shown in Appendix A, reporting for each the values of *eps* (*i.e.,* threshold used to previously assess coverage).

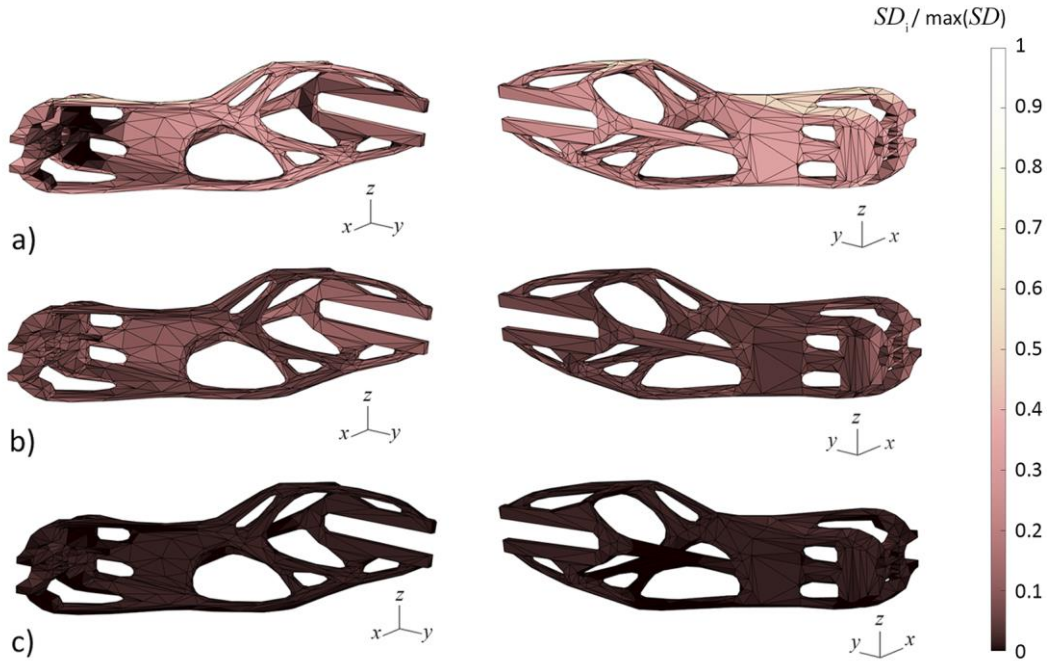

Figure 6.5 Mesh triangles coloured on sampling density. a) PG, b) FP and c) SL

6.2.2.3 Indicators of metrological performance making use of an associated triangle mesh

Example results in Figure 6.6 show the point-to-surface distances within each triangle, previously defined in Section 4.2.4. Colouring is proportional to the Euclidean distance between each measured point and its paired closest projected point located within the nearest triangle. The colour maps highlight the presence of critical areas in correspondence to features of size (for example slot holes), as it is evidently illustrated by the PG and the SL colour maps.

Figure 6.7 shows in graphical form the indicator of dispersion of signed distances to the triangle surfaces, previously defined in Section 4.2.4. It should be noted that, while in an actual quantitative comparison the values of dispersion of signed distances must be used as-is, in Figure 6.7 they have been normalised by division with the maximum value recorded, in order to obtain a visually clear distribution of the values across the geometry. The colour maps show minor differences in the distribution of the dispersion results across the datasets. In correspondence of critical areas (triangles coloured in green in Figure 6.7, and highlighted with colours from yellow to red in the point-to-surface distances indicator reported in Figure 6.6), the indicator shows significantly high dispersion results compared to other regions (coloured for instance in orange). Areas indicated in the maps in red colouring correspond to regions with no associated points.

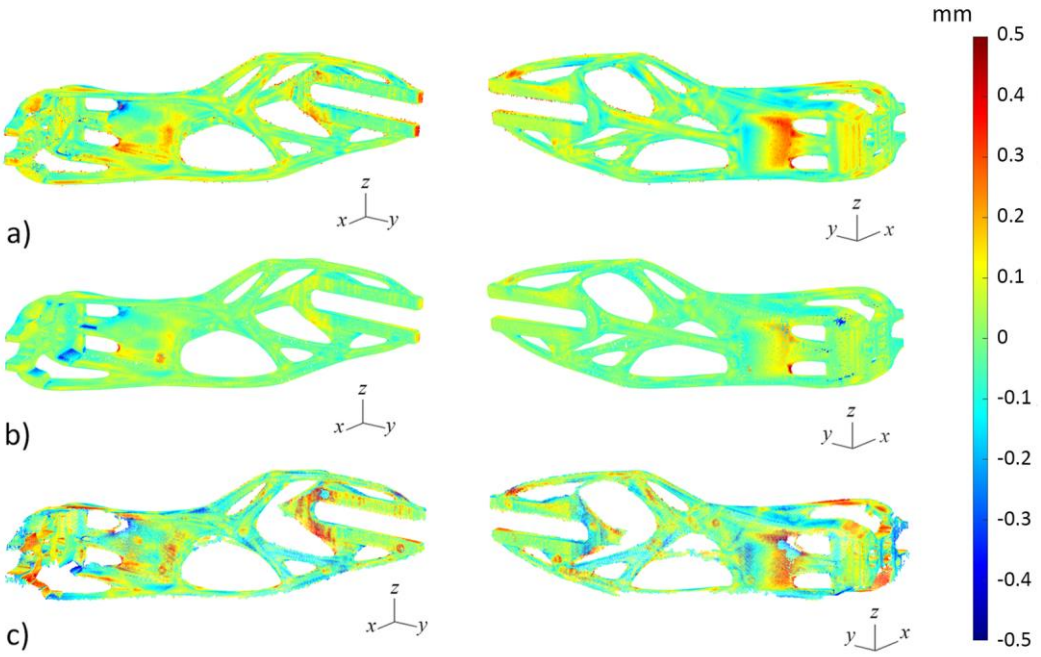

Figure 6.6 Point-to-surface distances within each triangle overlaid to the reference geometric model of the test sample. a) PG, b) FP and c) SL

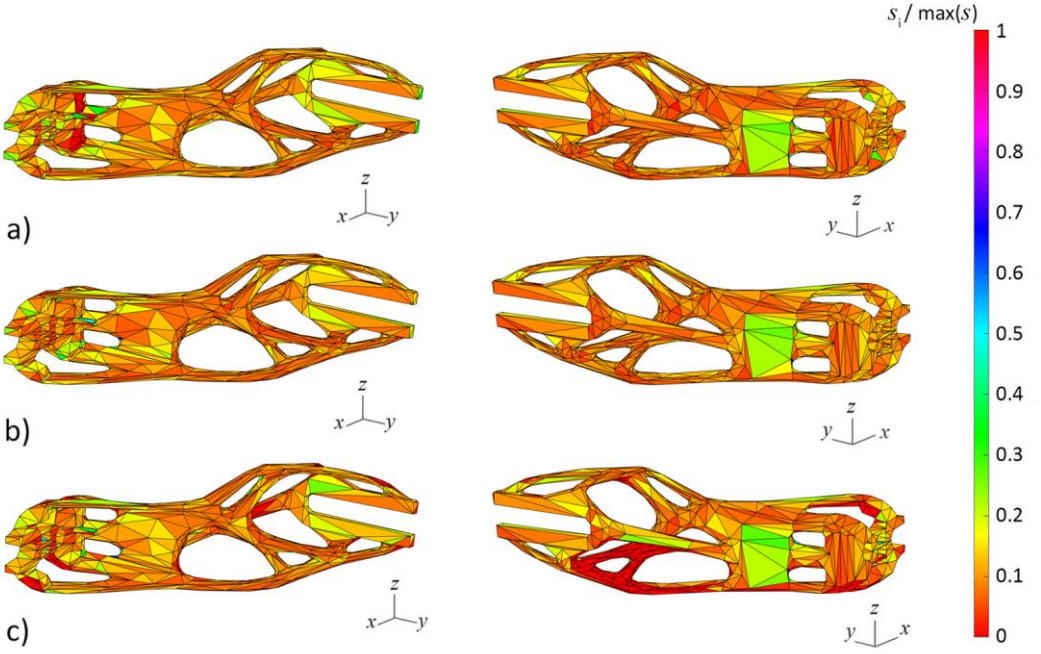

Figure 6.7 Triangles coloured using the dispersion of signed point-to-surface distances indicator. a) PG, b) FP and c) SL

The probability distributions of the values of the dispersion of signed distances are shown in Figure 6.8 for the first measurement repeat of PG, FP and SL respectively, indicated as s_1 (s_2, s_3, s_4 and s_5 probability distributions also for the other measurement repeats are reported in Appendix A). The values of the dispersion of signed distances are reported in non-normalised form, and thus are expressed in millimetres.

The statistics computed from the probability distributions are shown in Table 6.2, indicating better performance (smaller dispersion) for the SL measurements.

Table 6.2 Statistics of the distribution of dispersion of signed distances / mm

		s_1	s_2	s_3	s_4	s_5
PG	**mean(s)**	0.06	0.06	0.06	0.06	0.07
	st. dev(s)	0.03	0.03	0.03	0.03	0.03
	range(s)	0.00 - 0.39	0.00 - 0.42	0.00 - 0.43	0.00 - 0.41	0.00 - 0.35
FP	**mean(s)**	0.06	0.06	0.06	0.06	0.06
	st. dev(s)	0.03	0.03	0.03	0.03	0.03
	range(s)	0.00 - 0.50	0.00 - 0.48	0.00 - 0.54	0.00 - 0.60	0.00 - 0.46
SL	**mean(s)**	0.04	0.05	0.05	0.05	0.05
	st. dev(s)	0.04	0.04	0.04	0.04	0.05
	range(s)	0.00 - 0.45	0.00 - 0.41	0.00 - 0.36	0.00 - 0.39	0.00 - 0.60

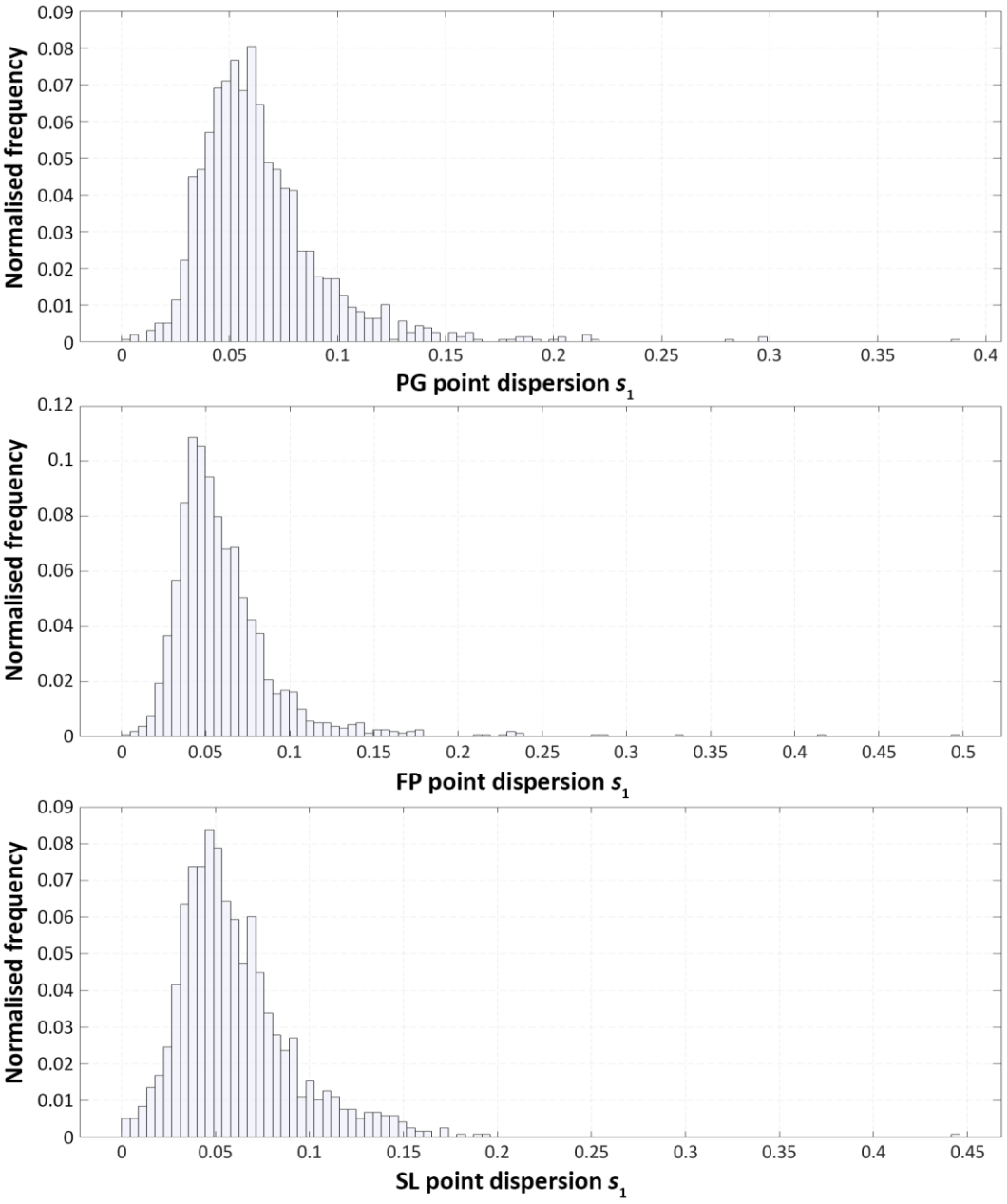

Figure 6.8 Histograms of dispersion of signed point-to-surface distance values for the first measurement repeats of PG, FP and SL indicated as s_1. Dispersion is expressed in millimetres; normalised frequency (vertical axes) is the number of occurrences of the values in a bin, divided by the total number of occurrences

6.2.2.4 Indicators for features of size

Following the National Physical Laboratory (NPL) good practice guide No. 41 [254], selected features of size (Figure 6.9) were measured using a tactile CMS. An error interval is reported, obtained from the maximum permissible error (MPE) provided by the manufacturer, *i.e.*, $E_0 = (1.7 + 3L/1000)\ \mu m$ (where L is the test length in millimetres) [254,255], and computed on the nominal features of size. The contact CMS measurement results are shown in Table 6.3.

In order to obtain the analogous dimensional values from the PG, FP and SL measurements, least-squares fitting procedures (see Section 2.2.5.1) were implemented using Polyworks Inspector [253], leading to the results shown in Table 6.4 (the values for the five repeats are indicated as $dx_1, dx_2, \ldots dx_5$).

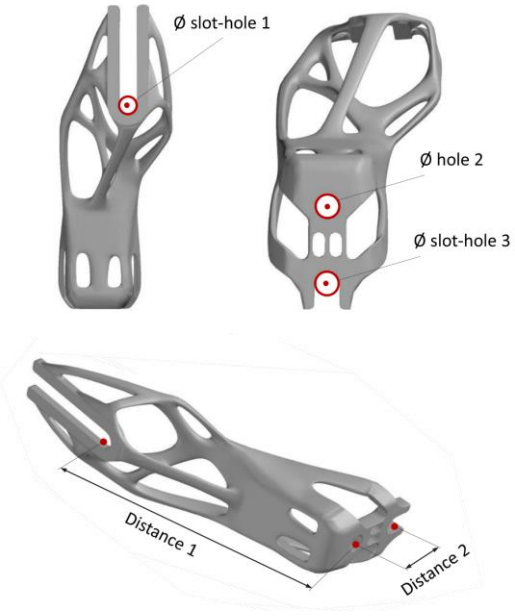

Figure 6.9 Digital 3D model of sample A showing the features of size (slot-holes and linear dimensions) subjected to inspection

Table 6.3 Contact CMS measurement results / mm

Feature	**Measurement type**	$\overline{dx}_{\mathbf{CMS}} \pm \mathbf{MPE}$
Ø slot-hole 1	Diameter	6.26 ± 0.002
Ø hole 2	Diameter	5.91 ± 0.002
Ø slot-hole 3	Diameter	5.99 ± 0.002
Distance 1	Linear distance	81.80 ± 0.002
Distance 2	Linear distance	17.89 ± 0.002

Table 6.4 Results for the features of size / mm

	Feature	dx_1	dx_2	dx_3	dx_4	dx_5	$\overline{dx}_{\mathrm{M}}$	u_{M}	U_{M}
PG	*Ø slot-hole 1*	6.07	5.99	6.06	6.00	5.99	6.02	0.02	0.04
	Ø hole 2	6.04	5.94	5.95	5.97	5.95	5.97	0.02	0.04
	Ø slot-hole 3	6.10	6.07	6.06	6.06	6.06	6.07	0.007	0.01
	Distance 1	81.72	81.82	81.75	81.73	81.87	81.80	0.03	0.06
	Distance 2	18.05	17.94	17.99	18.03	18.04	18.01	0.02	0.04
FP	*Ø slot-hole 1*	6.03	6.20	6.15	6.01	5.99	6.08	0.04	0.08
	Ø hole 2	5.94	5.91	5.95	5.92	5.91	5.93	0.008	0.02
	Ø slot-hole 3	6.04	6.10	5.88	5.94	5.97	5.99	0.04	0.08
	Distance 1	82.04	82.11	82.09	81.95	81.88	82.01	0.04	0.08
	Distance 2	17.92	18.06	17.94	17.95	18.01	17.98	0.03	0.06
SL	*Ø slot-hole 1*	6.39	6.53	6.37	6.05	6.25	6.32	0.08	0.16
	Ø hole 2	5.81	5.98	5.99	5.87	6.07	5.95	0.05	0.10
	Ø slot-hole 3	6.15	6.52	6.27	5.99	6.53	6.30	0.10	0.20
	Distance 1	81.95	81.98	81.83	81.86	81.91	81.91	0.02	0.05
	Distance 2	18.01	18.04	17.99	17.94	18.13	18.02	0.03	0.06

As stated in Section 4.2.5, the standard and expanded uncertainties only capture the precision-related characteristic of the performed measurements. For the evaluation of features of size, the proximity of measurement results to the true value is expressed through the identification of a bias value $\mathbf{bias}_{dx:(\mathbf{M-CMS})}$, computed considering the tactile CMS as reference. The bias indicator (end of Section 4.2.5) was defined as a means to provide accuracy-related information in a quantitative way. The bias values are reported in Table 6.5, and shown in Figure 6.10 for features Ø slot-hole 1, Ø hole 2 and Ø slot-hole 3 and in Figure 6.11 for Distance 1 and Distance 2 respectively.

Table 6.5 Bias values / mm

Feature	$\mathbf{bias}_{dx:(\mathbf{PG-CMS})}$	$\mathbf{bias}_{dx:(\mathbf{FP-CMS})}$	$\mathbf{bias}_{dx:(\mathbf{SL-CMS})}$
Ø slot-hole 1	0.23 ± 0.02	0.18 ± 0.04	0.06 ± 0.08
Ø hole 2	0.06 ± 0.02	0.02 ± 0.008	0.04 ± 0.05
Ø slot-hole 3	0.08 ± 0.007	0.00 ± 0.04	0.31 ± 0.10
Distance 1	0.00 ± 0.03	0.22 ± 0.04	0.11 ± 0.02
Distance 2	0.12 ± 0.02	0.09 ± 0.03	0.13 ± 0.03

ANOVA test for equal means performed separately on each feature of size resulted in the null hypothesis (PG, FP and SL having equal means) being rejected with p-values of 4.10×10^{-3}, 1.53×10^{-2} and 2.60×10^{-3} for Ø slot-hole 1, slot-hole 3 and Distance 1 respectively, meaning that the difference of biases can be considered as statistically significant (assuming a common CMS value as reference). The test resulted in the null hypothesis not being rejected at the 0.05 significance level for Ø hole 2 and Distance 2. For these latter cases it is possible that the observed difference in bias may become statistically significant with larger sample sizes.

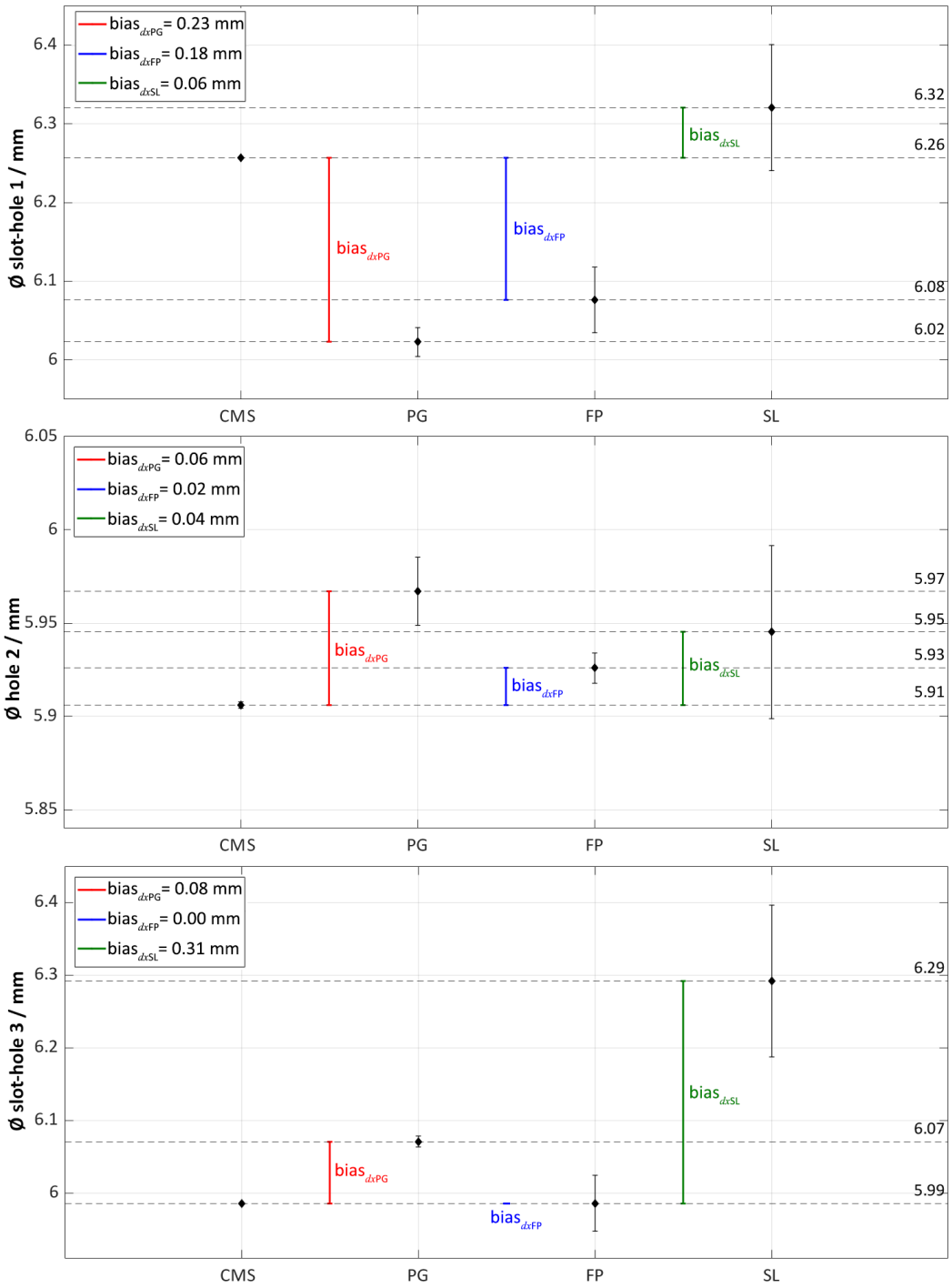

Figure 6.10 Features of size Ø slot-hole 1, Ø hole 2 and Ø slot-hole 3: bias values and standard uncertainties. The interval computed on the contact CMS measurements is the MPE calculated on the nominal features of size (quantitative values reported in Table 6.3)

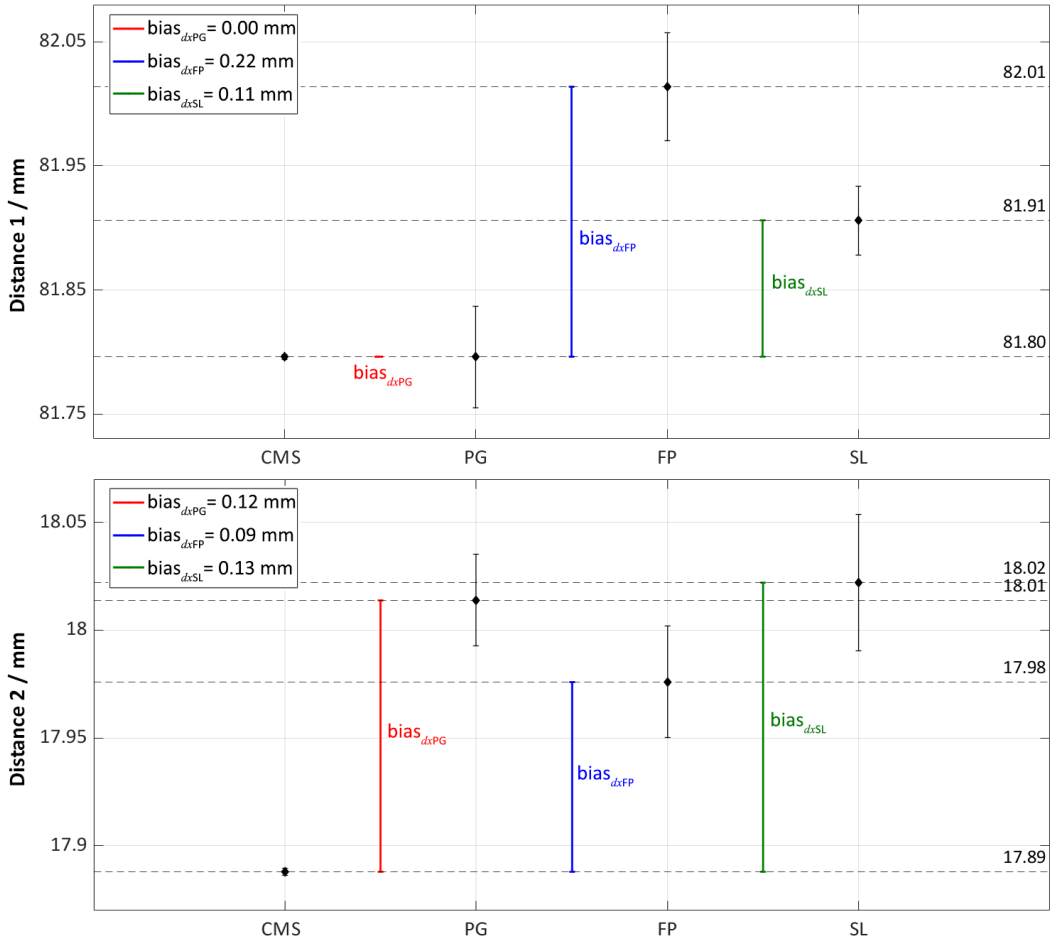

Figure 6.11 Features of size Distance 1 and Distance 2: bias values and standard uncertainties. The interval computed on the contact CMS measurements is the MPE calculated on the nominal features of size (quantitative values reported in Table 6.3)

The inspection of selected features of size shows discrepancies between the values obtained with the CMS and the optical measurements. The FP measurements for the diameters of hole 2 and slot-hole 3 resulted the closest to the CMS values, showing in the first case a bias of 0.02 mm and in the second case no bias. For slot-hole 1 instead the SL measurements resulted with the lowest bias of 0.06 mm. For the linear distances 1 and 2, while in the former the PG measurement showed the best result (no bias), for the latter

the best result is given by the FP measurements even if showing a large bias value. The PG and SL results for the linear distance 2 between the centroids of the slot-holes 2 and 3 were found in agreement with each other.

6.2.3 Section conclusions and discussion

The proposed series of original indicators gives useful suggestions for the comparison of multiple metrological solutions, representing a starting point for the outline of large measurement campaigns. In this scenario, rigorous investigations would surely lead to conclusions of general validity about the relationships existing between optical measurement technology, part geometry and metrological performances. In order to unravel the relationships between the physics of measurement and the results, the campaign would require a more significant endeavour in terms of explored technologies, implementations, test geometries, experimental repeats, *etc.*, as well as a more comprehensive investigation on the gathered data. The comparison illustrated in the previous sections showed a preliminary investigation of three optical technologies for a specific industrial application. The results highlighted the potential of the FP solution analysed in this work, resulting in the technology showing the highest coverage performances and low uncertainty in correspondence to critical areas (*i.e.,* internal regions and features of size), which could not be easily captured especially by SL nor contact probing.

Despite the limited measurement campaign, the illustrated observations provide the reader with interesting means (in the form of indicators) to perform quantitative comparisons and intent to raise awareness

that measurement performance should be assessed through multiple viewpoints, not necessarily limited to assessing uncertainty on dimensional results. Although the results did not indicate a clear winner, they highlighted the complexity of the comparison and showed how each measurement solution may be seen as prevailing when considering any specific performance aspect (for example sampling density, part coverage, *etc.*). This suggests that measurement solutions should be carefully selected depending on the test case, and a proper measurement workflow should be planned based on consideration of performance under multiple perspectives, in order to achieve optimal results.

6.3 Application of the statistical point cloud model indicators to sample B

The application of the indicators defined from the statistical point cloud model illustrated in Chapter 5 is demonstrated on sample B measured with the GOM ATOS Core 300 [233] commercial fringe projection (indicated in figures, tables, and results Section 6.3.2 as FP) system available at the MMT laboratory (Figure 6.12.a). A second high-density measurement was taken using the MMT Mitutoyo Crysta Apex S7106 tactile coordinate measuring system (indicated in figures, tables, and results Section 6.3.2 as CMS) with a ST25 probe [255] to act as a nominally more accurate reference (Figure 6.12.b). Both instruments have been previously described in Section 6.2.

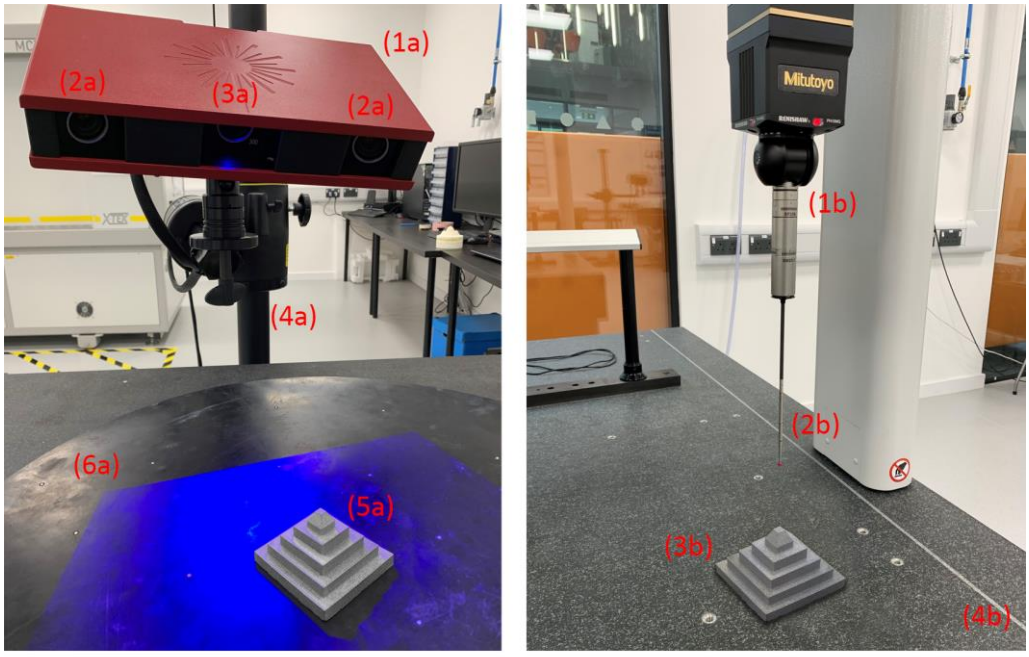

Figure 6.12 Measurement systems and setups selected for the test part. a) FP solution: (1a) sensor head, (2a) pair of cameras, (3a) blue light projector, (4a) tripod, (5a) sample B, (6a) rotary table. b) Contact CMS: (1b) touch-probe head, (2b) ball tipped stylus, (3b) sample B, (4b) working table

6.3.1 Data acquisition and processing

The test sample was measured in the MMT temperature-controlled laboratory at (20 ± 0.5) °C. Three measurement repeats were performed, resulting in raw point clouds of approximately 100,000 points obtained by scanning the part at 360°, having the sample placed on the rotary stage. The acquired data was directly processed using the software GOM Scan [235].

The cleaning and processing of the datasets obtained from the fringe projection system consisted in removal of points belonging to the background surfaces surrounding the part, application of a noise filter based on outlier

detection, and deletion of isolated points, following the same approaches described in Section 6.2.1. Once the point clouds were cleaned from the measuring artefacts, they were reduced in size (*i.e.,* point count) to contain the computational complexity of the statistical model, in particular in the estimation of the covariance matrix (see Chapter 5). Size reduction was performed by resampling (see Section 2.2.3.1) in order to achieve a target spacing between neighbouring points, using the grid average method [139]. The point spacing was set at 0.5 mm as a compromise between cloud density and the need for preserving the integrity of the part edges. The resampled point clouds from the fringe projection measurements contained approximately 12,000 points each (example in Figure 6.13.a). For tactile CMS measurement performed in the same laboratory, three repeats in scanning mode of 10 µm spacing between consecutive points in a scan line, and 200 µm spacing between parallel scanlines were executed. Again, the point clouds obtained by tactile CMS were resampled from 950,000 to approximately 85,000 points each for the same computational reasons (Figure 6.13.b).

The reason for resampling and targeting very similar point spacing within the available measurements (both optical and contact) was also to favour the construction of the Gaussian random field (GRF) with bias via a) interpolation between neighbours and b) computation of intersections along the local normals in order to resample the data needed to populate the random variables of the GRF, procedure previously discussed in Section 5.2.2. Relying on intersections computed from interpolation may introduce additional error, presumably increasing the lower the density. Therefore, in order to avoid such

additional error sources, both contact and optical point clouds were resampled in order to achieve a similar spatial density.

The point normal vectors were computed via PCA, in the same way as the normals of the measurements of sample A were estimated (as illustrated in Section 4.3.2, following the methods described in the literature of Section 2.2.4.1). Normal orientations were fixed (so that they would point outwards) by using the EMST method (see Section 2.2.4.1).

The alignment of the final point clouds to the reference model provided by the test case manufacturer in form of triangle mesh in STL format was performed following the registration strategy presented in Chapter 3.

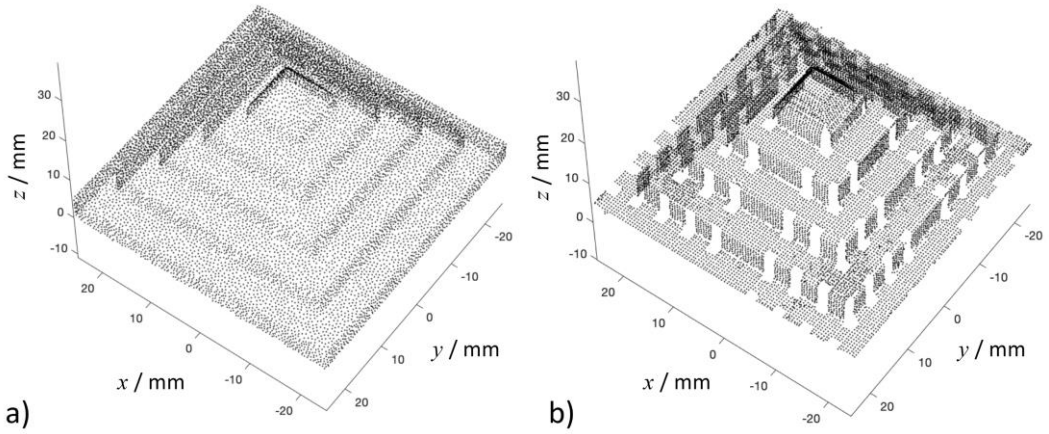

Figure 6.13 Example point clouds obtained from measurement of the pyramid sample B (after resampling). a) FP, b) contact CMS (visible gaps are non-measured regions to avoid collisions with the probe)

6.3.2 Results

The results shown in the following sections aim at addressing measurement quality and gain insights of the metrological performance of measurements, making the use of the statistical model and related indicators applied to sample B. Additional results obtained on simulated test cases can be found elsewhere [210], with the purpose of illustrating the performances of the proposed statistical model (as previously mentioned in Section 5.4) .

6.3.2.1 GRF-derived indicators

The results obtained from the application of the GRF-derived indicators described in Section 5.3.1 are shown in Figure 6.14 and Figure 6.15.

Figure 6.14 shows information regarding the variances in correspondence to specific regions of the measured part overlaid to the mean point cloud generated from the GRF, from FP measurement only. Figure 6.15 illustrates local bias information overlaid to the mean point cloud generated from the optical GRF of FP with respect to the GRF generated from tactile measurements, considered as reference. The map is produced only for those regions where the CMS data is available. Variance and bias values (reported in mm) have been truncated to allow for better visualisation of smaller differences.

The results of the local variance and local bias illustrated as spatially mapped return information about the instrument behaviour and performance in correspondence to specific form features on the measured part. The observation of the map of local variances for the optical GRF (Figure 6.14)

shows higher variance in correspondence to the base region of the test sample. The real test part (described at the beginning of Chapter 3) shows a clear warping at the base level, as a consequence of known shape bending often observed in Ti6Al4V parts fabricated by laser-powder bed fusion [238], as previously discussed in the registration results shown in Section 3.3.4.4.

The spatial distribution of bias (Figure 6.15) indicates that the FP measurement is positively biased at the bottom-most step of the pyramid, as well as in some of the tilted areas near the top of the sample. In the middle regions, bias appears to be consistently negative. To conclude, the deformation at the base of the test part may be responsible for both the observed bias and variance-related phenomena.

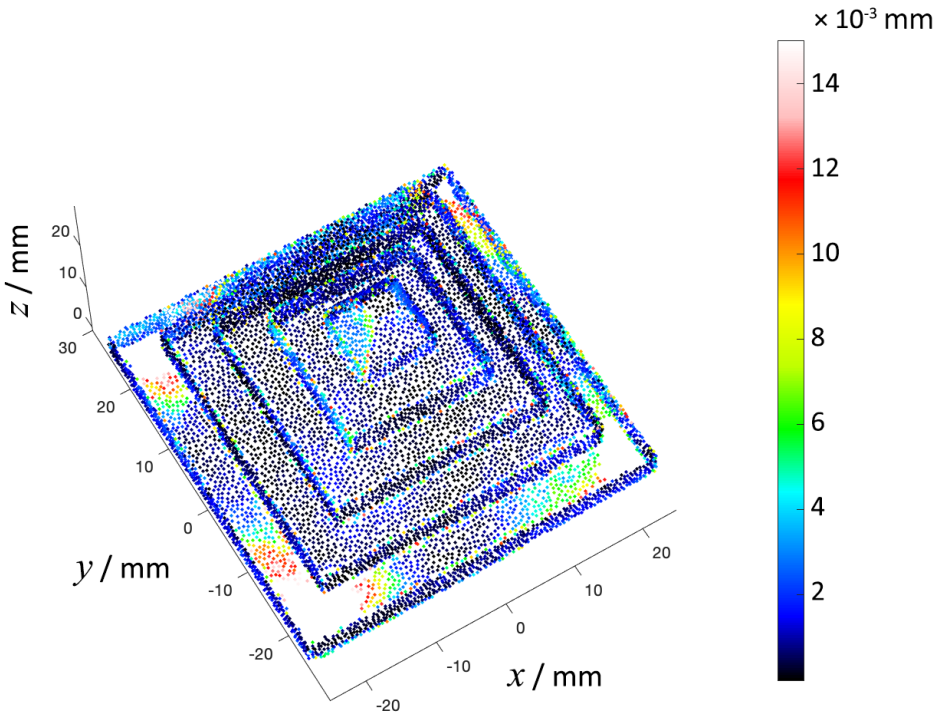

Figure 6.14 Spatial map of local variances for FP measurement of sample B. The mean point cloud from the optical GRF is coloured according to local variance (using optical GRF only)

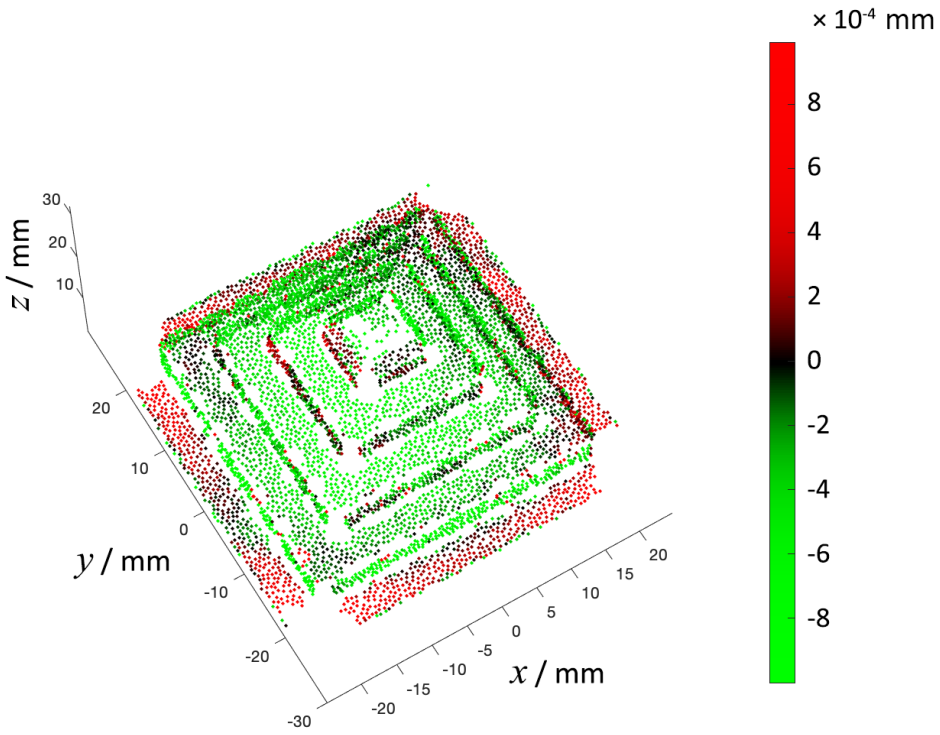

Figure 6.15 Spatial map of local bias for FP measurement of sample B. The mean point cloud from the optical GRF is coloured according to local bias (using the CMS GRF as reference)

6.3.2.2 Indicators based on new observations generated from the GRF

For the application of the indicators discussed in Section 5.3.2 related to the inspection and verification of shape and size, a typical point cloud processing pipeline consists of the segmentation of the point clouds into different segments (subsets of neighbouring points) and the subsequent fitting to datum surfaces. This procedure, previously illustrated in Section 5.3.2, is needed in order to select the features of size subjected to inspection and it is applied to all the point clouds available.

In this work, the pipeline was applied to the FP and contact-CMS point clouds of the test sample and consisted of the following steps:

- point cloud partitioning (Figure 6.16) using the signed direction of the local normal computed by PCA in combination with k-means clustering (see literature in Section 2.2.4.4). Points with similar orientation of local normal were grouped into clusters, isolating subsets of points belonging to the same planar face and thus partitioning the geometry of the sample in its constituent faces. Clustering was performed with $k = 5$ in order to compensate for the lack of points on the bottom surface (negative z orientation);
- splitting of each region recursively into subregions by running a second k-means clustering operation based on point placement along the axis identified by the direction associated to the cluster. For example, the region associated to the positive x direction was split into five sub-clusters to accommodate for the presence of five surfaces along the positive x axis;
- selection of the segmented regions of the point clouds and fitting of datum surfaces (Figure 6.17.a; the surfaces of each pair were individually fitted to planar datum features using Random sample consensus (RANSAC) and total least-squares - see Section 2.2.5.1);
- selection of one datum per pair as primary, and computation of the Euclidean distance between the datum centroid and the intersection with the other datum, computed along the direction of the local normal to the primary datum (Figure 6.17.b).

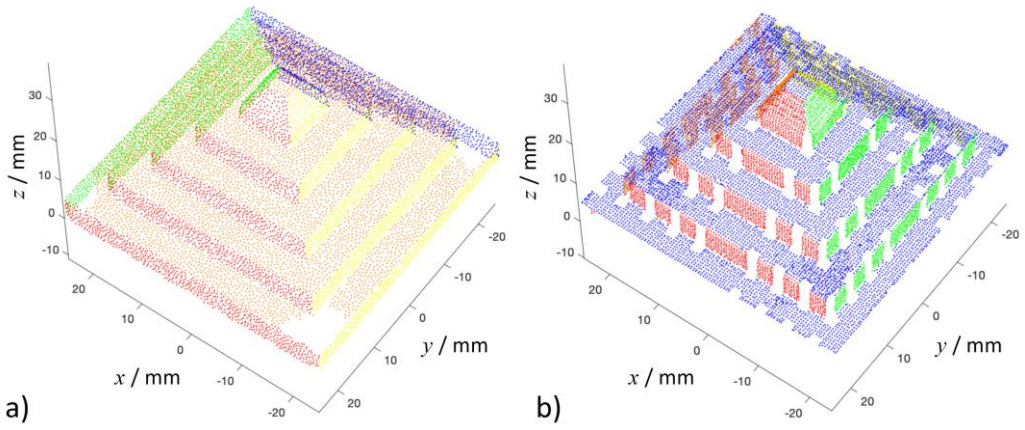

Figure 6.16 Results of the first segmentation step on the point clouds (k-means on local normals). a) FP, b) contact CMS (colours represent different clusters as identified by the k-means method)

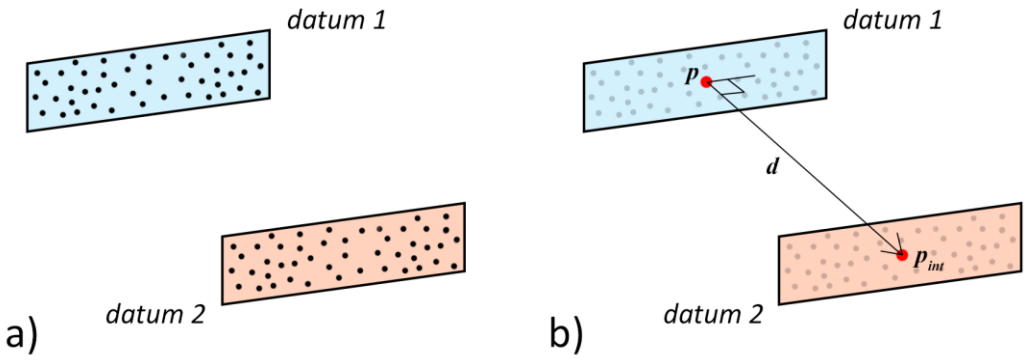

Figure 6.17 Procedure to determine a linear dimension as the distance between two datum planes. a) Two subsets of points (black dots) resulting from segmentation are isolated and independently fitted to datum planes (in light blue *datum 1* and in orange *datum 2*); b) a ray orthogonal to *datum 1* is drawn from the point $\boldsymbol{p}$ (resulting centroid computed by the projection of all the fitted points on their associated datum) to the intersection point $\boldsymbol{p}_{int}$ with *datum 2*. The Euclidean distance $\boldsymbol{d}$ between $\boldsymbol{p}$ and $\boldsymbol{p}_{int}$ is the linear dimension selected as target attribute

Figure 6.18 shows the two linear dimensions (distances $\boldsymbol{dx}$ and $\boldsymbol{dz}$, aligned to the x and z axes respectively) selected as the target attributes. The dimension $\boldsymbol{dx}$ refers to the distance between parallel walls measured at the first "step" of the pyramid, aligned to the x axis. The dimension $\boldsymbol{dz}$ refers to the vertical (*i.e.*, along the z axis) distance between the top surface of the pyramid and the surface of the first step.

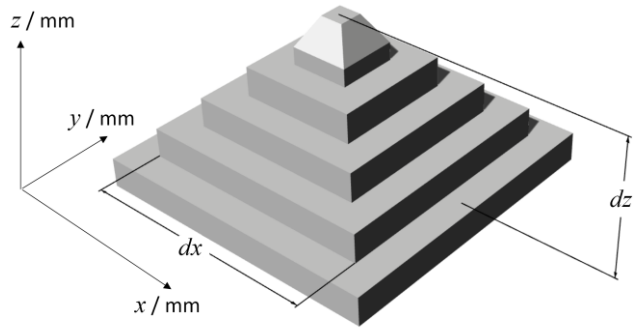

Figure 6.18 CAD model representation of the selected test part (sample B), indicating also the features of size (linear dimensions) selected for the characterisation

Figure 6.19 shows the results of the probability distributions for the selected dimensions $\boldsymbol{dx}$ (Figure 6.19.a) and $\boldsymbol{dz}$ (Figure 6.19.b). In the figure:

- the black line represents the value of the targeted feature of size, as the mean of three values obtained from the three contact CMS repeats ($\pm\,\mathrm{MPE}/\sqrt{3}$);
- the red line represents the value of the same feature of size, obtained by the statistical model, via Monte Carlo simulation over the FP repeats;
- the distance between the red and black line is the signed bias (defined as signed distance and signed percentage in Section 5.3.2) of the FP instrument with respect to the contact CMS.

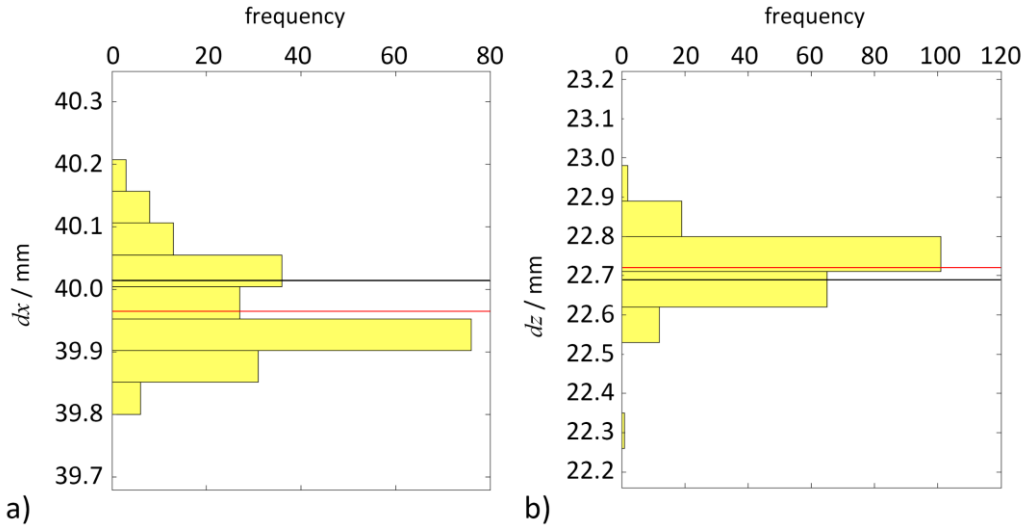

Figure 6.19 Histogram of the estimated distribution (yellow) with mean value (red line) compared to reference CMS result (black line). a) Feature of size dx, b) feature of size dz

Using the maximum permissible scanning probing error of the tactile CMS ($MPE_{THP} = 2.2$ µm) as reported by the manufacturer, the results for the biases defined as signed distance and as signed percentage for the selected features of size dx and dz are reported in Table 6.6, using equations (5.10) and (5.11) reported in Section 5.3.2. The biases resulted in approximately one order of magnitude larger than the CMS uncertainty.

Table 6.6 Bias for selected features of size

Feature	$\mathbf{bias}_{dx:(FP-CMS)}$	$\mathbf{bias\%}_{dx:(FP-CMS)}$
Distance dx	(-48.53 ± 1.27) µm	(-0.12 ± 0.03) %
Distance dz	(30.79 ± 1.27) µm	(0.13 ± 0.04) %

6.3.3 Discussion and section conclusions

From the application of the developed statistical point cloud model and derived indicators it was possible to investigate how measurement error can be spatially mapped to all the regions of any given part. Indicators related to spatial details on precision and bias can highlight the performances and behaviour of measurement technologies with respect to specific types of surface features (flat, curved, step-like, high aspect-ratio, smooth, irregular, *etc.*). In particular from the observations reported in the previous sections, bias emerged as a fundamental component of measurement error. In this work, it was possible to rely on a more accurate additional set of measurements performed with a tactile CMS and indicators of bias could be estimated and integrated into the proposed framework, providing an overall more complete depiction of measurement error.

The possibility to rely on a separate prediction mathematical model capable of producing bias information mapped to each location of a part geometry would be the ideal solution, especially when the availability of a more accurate set of measurements is not practicable. However, the generation of a bias-estimation model is far from straightforward, as demonstrated by current literature on the subject (see Section 2.1.1.1).

The proposed statistical model and set of indicators aim at contributing towards the development of a solution for point cloud uncertainty, even if the illustrated results are valid only for the specific test case and only for the repeatability and reproducibility conditions the measurements have been obtained in.

6.4 Chapter conclusions

In this chapter, a complete report of the results obtained from the application of the designed performance indicators on high-density optical measurements of selected industrial cases was presented.

The first series of performance indicators, designed to capture various aspect of measurement performance including extents of coverage and density, were applied to the comparative evaluation of measurement results obtained from single point clouds measured using three optical measuring systems on the same freeform, automotive AM part. Measurements obtained from a contact CMS were used as reference baseline.

The indicators generated from the statistical point cloud model provided a detailed depiction of the random component of measurement error (in repeatability or reproducibility conditions, depending on how the repeats are taken), and bias information (with the use of tactile measurements as reference). Results of the indicators designed to acquire information on how dispersion and bias vary locally over the surfaces of the measured part were shown, as well as indicators developed for the inspection and verification of targeted features of size.

Both proposed sets of indicators were designed in order to be integrated into measurement systems as new "smart" functionalities for full automation of measurement procedures and self-assessment of quality while the system is in operation. Thanks to those defined integrated smart functionalities, the systems will be capable of autonomously performing corrective actions in order to improve the final quality of the measurement result.

Chapter 7

Conclusions and outlook

The increased introduction of additive manufacturing (AM) technologies in the manufacturing industry, with parts featuring highly complex freeform shapes fabricated with great flexibility, as a large variety of different designs can be quickly made in low production volumes, is creating nowadays a pressing need for the development of new application-specific measurement systems and optimised measurement strategies. In particular, new measuring instruments (defined as smart and flexible systems in the "Manufacturing Metrology 2020" roadmap VDI/VDE-GMA [17,18], definitions of which are adopted in this thesis), combined with integrated algorithmic solutions, are envisioned as capable of measuring the complex form of the parts autonomously whilst ensuring accuracy and traceability, increasing confidence

in AM produced parts across all engineering industries, and self-assessing the quality of the measuring results in real-time.

In this context, metrology represents one of the most fundamental sciences in the engineering research and industry to contribute towards the development of such intelligent measurement means. The use of optical coordinate technologies, such as photogrammetry, structured light and laser-based triangulation, to measure the shape of freeform or otherwise complex geometries, is appealing given the high densities in point-based sampling, speed rates and ease of measurement. With such technologies, the inspection of a complex geometry is typically accomplished by a) acquiring three-dimensional (3D) point clouds with the optical instrument of choice, b) registering the point clouds to the nominal geometry (available as a CAD model), and then c) assessing the quality of the measured part (*i.e.,* comparing the points in the cloud with respect to the aligned surfaces of the CAD model, and evaluate the measurement uncertainty in selected geometric and dimensional features). Therefore, measurement is the main element to assess the quality of a part, and, in order to better understand how reliable the estimation of a part quality is, the assessment of the quality in the measurement result itself is crucial. Measurement uncertainty is one of such ways to estimate the quality of a measurement; however, it is not the only one, given the contents presented in this thesis.

Indeed, assessing the quality in measurement is not simply intended as evaluating indicators of metrological performance (such as accuracy, precision, *etc.*). As measurement technologies evolve, increasingly denser point clouds are being produced, capable of capturing information of measured parts with

higher level of details, whilst suggesting a number of new aspects worth being investigated for measurement quality evaluation. For instance, the calculation of measurement time rates (*i.e.,* data acquisition, point cloud reconstruction, *etc.*), the evaluation of the degree of coverage of a measurement (*i.e.,* percentage of the external surface of an object successfully measured), the assessment of part accessibility (*i.e.,* capability for a given measurement technology to reach occluded surfaces or hidden regions from the line-of-sight) are only a few examples of such analysis.

Furthermore, the displacement between any point of the measured cloud and the nominal surface of the CAD is not solely representative of the difference between the nominal and the real geometry, because of the presence of measurement-related error. Error encompasses several sources, the two primary ones being the error intrinsic to the technology and instruments used to acquire the point clouds (*i.e.,* error affecting the position of the points within the point cloud), and computational error (*i.e.,* error grown within the point cloud processing pipeline, such as filtering, stitching, registration, computation of distances, *etc.*).

Based on identified knowledge gaps and needs in the current research and industrial scenarios illustrated in Chapter 1, the proposed work presented in this thesis focused on the preliminary development of sets of algorithmic solutions in form of measurement quality indicators, designed in order to be integrated into the measurement pipeline, and guide optical coordinate measuring systems (CMSs) towards future full automation of part inspection and intelligent measurement planning.

In order to address the need for new smart measurement systems that can overcome the aforementioned limitations, especially encountered in the AM industry, Chapter 2 began with a general overview of metrology and uncertainty in measurement, along with the basic concepts of the most suitable non-contact coordinate technologies for the measurement of AM parts. Furthermore, as the main goal of this work is the development of a point cloud processing pipeline with integrated quality assessment algorithms, recent literature on measurement performance indicators and integration of available pre-existing knowledge into the measuring pipeline was reviewed. Additionally, a state-of-the-art review in point cloud analysis and processing was illustrated, covering several aspects of the pipeline, starting from point cloud formal representation, pre-processing, partitioning, fitting, registration and comparison to CAD, including methods for the incorporation of uncertainty into point cloud data.

7.1 Contributions to the field

The designed performance indicators aimed at providing insights related to both assessment of quality under broader perspectives (such as performance and behaviour of measurement at the point cloud level, for example coverage, accessibility of a part surface, sampling and density representativeness, and spatial dispersion of the points with respect to an associated reference surface), and evaluation of positional uncertainty in point cloud surface data. The main contributions of this thesis are summarised concisely by chapter, consisting of

the key findings and important observations of the work carried out and the answers to the research questions listed in Chapter 1.

Chapter 3 described the steps required to achieve registration of a measured point cloud to the reference geometry representing the part. Registration is a fundamental aspect of the measurement pipeline, key step needed in order to assess the localisation of the measured points with respect to the reference geometry and consequently compute the indicators. From the registration approach based on landmark matching using similarity metrics applied to selected industrial cases featuring AM components, the following observations are made:

- AM parts vary significantly in terms of shape and geometric features, therefore a procedure to determine suitable registration approaches should be performed for each new test case;
- the presence of geometric elements in the shape of a sample (for example hollow shapes, recesses, sharp edges, slot-holes) contributes to the identification of distinct attributes (i.e., local point features or regions with similar properties) used to perform registration. In the specific case of sample C (arm bracket), the presence of distinct geometric features represented a significant advantage and resulted in a successful convergence with the reference model despite the partially symmetric shape of the sample (see results reported in Section 3.3.5.4). On the other hand, the freeform shape of sample A (roof bracket) would have suggested an easy identification of similar landmark features between

the datasets, especially in correspondence of complex geometric elements; however, the results obtained were still contaminated by incorrect matches, justified by the presence of similar information (i.e., properties such as curvature and normals orientation) in the neighbouring points, thus reducing the selected local feature informative characteristics (see results reported in Section 3.3.3.4);

- symmetry in shape and large featureless surfaces (*i.e.,* large flat or spherical regions) characterising the sample can cause problems and lead the registration algorithm towards convergence failure. An important example is given by sample B (pyramid): its symmetric shape and the presence of large flat surfaces with similar attributes and characteristics contributed to the unsuccessful matching of correct correspondences (see results reported in Section 3.3.4.4). As previously mentioned, even in the case of a completely asymmetrical shape (Sample A) the absence of robust point attributes to fully constrain the transformation challenged the registration process (Section 3.3.3.4);
- the choice made in terms of point features or shape descriptors selected as landmarks for registration should be sufficiently discriminative and robust to point cloud density variation and completeness. This is demonstrated by the majority of the test results of samples A and C shown in Sections 3.3.3.4 and 3.3.5.4, as the complete datasets have always shown the best registration convergences. The best results were seen in the application of FPFH descriptors, due to their discriminative power and capability of encoding neighbourhood's geometrical properties more extensively than curvature values. The only exception

is given by the results obtained for sample B at Section 3.3.4.4: in this particular case, the symmetric shape caused significant convergence failures for both partial and complete datasets, regardless of the landmark feature selected to perform registration.

Chapter 4 introduced the first set of indicators, their definitions and related quantitative metrics, aimed at assessing the quality of individual high-density point clouds produced by optical technologies and registered to the available *a priori* triangle mesh geometry. This set of developed algorithmic solutions gave answers to the research questions, defining novel aspects of measurement quality with a deeper meaning. The findings and important observations from this chapter are:

- measurement quality is not solely defined by measurement uncertainty; multiple aspects, such as measurement effort, intrinsic properties of a point cloud, part coverage, density in point-based sampling, point dispersion, *etc.*, potentially describe the quality of a measurement result, the performances of a measuring instrument, and, in general, the quality of a measuring procedure;
- the indicators are designed to be integrated into the measurement pipeline as new "smart" functionalities for future full automation of measurement procedures and self-assessment of quality while the system is in operation; therefore, the numerical results, graphs and figures are all implemented in a fully automated way and plotted out from a chain

of customised knowledge-driven algorithms and functions scripted in MATLAB;

- the way the indicators are designed, based on points association to a reference datum, allows to tag the point cloud in regions of interest that have specific measurement requirements (for example coverage, and precision of critical areas). The indicators (in particular those of dispersion of point-to-surface distances) highlight the presence of critical areas, especially in correspondence of slot-holes, recesses, features of high aspect ratio. In these regions, the indicators depict areas with higher dispersion values, tagging them with different colours compared to other surfaces. This is demonstrated by the results reported in Chapter 6;
- the indicators represent the feedback mechanisms that can guide intelligent systems towards autonomous corrections and decisional actions, offering detailed maps of measurement performance and behaviour in correspondence to every region of the part. For instance, the indicator of part coverage results in colourmaps of covered and uncovered triangles, rendered using binary colouring. This green/red light system is designed to be implemented into measuring machines as a next-best-view planning algorithm (see results reported in Chapter 6 and Appendix A).

Chapter 5 presented the second set of indicators derived from the development of a statistical point cloud model for point positional uncertainty. The implemented computational procedure started from the

knowledge of nominal geometry and multiple point clouds obtained from measurement repeats produced by optical technologies. The findings and observations made in this chapter are:

- the statistical model is developed to predict the variation of point placement along the direction of the local normal within the point cloud across repeated measurements (*i.e.,* assessment of precision within the point cloud). This approach has been chosen in order to allow for a continuity with the indicators of metrological performance defined in Section 4.2.4, in particular those related to the local point scatter with respect to a reference surface (i.e., triangle facets in the reference mesh). In this way, the indicators of dispersion and variability presented in Chapters 4 and 5 are both modelled along the direction of normal vectors to each triangle, describing the local precision of the measurement (a single point cloud for the indicators of metrological performance in Section 4.2.4 and multiple measurements for the GRF-derived indicators in Section 5.3.1);
- the model can be aggregated with further measurement data from tactile measurements (assumed as accurate reference) in order to obtain accuracy-related information;
- the indicators provide new means to investigate how measurement error is spatially mapped to all the regions of any given part, useful in the routine inspection of manufactured parts in a production scenario, depicting for instance warping of the workpieces and presence of defects (see results reported in Chapter 6);

- the derived indicators cover aspects related to the dispersion of the points across measurement repeats, and to local bias (assuming the availability of a more accurate model or measurement to be considered as reference), as discussed in Section 5.3 (indicators of local bias, spatial maps of local bias and bias for features of size);
- the indicators based on new "virtual" observations generated from the statistical model in combination with Monte Carlo simulations are able to replicate the statistical properties of the original observations, saving the time and resources required in a real repeated measurement procedure;
- the derived indicators are designed to be directly useable in a smart measurement system mainly if it implements a measurement technology where taking multiple measurements is viable and does not imply excessive cost.

Chapter 6 illustrated the application of the indicators defined in Chapters 4 and 5 on selected industrial cases (described in Chapter 3) measured with different optical instruments. The findings of this chapter are:

- measurement performance should be assessed through multiple viewpoints, not necessarily limited to assessing uncertainty on dimensional results;
- measurement solutions should be carefully selected depending on the test case, and a proper measurement workflow should be planned based

on consideration of instruments performances, in order to achieve optimal results;

- the performance indicators applied to the test cases showed a preliminary investigation of the performances of different optical technologies under multiple perspectives, representing a starting point for the outline of large measurement campaigns;
- each measurement solution may be seen as prevailing when considering any specific performance aspect. For example, fringe projection resulted in the highest coverage and lower uncertainty in correspondence to critical areas (i.e., internal regions and features of size - see results reported in Sections 6.2.2.3 and 6.2.2.4, and Appendix A);
- all defined indicators (in particular those related to spatial maps of precision and bias) can highlight the performance and behaviour of measurement technologies with respect to specific types of surface features (flat, curved, step-like, high aspect-ratio, smooth, irregular, *etc.*), as it is shown by the numerical results and colourmaps reported in Chapter 6. In particular, the results of the application of the indicators to a real test case (see Section 6.3.2.1) show a clear warping at the base of test part sample B, as a consequence of known shape bending often observed in Ti6Al4V parts fabricated by laser-powder bed fusion;
- all defined indicators can be implemented to be spatially mapped both on the point clouds and onto the surface of the underlying reference model, showing immediate feedbacks and information of the measured results, as it is shown by the numerical results and colourmaps reported

in Section 6.2.2. For instance, from the results shown in Section 6.2.2.3 the colourmaps of point-to-surface distances and dispersion of point-to-surface distances highlighted the presence of critical areas, especially in correspondence of the slot-holes. In these regions, the indicators highlighted the presence of areas with higher dispersion values compared to other surfaces of the selected part (tagged with different colours).

7.1.1 Industrial impact

There are a number of notable outcomes that stem from the work presented in this Ph.D. thesis with applicability in real industrial environments. Novel methods of data/technology/instrument comparison and 3D point clouds uncertainty evaluation have been developed for the determination of appropriate measurement technologies for specific applications, and for the validation of optical form measurement instruments. In this work, these techniques have been demonstrated specifically in the case of form measurement of complex AM geometries; however, the developed methods are manufacturing technology, shape, scale, and material independent. As such, these methods can be applied to a large variety of industrial manufacturing metrology processes (such as in-line inspections and on-machine monitoring), but also extending, for example, to conventional fabrication methods not only limited to AM, assembly processes, and, in larger scale, surveying.

The results presented throughout this thesis imply that the developed indicators of measurement performance (*i.e.*, coverage, sampling density, *etc.*) present a potentially useful tool for the assessment of difficult-to-access

surfaces, and the consequent determination of next-best-view measurement planning. Establishing the methods presented in this work in industry will help speed up the inspection process, and so improve the production in high value manufacturing scenario. The major input is represented by the developed tools for establishing confidence in measurement: trust is the key demanded by modern industrial sectors, such as aerospace, automotive and biomedical ones, and, as a contribution to the metrology and manufacturing communities, the developed statistical model and related indicators will lead towards the complete estimation of uncertainty in 3D point clouds and will ultimately result in improved part quality and reduced manufacturing waste.

7.2 Areas for future work

There are many areas of future work that can be carried out in order to further the aims in developing methods for the assessment of measurement quality. The main areas for future developments reside in the definition of increasingly more advanced strategies for measurement planning optimisation, especially those making the use of available *a priori* knowledge and smart knowledge-driven algorithms (including machine learning). For what concerns point clouds, generally speaking every single phase of the processing pipeline, from partitioning and segmentation to registration and fitting, is an ongoing research area.

For instance, registration is still an active topic, leading researchers to develop always more optimised, efficient and fast algorithmic solutions. In

particular, from Chapter 3 emerged the major issue related to point cloud registration instability: featureless/symmetric shapes increase the challenges in the alignment procedure. In those cases, registration results might be contaminated with incorrect matches, causing lack of stability (sliding between the datasets, upside-down registration results between point cloud and reference CAD, *etc.*) and consequent failure of the final registration outcome. Therefore, new approaches for the registration of specifically targeted featureless/symmetric point clouds and shapes need to be developed, finding ways to constrain the rigid transformation, and optimise the detection of key points (*i.e.,* finding optimal correspondences between reference and target datasets).

The quality indicators proposed in Chapter 4 were designed for planning more optimised, additional measurement processes, envisioned as a starting point for the development of future intelligent measurement systems. In particular, the indicators have been implemented as customised knowledge-driven algorithms and functions scripted in MATLAB, designed in a way that allows direct future integration with physical instruments. By comparing the collected point clouds to the available mesh geometry, the system will be able to analyse point by point the dispersion of the measurements, as well as return feedbacks in real-time of any extra scan views required, locating occlusions or areas needing more data to satisfy sampling density criteria.

Furthermore, as previously mentioned in Section 7.1, the indicators could represent potential means for quantitative comparison in large measuring campaigns of test parts, measurement conditions, algorithmic solutions, and instruments, leading to general results and considerations. The

results of the indicators defined in Chapter 4 and applied to a real geometry showcased in Chapter 6 should be seen as an example application of the proposed novel methods for the assessment of measurement quality. The results represented a preliminary investigation of three optical technologies on a specific industrial application. Obviously, the presented comparison is limited to the instruments and technologies employed. Nevertheless, the indicators and related results provided elements of general interest, featuring a starting point for further investigations.

Following the same theme of full integration of the pipeline into a physical measurement system prototype and efficient implementation of the developed algorithms, the idea emerging from the method illustrated in Chapter 5 and applied to an example test case in Chapter 6 was that a smart measurement system should be able to autonomously build the statistical model from a set of repeated measurements and use it to autonomously return the results of derived indicators. More specifically, the construction of maps of local bias and variance could serve as guidance to assess where measurement performed better and where it performed worse, in order to plan further measurement actions.

In addition, error estimation associated to linear dimensions could assess immediate reliability in a part inspection scenario. Generally speaking, the developed procedure would be useful for detailed investigations of the general behaviour of measurement solutions in relation to specific types of geometries, materials, aspect ratios, types of surface features (flat, curved, step-like, high aspect-ratio, smooth, irregular, *etc.*). This will potentially suggest new correlations that will allow a valid uncertainty budget to be established.

Strictly related to the design of the statistical model developed, areas for future work involve investigation of different methods to estimate mean and covariance in the random field, and the analysis of the consequences of choosing different interpolation and normal projection strategies when aggregating observations (individual point clouds), as well as an investigation on the effects of geometric registration. Furthermore, an important step yet to be made is the incorporation of mathematical models to predict local bias, in order to remove the need for additional measurements with supposedly more accurate instruments.

Future work would also include the development of a Monte Carlo procedure to propagate the variation of points' position through all the algorithmic steps of the point cloud processing pipeline (*i.e.,* point cloud filtering, registration to CAD geometry, *etc.*); in addition, with the use of computational geometry and spatial statistics, the performance indicators of coverage and density recorded across measurement repeats would also be integrated into the frame of statistical point cloud models and propagated via simulations.

7.3 Summary

The research work presented in this thesis produced sets of knowledge-driven algorithmic solutions in form of performance indicators, suitable for implementation into optical form measuring instruments. The developed indicators and related metrics aim at contributing towards the development

of future smart measuring instruments and processes, with the goal of guiding such systems and providing feedback in real-time, while the measurements themselves are being executed. The indicators, working at a point cloud-level, were designed as integral parts of the measurement pipeline, starting from the sole knowledge of the input datasets (*i.e.,* measured point cloud and underlying triangle mesh geometry). A number of methodologies were developed throughout this thesis, which can be used for further investigation of quality enhancement in measurement and to increase the understanding of parts inspection and verification results in manufacturing sectors. The results from the application of the developed sets of indicators and point cloud statistical model represent an important step towards a better understanding of performance and behaviour for optical measurement systems. This work will help develop new intelligent means for optimised measurement planning procedures, helping measuring instruments, which are nowadays asked to inspect a large variety of different complex geometries, such as those produced by AM technologies, to assess quality for fabricated parts in the manufacturing industry.

7.3.1 Technology readiness level

According to the technology readiness level (TRL) rankings and metrics for technology assessment as adapted from NASA and DOD practice, this Ph.D. research can be set between TRL3 "Proof-of-concept" and TRL4 "Lab-scale demonstration ("low fidelity")". The developed performance indicators were tested on a limited number of selected technologies and test parts; therefore,

the technology is not yet ready for immediate use and deployment in industry. Being the indicators the result of an academic research effort, more resources and time will be needed to make them more reliable for marketing purposes. More specifically, with further testing campaigns involving multiple measurement technologies and test cases, the level of technology demonstration and fidelity will increase (TRL5), and the indicators will be ready to be integrated and tested into a real system prototype (TRL6). As mentioned throughout this thesis, the quality criteria have been implemented as customised knowledge-driven algorithms and functions scripted in MATLAB, designed since the beginning of the project in a user-friendly way that allows easy and direct integration into physical measuring instruments. More specifically, as output of the application of the indicators to real test geometries, a set of customised colourmaps and numerical results can be stored and easily decoded by any human operator and instrument.

References

[1] ISO/ASTM 52900 2015 *Additive manufacturing - General principles - terminology* (International Organisation for Standardisation)

[2] Savio E, De Chiffre L, Schmitt R 2007 Metrology of freeform shaped parts *CIRP Ann.* **56** 810-835

[3] ISO 17450 part 1 2011 *Geometrical Product Specifications (GPS) – General Concepts - Part 1: Model for geometrical specification and verification* (International Organization for Standardization)

[4] Gibson I, Rosen D W, Stucker B 2010 *Additive Manufacturing Technologies: 3D Printing, Rapid Prototyping, and Direct Digital Manufacturing* (New York, USA: Springer)

[5] Leach R K, Bourell D, Carmignato S, Donmez A, Senin N, Dewulf W 2019 Geometrical metrology for metal additive manufacturing *CIRP Ann.* **68** 677-700

[6] Aloisi V, Carmignato S 2016 Influence of surface roughness on X-ray computed tomography dimensional measurements of additive manufactured parts *Case Stud. Nondestruct. Test Eval.* **6**/B 104-110

[7] Boeckmans B, Tan Y, Welkenhuyzen Y, Guo F, Dewulf W, Kruth J

P 2015 Roughness offset differences between contact and non-contact measurements *Proc. euspen, Leuven, Belgium, Jun.* 189-190

[8] Carmignato S, Aloisi V, Medeossi F, Zanini F, Savio E 2017 Influence of surface roughness on computed tomography dimensional measurements *CIRP Ann.* **66** 499-502

[9] Rivas Santos V M, Thompson A, Sims-Waterhouse D, Maskery I, Woolliams P, Leach R K 2020 Design and characterisation of an additive manufacturing benchmarking artefact following a design-for-metrology approach *Addit. Manuf.* **32** 100964

[10] Stavroulakis P, Leach R K 2016 Review of post-process optical form metrology for industrial-grade metal additive manufactured components *Rev. Sci. Instrum.* **87** 041101

[11] Gao W, Haitjema H, Fang F Z, Leach R K, Cheung C F, Savio E, Linares J M 2019 On-machine and in-process surface metrology for precision manufacturing *CIRP Ann.* **68** 843-866

[12] Lee J, Bagheri B, Kao H A 2015 A Cyber-Physical Systems architecture for Industry 4.0-based manufacturing systems *Manuf. Lett.* **3** 18-23

[13] Monostori L, Kádár B, Bauernhansl T, Kondoh S, Kumara S, Reinhart G, Sauer O, Schuh G, Sihn W, Ueda K 2016 Cyber-physical systems in manufacturing *CIRP Ann.* **65** 621-641

[14] Varadan V K 2005 *Handbook of Smart Systems and Materials* (IOP Publishing: London)

[15] Pascual D G, Daponte P, Kumar U 2019 *Handbook of Industry 4.0 and SMART Systems* (CRC Press)

[16] Imkamp D, Berthold J, Heizmann M, Kniel K, Peterek M, Schmitt R, Seidler J, Sommer K-D 2016 Challenges and trends in manufacturing measurement technology – the "Industrie 4.0" concept *J. Sens. Sens. Syst.* **5** 325–335

[17] VDI/VDE-GMA 2011 *Fertigungsmesstechnik 2020: Technologie-Roadmap für die Messtechnik in der industriellen Produktion* (VDI-Verlag: Düsseldorf)

[18] Berthold J, Imkamp D 2013 Looking at the future of manufacturing metrology: roadmap document of the German VDI/VDE Society for Measurement and Automatic Control *J. Sens. Sens. Syst.* **2** 1–7

[19] Senin N, Leach R K 2018 Information-rich surface metrology *Proc. CIRP* **75** 19-26

[20] Leach R K, Bointon P, Feng X, Lawes S, Piano S, Senin N, Sims-Waterhouse D, Stavroulakis P, Su R, Syam W, Thomas M 2019 Information-rich manufacturing metrology *Proc. 8th IPAS 2018, Chamonix, France* 145-157

[21] Leach R K, Senin N, Feng X, Stavroulakis P, Su R, Syam W P, Widjanarko T 2017 Information rich metrology: changing the game *Commer. Micro Manuf.* **8** 33-39

[22] Carmignato S, De Chiffre L, Bosse H, Leach R K, Balsamo A, Estler W T 2020 Dimensional artefacts to achieve metrological traceability in advanced manufacturing *CIRP Ann.* **69** 693-716

[23] Catalucci S, Senin N 2020 *State of the art in point cloud analysis.* In: Leach R K *Advances in Optical Form and Coordinate Metrology* (IOP Publishing), Chap. 2

[24] BIPM, IEC, IFCC, ILAC, ISO, IUPAC, IUPAP and OIML 2012 *International Vocabulary of Metrology—Basic and General Concepts and Associated Terms* (Bureau International des Poids et Mesures) JCGM 200

[25] BIPM 2019 *Le Système International d'Unités* (Paris, France: Bureau International des Poids et Mesures), 9th edition

[26] Ferrucci M, Haitjema H, Leach R K 2018 Dimensional metrology. In: Leach R K, Smith S T *Basics of Precision Engineering* (CRC Press: New York), Chap. 5

[27] Haitjema H 2018 *Measurement uncertainty.* In: Leach R K, Smith S T *Basics of Precision Engineering* (CRC Press), Chap. 9

[28] JCGM 100 2008 *GUM 1995 with minor corrections, Evaluation of measurement data — Guide to the expression of uncertainty in measurement* (BIPM: France)

[29] Leach R K, Shaheen A 2020 *Post-process coordinate metrology.* In: R K Leach, S Carmignato *Precision Metal Additive Manufacturing* (CRC Press), Chap. 10

[30] Barchiesi D, Grosges T 2017 Propagation of uncertainties and applications in numerical modeling: tutorial *J. Opt. Soc. Am. A* **34** 1602-1619

[31] Gayton G, Su R, Leach R K, Bradley-Smith L 2019 Uncertainty evaluation of fringe projection based on linear systems theory *Proc. 35th CMSC, Orlando, USA*

[32] Lou S, Brown S B, Sun W, Zeng W, Jiang X, Scott P J 2019 An investigation of the mechanical filtering effect of tactile CMM in the

measurement of additively manufactured parts *Measurement* **144** 173-182

[33] ISO 15530 part 3 2011 *Geometrical Product Specifications (GPS) – Coordinate measuring machines (CMM): Technique for determining the uncertainty of measurement - Part 3: Use of calibrated workpieces or standards* (International Organization for Standardization)

[34] ISO/TS 15530 part 4 2008 *Geometrical Product Specifications (GPS) – Coordinate measuring machines (CMM): Technique for determining the uncertainty of measurement - Part 4: Evaluating task-specific measurement uncertainty using simulation* (International Organization for Standardization)

[35] Balsamo A, Di Ciommo M, Mugno R, Rebaglia B I, Ricci E, Grella R 1999 Evaluation of CMM Uncertainty through Monte Carlo simulations *CIRP Ann.* **48** 425-428

[36] Flack D 2013 Measurement Good Practice Guide No. 130 Co-ordinate measuring machine task-specific measurement uncertainties (National Physical Laboratory: London)

[37] Zhang B, Davies A, Evans C, Ziegert J 2018 Validity of the instrument transfer function for fringe projection metrology *Appl. Opt.* **57** 2795-2803

[38] Sims-Waterhouse D, Isa M, Piano S, Leach R K 2020 Uncertainty model for a traceable stereo-photogrammetry system *Precis. Eng.* **63** 1-9

[39] Vora H D, Sanyal S 2020 A comprehensive review: metrology in additive manufacturing and 3D printing technology *Prog. Addit.*

Manuf. **4**

[40] Leach R K 2020 *Advances in Optical Form and Coordinate Metrology* (IOP Publishing)

[41] Harding K 2016 *Handbook of Optical Dimensional Metrology* (CRC Press)

[42] Hocken R J, Pereira P H 2011 *Coordinate Measuring Machines and Systems* (CRC Press), 2nd edition

[43] Hammett P C, Guzman L G, Frescoln K D, Ellison S J 2005 Changing automotive body measurement system paradigms with 3D non-contact measurement systems *SAE 2005 World Congress & Exhibition*

[44] De Chiffre L, Hansen H N, Andreasen J L, Savio E, Carmignato S 2016 *Geometrical Metrology and Machine Testing* (Polyteknisk Boghandel)

[45] Se S, Pears N 2020 *Passive 3D imaging.* In: Liu Y, Pears N, Rosin P L, Huber P *3D Imaging, Analysis and Applications* (Springer), 2nd edition, Chap. 2

[46] Drouin M A, Beraldin J A 2020 *Active triangulation 3D imaging systems for industrial inspection.* In: Liu Y, Pears N, Rosin P L, Huber P *3D Imaging, Analysis and Applications* (Springer), 2nd edition, Chap. 3

[47] Guerra M G, Lavecchia F, Maggipinto G, Galantucci L M, Longo G A 2019 Measuring techniques suitable for verification and repairing of industrial components: A comparison among optical systems *CIRP—JMST* **27** 114-123

[48] Percoco G, Lavecchia F, Sánchez Salmerón A 2015 Preliminary study on the 3D digitization of millimeter scale products by means of

photogrammetry *Proc. CIRP* **33** 257-62

[49] Galantucci L, Pesce M, Lavecchia F 2016 A powerful scanning methodology for 3D measurements of small parts with complex surfaces and sub millimeter-sized features, based on close range photogrammetry *Precis. Eng.* **43** 211-9

[50] Sims-Waterhouse D, Piano S, Leach R K 2017 Verification of micro-scale photogrammetry for smooth three-dimensional object measurement *Meas. Sci. Technol.* **28** 055010

[51] Sims-Waterhouse D, Bointon P, Piano S, Leach R K 2017 Experimental comparison of photogrammetry for additive manufactured parts with and without laser speckle projection *Proc. SPIE* 10329

[52] Luhmann T, Robson S 2011 *Close Range Photogrammetry: Principles, Techniques and Applications* (Whittles Publishing)

[53] Westoby M J, Brasington J, Glasser N F, Hambrey M J, Reynolds J M 2012 "Structure-from-Motion" photogrammetry: A low-cost, effective tool for geoscience applications *Geomorphology* **179** 300-314

[54] Galantucci L M, Percoco G, Ferrandes R 2006 Accuracy issues of digital photogrammetry for 3D digitization of industrial products *Rev. Int. Ing. Numer.* **2**

[55] Galantucci L, Pesce M, Lavecchia F 2015 A stereo photogrammetry scanning methodology, for precise and accurate 3D digitization of small parts with sub-millimeter sized features *CIRP Ann.* **64** 507–510

[56] Remondino F, Baltsavias E, El-Hakim S, Picard M, Grammatikopoulos L 2008 Image-based 3D modeling of the Erechteion, Acropolis of

Athens *ISPRS Archives* 1083–1092

[57] Fraser C, Cronk S, Hanley H 2008 Close-range photogrammetry in traffic incident management *ISPRS Congress* 3–6

[58] Luhmann T 2010 Close range photogrammetry for industrial applications *ISPRS J. Photogramm. Remote Sens.* **65** 558–569

[59] Isa M A, Piano S, Leach R K 2020 *Laser triangulation.* In: Leach R K *Advances in Optical Form and Coordinate Metrology* (IOP Publishing), Chap. 3

[60] Bogue R 2010 Three-dimensional measurements: a review of technologies and applications *Sensor Review* **30** 102–106

[61] Blais F 2003 Review of 20 years of range sensor development *Videometrics VII* **5013** 62–77

[62] Fröhlich C, Mettenleiter M 2004 Terrestrial laser scanning - New perspectives in 3D surveying *ISPRS Archives* **36** 7–13

[63] Petrie G, Toth C K 2008 *Introduction to laser ranging, profiling, and scanning.* In: Shan J, Toth C K *Topographic Laser Ranging and Scanning* (CRC Press), 2nd edition, Chap. 1

[64] Amann M C, Bosch T M, Lescure M, Myllylae R A, Rioux M 2001 Laser ranging: a critical review of unusual techniques for distance measurement *Opt. Eng.* **40** 10–20

[65] Massa J S, Buller G S, Walker A C, Cova S, Umasuthan M, Wallace A M 1998 Time-of-flight optical ranging system based on time-correlated single-photon counting *Appl. Opt.* **37** 7298–7304

[66] Geng J 2011 Structured-light 3D surface imaging: a tutorial *Adv. Opt. Photonics* **3** 128-160

[67] Webster J G, Bell T, Li B, Zhang S 2016 *Structured Light Techniques and Applications.* In: Webster J G *Wiley Encyclopedia of Electrical and Electronics Engineering* (John Wiley & Sons)

[68] Salvi J, Fernandez S, Pribanic T, Llado X 2010 A state of the art in structured light patterns for surface profilometry *Pattern Recognit.* **43** 2666

[69] Zhang S 2018 High-speed 3d shape measurement with structured light methods: A review *Opt. Lasers Eng.* **106** 119–131

[70] Chen F, Brown G, Song M 2000 Overview of three-dimensional shape measurement using optical methods *Opt. Eng.* **39** 10–22

[71] Zhang S 2010 Recent progresses on real-time 3D shape measurement using digital fringe projection techniques *Opt. Lasers Eng.* **48** 149-158

[72] Zhang S 2016 *High-speed 3D Imaging with Digital Fringe Projection Techniques* (CRC Press)

[73] Gorthi S S, Rastogi P 2010 Fringe projection techniques: Whither we are? *Opt. Lasers Eng.* **48** 133-140

[74] Salvi J, Pagès J, Batlle J 2004 Pattern codification strategies in structured light systems *Pattern Recognit.* **37** 827

[75] Kersten T P, Lindstaedt M, Starosta D 2018 Comparative geometrical accuracy investigations of Hand-Held 3D scanning systems - An update *ISPRS Archives* **XLII-2** 487-494

[76] Hébert P 2001 A self-referenced hand-held range sensor *Proc. 3rd 3DIM* 5-12

[77] Xu J, Xi N, Zhang C, Shi Q, Gregory J 2011 Real-time 3D shape inspection system of automotive parts based on structured light

pattern *Opt. Laser Technol.* **43** 1-8

[78] Chan T O, Lichti D D, Belton D, Klingseisen B, Helmholz P 2016 Survey accuracy analysis of a hand-held mobile LiDAR device for cultural heritage documentation *J. Bionanoscience* **10** 153-165

[79] Mendikute A, Yagüe-Fabra J A, Zatarain M, Bertelsen Á, Leizea I 2017 Self-Calibrated In-Process photogrammetry for large raw part measurement and alignment before machining *Sensors* **17**

[80] Mendikute A, Leizea I, Herrera I, Yagüe-Fabra J A 2019 In-process portable photogrammetry using optical targets for large scale industrial metrology *Proc. 19th euspen, Bilbao, Spain*

[81] Stavroulakis P, Sims-Waterhouse D, Piano S, Leach R K 2017 Flexible decoupled camera and projector fringe projection system using inertial sensors *Opt. Eng.* **56** 104106

[82] ATOS ScanBox https://www.gom.com/metrology-systems/atos-scanbox.html

[83] BLAZE 600A https://www.hexagonmi.com/en-gb/products/white-light-scanner-systems/blaze-600a

[84] Weckenmann A, Jiang X, Sommer K D, Neuschaefer-Rube U, Seewig J, Shaw L, Estler T 2009 Multisensor data fusion in dimensional metrology *CIRP Ann.* **58** 701-721

[85] Leach R K, Sims-Waterhouse D, Medeossi F, Savio E, Carmignato S, Su R 2018 Fusion of photogrammetry and coherence scanning interferometry data for all-optical coordinate measurement *CIRP Ann.* **67** 599-602

[86] Wang J, Leach R K, Jiang X 2015 Review of the mathematical

foundations of data fusion techniques in surface metrology *Surf. Topogr. Metrol.* **3**

[87] Deetjen M E, Lentink D 2018 Automated calibration of multi-camera-projector structured light systems for volumetric high-speed 3D surface reconstructions *Opt. Express* **26** 33278-33304

[88] Gai S, Da F, Tang M 2019 A flexible multi-view calibration and 3D measurement method based on digital fringe projection *Meas. Sci. Technol.* **30** 025203

[89] Liu Z, Meng Z, Gao N, Zhang Z 2019 Calibration of the relative orientation between multiple depth cameras based on a three-dimensional target *Sensors* **19** 308

[90] Shaheen A, Sims-Waterhouse D, Bointon P, Piano S, Leach R K 2019 Automated characterisation of multi-view fringe projection system for three-dimensional measurement of additively manufactured parts *Proc. euspen/ASPE Advancing Precision in Additive Manufacturing, Nantes, France*

[91] Dickins A, Widjanarko T, Sims-Waterhouse D, Thompson A, Lawes S, Senin N, Leach R K 2020 Multi-view fringe projection system for surface topography measurement during metal powder bed fusion *J. Opt. Soc. Am. A* **37** B93-B105

[92] Vallejo M, De La Espriella C, Gómez-Santamaría J, Ramírez-Barrera A F, Delgado-Trejos E 2019 Soft metrology based on machine learning: A review *Meas. Sci. Technol.* **31**

[93] Eastwood J, Zhang H, Isa M, Sims-Waterhouse D, Leach R K, Piano S 2020 Smart photogrammetry for three-dimensional shape

measurement *Proc. SPIE* **11352** 113520A

[94] Calvez A 2019 Deep learning and 3D optical metrology improve complex feature detection and ranking *19th International Congress of Metrology* 03001

[95] Stavroulakis P, Chen S, Derlome C, Bointon P, Tzimiropoulos G, Leach R K 2019 Rapid calibration tracking of extrinsic projector parameters in fringe projection using machine learning *Opt. Lasers Eng.* **114** 7-14

[96] Hoppe H, DeRose T, Duchamp T, McDonald J, Stuetzle W 1992 Surface reconstruction from unorganized points *Comput. Graph. (ACM)* **26** 71-78

[97] Catalucci S, Senin N, Sims-Waterhouse D, Ziegelmeier S, Piano S, Leach R K 2020 Measurement of complex freeform additively manufactured parts by structured light and photogrammetry *Measurement* **164** 108081

[98] Moroni G, Petrò S 2014 Optimal inspection strategy planning for geometric tolerance verification *Precis. Eng.* **38** 71-81

[99] Wang J, Jiang X, Blunt L A, Leach R K, Scott P J 2012 Intelligent sampling for the measurement of structured surfaces *Meas. Sci. Technol.* **23** 085006

[100] Yu M, Zhang Y, Li Y and Zhang D 2013 Adaptive sampling method for inspection planning on CMM for free-form surfaces *Int. J. Adv. Manuf. Technol.* **67** 1967–1975

[101] Colosimo B M, Mammarella F, Petrò S 2010 *Quality control of manufactured surfaces.* In: Lenz H J, Wilrich P T, Schmid W *Frontiers*

in Statistical Quality Control 9 (Physica-Verlag HD) 55-70

[102] Stavroulakis P, Bointon P, Southon N, Leach R K 2016 Information-rich approach to non-destructive noncontact measurement planning, inspection and verification for additive manufacturing *Proc. ASPE/euspen Dimensional Accuracy and Surface Finish in Additive Manufacturing, Rayleigh, NC, USA*

[103] Syam W P, Rybalcenko K, Gaio A, Crabtree J, Leach R K 2019 Methodology for the development of in-line optical surface measuring instruments with a case study for additive surface finishing *Opt. Lasers Eng.* **121** 271-288

[104] Leach R K, Elmadih W, Piano S, Isa M A, Sims-Waterhouse D, Southon N, Syam W P 2020 Development of an all-optical dimensional measuring system *Proc. 20th euspen (virtual conference)*

[105] Kinnell P, Rymer T, Hodgson J, Justham L, Jackson M 2017 Autonomous metrology for robot mounted 3D vision systems *CIRP Ann.* **66** 483-486

[106] Zhang H, Eastwood J, Isa M, Sims-Waterhouse D, Leach R K, Piano S 2021 Optimisation of camera positions for optical coordinate measurement based on visible point analysis *Precis. Eng.* **67** 178-188

[107] Lartigue C, Contri A, Bourdet P 2002 Digitised point quality in relation with point exploitation *Measurement* **32** 193-203

[108] Mehdi-Souzani C, Thiébaut F, Lartigue C 2006 Scan planning strategy for a general digitized surface *J. Comput. Inf. Sci. Eng.* **6** 331-39

[109] Zuquete-Guarato A, Mehdi-Souzani C, Quinsat Y, Lartigue C, Sabri L 2012 Towards a new concept of in-line crankshaft balancing by contact

less measurement: Process for selecting the best digitizing system *ASME ESDA 2012* **82166** 17-25

[110] Karaszewski M, Adamczyk M and Sitnik R 2016 Assessment of next-best-view algorithms performance with various 3D scanners and manipulator *ISPRS Archives* **119** 320-33

[111] Rusu R B, Cousins S 2011 3D is here: point cloud library *IEEE Int. Conf. Robot. Autom.* 1-4

[112] Aldoma A, Marton Z C, Tombari F, Wohlkinger W, Potthast C, Zeisl B, Rusu R, Gedikli S, Vincze M 2012 Tutorial: point cloud library: three-dimensional object recognition and 6 DOF pose estimation *Robot. Autom. Mag.* **19** 80-91

[113] Saval-Calvo M, Orts-Escolano S, Azorin-Lopez J, GarcÍa RodrÍguez J, Fuster-Guillo A, Morell-Gimenez V, Cazorla M 2015 A comparative study of downsampling techniques for non-rigid point set registration using color *IWINAC* 281-290

[114] Alexa M, Gross M, Pauly M, Pfister H, Stamminger M, Zwicker M 2004 Point-based computer graphics *ACM SIGGRAPH '04 Course Notes, Los Angeles, USA*

[115] Kobbelt L, Botsch M 2004 A survey of point-based techniques in computer graphics *Comput. Graph.* **28** 801-814

[116] Sun J, Jiang Y, Jiang J, Bai X 2016 Triangular mesh construction based on point cloud matrix and edge feature extraction *IEEE ITNEC* 275-279

[117] Weinmann M 2016 *Preliminaries of 3D point cloud processing.* In: Weinmann M *Reconstruction and Analysis of 3D Scenes* (Springer

International Publishing: Cham), Chap. 2

[118] Landa J, Prochazka D, Štastny J 2013 Point cloud processing for smart systems *Acta Univ. Agric. Silvic. Mendel. Brun.* **61** 2415-2421

[119] Huber D 2011 The ASTM E57 file format for 3d imaging data exchange *Proc. SPIE* **7864A**

[120] Turk G 1994 *The PLY Polygon File Format* (Stanford University archives)

[121] Tam G K L, Cheng Z Q, Lai Y K, Langbein F C, Liu Y, Marshall D, Martin R R, Sun X F, Rosin P L 2013 Registration of 3D point clouds and meshes: a survey from rigid to nonrigid *IEEE T. Vis. Comput. Gr.* **19** 1199-1217

[122] De Berg M, Cheong O, Van Kreveld M, Overmars M 2008 *Computational Geometry: Algorithms and Applications* (Springer-Verlag: Berlin), 3rd edition

[123] Schneider P J, Eberly D H 2003 *Geometric Tools for Computer Graphics* (Morgan Kaufmann Publisher Inc.: San Francisco)

[124] Abdi H 2009 Centroids *Wiley Interdiscip. Rev. Comput. Stat.* **1** 259-260

[125] James G, Witten D, Hastie T, Tibshirani R 2013 *An Introduction to Statistical Learning with Applications in R* (Springer: New York)

[126] Jolliffe I T 2002 *Principal Component Analysis* (Springer-Verlag: New York)

[127] van den Bergen G 1997 Efficient collision detection of complex deformable models using AABB trees *J. Graph. Tools* **2** 1-13

[128] Jiménez P, Thomas F, Torras C 2001 3D collision detection: a survey

Comput. Graph. **25** 269-285

[129] Bentley J L 1975 Multidimensional binary search trees used for associative searching *Commun. ACM* **18** 509-517

[130] Samet H 1989 *Applications of Spatial Data Structures: Computer Graphics, Image Processing, and GIS* (Addison-Wesley Longman Publishing Co.: Boston)

[131] Samet H 1990 *The Design and Analysis of Spatial Data Structures* (Addison-Wesley Longman Publishing Co.: Boston)

[132] Aluru S 2004 *Quadtrees and octrees.* In: Mehta D P, Sahni S *Handbook of Data Structures and Applications* (Chapman and Hall/CRC), 2nd edition

[133] Shapiro V 2002 *Solid modeling.* In: Farin G, Hoschek J, Kim M S *Handbook of Computer Aided Geometric Design* (Elsevier Science Publishers: Amsterdam), Chap. 20

[134] Hosoi F, Omasa K 2006 Voxel-based 3-D modeling of individual trees for estimating leaf area density using high-resolution portable scanning lidar *IEEE Trans. Geosci. Remote Sens.* **44** 3610-3618

[135] Rusu R B 2009 Semantic 3D object maps for everyday manipulation in human living environments *PhD Thesis Computer Science department, Technische Universität Müchen, Germany*

[136] Elseberg J, Magnenat S, Siegwart R, Andreas N 2012 Comparison of nearest-neighbor-search strategies and implementations for efficient shape registration *J. Softw. Eng. Robot.* **3** 2-12

[137] Schall O, Belyaev A, Seidel H P 2008 Adaptive feature-preserving non-local denoising of static and time-varying range data *Computer-Aided*

Design **40** 701-707

[138] Linsen L 2001 Point cloud representation *University of Karlsruhe, Germany Technical Report, Faculty of Informatics*

[139] Pauly M, Gross M, Kobbelt L P 2002 Efficient simplification of point-sampled surfaces *Proc. IEEE VIS '02, Boston, USA* 163-170

[140] Taubin G 1995 Signal processing approach to fair surface design *ACM SIGGRAPH '95, New York, USA* 351-358

[141] Xiaohui D, Baocai Y, Dehui K 2007 Adaptive out-of-core simplification of large point clouds *Proc. IEEE ICME, Beijing, China* 1439-1442

[142] Schall O, Belyaev A, Seidel H P 2005 Robust filtering of noisy scattered point data *Symposium Point-Based Graphics '05, Stony Brook, USA* 71-77

[143] Sotoodeh S 2006 Outlier detection in laser scanner point clouds *ISPRS Archives* XXXVI-**5** 297-302

[144] Sultani Z N, Ghani R F 2015 Kinect 3D point cloud live video streaming *Procedia Comput. Sci.* **65** 125-132

[145] Rabbani T, van den Wildenberg F, Vosselman G 2006 Segmentation of point clouds using smoothness constraint *Int. Arch. Photogramm. Remote Sens. Spat. Inf. Sci.* **35** 248-253

[146] Pauling F, Bosse M, Zlot R 2009 Automatic segmentation of 3D laser point clouds by ellipsoidal region growing *Proc. ACRA '09, Sidney, Australia*

[147] Han X F, Jin J S, Wang M J, Jiang W, Gao L, Xiao L 2017 A review of algorithms for filtering the 3D point cloud *Signal Process. Image Commun.* **57** 103-112

[148] Edelsbrunner H 2009 *Delaunay triangulations.* In: Edelsbrunner H *Geometry and Topology for Mesh Generation* (Cambridge University Press: Cambridge)

[149] Owen S 1998 A survey of unstructured mesh generation technology *7th Int. Meshing Roundtable* 239-267

[150] Bommes D, Lévy B, Pietroni N, Puppo E, Silva C, Tarini M 2013 Quad-mesh generation and processing: a survey *Comput. Graph. Forum* **32** 51-76

[151] Berger M, Tagliasacchi A, Seversky L M, Alliez P, Levine J A, Sharf A, Silva C T 2014 State of the art in surface reconstruction from point clouds *Proc. EG '14, Strasbourg, France* 161-185

[152] Berger M, Tagliasacchi A, Seversky LM, Alliez P, Guennebaud G, Levine J A, Sharf A, Silva C T 2017 A survey of surface reconstruction from point clouds *Comput. Graph. Forum* **36** 301-329

[153] Han X F, Jin J S, Xie J, Wang M J, Jiang W 2018 A comprehensive review of 3d point cloud descriptors *arXiv:1802.02297*

[154] Holzer S, Rusu R B, Dixon M, Gedikli S, Navab N 2012 Adaptive neighborhood selection for real-time surface normal estimation from organized point cloud data using integral images *IEEE/RSJ* 2684-2689

[155] Fisher R B 1989 *Description of three dimensional structures.* In: Fisher R B *From Surface To Objects: Computer Vision and Three Dimensional Scene Analysis* (John Wiley and Sons: Chichester)

[156] Bär C 2010 *Elementary Differential Geometry* (Cambridge University Press: Cambridge)

[157] Pressley A 2010 *Curvature of surfaces.* In: Pressley A *Elementary*

Differential Geometry (Springer: London)

[158] Meyer M, Desbrun M, Schröder P, Barr A H 2003 *Discrete differential-geometry operators for triangulated 2-manifolds*. In: Hege H C, Polthier K *Visualization and Mathematics III* (Springer-Verlag: Berlin)

[159] Magid E, Soldea O, Rivlin E 2007 A comparison of gaussian and mean curvature estimation methods on triangular meshes of range image data *Comput. Vis. Image Underst.* **107** 139-159

[160] Mérigot Q, Ovsjanikov M, Guibas L J 2011 Voronoi-based curvature and feature estimation from point clouds *IEEE Trans. Vis. Comput. Graph.* **17** 743-756

[161] Dyn N, Hormann K, Kim S J, Levin D 2001 *Optimizing 3D triangulations using discrete curvature analysis.* In: Lyche T, Schumaker L L *Mathematical Methods for Curves and Surfaces* (Vanderbilt University: Nashville)

[162] Rusu R B, Blodow N, Beetz M 2009 Fast Point Feature Histograms (FPFH) for 3D registration *IEEE ICRA, Kobe, Japan* 1848–1853

[163] Rusu R B, Blodow N, Marton Z C, Beetz M 2008 Aligning point cloud views using persistent feature histograms *2008 IEEE/RSJ IROS* 3384–3391

[164] Szeliski R 2011 *Computer Vision: Algorithms and Applications* (Springer: London)

[165] Nguyen A, Le B 2013 3D point cloud segmentation: a survey *6th IEEE RAM Proc., Manila, Philippines* 225-230

[166] Catalucci S, Senin N, Piano S, Leach R K 2019 Intelligent systems for optical form measurement: automated assessment of pose and coverage

Proc. 34th ASPE, Pittsburgh, USA 145-150

[167] Grilli E, Menna F, Remondino F 2017 A review of point clouds segmentation and classification algorithms *ISPRS Archives* **XLII-2/W3** 339-344

[168] Xie Y, Tian J, Zhu X X 2020 Linking points with labels in 3D: a review of point cloud semantic segmentation *IEEE Geosc. Rem. Sen. M. (early access)*

[169] Forbes A B, Minh H D 2011 Form assessment in coordinate metrology *Appr. Alg. Complex Syst. Springer Proc. Math.* **3** 69-90

[170] Forbes A B, Minh H D 2012 Generation of numerical artefacts for geometric form and tolerance assessment *Int. J. Metrol. Qual. Eng.* **3** 145-150

[171] Feng S C, Hopp T 1991 A review of current geometric tolerancing theories and inspection data analysis algorithms *NIST Interagency/Internal Report (NISTIR – 4509)*

[172] Gruen A, Akca D 2005 Least squares 3D surface and curve matching *ISPRS J. Photogramm. Remote Sens.* **59** 151-174

[173] Monserrat O, Crosetto M 2008 Deformation measurement using terrestrial laser scanning data and least squares 3D surface matching *ISPRS J. Photogramm. Remote Sens.* **63** 142-154

[174] Moroni G, Petrò S 2008 Geometric tolerance evaluation: a discussion on minimum zone fitting algorithms *Precis. Eng.* **32** 232-237

[175] Fischler M A, Bolles R C 1981 Random Sample Consensus: a paradigm for model fitting with applications to image analysis and automated cartography *Commun. ACM* **24** 381-395

[176] Strutz T 2016 *Data Fitting and Uncertainty. A Practical Introduction to Weighted Least Squares and Beyond* (Springer: Vieweg)

[177] Schnabel R, Wahl R, Klein R 2007 Efficient RANSAC for point-cloud shape detection *Comput. Graph. Forum* **26** 214-226

[178] Pulli K 1999 Multiview registration for large data sets *Proc. 3DIM, Ottawa, Canada* 160-168

[179] Brown B J, Rusinkiewicz S 2007 Global non-rigid alignment of 3-D scans *ACM Trans. Graph.* **26** 21

[180] Salvi J, Matabosch C, Fofi D, Forest J 2007 A review of recent range image registration methods with accuracy evaluation *Image Vision Comput.* **25** 578-596

[181] Ramasamy S K, Raja J, Boudreau B D 2013 Data fusion strategy for multiscale surface measurements *J. Micro Nano-Manuf.* **1** 011004

[182] Horn B K P 1987 Closed-form solution of absolute orientation using unit quaternions *J. Opt. Soc. Am. A* **4** 629-642

[183] Lourakis M 2016 An efficient solution to absolute orientation *Proc. 23rd Int. Conf. Pattern Recogn., Cancun, Mexico* 3816-3819

[184] Arun K S, Huang T S, Blostein S D 1987 Least-squares fitting of two 3-D point sets *IEEE Trans. Pattern Anal. Mach. Intell.* **PAMI-9** 698-700

[185] Horn B K P, Hilden H M, Negahdaripour S 1988 Closed-form solution of absolute orientation using orthonormal matrices *J. Opt. Soc. Am. A* **5** 1127-1135

[186] Eggert D W, Lorusso A, Fisher R B 1997 Estimating 3-D rigid body transformations: a comparison of four major algorithms *Mach. Vision*

Appl. **9** 272-290

[187] Kendall D G 1989 A survey of the statistical theory of shape *Stat. Sci.* **4** 87-99

[188] Besl P, McKay N 1992 A method for registration of 3-D shapes *IEEE Trans. Pattern Anal. Mach. Intell.* **14** 239-256

[189] Rusinkiewicz S, Levoy M 2001 Efficient variants of the ICP algorithm *Proc. 3DIM, Quebec, Canada* 145-152

[190] Chen Y, Medioni G 1992 Object modelling by registration of multiple range images *Image Vis. Comput.* **10** 145-155

[191] Bergevin R, Soucy M, Qagnon H, Laurendeau D 1996 Towards a general multi-view registration technique *IEEE Trans. Pattern Anal. Mach. Intell.* **18** 540-547

[192] Gelfand N, Ikemoto L, Rusinkiewicz S, Levoy M 2003 Geometrically stable sampling for the ICP algorithm *Proc. 3DIM, Banff, Canada* 260-267

[193] Blais G, Levine M D 1995 Registering multiview range data to create 3D computer objects *IEEE Trans. Pattern Anal. Mach. Intell.* **17** 820-824

[194] Holz D, Ichim A E, Tombari F, Rusu R B, Behnke S 2015 Registration with the point cloud library: a modular framework for aligning in 3-D *Robot. Autom. Mag.* **22** 110-124

[195] Tombari F, Salti S, Di Stefano L 2010 *Unique signatures of histograms for local surface description.* In: Daniilidis K, Maragos P, Paragios N *Computer Vision – ECCV 2010* (*Lecture Notes in Computer Science* vol 6313) (Springer: Berlin Heidelberg)

[196] Bellekens B, Spruyt V, Berkvens R, Penne R 2015 A benchmark survey of rigid 3D point cloud registration algorithms *IARIA* **8** *118-127*

[197] Gelfand N, Mitra N J, Guibas L J, Pottmann H 2005 Robust global registration *Symposium on geometry processing* 197-206

[198] Cignoni P, Rocchini C, Scopigno R 1998 Metro: measuring error on simplified surfaces *Comput. Graph. Forum* **17** 167-174

[199] Aspert N, Santa-Cruz D, Ebrahimi T 2002 MESH: Measuring errors between surfaces using the Hausdorff distance *Proc. 2002 IEEE ICME* **1** 705-708

[200] Mémoli F, Sapiro G 2004 Comparing point clouds *SGP '04 Proc.*

[201] Girardeau-Montaut D, Roux M, Marc R, Thibault G 2005 Change detection on points cloud data acquired with a ground laser scanner *ISPRS Archives J. Photogramm. Remote Sens.* **XXXVI** 30-35

[202] Antova G 2019 Application of areal change detection methods using point clouds data *IOP Conference Series: Earth and Environmental Science* **221**

[203] Lague D, Brodu N, Leroux J 2013 Accurate 3D comparison of complex topography with terrestrial laser scanner: Application to the Rangitikei canyon (N-Z) *ISPRS Archives J. Photogramm. Remote Sens.* **82** 10-26

[204] Jones M 1995 *3D distance from a point to a triangle (Technical Report CSR) Comput. Sci. Univ. Wales* 5-95

[205] Eberly D 2003 *Distance Between Point and Triangle in 3D.* In: Eberly D H, Schneider P J *Geometric Tools for Computer Graphics* (Morgan Kaufmann Publisher Inc.: San Francisco), Chap. 10

[206] Leach R K 2014 *Fundamental principles of engineering nanometrology* (Elsevier), 2nd edition

[207] De Chiffre L, Carmignato S, Kruth J P, Schmitt R, Weckenmann A 2014 Industrial applications of computed tomography *CIRP Ann.* **63** 655-677

[208] Forbes A B 2018 Uncertainties associated with position, size and shape for point cloud data *J. Phys. Conf. Ser.* **1065** 142023

[209] Mezian M, Vallet B, Soheilian B, Paparoditis N 2016 Uncertainty propagation for terrestrial mobile laser scanner *ISPRS Archives* **XLI-B3** 331–335

[210] Senin N, Catalucci S, Moretti M and Leach R K 2021 Statistical point cloud model to investigate measurement uncertainty in coordinate metrology *Precis. Eng.* **70** 44-62

[211] Forbes A B 2006 Surface fitting taking into account uncertainty structure in coordinate data *Meas. Sci. Technol.* **17** 553-558

[212] Forbes A B 2006 Uncertainty evaluation associated with fitting geometric surfaces to coordinate data *Metrologia* **43** 282-290

[213] Anwer N, Ballu A, Mathieu L 2013 The skin model, a comprehensive geometric model for engineering design *CIRP Ann.* **62** 143-146

[214] Zhang M, Anwer N, Mathieu L, Zhao H B 2011 A discrete geometry framework for geometrical product specifications *Proc. CIRP Design Conf., Korea*

[215] Zhang M, Anwer N, Stockinger A, Mathieu L, Wartzack S 2013 Discrete shape modeling for skin model representation *P. I. Mech. Eng. B-J. Eng.* **227** 672-680

[216] Thompson A, Senin N, Giusca C, Leach R K 2017 Topography of selectively laser melted surfaces: a comparison of different measurement methods *CIRP Ann.* **66** 543-546

[217] Evans C J 2008 Uncertainty evaluation for measurements of peak to valley surface form errors *CIRP Ann.* **57** 509-512

[218] Evans C J 2010 Certification, self-calibration, and uncertainty in testing optical flats *Proc. SPIE* **7656** 76560S

[219] Evans C, Davies A 2013 Certification, self-calibration and uncertainty in optical surface testing *Int. J. Precis. Technol.* **3** 388-401

[220] Moroni G, Syam W P, Petrò S 2018 A simulation method to estimate task-specific uncertainty in 3D microscopy *Measurement* **122** 402-416

[221] Yang T H, Jackman J 2000 Form error estimation using spatial statistics *J. Manuf. Sci. Eng. Trans. ASME* **122** 262-272

[222] Fei L, Dantan J Y, Baudouin C, Du S 2019 Calibration and uncertainty estimation of non-contact coordinate measurement systems based on Kriging models *Precis. Eng.* **57** 16-29

[223] Pauly M, Mitra N J, Guibas L 2004 Uncertainty and variability in point cloud surface data *SPBG '04, Goslar, Germany* 77-84

[224] Chen X, Zhang G, Zhang J, Wu H, Lu T, Xuan W 2016 An average error ellipsoid model for evaluating precision of point cloud from TLS *J. Ind. Soc. Remote Sens.* **44** 865-873

[225] Du Z, Wu Z, Yang J 2016 Error ellipsoid analysis for the diameter measurement of cylindroid components using a laser radar measurement system *Sensors* **16** 714

[226] Du Z, Wu Z, Yang J 2016 Point cloud uncertainty analysis for laser radar measurement system based on error ellipsoid model *Opt. Laser Eng.* **79** 78-84

[227] Ozendi M, Akca D, Topan H 2016 An emprical point error model for TLS derived point clouds *ISPRS Archives* **XLI-B5** 557-563

[228] Niemeier W, Tengen D 2017 Uncertainty assessment in geodetic network adjustment by combining GUM and Monte-Carlo simulations *J. Geodesy* **11** 67-76

[229] ISO/DIS 10360 part 13 2020 *Geometrical product specifications (GPS) - Acceptance and reverification tests for coordinate measuring systems (CMS) - Part 13: Optical 3D CMS* (International Organization for Standardization)

[230] Guo Y, Bennamoun M, Sohel F, Lu M, Wan J, Kwok N M 2016 A comprehensive performance evaluation of 3d local feature descriptors *Int. J. Comput. Vis.* **116** 66–89

[231] Dangeti P 2017 *Statistics for Machine Learning: Techniques for exploring supervised, unsupervised, and reinforcement learning models with Python and R* (Packt Publishing)

[232] Moylan S P, Slotwinski J A, Cooke A L, Jurrens K K, Domnez M A 2012 Proposal for a standardized test artifact for additive *Solid Free. Fabr. Symp.*

[233] GOM ATOS Core 300 https://www.gom.com/metrology-systems/atos/atos-core.html

[234] MATLAB 2020 v.R2020b (The MathWorks Inc.: Natick, Massachusetts)

[235] GOM Scan: GOM software v.2018 https://www.gom.com/

[236] Mokhtarian F, Khalili N, Yuen P 2001 Multi-scale free-form 3D object recognition using 3D models *Image Vis. Comput.* **19** 271-281

[237] Mokhtarian F, Khalili N, Yuen P 2002 Estimation of error in curvature computation on multi-scale free-form surfaces *Int. J. Comput. Vis.* **48** 131–149

[238] Leach R K, Carmignato S 2020 *Precision Metal Additive Manufacturing* (CRC Press)

[239] Gal R, Cohen-Or D 2006 Salient geometric features for partial shape matching and similarity *ACM Trans. Graph.* **25** 130-150

[240] BS ISO 22514 part 7 2012 *Statistical methods in process management - Capability and performance - Part 7: Capability of measurement processes* (International Organization for Standardization)

[241] Blender v.2.91.0 https://www.blender.org/

[242] Woop S, Schmittler J, Slusallek P 2005 RPU: A programmable ray processing unit for realtime ray tracing *SIGGRAPH '05* **24**

[243] Glassner A S 1989 *An Introduction to Ray Tracing* (Academic Press: New York)

[244] Cressie N A C 2015 *Statistics for Spatial Data, Revised Edition* (John Wiley & Sons, Inc.)

[245] Rasmussen C E, Williams C K I 2018 *Gaussian Processes for Machine Learning* (Cambridge, Massachusetts: The MIT Press)

[246] Genton M G 2002 Classes of kernels for machine learning: a statistics perspective *J. Mach. Learn. Res. – JMLR* **2** 303-304

[247] Chen Y, Wiesel A, Eldar Y C, Hero A O 2010 Shrinkage algorithms

for MMSE covariance estimation *IEEE Trans. Signal Process.* **58** 5016-5029

[248] Mehdi-Souzani C, Digne J, Audfray N, Lartigue C, Morel J M 2010 Feature extraction from high-density point clouds: toward automation of an intelligent 3D contactless digitizing strategy *Comput. Aided. Des. Appl.* **7** 863-874

[249] Massey F J 1951 The Kolmogorov-Smirnov test for goodness of fit *J. Am. Stat. Assoc.* **46** 68-78

[250] Artec Space Spider 3D scanner https://www.artec3d.com

[251] Lingua A, Marenchino D, Nex F 2009 Performance analysis of the SIFT operator for automatic feature extraction and matching in photogrammetric applications *Sensors* **9** 3745-3766

[252] Agisoft Metashape: Standard edition v. 1.5.5 https://www.agisoft.com

[253] Polyworks Innovmetric: Metrology Suite 2019 IR1 https://www.innovmetric.com

[254] Flack D 2014 Measurement Good Practice Guide No. 41 CMM measurement strategies (National Physical Laboratory: London)

[255] Mitutoyo Crysta Apex S7106 CMM https://www.mitutoyo.co.uk

Appendix A

Graphical results of measurement quality indicators

This appendix includes a complete reporting of the results obtained from the application of measurement quality indicators discussed in Chapter 4 on a selected industrial case. The sample (indicated as sample A in this thesis) is described in Chapter 3.

The results of the indicators applied to individual high-density point clouds are presented into separate sections, divided according to the optical measuring instrument employed. In figures and tables, the point clouds are indicated as "Repeat N_M", where N is the number of the measured observation (five measurement repeats for each instrument) and M is the measuring instrument (PG - photogrammetry system; FP - fringe projection

system; SL - structured light speckle projection system). The results illustrated in this appendix include the information related to the intrinsic properties of each measured point clouds, colour maps of the performance indicators overlaid to the reference CAD geometry available in form of triangle mesh (specifically coverage ratio, sampling density, point-to-surface distances, and dispersion of signed distances respectively), the number of zero-coverage triangles, bar plots of sampling density, and histograms of the dispersion of signed point-to-surface distances.

A.1 Results for photogrammetry

The following table and figures reported in this section of the appendix show the complete collection of the results obtained via the application of the performance indicators on the point clouds acquired with photogrammetry. The graphs and colour maps are grouped and shown based on measurement repeat (indicated as “Repeat 1_PG” to “Repeat 5_PG”).

Table A.1 Photogrammetry repeats: intrinsic properties of the measured point clouds

	Repeat 1_PG	**Repeat 2_PG**	**Repeat 3_PG**	**Repeat 4_PG**	**Repeat 5_PG**
Number of points in the raw dataset	16,950,195	18,573,175	18,180,340	17,720,639	17,854,193
Number of points in the final point cloud	2,073,468	2,048,705	1,989,348	2,192,714	2,374,796
Point-to-point spacing	0.044 mm	0.046 mm	0.046 mm	0.044 mm	0.044 mm

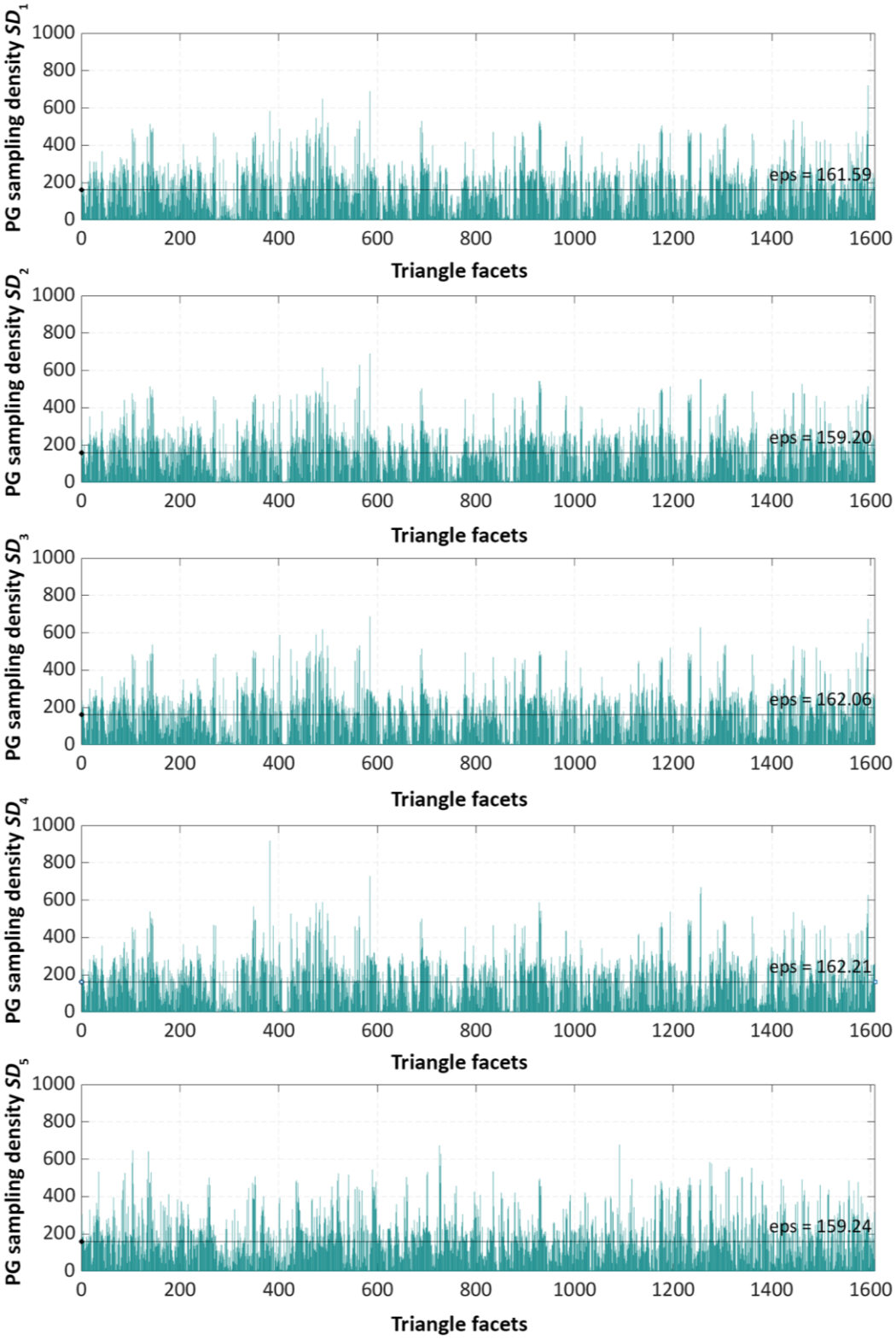

Figure A.1 Bar plots proportional to sampling density for each PG measurement repeat. Sampling density expresses the number of points per unit area of each triangle facet; eps indicates the threshold value at 75% of total detected density

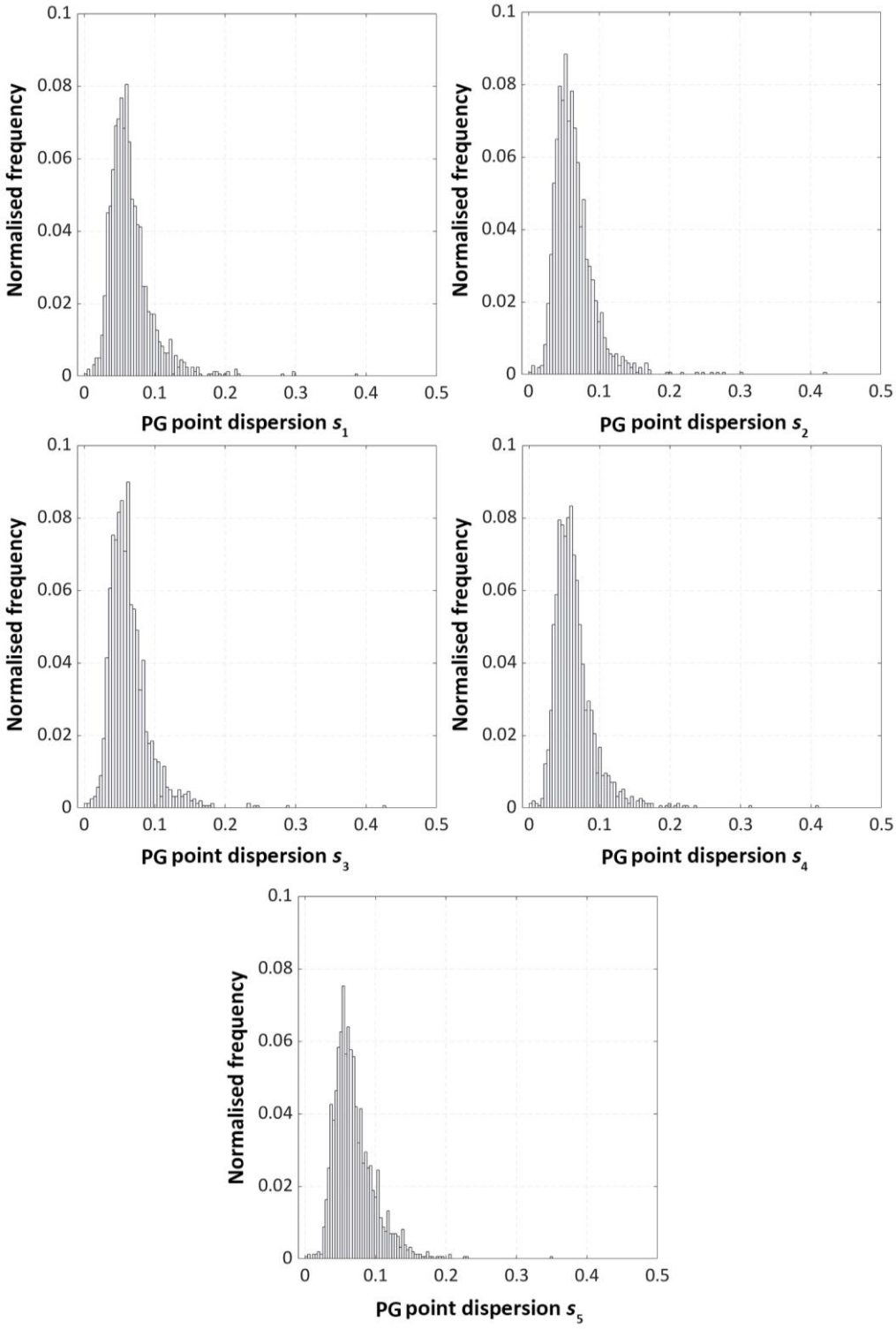

Figure A.2 Histograms of point dispersion values for each measurement repeat of PG, indicated as $s_1, s_2, \ldots, s_5$. Point dispersion is expressed in millimetres; normalised frequency (vertical axes) is the number of occurrences of the values in a bin, divided by the total number of occurrences

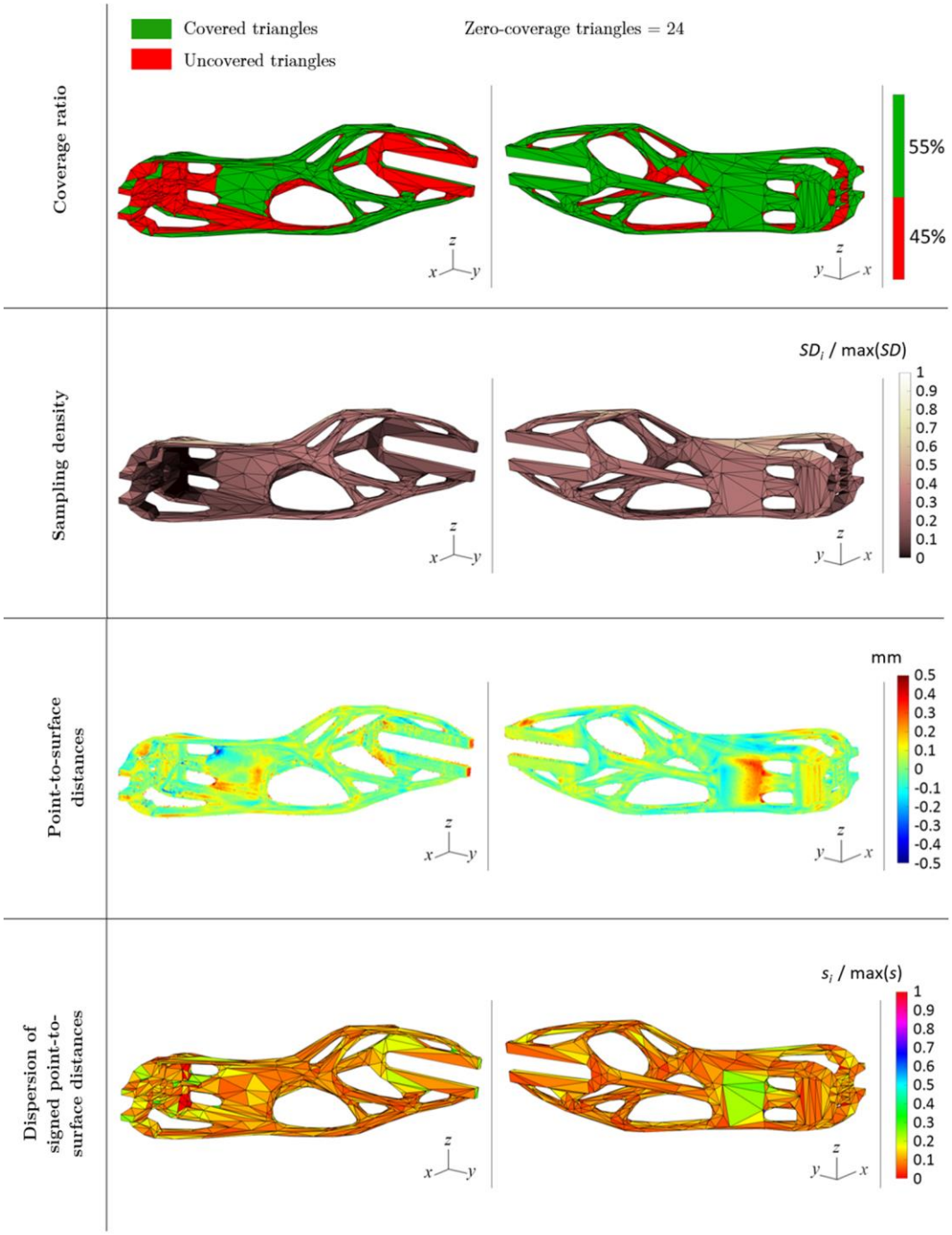

Figure A.3 Repeat 1_PG indicators results in form of customised colour maps (front and back views): coverage ratio reporting covered and uncovered triangles rendered using binary colouring (zero coverage triangles = 24), sampling density overlaid to triangle mesh (shown in normalised form), point-to-surface distances within each triangle (range of ±0.5 mm), mesh triangles coloured using the dispersion of signed point-to-surface distances (shown in normalised form)

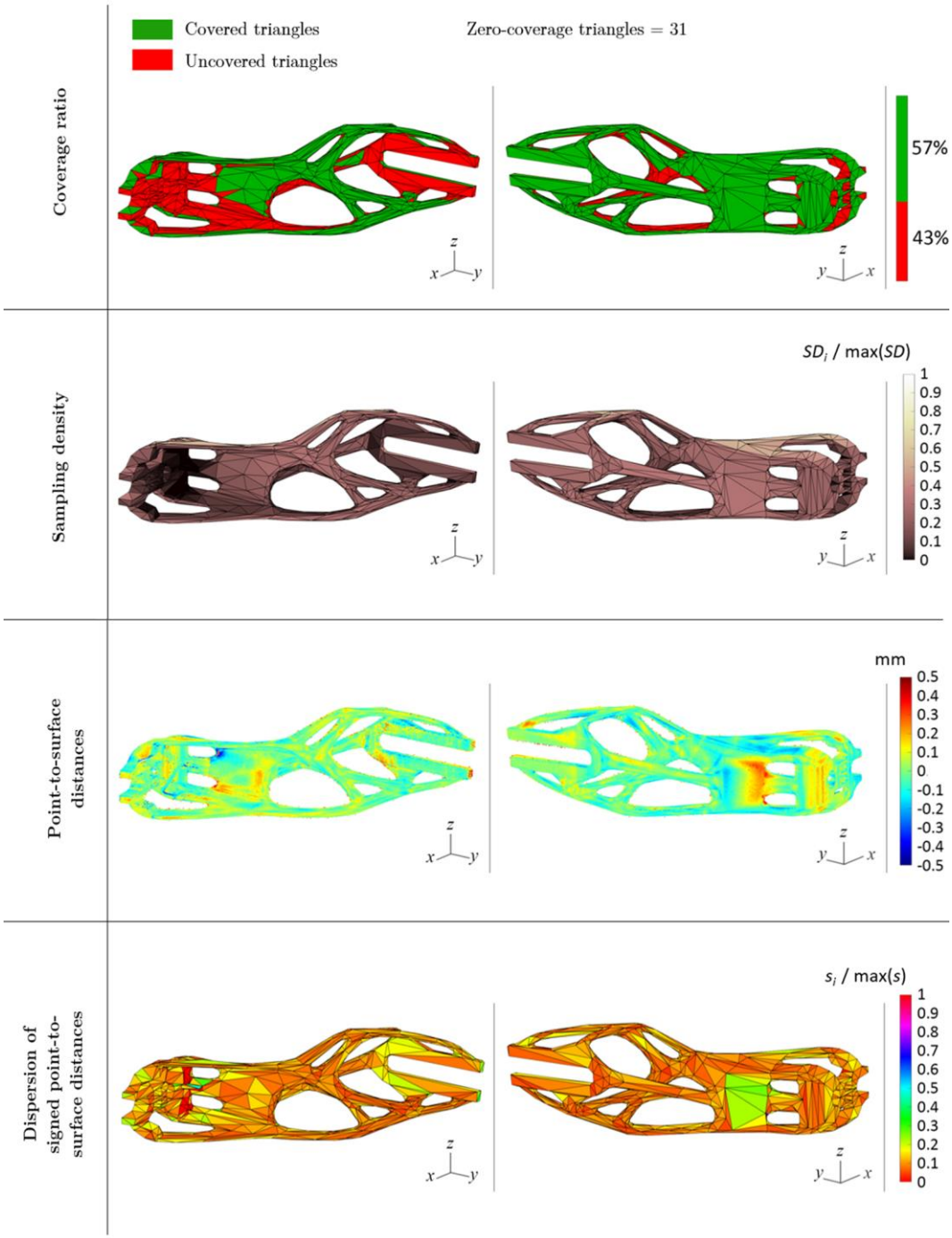

Figure A.4 Repeat 2_PG indicators results in form of customised colour maps (front and back views): coverage ratio reporting covered and uncovered triangles rendered using binary colouring (zero coverage triangles = 31), sampling density overlaid to triangle mesh (shown in normalised form), point-to-surface distances within each triangle (range of ±0.5 mm), mesh triangles coloured using the dispersion of signed point-to-surface distances (shown in normalised form)

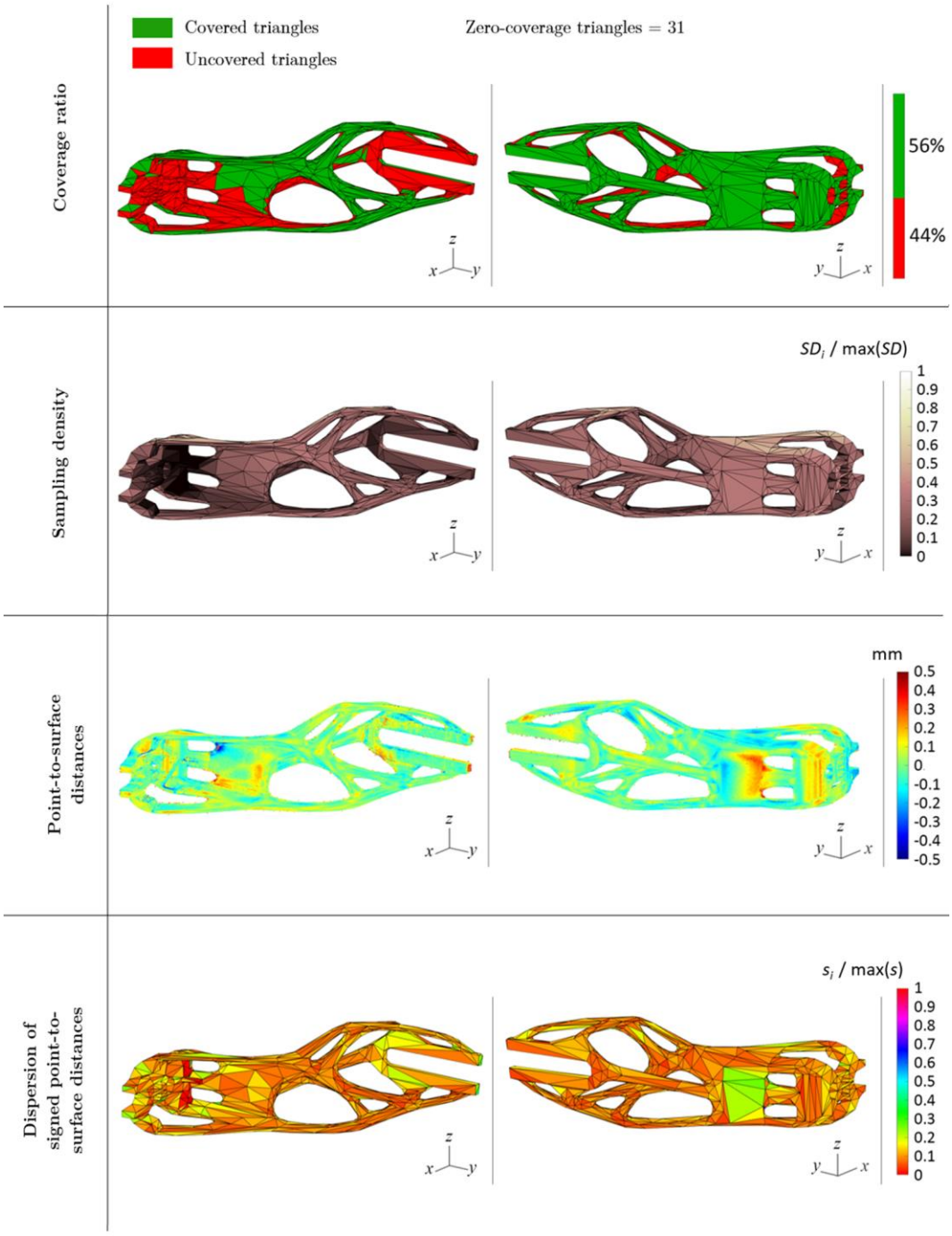

Figure A.5 Repeat 3_PG indicators results in form of customised colour maps (front and back views): coverage ratio reporting covered and uncovered triangles rendered using binary colouring (zero coverage triangles = 31), sampling density overlaid to triangle mesh (shown in normalised form), point-to-surface distances within each triangle (range of ±0.5 mm), mesh triangles coloured using the dispersion of signed point-to-surface distances (shown in normalised form)

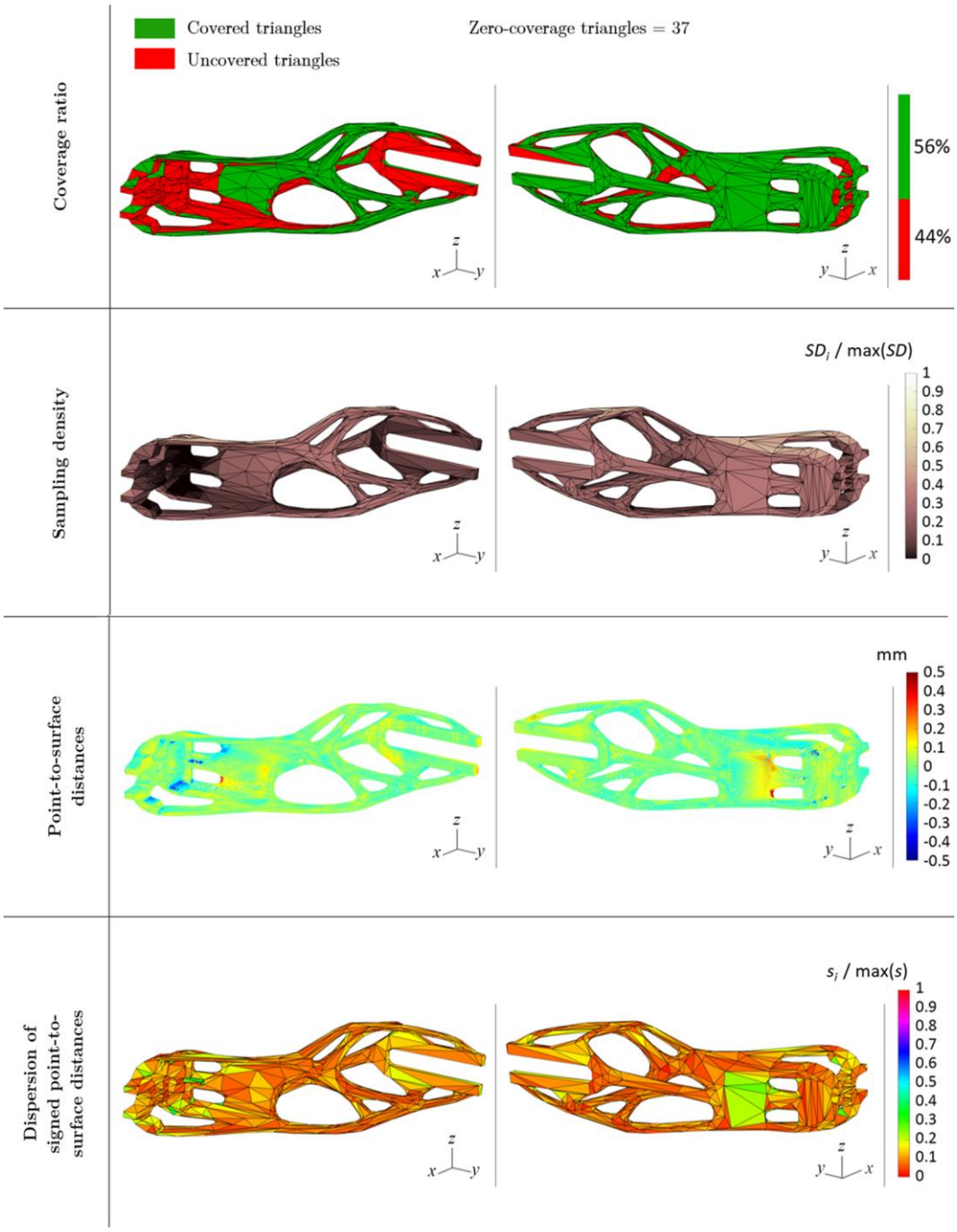

Figure A.6 Repeat 4_PG indicators results in form of customised colour maps (front and back views): coverage ratio reporting covered and uncovered triangles rendered using binary colouring (zero coverage triangles = 37), sampling density overlaid to triangle mesh (shown in normalised form), point-to-surface distances within each triangle (range of ±0.5 mm), mesh triangles coloured using the dispersion of signed point-to-surface distances (shown in normalised form)

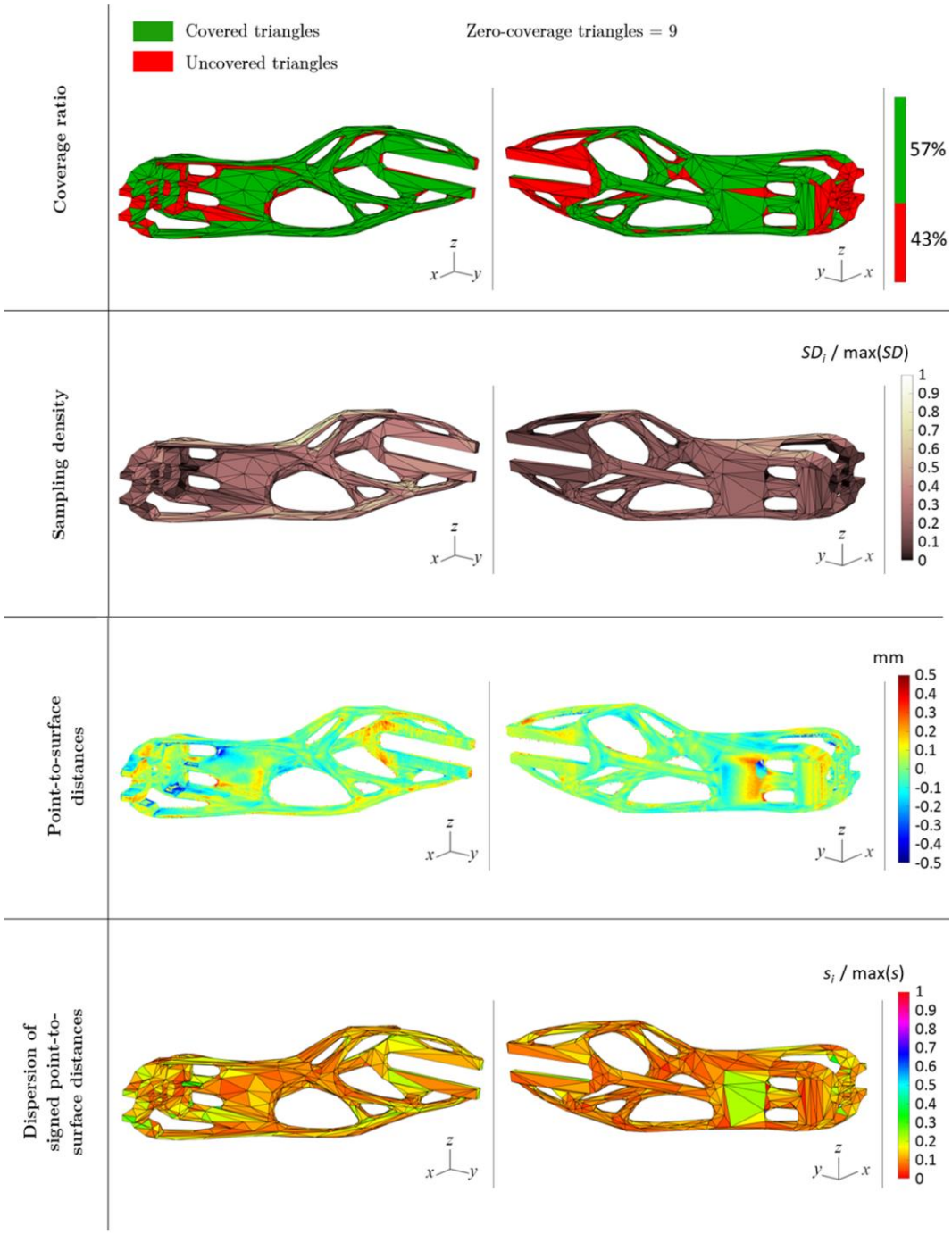

Figure A.7 Repeat 5_PG indicators results in form of customised colour maps (front and back views): coverage ratio reporting covered and uncovered triangles rendered using binary colouring (zero coverage triangles = 9); sampling density overlaid to triangle mesh (shown in normalised form), point-to-surface distances within each triangle (range of ±0.5 mm), mesh triangles coloured using the dispersion of signed point-to-surface distances (shown in normalised form)

A.2 Results for fringe projection

The following table and figures reported in this section of the appendix show the complete collection of the results obtained via the application of the performance indicators on the point clouds acquired with fringe projection. The graphs and colour maps are grouped and shown based on measurement repeat (indicated as "Repeat 1_FP" to "Repeat 5_FP").

Table A.2 Fringe projection repeats: intrinsic properties of the measured point clouds

	Repeat 1_FP	**Repeat 2_FP**	**Repeat 3_FP**	**Repeat 4_FP**	**Repeat 5_FP**
Number of points in the raw dataset	912,502	956,247	848,886	829,648	948,120
Number of points in the final point cloud	524,201	552,880	476,991	463,602	547,077
Point-to-point spacing	0.123 mm	0.120 mm	0.127 mm	0.129 mm	0.121 mm

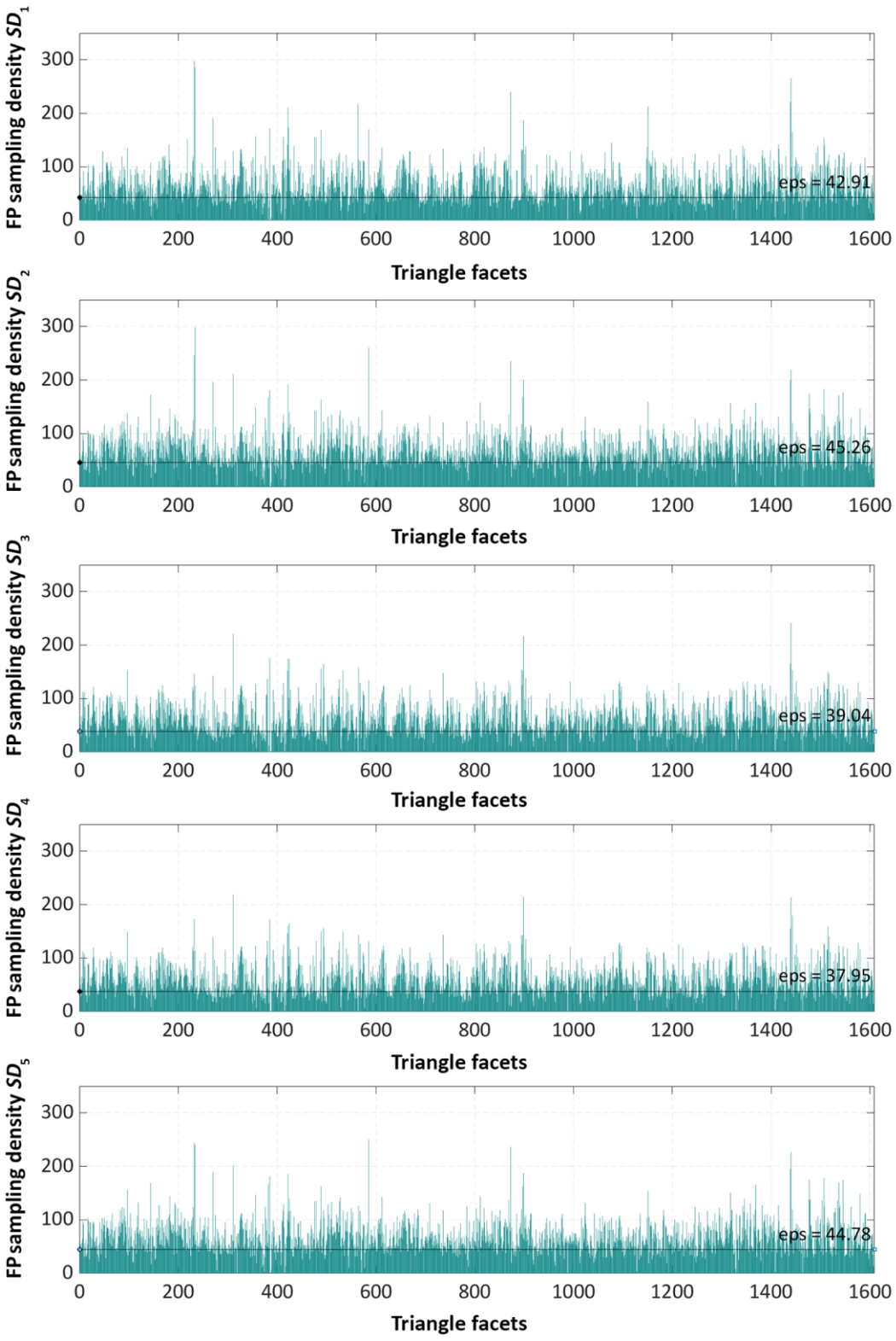

Figure A.8 Bar plots proportional to sampling density for each FP measurement repeat. Sampling density expresses the number of points per unit area of each triangle facet; eps indicates the threshold value at 75% of total detected density

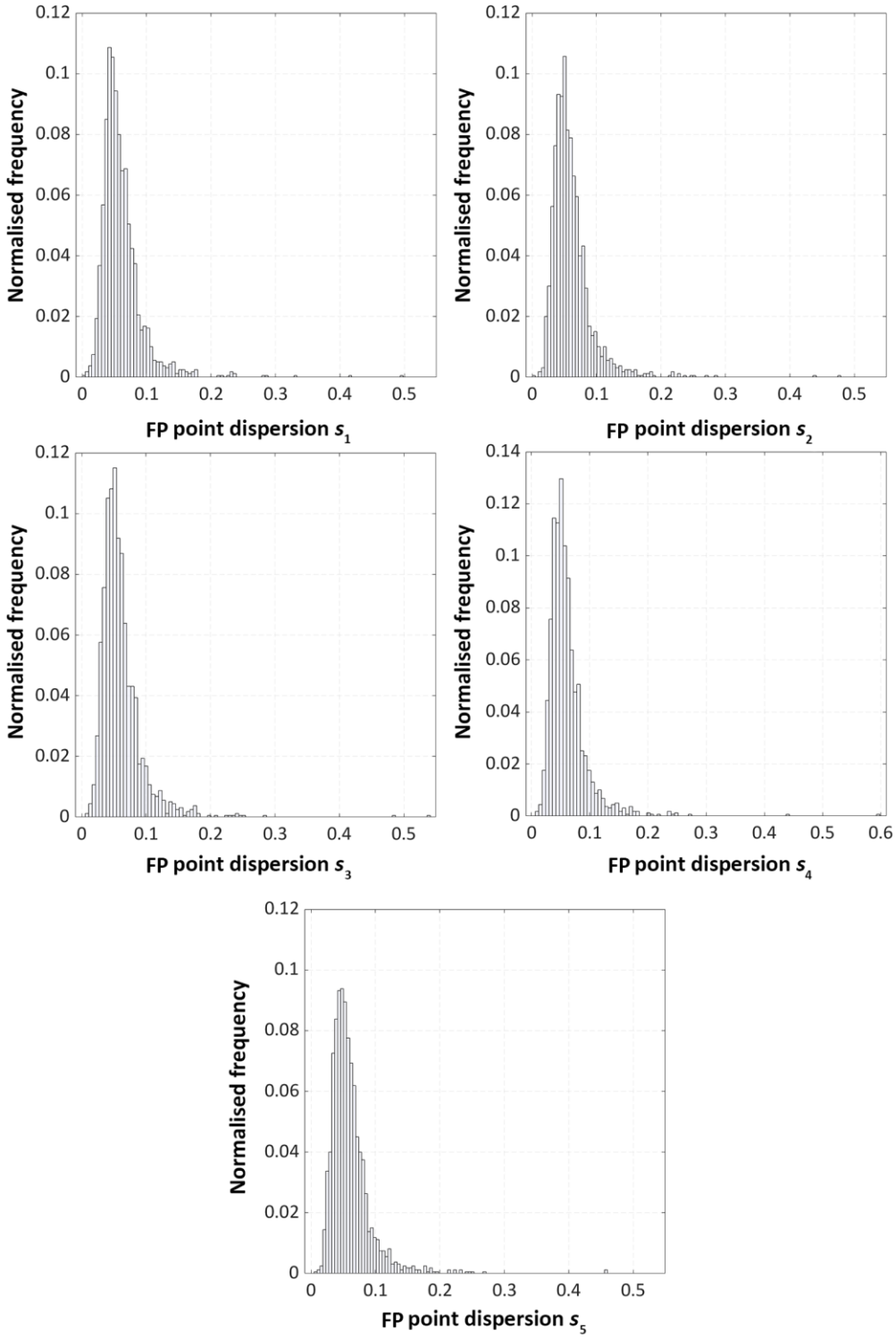

Figure A.9 Histograms of point dispersion values for each measurement repeat of FP, indicated as $s_1, s_2, \ldots, s_5$. Point dispersion is expressed in millimetres; normalised frequency (vertical axes) is the number of occurrences of the values in a bin, divided by the total number of occurrences

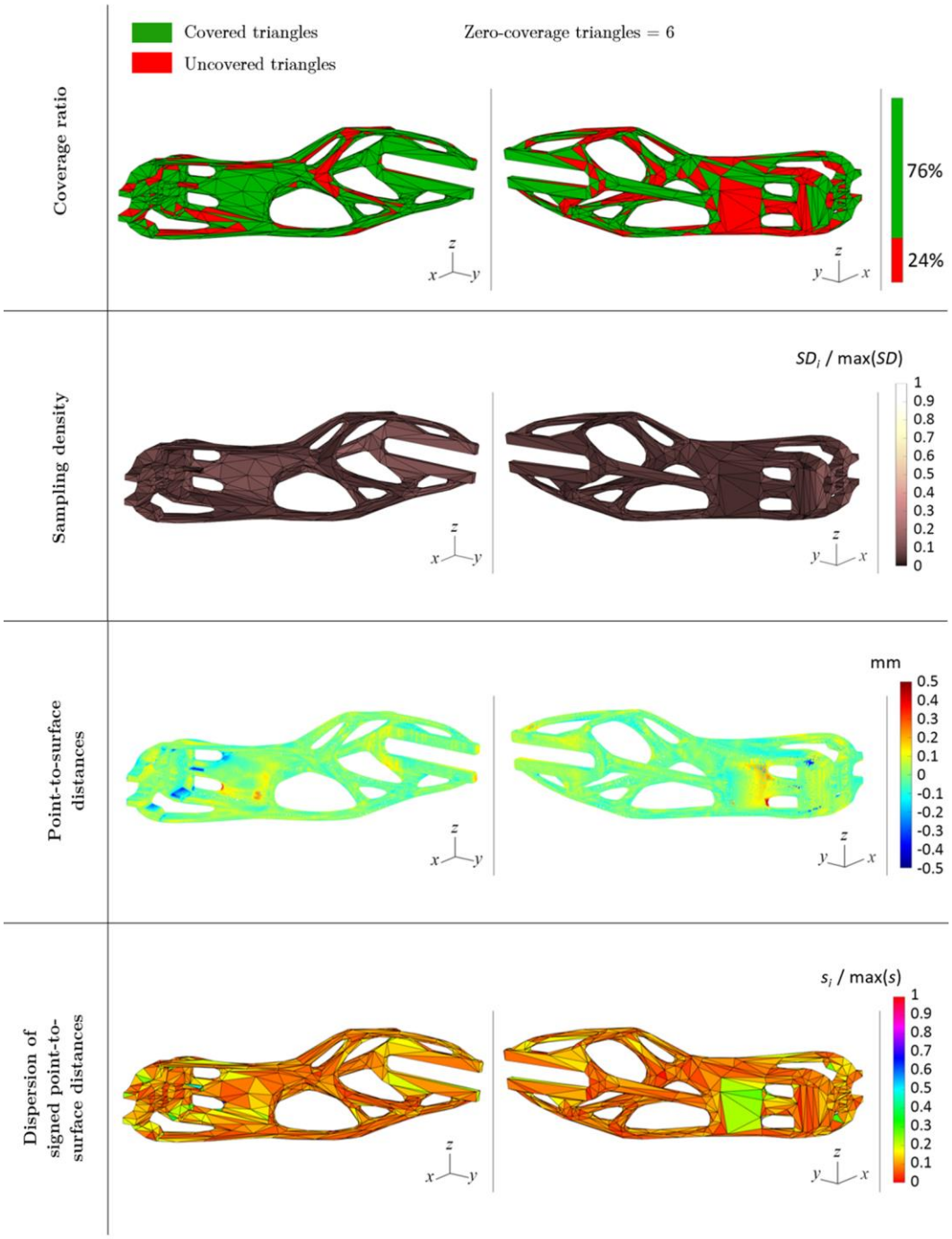

Figure A.10 Repeat 1_FP indicators results in form of customised colour maps (front and back views): coverage ratio reporting covered and uncovered triangles rendered using binary colouring (zero coverage triangles = 6); sampling density overlaid to triangle mesh (shown in normalised form), point-to-surface distances within each triangle (range of ±0.5 mm), mesh triangles coloured using the dispersion of signed point-to-surface distances (shown in normalised form)

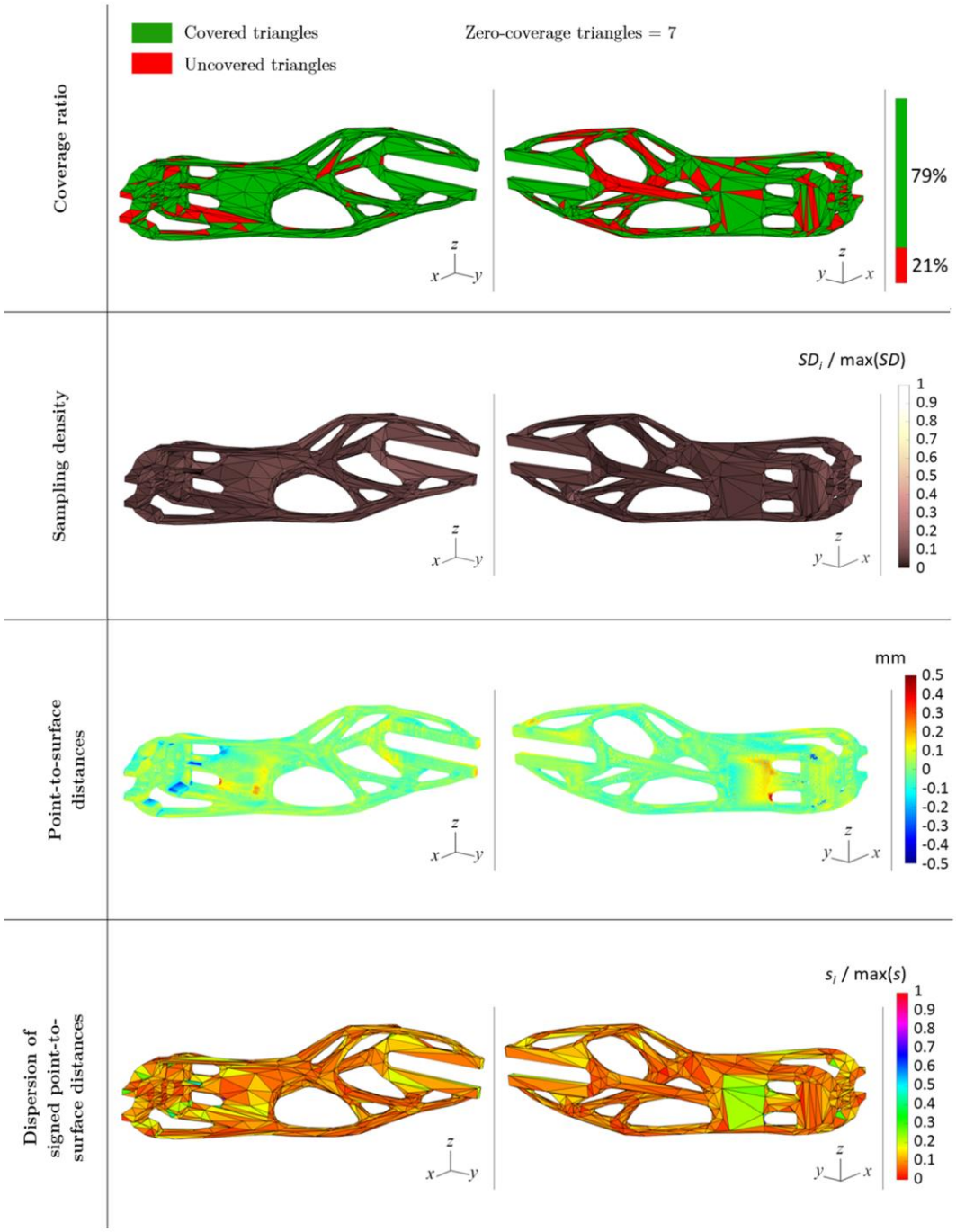

Figure A.11 Repeat 2_FP indicators results in form of customised colour maps (front and back views): coverage ratio reporting covered and uncovered triangles rendered using binary colouring (zero coverage triangles = 7); sampling density overlaid to triangle mesh (shown in normalised form), point-to-surface distances within each triangle (range of ±0.5 mm), mesh triangles coloured using the dispersion of signed point-to-surface distances (shown in normalised form)

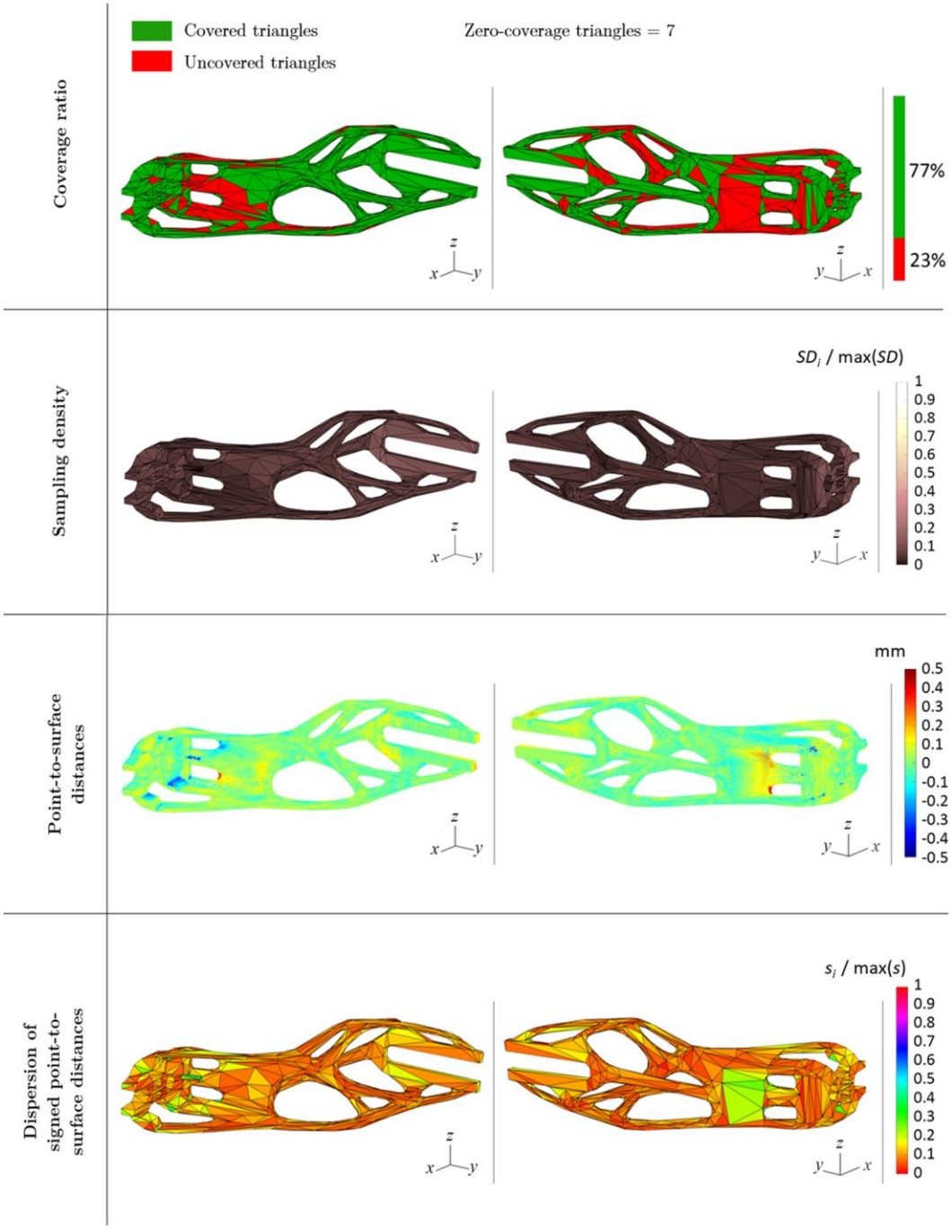

Figure A.12 Repeat 3_FP indicators results in form of customised colour maps (front and back views): coverage ratio reporting covered and uncovered triangles rendered using binary colouring (zero coverage triangles = 7); sampling density overlaid to triangle mesh (shown in normalised form), point-to-surface distances within each triangle (range of ±0.5 mm), mesh triangles coloured using the dispersion of signed point-to-surface distances (shown in normalised form)

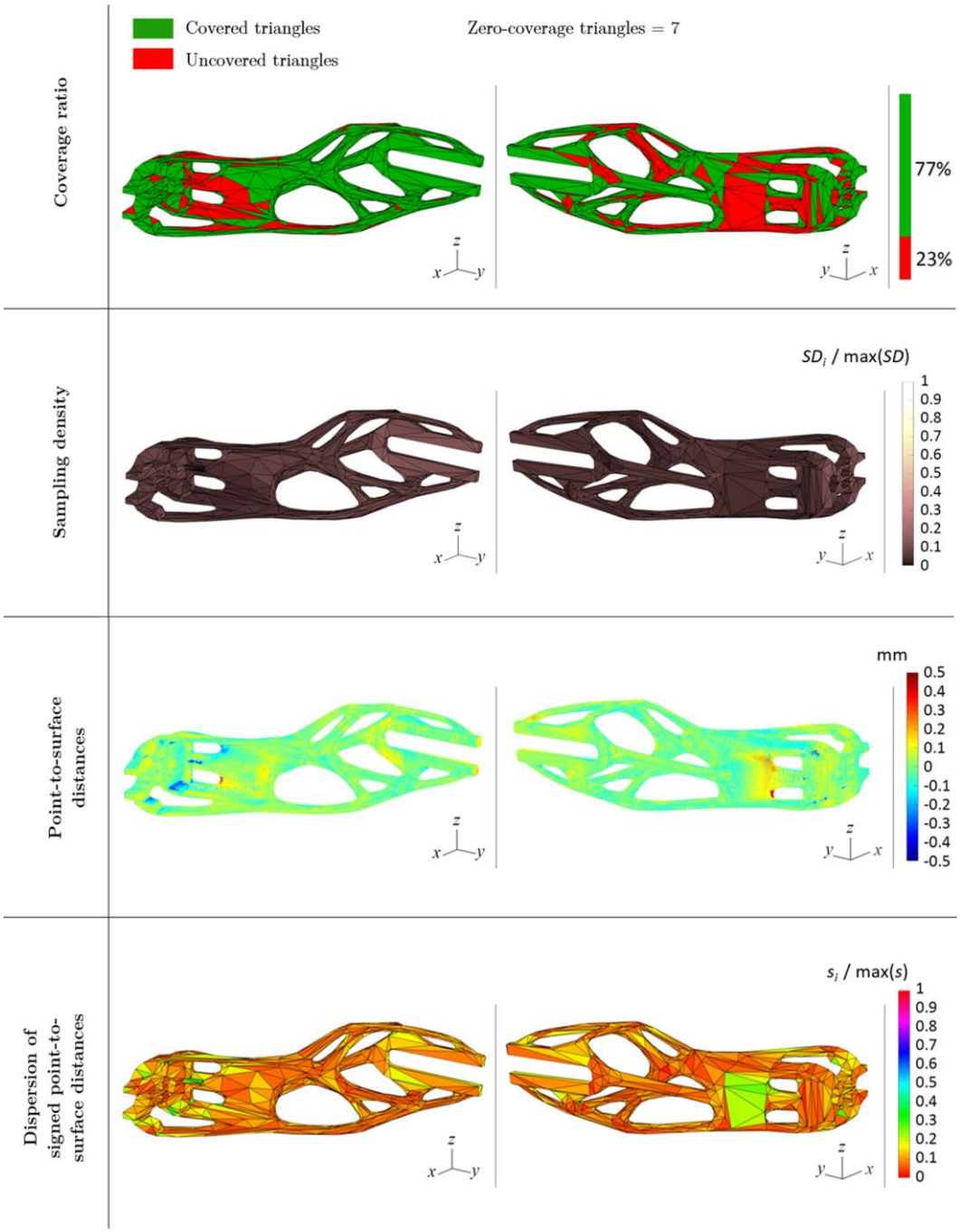

Figure A.13 Repeat 4_FP indicators results in form of customised colour maps (front and back views): coverage ratio reporting covered and uncovered triangles rendered using binary colouring (zero coverage triangles = 7); sampling density overlaid to triangle mesh (shown in normalised form), point-to-surface distances within each triangle (range of ±0.5 mm), mesh triangles coloured using the dispersion of signed point-to-surface distances (shown in normalised form)

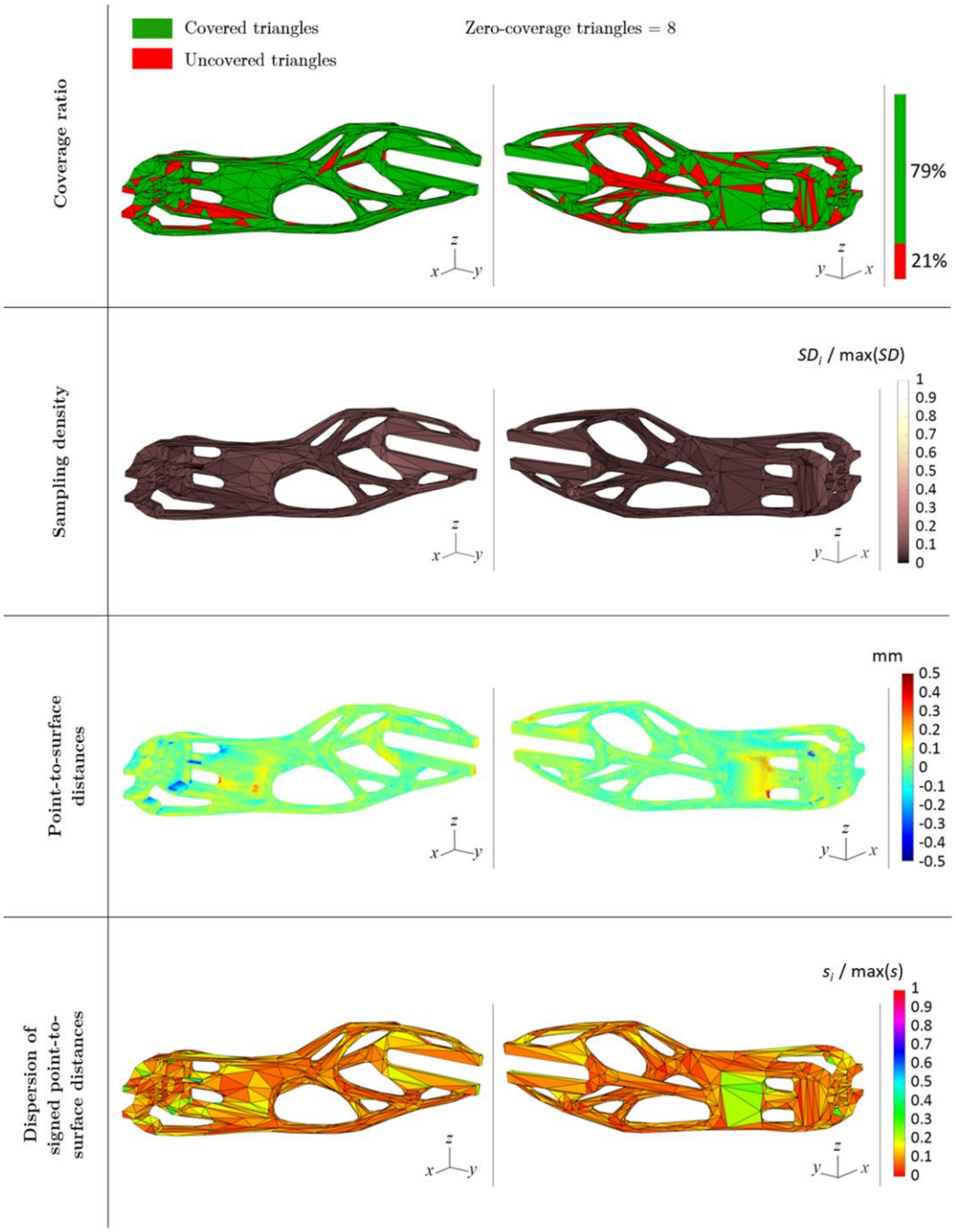

Figure A.14 Repeat 5_FP indicators results in form of customised colour maps (front and back views): coverage ratio reporting covered and uncovered triangles rendered using binary colouring (zero coverage triangles = 8); sampling density overlaid to triangle mesh (shown in normalised form), point-to-surface distances within each triangle (range of ±0.5 mm), mesh triangles coloured using the dispersion of signed point-to-surface distances (shown in normalised form)

A.3 Results for structured light speckle projection

The following table and figures reported in this section of the appendix show the complete collection of the results obtained via the application of the performance indicators on the point clouds acquired with structured light speckle projection. The graphs and colour maps are grouped and shown based on measurement repeat (indicated as "Repeat 1_SL" to "Repeat 5_SL").

Table A.3 Structured light repeats: intrinsic properties of the measured point clouds

	Repeat 1_SL	**Repeat 2_SL**	**Repeat 3_SL**	**Repeat 4_SL**	**Repeat 5_SL**
Number of points in the raw dataset	1,242,760	1,084,973	1,084,973	1,091,913	1,050,946
Number of points in the final point cloud	79,381	81,809	97,756	100,272	85,337
Point-to-point spacing	0.173 mm	0.175 mm	0.168 mm	0.163 mm	0.167 mm

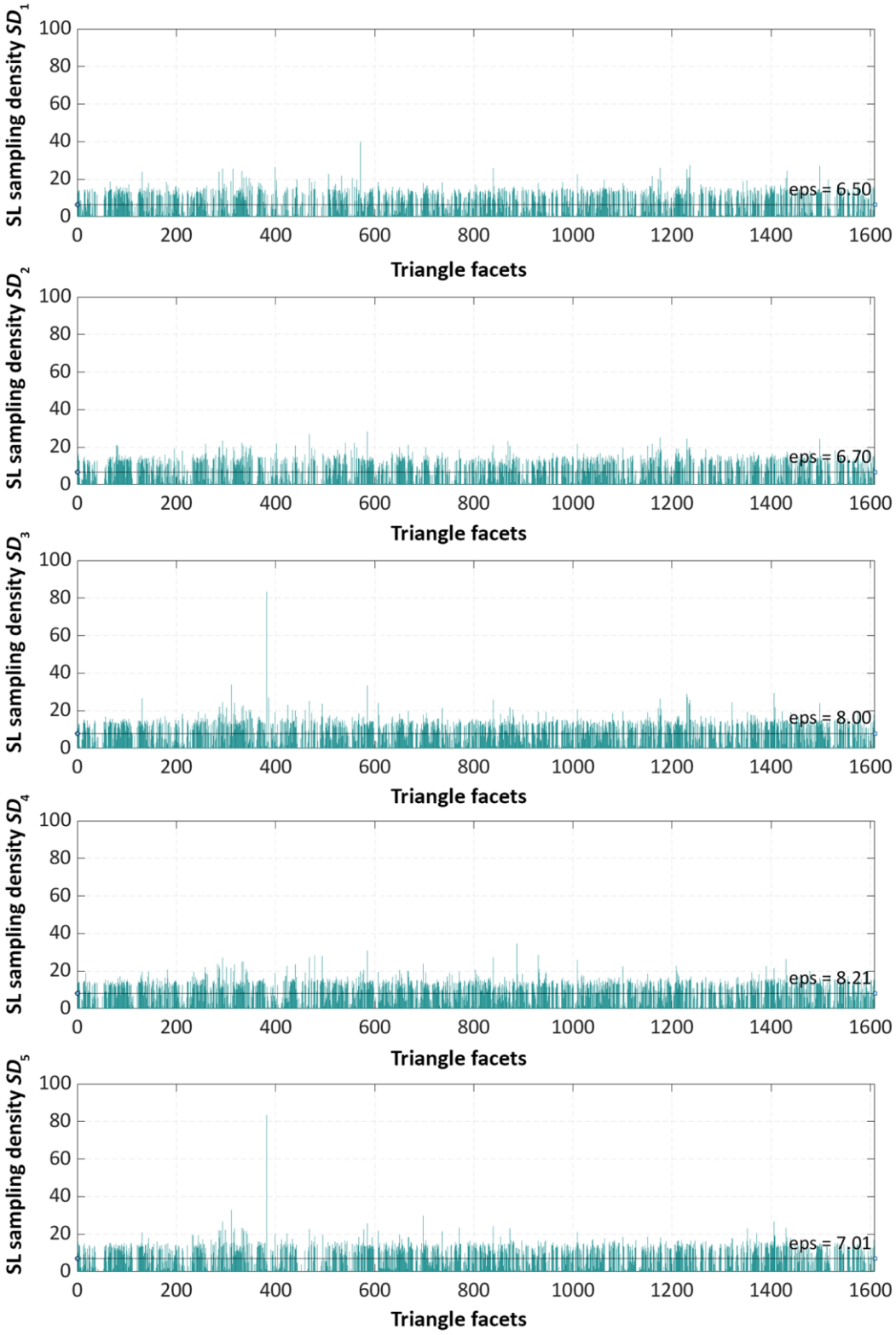

Figure A.15 Bar plots proportional to sampling density for each SL measurement repeat. Sampling density expresses the number of points per unit area of each triangle facet; eps indicates the threshold value at 75% of total detected density

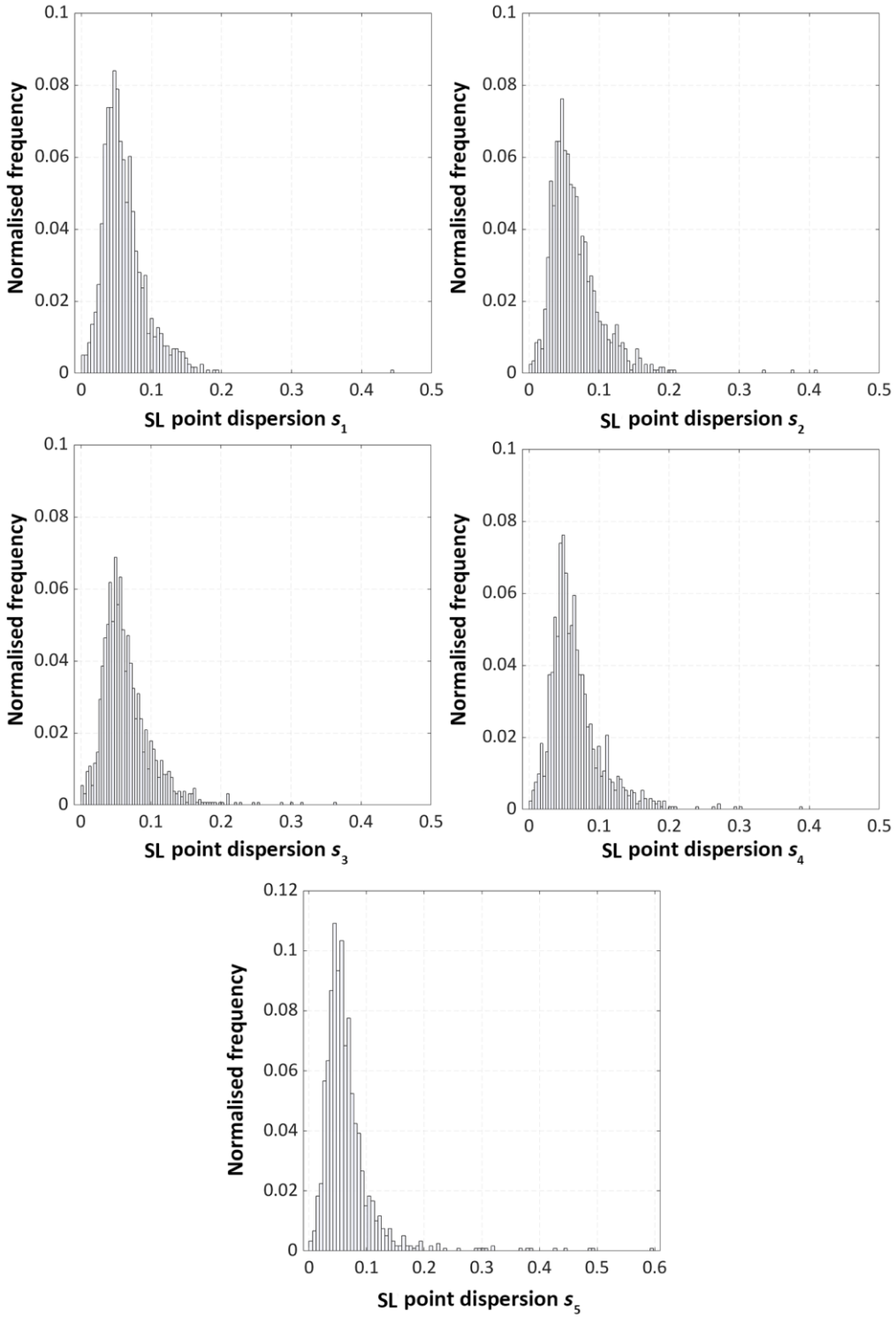

Figure A.16 Histograms of point dispersion values for each measurement repeat of SL, indicated as $s_1, s_2, \ldots, s_5$. Point dispersion is expressed in millimetres; normalised frequency (vertical axes) is the number of occurrences of the values in a bin, divided by the total number of occurrences

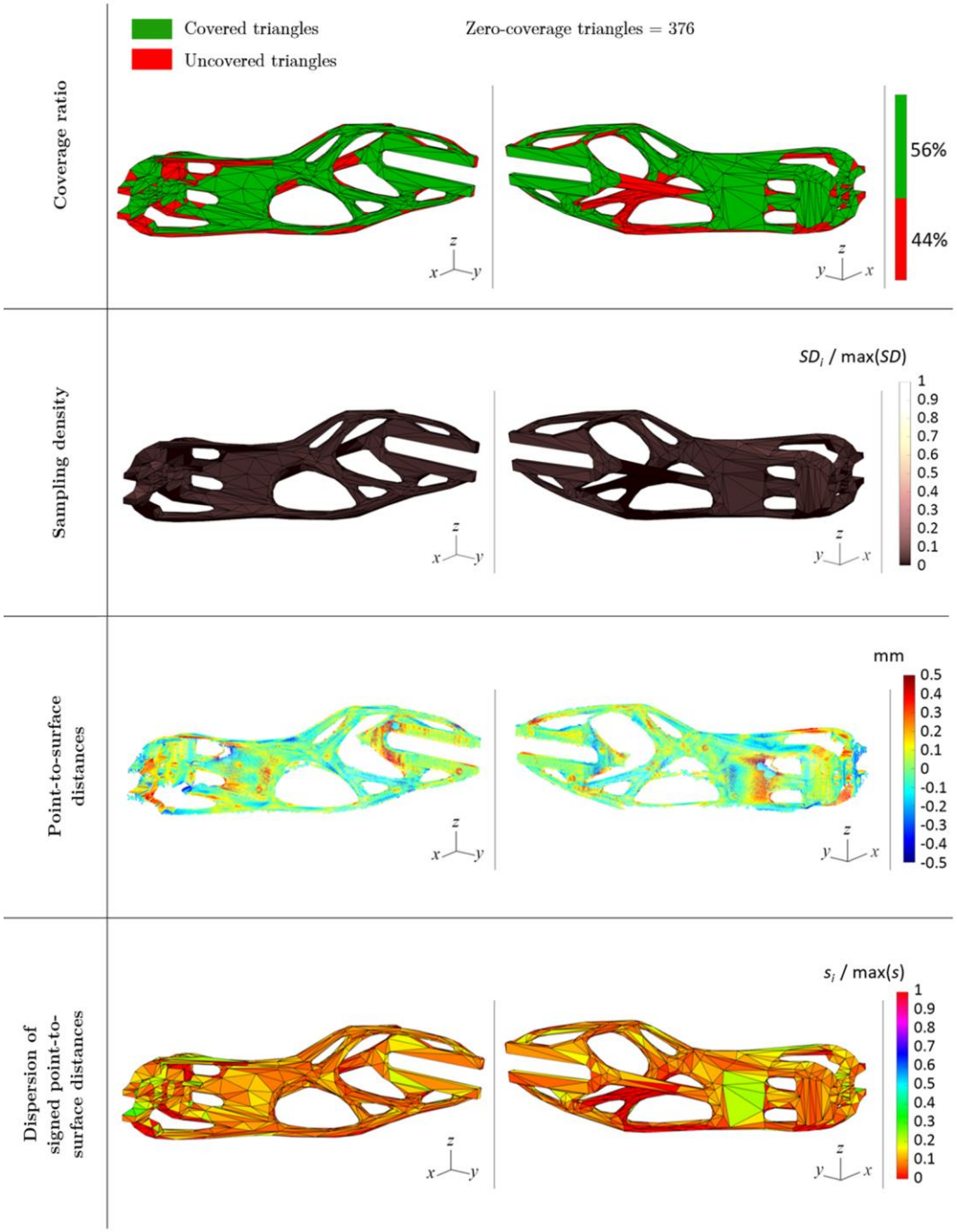

Figure A.17 Repeat 1_SL indicators results in form of customised colour maps (front and back views): coverage ratio reporting covered and uncovered triangles rendered using binary colouring (zero coverage triangles = 376); sampling density overlaid to triangle mesh (shown in normalised form), point-to-surface distances within each triangle (range of ±0.5 mm), mesh triangles coloured using the dispersion of signed point-to-surface distances (shown in normalised form)

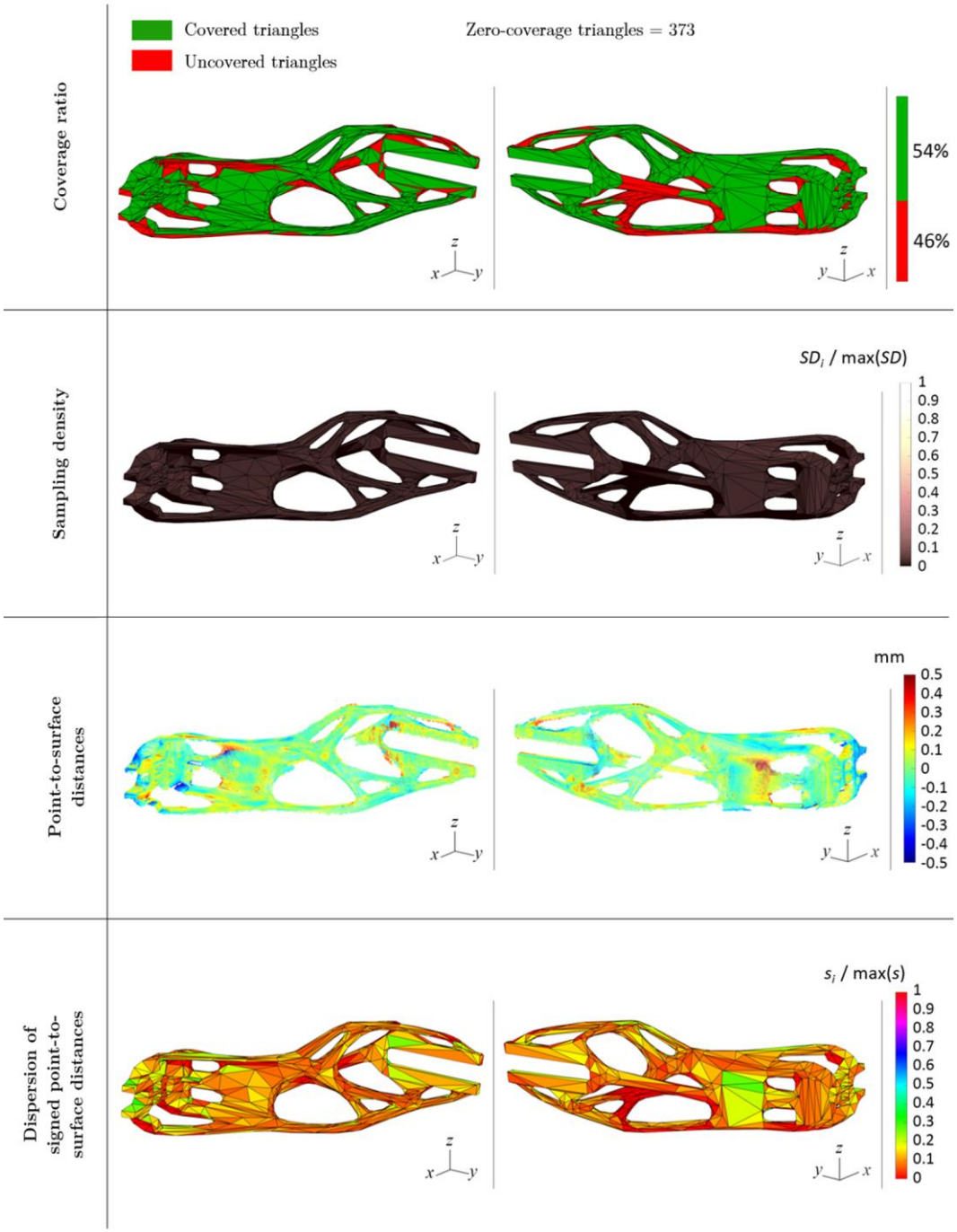

Figure A.18 Repeat 2_SL indicators results in form of customised colour maps (front and back views): coverage ratio reporting covered and uncovered triangles rendered using binary colouring (zero coverage triangles = 373); sampling density overlaid to triangle mesh (shown in normalised form), point-to-surface distances within each triangle (range of ±0.5 mm), mesh triangles coloured using the dispersion of signed point-to-surface distances (shown in normalised form)

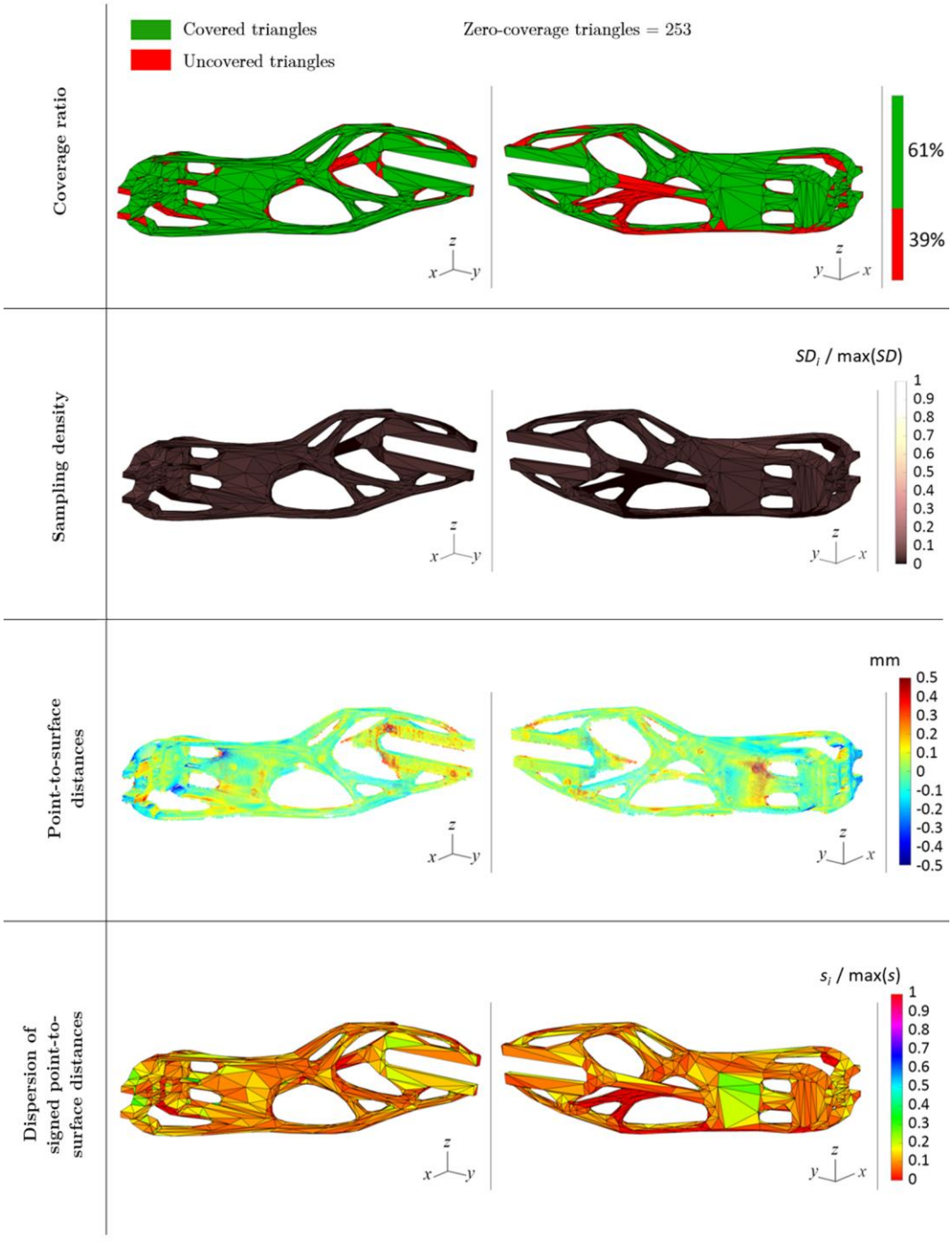

Figure A.19 Repeat 3_SL indicators results in form of customised colour maps (front and back views): coverage ratio reporting covered and uncovered triangles rendered using binary colouring (zero coverage triangles = 253); sampling density overlaid to triangle mesh (shown in normalised form), point-to-surface distances within each triangle (range of ±0.5 mm), mesh triangles coloured using the dispersion of signed point-to-surface distances (shown in normalised form)

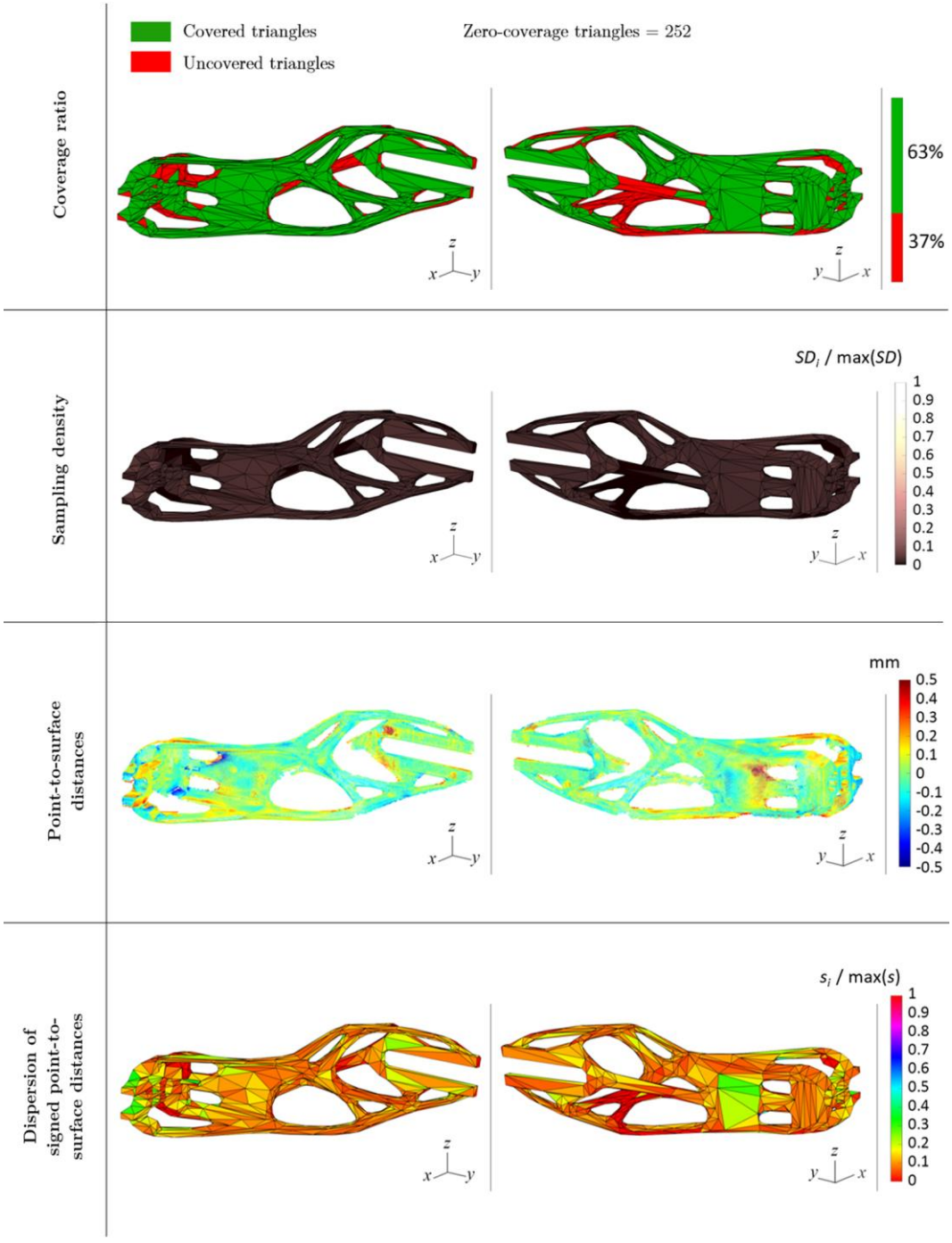

Figure A.20 Repeat 4_SL indicators results in form of customised colour maps (front and back views): coverage ratio reporting covered and uncovered triangles rendered using binary colouring (zero coverage triangles = 252); sampling density overlaid to triangle mesh (shown in normalised form), point-to-surface distances within each triangle (range of ±0.5 mm), mesh triangles coloured using the dispersion of signed point-to-surface distances (shown in normalised form)

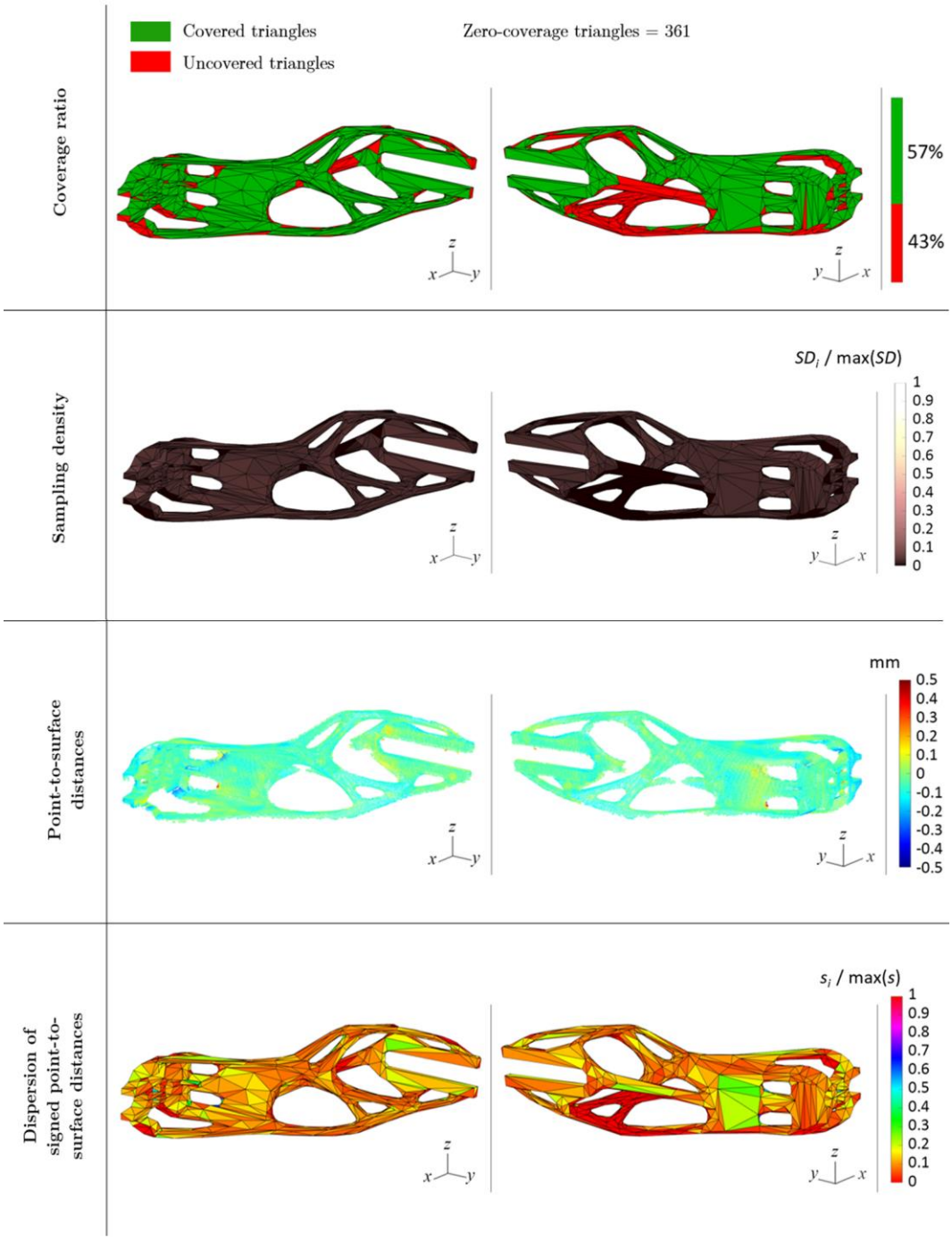

Figure A.21 Repeat 5_SL indicators results in form of customised colour maps (front and back views): coverage ratio reporting covered and uncovered triangles rendered using binary colouring (zero coverage triangles = 361); sampling density overlaid to triangle mesh (shown in normalised form), point-to-surface distances within each triangle (range of ±0.5 mm), mesh triangles coloured using the dispersion of signed point-to-surface distances (shown in normalised form)